

# **Micromechanical Analysis of Pharmaceutical Granules using Advanced Experimental Imaging Methodologies**

By

**Saeed Mohammed A. Albaraki**

Submitted in accordance with the requirements for the degree of  
**Doctor of Philosophy**

**The University of Leeds**  
**Institute of Particle Science and Engineering**  
**School of Chemical and Process Engineering**

**October 2015**

The candidate confirms that the work submitted is his own, except where work which has formed part of jointly-authored publications has been included. The contribution of the candidate and the other authors to this work has been explicitly indicated below. The candidate confirms that appropriate credit has been given within the thesis where reference has been made to the work of others.

Chapters 3-6 of this thesis contain some materials from previous jointly authored publications as shown below. Furthermore, manuscripts for journal publications are currently being made.

Albaraki, S. & Antony, S. J. 2014. How does internal angle of hoppers affect granular flow? Experimental studies using Digital Particle Image Velocimetry. *Powder Technology*, 268, 253-260.

Albaraki, S., Antony, S. J. & Arowosola, C. B. 2013. Visualising shear stress distribution inside flow geometries containing pharmaceutical powder excipients using photo stress analysis tomography and DEM simulations. *AIP Conference Proceedings*, 2013. 706-709.

Antony, S. J., Albaraki, S., Mandare, A. & Arowosola, B. C. 2014. Current developments on the flow behaviour of particulate materials using advanced simulations and tomography experiments. *Particulate Systems Analysis* 2014, Manchester, UK

Antony, S. J., Barakat, T., Hammond, R. B., Sheeba, K. N., Amanbayev, T., Okeke1, G., Albaraki, S., Arowosola, C. B. & Olugbenga, A. 2013. Multiscale particulate mechanics in multi-disciplinary engineering applications, UK-China International Particle Technology Forum, China.

Albaraki, S. & Antony, S. J. 2013. Investigation on the effects of initial stress state of powder packing on macroscopic powder flow properties The International Porous and Powder Materials Symposium and Exhibition Izmir, Turkey.

Albaraki, S., Afzal, Z., Arowosola, B. & Antony, S. J. 2013. Effect of granular microscopic characteristics on flow macroscopic behaviour. *PharmSci*. Nottingham,UK.

Antony, S. J., Albaraki, S., Arowosola, B. C. & Agarwal, N. 2012. Novel visual Probing of shear stress distribution inside pharmaceutical powder packing within constrained geometries using photo stress analysis tomography *PharmSci*. Nottingham,UK.

This copy has been supplied on the understanding that it is copyright material and that no quotation from the thesis may be published without proper acknowledgement.

© 2015 The University of Leeds and Saeed Mohammed Albaraki

*In Memory of My Parents*

*Dedicated to*

*My wife, my sons and daughters*

## **Acknowledgment**

During the development and progress of this research project, I had a great opportunity to work with many wonderful and extremely helpful colleagues throughout, with well-equipped laboratories within the University of Leeds in general, and the School of Chemical and Process Engineering in particular. Firstly, and most importantly I would like to thank Almighty Allah for his generous mercy over me, and for giving me the strength to finish this project. Second, I would like to take this opportunity to express my grateful thanks to my supervisor, Dr Joseph Antony for his patience and for his continuous outstanding support, motivation and supervision throughout the period of my PhD research.

I would also extend my thanks to Dr Gareth Keevil in the School of Earth Science for his appreciated help to start the application of digital particle image velocimetry. Thanks also must go to Prof. Michael Fairweather and John Vickers for allowing me to use their DPIV facilities before my research group procured. Many thanks to Dr Timothy Comyn for his valuable help with the XRDS characterisation of the granular materials used in this study. I would also like to thank Prof. Mojtaba Ghadiri and his research group, especially Dr Umair Zafar for allowing me to use the laboratories for characterising granules and conducting compression tests using Instron machines.

I would also like to thank Mr Adrian Eagles in the School of Mechanical Engineering for helping to measure the surface roughness of the materials. I would like to acknowledge the support of Mr Graham Brown and his colleagues in the mechanical engineering workshop for helping in the fabrication of compression chamber and hopper geometries.

I would also like express my appreciation to my research group member Mr Arowosola, Babatunde who helped in conducting the DEM simulations for the comparison purposes with the experimental approaches.

I would also like to thank the members of my research group Dr George Okeke and Mrs. Adeola Olugbenga for their support and company during my stay in Leeds.

## **Abstract**

Fundamental level understandings on the processing behaviours of materials in granular and powder form is of high interest to number of engineering industries for example, mining, mineral, pharmaceutical, geotechnical and for advanced material processing applications. Handling and processing of pharmaceutical powders through confined geometries have very important role in pharmaceutical industry and many related powder process engineering sectors. Smooth flow of powders and granules mixtures from the feeding hopper to the compression chamber plays a very crucial role to achieve the integrity and quality of the final product. In this context, establishing clear understandings on the flow and compaction characteristics of particulates is vital.

The mechanical behaviour of particulate materials such as powders and grains are different from the conventional states of matter. Depending on the loading levels and geometrical conditions, often they display combined features of solid, liquid and gaseous states. Though an extensive amount of studies are reported in the existing literatures on their mechanical response to loading, there are still a number of challenges to address: (i) Sensing stress distribution in particulate systems is not yet established especially when the size of the particulates are less than a millimetre (ii) Understanding is lacking on whether the stress distribution in initial static filling would influence the dynamic flow trajectories of the particulates when they are allowed to flow from the static state (iii) Micromechanical behaviour of particulates under low levels of external loading is still lacking and (iv) Interaction characteristics of stress and velocity distributions in particulate systems as a function of grain-scale properties and geometrical arrangements are still lacking. The present thesis addresses all of these important challenges in a systematic manner. The research is primarily based on the application of sensing stresses and displacements in particulates using advanced photo stress analysis tomography (PSAT), qualitative velocimetry using colour coding technique (CCT) and quantitative digital particle image velocimetry (DPIV). The required grain-scale properties are characterised comprehensively using a number of standard experimental methods. Where possible, experimental results on the stress and

velocity distribution for particulate systems are compared with simulations using discrete element method (DEM) and analytical equations respectively, though the primary focus is on the experimental approaches. A number of outcomes from this research shed new lights and provide fundamental level understandings on the micromechanical properties of particulate systems with relevance to pharmaceutical granules processes.

## **Table of Contents**

<b>Acknowledgment .....</b>	<b>IV</b>
<b>Abstract .....</b>	<b>VI</b>
<b>Table of Contents .....</b>	<b>VIII</b>
<b>List of Figures .....</b>	<b>XII</b>
<b>List of Tables .....</b>	<b>XXII</b>
<b>Nomenclature .....</b>	<b>XXIII</b>
<b>Chapter 1 Introduction to the Project.....</b>	<b>1</b>
1.1    Introduction .....	1
1.2    Aim of thesis .....	4
1.3    Structure of the Thesis .....	6
<b>Chapter 2 : Mechanical Behaviour of Granular Materials: Background and Recent Technical Developments.....</b>	<b>7</b>
2.1    Granular Materials Background.....	7
2.1.1 Contact Force Network in Granular Materials.....	9
2.1.2 Stress Analysis: Background in Brief .....	13
2.2    Granular Materials Flow Behaviours inside Silos and Hopper Geometries .....	17
2.2.1 Analytical Methods .....	20
2.2.2 Experimental Methods .....	27
2.2.3 Simulation Methods .....	30
2.3    Powders and Granular Materials Subjected to Compression.....	33
2.3.1 Mathematical Methods.....	35
2.3.2 Heckel's Equation .....	35
2.3.3 Computational Methods .....	38
2.3.4 Compression Process Cycle .....	41
2.4    Photostress Measurements .....	44
2.4.1 Background of Photoelasticity .....	45
2.4.2 Light Principles and Physics .....	45
2.4.3 Polariscopes .....	47
2.4.4 Isoclinic and Isochromatic Fringes .....	49
2.4.5 Birefringence and Optical Anisotropy .....	50
2.4.6 Advanced Applications of Photoelasticity .....	52

2.4.7 Application of Photoelasticity in Pharmaceutical Industry.....	53
2.5 Digital Particle Image Velocimetry .....	54
2.5.1 Application of DPIV and PIV: Granular Flows.....	55
2.5.2 Application of DPIV and PIV: Granular Materials Subjected to Compression .....	59
2.6 Conclusions.....	60
<b>Chapter 3 : Fabrication and Characterisation of Pharmaceutical Granules for PSAT and DPIV Applications.....</b>	<b>62</b>
3.1 Introduction .....	62
3.1.1 Starch.....	62
3.1.2 Granulation Technique.....	68
3.2 Fabrication of Stress Responsive Granules for PSAT Applications.....	71
3.2.1 Materials and Methodology .....	71
3.2.2 Characterisation and Physiomechanical Properties of the Stress Responsive Granules .....	74
3.3 Fabrication of Colour Coded Granules for Qualitative Dynamic Flow Analysis and DPIV Applications .....	83
3.3.1 Materials and Methodology .....	83
3.3.2 Materials.....	83
3.3.3 Method of Fabrication.....	83
3.3.4 Physiomechanical Properties of the Fabricated Granules .....	83
3.4 Conclusions .....	84
<b>Chapter 4 : Experimental Visualising and Analysis of Maximum Shear Stress Distribution and Direction of Principal stresses inside particulate packing at Static Condition .....</b>	<b>85</b>
4.1 Introduction .....	85
4.2 Material and Methodology .....	87
4.2.1 Material .....	87
4.2.2 Methodology .....	88
4.2.3 PSAT System Limitations.....	89
4.3 Results and Discussions .....	90
4.3.1 Hopper Geometry Having a 30° Internal Angle.....	90
4.3.2 Hopper Geometry Having a 60° Internal Angle.....	95
4.3.3 Hopper Geometry Having a 90° Internal Angle.....	100
4.3.4 General Remarks for the Experimental Results and Numerical Validation of the Stress Profiles Distribution. ....	105

4.4 Conclusions .....	109
<b>Chapter 5 Analysis of Bulk Dynamic Flow characteristics of grains inside 2D Converging Hopper Geometries Using Colour Coding Technique ...</b>	<b>112</b>
5.1 Introduction .....	112
5.2 Material and Methodology .....	113
5.2.1 Material .....	113
<b>5.2.2 Methodology .....</b>	<b>113</b>
5.3 Results and Discussions .....	115
5.3.1 Hopper Geometry Having a 30° Internal Angle .....	115
5.3.2 Hopper Geometry Having a 60° Internal Angle .....	117
5.3.3 Hopper Geometry Having a 90° Internal Angle .....	124
5.4 Conclusions .....	130
<b>Chapter 6 Analysis of the Granular Materials Dynamic Flow trend inside 2D Converging Hopper Geometries Using Digital Particle Image Velocimetry (DPIV) .....</b>	<b>132</b>
6.1 Introduction .....	132
6.2 Material and Methodology .....	133
6.2.1 Material .....	133
6.2.2 Methodology .....	133
6.3 Results and Discussion.....	136
6.3.1 Hopper Geometry Having a 30° Internal Angle .....	136
6.3.2 Hopper Geometry Having a 60° Internal Angle .....	149
6.3.3 Hopper Geometry Having a 90° Internal Angle .....	164
6.3.4 General Remaks .....	181
6.4 Conclusions .....	184
<b>Chapter 7 Visual Mapping of Stress Distribution Profiles within Pharmaceutical Granular Bed Subjected to Relatively Low Uniaxial Confined Compression Using PSAT .....</b>	<b>186</b>
7.1 Introduction .....	186
7.2 Material and Methodology .....	188
7.2.1 Material .....	188
7.2.2 Methodology .....	189
7.3 Results and Discussion.....	190
7.4 Conclusions .....	201

<b>Chapter 8 Velocity Profiles Distribution inside Pharmaceutical Granules Subjected to Relatively Low Uniaxial Confined Compression Using DPIV .....</b>	203
8.1    Introduction .....	203
8.2    Material and Methodology .....	204
8.2.1 Material .....	204
8.2.2 Methodology .....	204
8.3    Results and Discussions .....	206
8.4    Conclusions .....	216
<b>Chapter 9 Conclusions and Recommended Future Work .....</b>	217
9.1    Conclusions .....	217
9.2    Relevance of Experiments to the Framework of Forces and Mobilised Shear Stress Propagation under Relatively Low Uniaxial Compression.....	221
9.3    Recommended Future Work .....	225

## List of Figures

Figure 1.1 Project overview .....	5
Figure 2.1 Solid, liquid, and gas regions in steel particles in rotating drum (Forterre and Pouliquen, 2008) .....	8
Figure 2.2 Bunkers wall pressure and stress profile distribution respectively, in bulk solids and liquids (Schulze, 2008) .....	9
Figure 2.3 Force network of granular matter is non-homogeneous in space as observes using photoelastic disks, (a) macroscopic view within the entire bed, (b) circles illustrates true contact, square show fales apparent contact, (c) single particle level contacts, (Majmudar et al., 2007) .....	10
Figure 2.4 Force network and sliding contact in granular system using 2-D DEM application. Thickness of the lines is proportional to normal force magnitude (Antony, 2007) .....	12
Figure 2.5 Stress tensor components in rectangular coordinates (Smith, 1990 ).....	14
Figure 2.6 2D stress mathematical and graphical case (a) stress cube, and (b) Mohr's circle construction .....	15
Figure 2.7 Maximum shear stress and average stress in Mohr's circle for two dimensional stress system .....	17
Figure 2.8 Classification of flow behaviour in silos (Watson and Rotter, 1996)....	19
Figure 2.9 Diagram of element slice method and its wall contacts .....	21
Figure 2.10 Active and passive wall stress state and major pressure directions in vertical silo and hopper sections (Jenike and Johanson, 1969) .....	24
Figure 2.11 Initial hopper wall pressure exerted by bulk solids at the filling phase (Walker, 1966) .....	25
Figure 2.12 Walker and Walter slice element method .....	27
Figure 2.13 Wall stress measurement method using embedded loading gauges on hopper walls; (a) location of gauges and hopper internal angles (b) drawing diagram of gauge (Chou and Chen, 2003) .....	28
Figure 2.14 Multiple stages involved in tablet manufacturing Modified from Muzzio et al. (2002).....	33
Figure 2.15 Schematic plot of Heckel profile during compression and decompression process (Modified from (Comoglu, 2007) .....	36
Figure 2.16 Linear Kawakita plot for powder compression (Modified from (Kawakita and Lüdde, 1971).....	38
Figure 2.17 Light propagation and polarisation using simple polariser.....	46

Figure 2.18 Diagram illustrating the proper arrangement of plane polariscope (McKenzie and Hand, 1999).....	48
Figure 2.19 Diagram illustrating the arrangement of circular polariscope (McKenzie and Hand, 1999).....	49
Figure 2.20 Photoelastic fringes; a) isoclinic fringes, b) isochromatic fringes for a disk under axial compression (McKenzie and Hand, 1999).....	50
Figure 2.21 Advanced Photo stress analysis system; a) Computer based photo stress system, b) Maximum shear stress profiles using coating materials (Calvert et al., 2002) .....	53
Figure 3.1 Meyer Bernfeld tree structure for amylopectin .....	63
Figure 3.2 Birefringence of stained starch granules under polarised light microscope as Maltese Cross (Starches, 2015).....	65
Figure 3.3 X-Ray diffraction patterns of (a) native maize starch and (b) low temp incubated maize starch (LT) and (c) high incubated maize starch (HT) (Shamai et al., 2003) .....	67
Figure 3.4 The crystalline and amorphous regions in native starch (Huang et.al., 2007) .....	67
Figure 3.5 Modern approach in wet granulation (Iveson et al., 2001).....	70
Figure 3.6 Very fine native starch powder used for stress responsive granules fabrication .....	72
Figure 3.7 Image of stress responsive granules using iodised corn starch paste .....	73
Figure 3.8 Image of stress responsive granules using non iodised corn starch paste .....	74
Figure 3.9 Comparison of birefringence intensity of the prepared granules, (a) Isochromatic fringes of iodised granules and (b) Isochromatic fringes of non-iodised granules .....	75
Figure 3.10 Particle size distribution of stress responsive granules used in the experimental work for PSAT study .....	79
Figure 3.11 X-Ray diffraction patterns of semi-crystalline native corn starch.....	80
Figure 3.12 X-Ray diffraction patterns of the fabricated stress responsive granules .....	80
Figure 3.13 SEM image of native corn starch and stress responsive granules at different magnification powers .....	82
Figure 3.14 Surface pores on both (a) native starch granules and (b) stress responsive granules .....	82

Figure 4.1 Schematic diagram of 2D hopper geometry internal angle filled by stress responsive granules used in the PSAT study .....	87
Figure 4.2 Experimental setup of the PSAT system for maximum shear stress measurement within granular materials inside hopper geometries; (a) hopper geometry, (b) PSAT software, and (c) PSAT 2D setup.....	88
Figure 4.3 Selected heights for maximum shear stress analysis across the width of the stress responsive granules.....	90
Figure 4.4 Experimental 2D PSAT setup results: (a) maximum shear stress profiles distribution and (b) major principal stress direction inside stress responsive granules at 30° internal angle hopper geometry.....	91
Figure 4.5 Normalised maximum shear stress distribution profiles inside 30° internal angle hopper at multiple heights; H/ $\infty$ , H/4 and H/2 .....	91
Figure 4.6 Normalised average maximum shear stress magnitudes inside 30° internal angle hopper at multiple heights; H/ $\infty$ , H/4 and H/2 .....	92
Figure 4.7 Granular materials equal slices inside 30° internal angle hopper geometry and the point of stress measurement.....	94
Figure 4.8 Normalised maximum shear stress exerted on the hopper wall at the end of the filling process inside 30° hopper geometry .....	94
Figure 4.9 Experimental 2D PSAT setup results: (a) maximum shear stress profiles distributions, and (b) major principal stress directions inside stress responsive granules at 60° internal angle hopper geometry .....	96
Figure 4.10 Normalised maximum shear stress value distribution and its average magnitudes inside 60° internal angle hopper at multiple heights; H/ $\infty$ , H/4 and H/2 .....	97
Figure 4.11 Normalised maximum shear stress exerted on the hopper wall at the end of the filling process inside 60° hopper geometry .....	99
Figure 4.12 Potential flow zones according to the stress magnitudes and the directions of the major principal stresses inside 60° internal angle hopper geometry .....	99
Figure 4.13 Experimental 2D PSAT setup results: (a) maximum shear stress profiles distributions, and (b) major principal stress direction inside stress responsive granules at 90° internal angle hopper geometry .....	100
Figure 4.14 Normalised maximum shear stress profiles distribution and its average values inside 90° internal angle hopper at multiple heights; H/ $\infty$ , H/4 and H/2 .....	102
Figure 4.15 Normalised maximum shear stress exerted on the hopper wall at the end of the filling process inside 90° hopper geometry .....	103

Figure 4.16 Expected flow zones according to the stress magnitudes and the directions of the major principal stresses inside 90° internal angle hopper geometry .....	105
Figure 4.17 Normalised magnitude of maximum shear stress distribution across the width of the hopper at H <sub>00</sub> , H <sub>4</sub> and H <sub>2</sub> within the selected hopper geometries .....	106
Figure 4.18 Cross section of the hopper (schematic) and the confinement of particles .....	108
Figure 4.19 Maximum shear stress distribution for granular bed using DEM simulation (dashed lines) and PSAT experimental work (solid lines) at H/2 across all hoppers geometries .....	109
Figure 5.1 A typical image of granular layers filled inside the hopper ( $\theta=60^\circ$ ) ....	113
Figure 5.2 Diagram of experimental 2D setup of the dynamic flow assessment using coloured granules and high speed camera.....	115
Figure 5.3 Early stage of the dynamic flow process at 30° internal hopper angle .....	115
Figure 5.4 Serial of images show the flow process at late stages of the flow process inside 30° internal angle hopper.....	116
Figure 5.5 Generation of plug flow zone (first flow zone) at 60° internal hopper angle at axisymmetric axis during the early stage of the flow.....	118
Figure 5.6 Tracking of the expansions and changes of the flow zone (second flow zone) at 60° internal hopper angle at second stage of the flow process.....	119
Figure 5.7 Flow process tracking and changes of the flow zone (third flow zone) inside 60° internal hopper angle at the third stage of the flow process.....	120
Figure 5.8 Evolution of the of plug flow zone height measured in the symmetry axis at 60° internal angle hopper geometry .....	121
Figure 5.9 Stagnant zones shapes at the middle and top granular layers at two stages of the flow process .....	122
Figure 5.10 Measurements of stagnant zone dimension changes at the top and middle of 60° internal angle hopper geometry .....	123
Figure 5.11 Generation of plug flow zone (first flow zone) at 9 0° internal hopper angle at axisymmetric axis during the early stage of the flow.....	125
Figure 5.12 Tracking of the expansions and changes of the flow zone (second flow zone) at 90° internal hopper angle at the second stage of the flow process.....	126

Figure 5.13 Tracking of the expansions and changes of the flow zone (third flow zone) at 90° internal hopper angle at third stage of the flow process ....	127
Figure 5.14 Evolution of the height of plug flow zone measured in the symmetry axis at 90° internal angle hopper .....	128
Figure 5.15 Stagnant zones at different hopper segments inside 90° internal angle hopper geometry.....	129
Figure 5.16 Measurments of stagnant zone dimension changes at the top and middle of 90° internal angle hopper geometry.....	130
Figure 6.1 Multiple pharmaceutical excipient granular materials layers inside the hopper ( $\theta = 90^\circ$ ) .....	134
Figure 6.2 Digital particle image velocimetry data analysis fundamentals; area of interest (AOI) and interrogation area (IA).....	135
Figure 6.3 Mean resultant velocity vectors map inside the 30° internal angle hopper geometry filled by coloured pharmaceutical excipient granules .....	137
Figure 6.4 Vertical velocity component plot inside 30° internal angle hopper geometry having a 7mm outlet size measured at three heights ( $H/\infty$ , $H/4$ and $H/2$ ) in 2 <sup>nd</sup> order polynomial plot.....	138
Figure 6.5 Averagr vertical velocity component plot across the hopper width inside 30° internal angle hopper geometry having 7mm outlet size at three heights ( $H/\infty$ , $H/4$ and $H/2$ ).....	138
Figure 6.6 The maximum recorded vertical velocity component values at selected time intervals during the flow process inside 30° internal angle hopper geometry .....	139
Figure 6.7 Mean resultant velocity vectors profiles at 30° internal angle hopper during different time intervals and the corresponding visual images of the dynamic granular flow.....	141
Figure 6.8 Vertical velocity component plot inside 30° internal angle hopper geometry having 10 mm outlet size measured at three heights ( $H/\infty$ , $H/4$ and $H/2$ ) in 2 <sup>nd</sup> order polynomial plot.....	142
Figure 6.9 Average vertical velocity component plot across the hopper width inside 30° internal angle hopper geometry at 7 mm and at 10mm outlet sizes at three heights ( $H/\infty$ , $H/4$ and $H/2$ ) .....	143
Figure 6.10 Vertical velocity component plot inside lubricated 30° internal angle hopper geometry having 7mm outlet size measured at three heights ( $H/\infty$ , $H/4$ and $H/2$ ) in 2 <sup>nd</sup> order polynomial plot.....	144
Figure 6.11 Average vertical velocity component plot across the hopper width inside lubricated 30° internal angle hopper geometry for lubricated and non lubricated systems at three heights ( $H/\infty$ , $H/4$ and $H/2$ ) .....	145

Figure 6.12 Hopper walls roughness by gluing sandpapper on Perspex smooth walls .....	146
Figure 6.13 Experimental measurements of the wall roughness in laboratory using Taylor-Hobson, (a) rough surface results, (b) smooth wall results and (c and d) the measurement procedure .....	147
Figure 6.14 Vertical velocity component plot inside smooth and rough wall 30° internal angle hopper geometry having 7mm outlet size, solid line are smooth walls and dashed lines are rough walls measured at three heights ( $H/\infty$ , $H/4$ and $H/2$ ) in 2 <sup>nd</sup> order polynomial plot .....	148
Figure 6.15 Mean vertical velocity component plot across the hopper width inside smooth and rough wall 30° internal angle hopper geometry for smooth and rough walls at three heights ( $H/\infty$ , $H/4$ and $H/2$ ).....	149
Figure 6.16 Mean resultant velocity vectors map inside the 60° internal angle hopper geometry filled by coloured pharmaceutical excipient granules .....	150
Figure 6.17 Vertical velocity component plot inside 60° internal angle hopper geometry having 7mm outlet size measured at three heights ( $H/\infty$ , $H/4$ and $H/2$ ) in 2 <sup>nd</sup> order polynomial plot.....	151
Figure 6.18 Average vertical velocity component plot across the hopper width inside 60° internal angle hopper geometry having 7mm outlet size at three heights ( $H/\infty$ , $H/4$ and $H/2$ ).....	152
Figure 6.19 The maximum recorded vertical velocity component values at selected time intervals during the flow process inside 60° internal angle hopper geometry .....	153
Figure 6.20 Mean resultant velocity vector profiles at 60° internal angle hopper and its corresponding visual images during the central plug flow propagation (first flow zone) .....	154
Figure 6.21 Mean resultant velocity vector profiles at 60° internal angle hopper and its corresponding visual images during 2 <sup>nd</sup> stage of the flow process (second flow zone) .....	156
Figure 6.22 Mean resultant velocity vector profiles at 60° internal angle hopper and their corresponding visual images during 3 <sup>rd</sup> stage of the flow process (third flow zone) .....	157
Figure 6.23 Vertical velocity component plot inside 60° internal angle hopper geometry having 10 mm outlet size measured at three heights ( $H/\infty$ , $H/4$ and $H/2$ ) in 2 <sup>nd</sup> order polynomial plot.....	158
Figure 6.24 Average vertical velocity components plot across the hopper width inside 60° internal angle hopper geometry at 7 mm and 10mm outlet sizes at three heights ( $H/\infty$ , $H/4$ and $H/2$ ) .....	159

Figure 6.25 Vertical velocity component plot inside lubricated 60° internal angle hopper geometry having 7mm outlet size measured at three heights (H/ $\infty$ , H/4 and H/2) in 2 <sup>nd</sup> order polynomial plot.....	160
Figure 6.26 Average vertical velocity component plot across the hopper width inside lubricated 60° internal angle hopper geometry for lubricated and non lubricated systems at three heights (H/ $\infty$ , H/4 and H/2) .....	161
Figure 6.27 Vertical velocity component plot inside smooth and rough wall 60° internal angle hopper geometry having 7mm outlet size, solid line are smooth walls and dashed lines are rough walls measured at three heights (H/ $\infty$ , H/4 and H/2) in 2nd order polynomial plot.....	162
Figure 6.28 Average vertical velocity component plot across the hopper width inside smooth and rough wall 60° internal angle hopper geometry at three heights (H/ $\infty$ , H/4 and H/2).....	163
Figure 6.29 Mean resultant velocity vectors map inside the 90° internal angle hopper geometry filled by coloured pharmaceutical excipient granules .....	164
Figure 6.30 Vertical velocity component plot inside 90° internal angle hopper geometry having 7mm outlet size measured at three heights (H/ $\infty$ , H/4 and H/2) in 2 <sup>nd</sup> order polynomial plot.....	165
Figure 6.31 Vertical velocity component plot inside 90° internal angle hopper geometry having 7mm outlet size measured at three heights (H/ $\infty$ , H/4 and H/2) in normal plot distribution .....	167
Figure 6.32 Average vertical velocity component plot across the hopper width inside 90° internal angle hopper geometry at three heights (H/ $\infty$ , H/4 and H/2) .....	168
Figure 6.33 The maximum recorded vertical velocity component values at selected time intervals during the flow process inside 90° internal angle hopper geometry .....	169
Figure 6.34 Mean resultant velocity vector profiles at 90° internal angle hopper and its corresponding visual images during the central plug flow propagation (first flow zone) .....	170
Figure 6.35 Mean resultant velocity vector profiles at 90° internal angle hopper and its corresponding visual images during the 2 <sup>nd</sup> stage of flow process.....	171
Figure 6.36 Mean vertical velocity contour map Y-shaped flow region (a) and its corresponding visual image (b) inside 90° hopper geometry at 4.504 sec .....	172

Figure 6.37 Mean resultant velocity vectors profiles at 90° internal angle hopper and its corresponding visual images during the 3 <sup>rd</sup> stage of flow process.....	173
Figure 6.38 Vertical velocity component plot inside 90° internal angle hopper geometry, having a 10 mm outlet size measured at three heights ( $H/\infty$ , $H/4$ and $H/2$ ) in 2 <sup>nd</sup> order polynomial plot.....	174
Figure 6.39 Vertical velocity component plot inside 90° internal angle hopper geometry having 7mm outlet size measured at three heights ( $H/\infty$ , $H/4$ and $H/2$ ) in normal plot distribution .....	175
Figure 6.40 average vertical velocity component plot across the hopper width inside 90° internal angle hopper geometry at 7 mm and 10mm outlet sizes at three heights ( $H/\infty$ , $H/4$ and $H/2$ ) .....	176
Figure 6.41 Vertical velocity component plot inside lubricated 90° internal angle hopper geometry having 7mm outlet size measured at three heights ( $H/\infty$ , $H/4$ and $H/2$ ) in 2 <sup>nd</sup> order polynomial plot.....	177
Figure 6.42 Average vertical velocity component plot across the hopper width inside lubricated 60° internal angle hopper geometry for lubricated and non lubricated sysytems at three heights ( $H/\infty$ , $H/4$ and $H/2$ ) .....	178
Figure 6.43 Vertical velocity component plot inside smooth and rough wall 90° internal angle hopper geometry having 7mm outlet size, solid line are smooth walls and dashed lines are rough walls measured at three heights ( $H/\infty$ , $H/4$ and $H/2$ ) in 2nd order polynomial plot.....	179
Figure 6.44 Vertical velocity component plot inside 90° internal angle hopper geometry having 7mm outlet size and rough walls measured at three heights ( $H/4$ and $H/2$ ).....	180
Figure 6.45 Average vertical velocity component plot across the hopper width inside smooth and rough walls at 90° internal angle hopper geometry for smooth and rough walls at three heights ( $H/\infty$ , $H/4$ and $H/2$ ).....	180
Figure 6.46 Comparison of the theoretical and the experimental granular discharging rates at different internal hopper angle.....	182
Figure 6.47 Central flow zone wave propagation cycle inside high internal angle silo geometries; (a,b and c) inside 60° silo geometry and (d,e and f) inside 90° silo geometry .....	183
Figure 7.1 Fabricated compression chamber (a) actual image of the rig and (b) schematic diagram of the rig and its dimensions .....	188

Figure 7.2 Experimental setup for granular material compression at relatively low uniaxial compression using the PSAT technique: (a) central guide lines at the top part of the rig (b) manual compression rig and (c) PSAT system arrangement .....	189
Figure 7.3 Maximum shear stress profiles propagation within the sensor particles under different external loads and their corresponding heights .....	191
Figure 7.4 Tracking of increasing wall pressure at left side of the die boundaries (marked by red line) and stress diffision from the die top to the base (yellow lines) .....	192
Figure 7.5 Three levels of maximum shear stress distribution profiles evaluation inside compression die .....	195
Figure 7.6 Normalised maximum shear stress magnitudes across the compression die at three selected heights at 5N and 34N compression forces .....	196
Figure 7.7 Normalised average shear stress at the die central zone and boundaries at 5N load .....	197
Figure 7.8 Normalised average shear stress at the die central zone and boundaries at 34N load .....	199
Figure 7.9 Normalised average shear stress at the selected die heights at 5N and 34N loads .....	200
Figure 7.10 Normalised maximum shear stress values across the compression die at the top and bottom sections under 5N and 34N compression loads ....	201
Figure 8.1 Compression of pharmaceutical granules using the Instron machnie: (a) central guide lines at the top part of the rig, and (b) DPIV experimental setup .....	204
Figure 8.2 Area of interest (AOI) within the compression die (red colour) and interrogation area (IA) in (blue colour).....	206
Figure 8.3 Mean velocity vectors map of pharmaceutical stress responsive granules inside the compression die at the end of the compression cycle at 34N .....	207
Figure 8.4 Superimposed mean velocity vectors on the resultant velocity contours according to the vectors length within the die geometry at 34N.....	207
Figure 8.5 Qualitative analysis of the granular materials density profiles distributions using multiple colour coded granular layers: (a) initial uniform packing, and (b) non-uniform packing at the end of the compression process at 34N.....	208

Figure 8.6 Vertical velocity components and average vertical velocity across the compressed granular bed at the top and middle sections of the die at 34N.....	210
Figure 8.7 Maximum and average vertical velocity component at the top and middle section reported at the centre and boundaries of the die at 34N load.....	211
Figure 8.8 Superimposed mean velocity vectors on the resultant velocity contours, according to vector length within the die geometry at early stage of compression force at 5N load.....	213
Figure 8.9 Superimposed mean velocity vectors on the resultant velocity contours according to the vectors length within the die geometry at last stage of compression cycle at 34N load.....	214
Figure 8.10 Vertical velocity components and average vertical velocity across the compressed granular bed at the top, middle and bottom sections of the die at 34N compression force.....	214
Figure 8.11 Maximum shear stress magnitudes across the compression die at at the top, middle and bottom sections of the die at 34N compression force, Section 7.2 .....	215
Figure 9.1 Maximum shear stress profiles development (a), and the mean resultant velocity vectors of granules under relatively low uniaxial compression .....	221
Figure 9.2 Forces act on compressed granular assembly and mobilised shear stress development under relatively low uniaxial compression at early stage of the compression cycle.....	223

## List of Tables

Table 3.1 Experimental results of the physical and mechanical properties of the birefringent granules used in PSAT study .....	78
Table 3.2 Experimental results of the physical and mechanical properties of the granules used in colour coding and DPIV study (Albaraki and Antony, 2014) .....	84
Table 4.1 Normalised maximum shear stress findings and comparisons inside the 30° internal angle hopper geometry .....	93
Table 4.2 Normalised maximum shear stress findings and comparisons inside the 60° internal angle hopper geometry .....	98
Table 4.3 Normalised maximum shear stress findings and comparisons inside the 90° internal angle hopper geometry .....	103
Table 4.4 Properties of particles used in DEM simulations.....	107
Table 7.1 Shear stress comparisons inside the compressed granular bed at 5N load.....	198
Table 7.2 Shear stress comparisons inside the compressed granular bed at 34N load.....	199

## Nomenclature

$\sigma$	Normal stress
$\sigma_1$	Major principal stress
$\sigma_3$	Minor principal stress
F	Force applied
$\sigma_{av}$	Average stress
A	Area
$\tau$	Shear stress
$\tau_{max}$	Maximum shear stress
$\alpha$	Hopper half angle
$\varphi$	Angle of wall friction
$\mu$	Coefficient of wall friction
$\emptyset$	Angle of internal friction
$ff_c$	Flow factor
$\rho$	Bulk solid density
$\sigma_h$	Horizontal normal stress
$\sigma_v$	Vertical Normal Stress
$g$	Gravity
I	Carr's index
$V_b$	Bulk density
$V_t$	Tapped density
$\lambda$	Light wavelength
$H/\infty$	Reference level of hopper orifice
$H/4$	1/4 <sup>th</sup> level of hopper from reference level
$H/2$	Mid level of hopper from reference level

$F_u$	Axial applied force
$F_L$	Transmitted force to the die base
$F_W$	Frictional force acting on die wall
$F_D$	Radial force
$f_w$	Particle wall friction
$f_i$	Interparticle friction
$\mu_w$	Particle wall friction coefficient
$\mu_i$	Interparticle friction coefficient
$\varepsilon$	Compressed bed porosity
$\delta$	Retardation of light wave

## Acronyms

PSAT	Photo Stress Analysis Tomography
DPIV	Digital Particle Image Velocimetry
CCT	Colour Coding Technique
DEM	Discrete Element Method
FEM	Finite Element Method
XRDS	X-Ray Differential Scanning
SEM	Scanning Electron Microscope
2D	Two Dimensional
3D	Three Dimensional

# **Chapter 1 Introduction to the Project**

## **1.1 Introduction**

Powders and granules are everywhere in numerous industries and manufacturing processes. These include pharmaceutical manufacturing, foods, detergents, cosmetics and multiple engineering applications. During manufacturing and handling processes, powders and granules are filled and stored inside multiple storage bin geometries for further manufacturing phases. The common transient storage bins in pharmaceutical industries are feeding hoppers, blenders and compression dies. In pharmaceutical industries, powder flowability through feeding hoppers and compression inside confined chambers are very complex processes influenced by a combination of multiple internal and external factors and crucially influences the integrity and quality of the final products (Prescott and Barnum, 2000, Ganesan et al., 2008, Davies, 2009, Kuentz and Schirg, 2013). The behaviour of such discrete particulates is very complex when viewed at the micro-scale level, where the inter-particulate force network greatly influences the macroscopic behaviour (Jaeger et al., 1996, Antony, 2007, Kruyt and Antony, 2007).

Fundamental understanding of stress distribution profiles and major principal stress directions within granular material assemblies stored in hoppers and silos in either static or dynamic condition is essential for designing granular flow process (Jenike and Johanson, 1969, Walker and Blanchard, 1967, Jenike et al., 1973, Walters, 1973a, Walters, 1973b, Nedderman et al., 1982, Radjai et al., 1998, Antony, 2007). The literatures classified the stress status inside hoppers and silos for active and passive stress states at static and dynamic conditions respectively (Jenike and Johanson, 1969, Nedderman et al., 1982). Multiple analytical, experimental and computational methods have been developed and applied to measure the stress distribution and wall pressure exerted by granular materials and the results showed widely varying agreements and disagreements (Ding et al., 2011, Wang et al., 2013, Ezz El-Arab, 2014, Wang and Ooi, 2015). The analytical methods measure the stress magnitudes based on various assumptions that became incorrect recently when advanced

technologies were applied (Atewologun and Riskowski, 1991, Puglisi, 2001, Antony, 2007). In general, the literatures described the state of stress and direction of major stress in static conditions (after filling) as vertical lines along the central axis of the bin, with some minor deviation to the wall direction close to the boundaries. On the other hand, in case of passive stress status and due to granular bed dilation after outlet opening, passive pressure fields generate and the major pressure lines arch across the hopper. Similar results have been reported in some computational simulation researches using FEM for low internal hopper angles (Wang et al., 2013).

Up to date, the influence of the storage bin geometries on the shear stress distribution profiles and directions inside actual micro granules at static condition are still not clear yet and no experimental study has shed the light deeply to this area. Moreover, the influence of the initial stress packing conditions on the dynamic granular material flow trend is still a challenge for the researchers using particulate of micron size distribution.

Pharmaceutical solid dosage form manufacturing process requires granules to flow through the feeding hopper to accurately fill the die chamber for tabletting. Large amounts of external load usually applied to consolidate the loose bulk granules in dense solid form, known as oral tablets. Granular flow, die filling and stress propagation mechanisms within compressed granular assembly inside the die are very essential and crucially influence the quality and integrity of the manufactured tablets. Multiple experiments and computational simulation have been adapted to investigate the stress status development inside compression die under high loading conditions (Heckel, 1961b, Heckel, 1961a, Kawakita and Lüdde, 1971, Michrafy et al., 2002, Hassanpour and Ghadiri, 2004, Sinha et al., 2010). The main results of the established methods were limited to the density profile changes under external high loads. This pertains to the final stress magnitudes and shear stress band at the end of the compression cycle and decompression phase (Heckel, 1961b, Kawakita and Lüdde, 1971, Sinha et al., 2010).

The early phase of the compression cycle which is technically known as the rearrangement compression stage is a very critical phase as the stress propagation initially starts to develop at this early stage of the compression cycle. A non-linear

plot of Heckel's equation which relates the compression force and the bed porosity, is attributed to the changes that occur at this stage of compression and further researches at this stage are recommended for better understanding at microscale level (Denny, 2002, Comoglu, 2007, Davies, 2009). Numerous literatures mentioned that the influence of interparticle friction is more dominant than particle wall friction in bearing stress at this stage of compression and further investigation is required to clarify the nature of propagation and distribution (Michrafy et al., 2003, Michrafy et al., 2004, Ismail, 2008). Deep investigation of stress propagation at this stage will help to understand the ambiguous stress changes at this stage and it is highly needed (Denny, 2002).

The lack of understanding of stress distribution characteristics within micron size real granular materials and their relevance to flow and compaction properties especially under low stress levels are the main motivations for this research project. Up to date, no experimental study shed light sufficiently on the influences of the stress distribution profiles at static condition on the dynamic flow behaviour using particulates of micron size distribution. It is worth remembering that previous studies such as photoelasticity for understanding stress distribution in granular materials consider the grain size in the order of a few centimetres (Antony and Chapman, 2010). Moreover, the influence of particle motion, inter particle friction and wall particle friction on propagation and distribution nature of the stress and under relatively low uniaxial compression is urgently needed and not investigated deeply before using any advanced visualising experimental tomography.

To address this issue, two advanced imaging techniques; photo stress analysis tomography (PSAT) and digital particle image velocimetry (DPIV) have been adapted to investigate the micro and macroscale mechanical properties using free-flowing pharmaceutical granules. PSAT and DPIV are non-invasive, accurate, real time and quantitative visualising techniques at microscale levels. Colour coding technique (CCT) is another qualitative imaging method applied to study the flow trajectories and the macroscale flow properties.

In the first part of the research project, PSAT has been adapted to probe the stress distribution profiles and direction inside actual micron size poly dispersed free-flowing pharmaceutical granules stored in multiple hopper geometries under its own

weight. The obtained results help to propose a hypothesis for the dynamic flow behaviour based on the magnitudes of the maximum shear stress profiles, stress distribution homogeneity and the direction of the major principal stress inside the confined hopper geometries. DPIV method and colour coding technique have been adapted for quantitative and qualitative evaluation of the dynamic flow process and to validate the hypothesis of the flow respectively. The experimental work has been conducted using the same hopper geometries at same experimental conditions.

In the second part of the research project, stress propagation characteristics within free flowing granular material assembly subjected to relatively low uniaxial confined compression was evaluated using PSAT. The particle motion and bed deformation during the compression process was investigated by applying DPIV method using the same fabricated compression chamber and at same experimental conditions. The obtained results help to link the influence of particle motion, the developed particle-particle friction and particle wall friction on the nature of stress evolution inside the compression die.

The obtained outcomes provide valuable and promising results and enlighten a deeper level understanding of the influence of microscale characteristics of freely flowing granular materials on their macroscale behaviour during flow and compression processes. More importantly, the present research provides combined information on the stress and velocity distributions of micron size granular materials under prescribed experimental environments for both flow and compression process. This can help to design uniform flow devices without segregation of particles as well as understanding of the stress development mechanism within granular bed subjected to external loading conditions.

## 1.2 Aim of thesis

In general, the main aim of this thesis is to fully explore experimentally the influence of initial granular material packing on the stress profile distribution and directions inside multiple hopper geometries and its subsequent influences on the dynamic flow trend using advanced visualising techniques. Moreover, the project aim to investigate the influence of particle motion, particle-particle and particle wall frictions on the nature of stress propagation and evolution inside compression die

under relatively low uniaxial compression. The correlation of the findings will help to predict the influence of the microscale granular characteristics on the macroscale flow and compression behaviours. The project overview plan in Figure 1.1 shows clearly the steps and tasks performed to achieve these objectives.

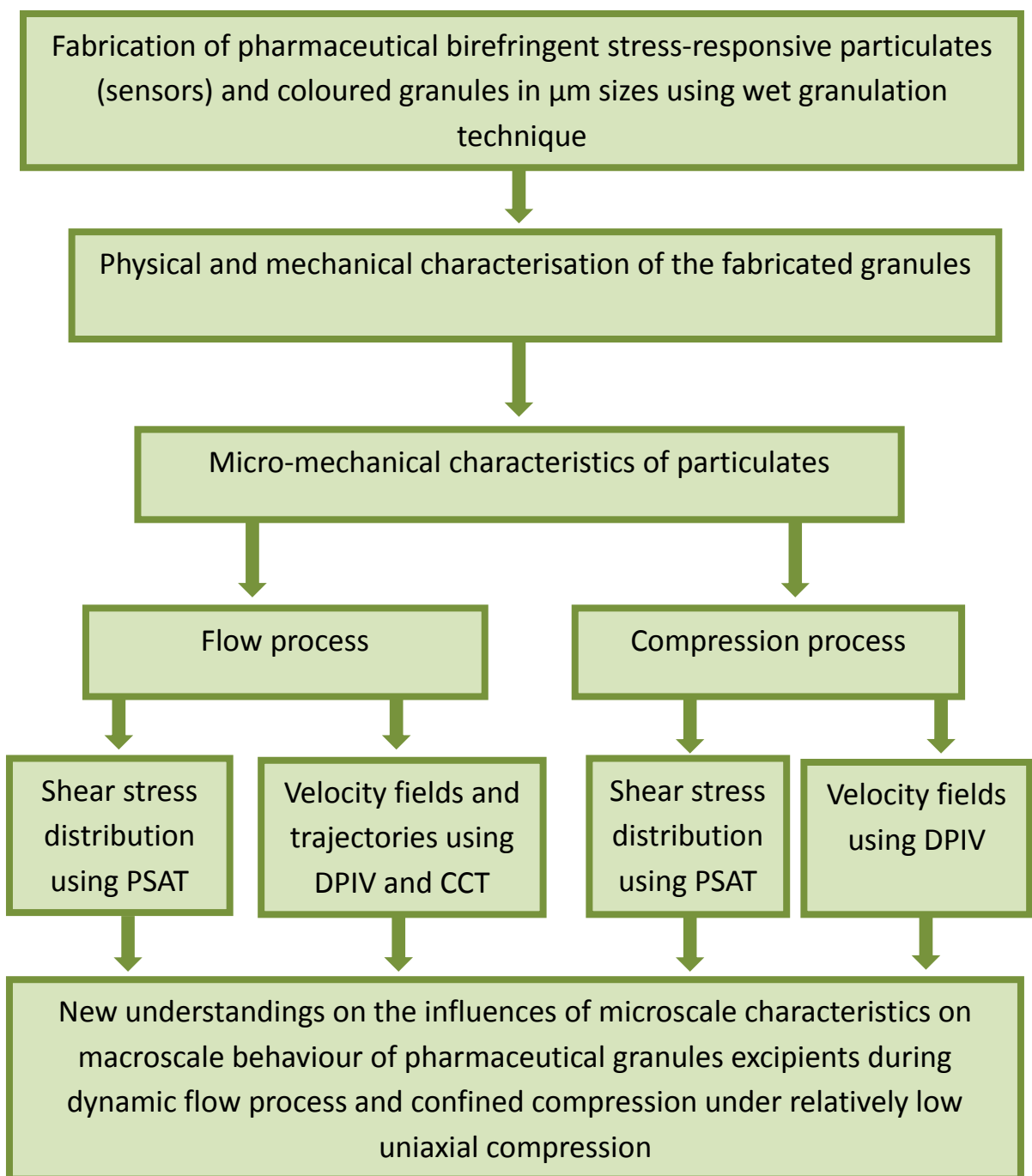


**Figure 1.1** Project overview

### **1.3 Structure of the Thesis**

In general, this thesis involves nine chapters. Chapter 1 comprises of brief background and introduction about the research project including the aim and the experimental work plan. Chapter 2 includes comprehensive literature reviews for granular materials behaviour during storage, discharge and compression processes including theoretical, experimental and computational methods for assessment. Moreover, it includes the main fundamentals of the applied experimental techniques in this research project, PSAT and DPIV. Chapter 3 summarises the physical and mechanical characterisations of the pharmaceutical excipient granules fabricated for the experimental work in the next chapters and their methods of assessment. Chapter 4 reports the experimental visualisation of stress profile distribution and directions inside the fabricated sensors stored in multiple hopper geometries in a static condition as well as the validation of the PSAT stress distribution results using DEM computational modelling method. Moreover, it includes the predicted hypotheses of flow based on the initial packing stress status. Chapter 5 describes the experimental qualitative validation of the predicted flow hypothesis during the dynamic flow process and the stagnation tendency inside hopper geometries using the colour coding technique. Chapter 6 focuses on the quantitative validation of the flow hypothesis by applying DPIV and investigation of the flow trend and trajectories inside the hopper geometries according to the mean velocity vectors magnitudes and direction. Chapter 7 investigates experimentally the stress profile propagation and evolutions inside confined die under relatively low uniaxial loading condition using PSAT. Chapter 8 describes the particulates motion and granular bed deformation inside the compression die chamber under loading conditions in order to link the results and analyse the influence of the interparticle and wall friction on the stress evolution. Chapter 9 summarises the overall conclusions of this experimental project on micro and macro mechanical behaviour of granular materials, functional theory for the acting forces and mobilised shear stress development under relatively low compression force and recommendations for future works.

## **Chapter 2 : Mechanical Behaviour of Granular Materials: Background and Recent Technical Developments**

The aim of this chapter is to provide an extensive overview of the general behaviour of the granular materials during the storage and discharge process from the storage bins. The chapter sheds light on the analytical, numerical and experimental methods applicable to measure the stress exerted by the granular materials. In the second part, the granular material compression within confined geometry and the relevant methods applied for the evaluation of such process are discussed in details. In the last part of this chapter, historical and recent technical improvements of photo stress analysis tomography (PSAT) and Digital particle image velocimetry (DPIV) have been discussed in detail as they are the main experimental advanced visualising techniques applied in this research project.

### **2.1 Granular Materials Background**

Granular materials are essential in multiple industries for several applications. These industries involve pharmaceutical, cosmetics, detergents, chemical and civil engineering and food industries. For example, involvement of granular materials for various industrial applications in USA contributes not less than one trillion dollars to the local economy (Rosato and Blackmore, 2000). Pharmaceutical industries delivered more than 75% of their final products in solid dosage form in either capsules or tablets (Muzzio et al., 2003) and both forms involved powders and/or granules during their manufacturing process in single or multiple stages.

The British pharmacopeia classified the granular materials to six main categories according to their particle sizes, the classification ranged from coarse powder to ultrafine powder (Pakowski and Mujumdar, 2006). This classification is widely used in multiple pharmaceutical applications and processes and crucially influences the manufacturing process of pharmaceutical dosage forms.

The granular materials were classified second to the water in its importance to the human multiple actions and activities (Duran, 2000, de Gennes, 2008). Granular materials are simply defined as an aggregate of discrete particles in contact and surrounded by air voids (Oda and Iwashita, 1999, Kozicki and Tejchman, 2011).

These particles are able to move and alter their arrangement individually or as aggregates depending on their initial packing density and environmental loading conditions (Kozicki and Tejchman, 2011).

In general, the micromechanical behaviour of such particulate aggregation is basically discontinuous, non-homogenous and anisotropic (Oda and Iwashita, 1999, Kozicki and Tejchman, 2011). Their mechanical behaviour is different from conventional solid, liquid and gaseous matter states (Jaeger et al., 1996, Forterre and Pouliquen, 2008). Figure 2.1 simply illustrates the three combined states of the granular materials as an example of heap or pile of grains poured on a flat surface. At rest, while the pile slope is lower than the angle of repose of the granular materials, it behaves as a solid and the grains show no motion. Slight changing of the pile slope above its angle of repose, allows the granular materials to flow smoothly and show three layers within the stream. The inner layer of the granular materials shows almost no motion and behaves like solid state matter. The middle layer behaves like a liquid state and start to flow smoothly. The particle motion takes place in the boundary layer of the pile surface. The gaseous state behaviour is reported at the outer layer as messy bounce of the particles in different directions.

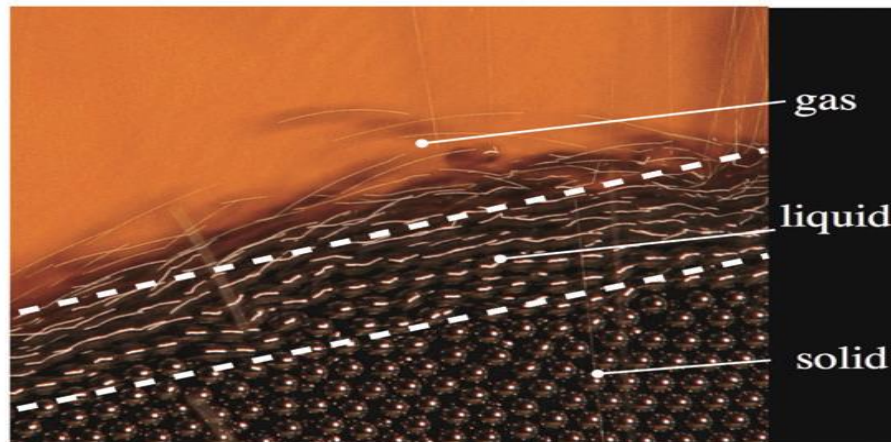


**Figure 2.1** Solid, liquid, and gas regions in steel particles in rotating drum (Forterre and Pouliquen, 2008)

Granular material behaviour is extremely complex when viewed at the micro-scale level and below and greatly influences its macroscopic behaviour and challenges the existing physics laws (Jaeger et al., 1996). The complex and unpredictable behaviour of granular materials comparing to solids, liquids and gases, allow

scientists to consider them as an additional state of matter in their own right (Campbell, 1990, Jaeger et al., 1996, Forterre and Pouliquen, 2008). Two main features have been reported to alter crucially the behaviour of the granular materials comparing to other matter state (Lee et al., 2000). Initially, air voids resulting by air entrapment between the particles, influences the powder bed expansion or contraction. Secondly, the required shear force for bed deformation and liquid flow like behaviour as a function of the applied load or position changes.

### 2.1.1 Contact Force Network in Granular Materials

Different to viscous fluids, granular material flow from their storage bins such as silos or bunkers, does not depend on the height of the stored materials inside the bin (Schulze, 2008, Perge et al., 2012). Unlike fluids, bulk solids are able to transmit shear stresses at rest and alter the bulk behaviour (Schulze, 2008). Figure 2.2 summarises the main differences in wall stress trend in cases of liquids and bulk solids.

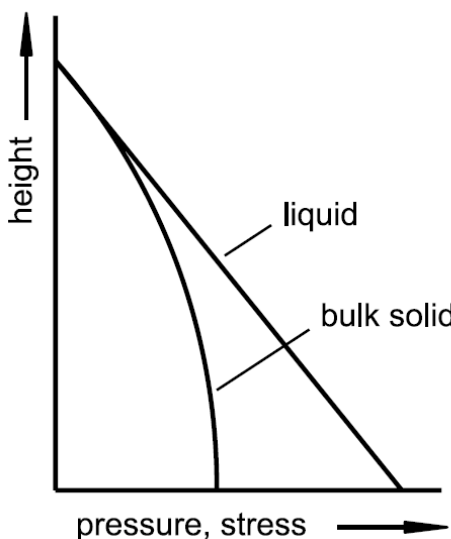


**Figure 2.2** Bunkers wall pressure and stress profile distribution respectively, in bulk solids and liquids (Schulze, 2008)

In fluid dynamics, wall pressure increases linearly with the depth of the sample inside the bunker, while in the case of bulk solids pressure plot does not show this linearity(Schulze, 2008). Granular materials show a linear increase in the stress for a shallow depth, reaches a maximum value after a certain height is exceeded and above that the pressure saturates. The proper scientific explanation of this

phenomenon is known as Janssen effect; where the particle friction re-diverts the exerted pressure by the bulk solid bed weight to the bunker walls. (Duran, 2000, Perge et al., 2012). The pressure deviation toward the bunkers wall, also known as shear stress transmission, and can be attributed to high contact forces between the granular materials and the static friction between the particles and the bunker boundaries (Jaeger et al., 1996, Schulze, 2008, Kheiripour Langroudi et al., 2010).

Under loading conditions, granular material assemblies are able to generate and build up force chains between the particulates to support their bulk packing and underlying structure (Majmudar and Behringer, 2005, Antony, 2007, Majmudar et al., 2007). The bulk properties of the granular material assemblies such as load bearing ability, interparticle arching, jamming and shear banding are greatly influenced by the nature of the generated contact forces (Guyon et al., 1990, Majmudar et al., 2007, Kondic et al., 2012). In a dense granular packing, the forces between particles are transferred through the contacts between the particles and build up a skeleton frame within the granular assembly as show in Figure 2.3.

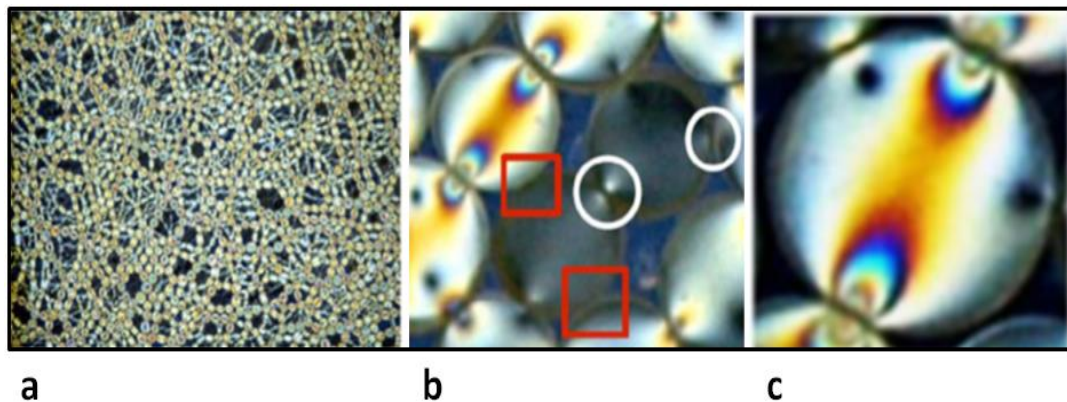


**Figure 2.3** Force network of granular matter is non-homogeneous in space as observes using photoelastic disks, (a) macroscopic view within the entire bed, (b) circles illustrates true contact, square show fales apparent contact, (c) single particle level contacts, (Majmudar et al., 2007)

The interparticle contact points show multi-fringe colours depending of the magnitude of the load transmitted at these points (Majmudar and Behringer, 2005, Majmudar et al., 2007, Antony and Chapman, 2010). The contact natures might be strong contact carrying greater than average normal force, or weak contacts carrying low magnitude of the average normal force (Radjai et al., 1996, Antony et al., 2005, Antony, 2007). Radjai et al. (1998) has reported that the distribution of the average

force of sheared assembly grain contacts in two dimensional granular systems is bimodal. In this system, the strong force network (load-bearing network) is able to carry force magnitude higher than the average force (deviatoric load) while the weak force network (dissipative network) is carrying less than the average force (Antony, 2001, Antony et al., 2005). The strong contact network or “load-bearing network” represents around 40% of the total contacts networks and reflects the system anisotropicity (Radjai et al., 1998). The direction of these strong networks is aligned with the direction of compression axis or the major principal stress direction. Therefore, the anisotropicity of the sheared assembly is directly proportional to the strong force network contribution at any particular zone (Radjai et al., 1998, Antony, 2007). The weak force network contribution to transmit the deviatoric stress within sheared system is insignificant. The bimodal characteristic of force distribution is also confirmed in three dimensional granular systems (Thornton and Antony, 1998).

Generally, sliding take place dominantly through the weak force network which represents the majority of the networks within sheared bed (Radjai et al., 1998, Antony, 2007). The contribution of the strong network forces in sliding is negligible, as they show some resistance to sliding.

The unpredictable and complex spatial and temporal behaviour of the granular material assemblies influenced greatly by the interparticle force network arrangement (Kondic et al., 2012). The transmission of force within particulate materials occurs through the inter-particle contacts, but each contact force is highly sensitive to the local arrangement of the surrounding particles and boundary loading conditions (Antony et al., 2005, Antony and Chapman, 2010). Because of this strong dependence on particle arrangement, contact forces will usually be distributed in a complex, non-uniform manner, even when an isotropic and homogeneous assembly of particles is subjected to uniform loading conditions (Antony et al., 2005, Majmudar and Behringer, 2005, Antony, 2007). As a result, the force is transmitted between the particles in non-homogenous way.

Over the past few decades, there have been several numerical and experimental studies made to characterise the force network and link that to the granular materials’ macroscopic behaviour (Radjai et al., 1996, Radjai et al., 1998, Peters et al., 2005, Antony, 2007, Majmudar et al., 2007).

Experimental visualising of the force network, dilation and stress temporal fluctuations is led by a pioneer group of scientists in University of Duke, USA (Behringer et al., 2014). The investigations focused on quantifying the force network's propagation, stress transmission, particle jamming and distribution within particulate assemblies using transparent light-transmitting photoelastic disks in centimetre sizes (Majmudar and Behringer, 2005, Majmudar et al., 2007, Wambaugh et al., 2010). The experimental works have been conducted using a 2D experimental setup and the term force chain has been identified through the observation of these contacts between the particles in a chain-like structure. A recent 3D study using fluorescence technique coupled with laser-sheet scanning, described the interparticle forces in particulate assembly as filament networks (Kondic et al., 2012).

The simulation based observation of the contact force and force transmission can be visualised using discrete element method (DEM) (Matuttis et al., 2000, Antony, 2007, Nitka et al., 2009, Tordesillas et al., 2010, Wang et al., 2015). DEM, considered as a powerful numerical technique, helps to predict the discrete dynamics of particles such as mechanical strength, force network shape and evolution under external loading conditions. Figure 2.4 shows the force network and interparticle sliding contacts using DEM in a 2D granular setup, where the thickness of the network lines is directly proportional to the magnitude of contact forces within the assembly.

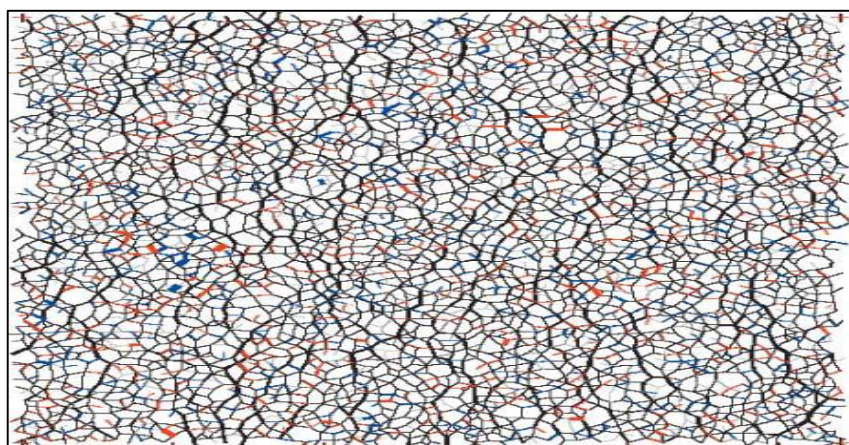


**Figure 2.4** Force network and sliding contact in granular system using 2-D DEM application. Thickness of the lines is proportional to normal force magnitude (Antony, 2007)

It is obvious that the force network distribution is non-homogenous within the assembly and varies depending on the location, load magnitude and the number of contacts points between the particles. The external shearing force on granular material assembly changes the initially isotropic packing of the material to an anisotropic contact network (Radjai et al., 1998, Antony, 2007, Alonso-Marroquín et al., 2008).

Two main interesting areas of research have been investigated thoroughly to show the influence of the force network on macro-scale behaviours. These include granular material flow from storage bins and particulate assemblies compression (Antony et al., 2005, Majmudar and Behringer, 2005, Kruyt and Antony, 2007, Majmudar et al., 2007). In powders and granular material flow process, shear stress ratio, which represents the ratio of the normal stress to shear stress is essentially fundamental for the understanding of their macro-scale behaviour (Schulze, 2008). Stress distribution within a granular bed occurs through the nonhomogeneous force network and influenced dramatically by multiple factors, including single-particle characteristics (Antony and Kuhn, 2004, Zheng and Yu, 2015), particulate initial packing (Antony, 2007), particle size (Hassanpour et al., 2004, Hassanpour et al., 2007) and location from the boundaries (Antony and Chapman, 2010). Shear forces inside the granular assemblies are generated due to the motion of the particles in addition to the interparticle interactions and frictions. Increasing the inter-particle friction increase the anisotropicity of the sheared granular assembly as well as the system inhomogeneity. However, low internal friction system provides more homogenous strong network distribution (Tardos et al., 2003, Antony and Sarangi, 2006).

### **2.1.2 Stress Analysis: Background in Brief**

A better understanding of the forces acting on granular material assembly requires more and adequate consideration of its stress components. Stress is simply defined as the average measure of the internal resistance or counterforce of material to the distorting effects of an external force. Mathematically the average stress ( $\sigma$ ) acting on a plane is equated to the load applied or force (F) per unit area or cross sectional area (A) using equation (2.1).

$$\text{Stress} = \sigma = \frac{F}{A}$$

Eq. 2.1

Where

$\sigma$  = Normal stress

$F$  = Applied force

$A$  = Cross sectional area

For a three dimensional object, there is one normal stress component ( $\sigma$ ) and two shear stress components ( $\tau$ ) acts on each plane as shown in Figure 2.5. At all planes there will be nine stress components acting on the object known as stress tensor. The stress tensor consists of three normal stress components and six shear stress components.

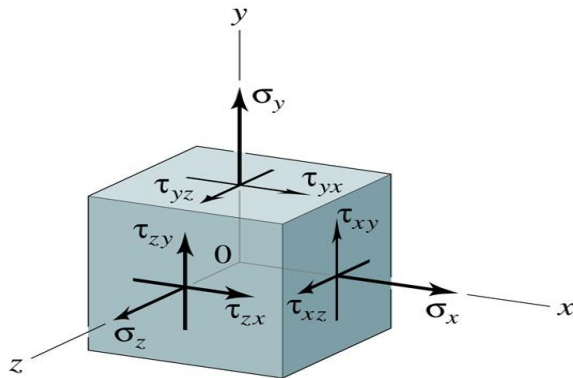


**Figure 2.5** Stress tensor components in rectangular coordinates (Smith, 1990 )

In the case of a normal stress component, the subscript represents the plane which the stress acts on;  $x$ ,  $y$  and  $z$ . On the other hand, the shear stress component has two subscripts; the first one denotes the plane which the stress acts on and the second one is the direction on the plane. The nine stress components (stress tensor) are usually arranged in a matrix of  $3 \times 3$  and constructed as shown in equation 2.2, row is the plane and column is the direction of the stress (Parry, 2004).

$$T_\sigma = \begin{bmatrix} \sigma_{xx} & \tau_{xy} & \tau_{xz} \\ \tau_{yx} & \sigma_{yy} & \tau_{yz} \\ \tau_{zx} & \tau_{zy} & \sigma_{zz} \end{bmatrix}$$

Eq. 2.2

In case of a two dimensional stress analyses (may be called plane stress state sometimes) the stress tensor in equation 2.2 changed from nine components to a symmetrical four component matrix as illustrated in equation 2.3;

$$T_\sigma = \begin{bmatrix} \sigma_{xx} & \tau_{xy} & 0 \\ \tau_{yx} & \sigma_{yy} & 0 \\ 0 & 0 & 0 \end{bmatrix} = \begin{bmatrix} \sigma_{xx} & \tau_{xy} \\ \tau_{yx} & \sigma_{yy} \end{bmatrix} \quad \text{Eq. 2.3}$$

The equation is a second order equation and the stress on the planes is well defined independently by the three stress components, two normal stress components ( $\sigma_{xx}$  and  $\sigma_{yy}$ ) and the shear stress component  $\tau_{xy}$ . From the matrix and as it is called plane stress, the shear component  $\tau_{xy} = \tau_{yx}$ .

For multiple engineering and industrial purposes, stress measurements and relationships are representing simply by applying Mohr's circle. Mohr's circle is a graphical method enabling stress measurement in case of 3D and 2D systems. It was discovered by Culmann (1866) and developed latterly by a German scientist Otto Mohr (1835-1918). Mohr's circle is plotted and drawn using the values of normal stress ( $\sigma$ ) on (X) axis and shear stress ( $\tau$ ) on (Y) axis. To measure any stress conditions in 2D by drawing Mohr's circle, the required coordinates are the normal stresses ( $\sigma_{xx}$  and  $\sigma_{yy}$ ) and shear stress ( $\tau_{xy}$ ) act on the plan as shown in Figure 2.6.

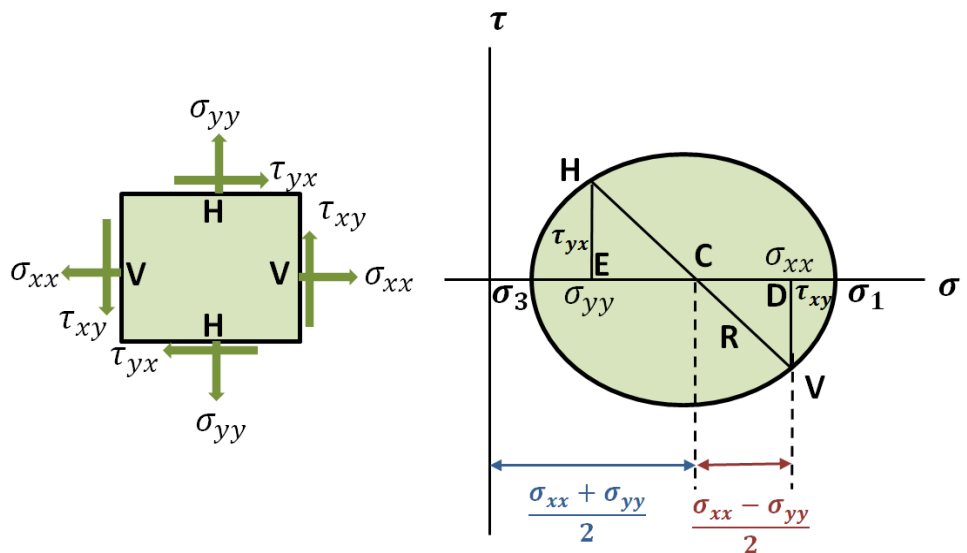


**Figure 2.6** 2D stress mathematical and graphical case (a) stress cube, and (b) Mohr's circle construction.

Point C represents the centre of the circle and the coordinates are ( $\frac{\sigma_{xx} + \sigma_{yy}}{2}$ , 0). From Figure 2.6, CD is equal to ( $\frac{\sigma_{xx} - \sigma_{yy}}{2}$ ) and by applying Pythagorean theory;

$$R = \sqrt{\left[\frac{\sigma_{xx} - \sigma_{yy}}{2}\right]^2 + \tau_{xy}^2} \quad \text{Eq. 2.4}$$

Frome Figure 2.6, R value is equal to the radius of Mohr's circle.

The centre of Mohr's circle is calculated using equation 2.5 as follow;

$$C = \rho_{av} = \left(\frac{\sigma_{xx} + \sigma_{yy}}{2}\right) \quad \text{Eq. 2.5}$$

It is worth remembering that the acting stress on different planes is twice the angle between the planes. For example, in Figure 2.6 the angle between the planes is 90° and represented on Mohr's circle as 180°.

In 2D stress concepts,  $\sigma_1$  is known as major principal stress,  $\sigma_3$  is the minor principal stress which is perpendicular to  $\sigma_1$ . From equations 2.4 and 2.5, major principal stress  $\sigma_1$  and minor principal stress  $\sigma_3$  are equated as follow;

$$\sigma_1 = \left(\frac{\sigma_{xx} + \sigma_{yy}}{2}\right) + \sqrt{\left[\frac{\sigma_{xx} - \sigma_{yy}}{2}\right]^2 + \tau_{xy}^2} \quad \text{or} \quad \sigma_3 = \rho_{av} + R \quad \text{Eq. 2.6}$$

$$\sigma_3 = \left(\frac{\sigma_{xx} + \sigma_{yy}}{2}\right) - \sqrt{\left[\frac{\sigma_{xx} - \sigma_{yy}}{2}\right]^2 + \tau_{xy}^2} \quad \text{or} \quad \sigma_3 = \rho_{av} - R \quad \text{Eq. 2.7}$$

Stress analysis using a two dimensional applications is much easier, practical and convenient to solve most industrial problems compared to a three dimension system (Schulze, 2008). Experimentally and graphically, maximum shear stress ( $\tau_{max}$ ) value in case of the 2D system equates as follows:

$$\tau_{max} = \frac{(\sigma_1 - \sigma_3)}{2} \quad \text{Eq. 2.8}$$

Mohr's circle in Figure 2.7 summarise graphically the maximum and minimum shear stress values as well as the average stress values. Applying Mohr's circle concept in industry helps to assess the powder cohesivity and flowability as well as the proper designing of silos and hoppers achieving the required flow trend (Schulze, 2008).

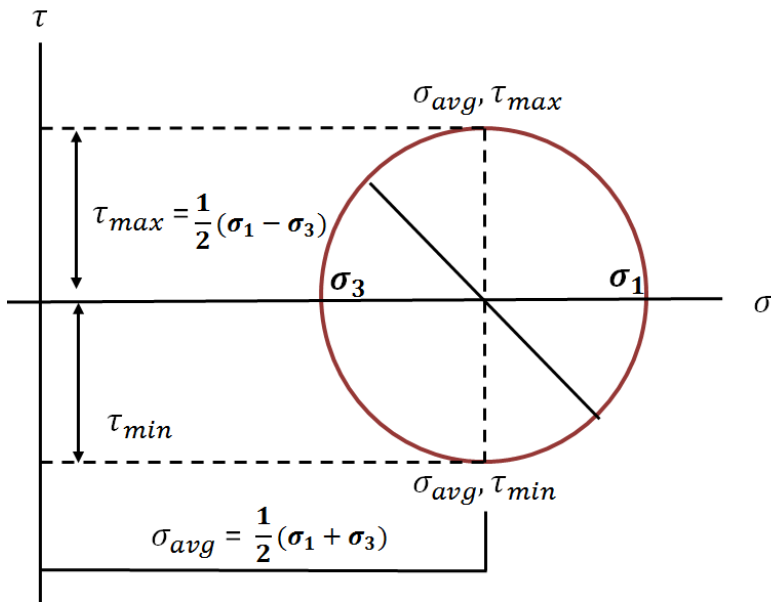


**Figure 2.7** Maximum shear stress and average stress in Mohr's circle for two dimensional stress system.

## 2.2 Granular Materials Flow Behaviours inside Silos and Hopper Geometries

Granular materials flow is a very interesting area of research and the total annual number of experimental and numerical publications increased dramatically, reaching 480 articles during 2010 (Lumay et al., 2012). However, fundamental information on how particles sustain stresses and velocity fields inside flow devices is still lacking. Their flow assessment and behaviour has been well sought by many researchers since the early 17<sup>th</sup> century and back dated to Reynolds (1885), Coulomb (1773), Culmann (1866), Collin (1846) and Mohr (1882). They have applied multiple experimental and analytical methods for flow assessment (Nedderman, 1992). The first reported pioneered experimental work to measure the deformation of the soil surfaces was conducted by Collin (1846) using simple shear box tester (Nedderman, 1992, Parry, 2004, Powrie, 2004). Granular material shearing and flow evaluation using simple graphical drawings was discovered by Culmann (1866) and developed later by Mohr (1882) which is still considered as one of the fundamentals in soil and granular material mechanical dynamics (Parry, 2004). Reynolds (1885)

described the tendency of a compacted granular material to dilate as it is exposed to shear forces, this is known as Reynolds principle of dilatancy (Nedderman, 1992).

Brown and Hawksley (1947) summarised the flow trend from bunkers to four regions or zones. The first zone is the flowing zone that is located directly above the outlet region and second is the “creeping” zone follow the flowing zone. The third zone is the “cascading” zone at the top boundary of the granular materials and the last zone is the stagnant zone close to the bunker boundaries (Nedderman, 1992).

During the middle of the last century, Jenike (1961) and his co-workers provided a very comprehensive and detailed descriptive study on the flow behaviour inside the silo geometry (Jenike, 1964). They classified the nature of the granular flow from silos to two main categories; mass flow and funnel flow. In cases of mass flow, all particles inside the storage bins are in continuous motion during the discharging process while funnel flow is defined as the flowing of the particles through a plug, surrounded by stagnant zones or any form which is not mass flow (Jenike and Johanson, 1969). The new Jenike method (1987) is more reliable to predict the nature of the mass or funnel flow in conical hopper geometry and the outlet diameter (Kruyt, 1993).

The first efforts to define the boundary of the stagnant zone inside the hoppers for both cohesive and non-cohesive materials, goes back to (Gardner, 1966). He defined this region according to the angle of internal friction. His assumption considered the distribution of the stress within the steady flowing material as radial. On the other hand, Jenike’s (1961) method for radial stress field is slightly different from Gardner as it takes into consideration the angle of hopper in addition to the angle of internal friction. Jenike’s method is applicable only when the hopper half angle calculated using the following equation;

$$\alpha = \frac{\pi}{2 - \varphi} \quad \text{Eq. 2.9}$$

Where ( $\alpha$ ) hopper half angle and ( $\varphi$ ) angle of internal friction (Tüzün and Nedderman, 1982).

Watson and Rotter (1996) furthermore subdivided the nature of the funnel flow trend to internal (or pipe) flow and semi-mass flow as shown in Figure 2.8.

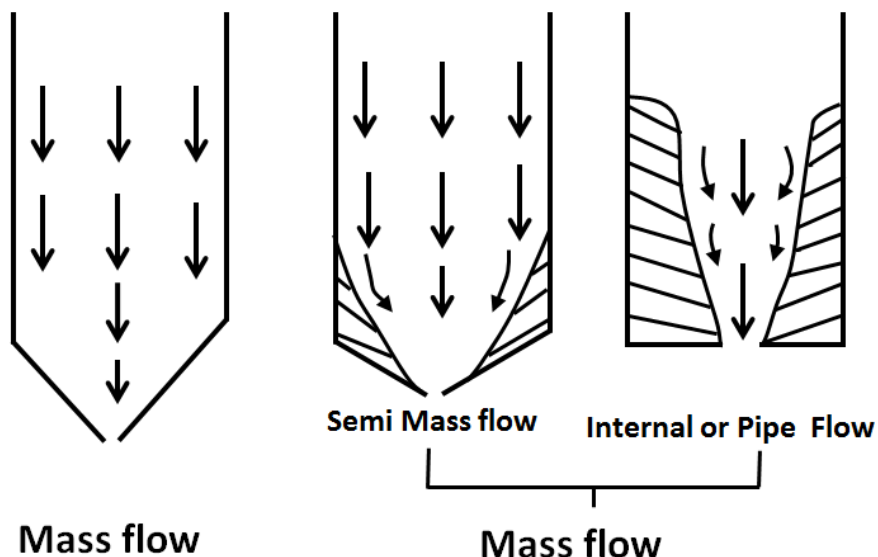


**Figure 2.8** Classification of flow behaviour in silos (Watson and Rotter, 1996)

Discharging of the granular materials from silos depend on the ratio of the granular layer thickness to the diameter. Exceeding the ratio of 1.2 times saturates the pressure at the bottom of the silo and the flow rate remains constant (Mankoc et al., 2007). The granular flow rate becomes independent of the diameter of the silo in two conditions; firstly, if the silo diameter ( $D$ ) is 2.5 times greater than the silo outlet diameter ( $D_0$ ) and second, if  $(D - D_0)$  is 30 times greater than the particle size (Nedderman et al., 1982).

Fundamental understanding of the strengthening and consolidation of powders and granular materials is directly related to reliable understanding of effective stress and stress distribution within the granular bed. Direction of major and minor principal stress in both static and dynamic conditions is playing a very important role in the granular flow behaviour and can help in proper device designing (Radjai et al., 1998, Antony, 2007, Antony et al., 2012, Albaraki et al., 2013). Proper and accurate measuring and prediction of granular stress status inside silos and hoppers during the granular material filling or discharging process is required in many advanced technologies to be able to measure stress development within single granular material (Ding and Enstad, 2003).

Methods applied for measuring silos and hoppers pressure and stress conditions are mainly based on (i) analytical methods (ii) experimental methods and (iii) simulation or computational methods.

## 2.2.1 Analytical Methods

Up to date, several pioneering studies have been reported to evaluate silo wall pressure, radial stress and velocity fields of flowing granular materials, starting from the late 19th century by Janssen (1895), then in the early 1960s by Jenike (1961, 1964), Beverloo (1961), Johanson and Jenike (1962) and Jenike and Holt (1965) are still applied widely in industries. Latterly, Jenike (1969) and Jenike (1973) corrected Janssen's theory and criticised his assumptions (Nedderman, 1992, Chou and Chen, 2003). Further valuable works have been conducted by Walker (1966), Walker and Blanchard (1967) and Walters (1973a) and (Walters, 1973b) for further clarification of stress exerted by granular materials on hoppers' walls.

### 2.2.1.1 Janssen Theory and Assumptions

Janssen (1895) derived simple interpretation to measure the vertical wall pressure produced by granular materials inside vertical cylinder storage bins such as silos at rest as a function of bed depth (Nedderman, 1992, Hemmingsson et al., 1997). The equated vertical wall pressure can be calculated using the following formula;

$$P_v = \frac{\rho^0 g D}{4\mu K g_c} \left( 1 - \exp \left( -\frac{4\mu K z}{D} \right) \right) \quad \text{Eq. 2.10}$$

Where the  $\rho^0$  is the grain density in ( $\text{kg/m}^3$ ),  $g$  is the gravity in ( $\text{m/s}^2$ ),  $D$  is the silo height in (m),  $\mu$  is the coefficient of wall friction,  $K$  is known as Janssen's constant and it reflects the ratio of the vertical stress and horizontal stress  $K = \sigma_h/\sigma_v$ ,  $g_c$  is the gravity constant conversion factor (convert unit mass to unit force) and  $z$  is the silo diameter in (m). At fully mobilised case, friction coefficient can be calculated as follow;

$$\mu = \tan \varphi_w = \frac{\tau_w}{\sigma_w} \quad \text{Eq. 2.11}$$

Where  $\varphi_w$  is the angle of wall friction,  $\tau_w$  is shear stress acting on the wall and  $\sigma_w$  is normal stress acting on the wall. The accuracy of Janssen equation is not unlimited as the above analysis is applicable only in the case of cohesionless granular materials stored in flat face bunkers or deep silos ignoring the influence of end part geometry. Generally, it has been reported that the accuracy of Janssen's equation

was based on and influenced critically by the value of the constant K, and big debates between the researchers have been raised about K value (Atewologun and Riskowski, 1991). This is due to the significant influence of K values on the distribution of the stress within particulates and the walls of the silo. Janssen derived his equation to analyse the active stress state inside the vertical silo section using slice element method. The method takes into consideration the normal stress load of the layers located above the slice which act downward on the surface area. The edges of the element slice are in direct contact with the walls of the silo in a perpendicular direction as shown in Figure 2.9.

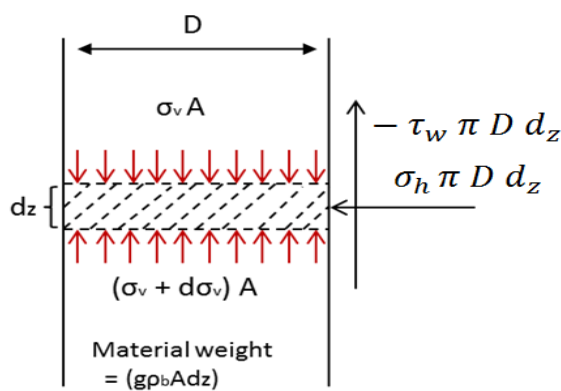


**Figure 2.9** Diagram of element slice method and its wall contacts

Janssen's equation is based on multiple assumptions that are not fully tested up to date (Nedderman, 1992, Hemmingsson et al., 1997, Landry et al., 2004, Bratberg et al., 2005). In general, Janssen considers four assumptions in his theory for the silo wall pressure calculation (Hemmingsson et al., 1997), some references mentioned only two main assumptions (Nedderman, 1992, Ding and Enstad, 2003, Bratberg et al., 2005).

The four assumptions of the Janssen theory are as follows:

- The constant (K) value which represents the ratio of horizontal pressure  $P_h$  to the vertical pressure  $P_v$  is constant throughout the silo; both pressures are denoted as principal stresses.
- The vertical pressure is constant and uniformly distributed across the horizontal plane.

- The density of the solid bulk material is constant inside the silo and can be treated as continuum material.
- The wall friction is fully mobilised.

Janssen's law is still applied in multiple engineering industries for the measurement of the storage bins wall pressure although recent research findings showed that some of those assumptions are not totally correct (Hemmingsson et al., 1997, Ooi and She, 1997, Marconi et al., 2000, Puglisi, 2001, Landry et al., 2004, Bratberg et al., 2005, Saada, 2005, Goda and Ebert, 2005).

The main limitation of Janssen's theory is the assumption that the vertical pressure is constant in the horizontal plane which is not correct (Puglisi, 2001). The pressure and stress distribution on a single particle is greatly influenced by the location of those particles along the horizontal axis and boundaries have great influences on the magnitude (Jaeger et al., 1996, Ooi and She, 1997, Marconi et al., 2000, Geng et al., 2001, Antony and Chapman, 2010, Albaraki et al., 2013). The ability of granular materials to build up a force network between the discreet particles inside the storage bins could greatly alter stress distribution within granular assembly and result a high degree of inhomogeneity across the bed geometry (Thornton and Antony, 1998, Geng et al., 2001, Antony and Kuhn, 2004, Antony, 2007, Antony et al., 2012).

The other limitations concerning Janssen's theory are related to the value of constant ( $K$ ) used in the equation and the suitable method to calculate it (Atewologun and Riskowski, 1991), friction coefficient value (Martinez et al., 2002), granular bulk density (Haque, 2013) and the angle of wall friction. (Jenike et al., 1973). Multiple opinions about choosing the value of ( $K$ ) in Janssen's equation have been reported in literatures (Bagster, 1971, Jenike et al., 1973, Martinez et al., 2002). Some researchers claim it as a function of internal angle of friction (Atewologun and Riskowski, 1991) and others such as Jenike for example assumed  $K = 0.4$  able to provide well compared experimental results for the initial pressure for different granular materials (Jenike et al., 1973).

### **2.2.1.2 Jenike Theory**

The first published classification of granular materials in relation to their flow behaviour was reported by Jenike at (1960's) as "mass" and "funnel" flow. Mass flow may be referred to in literatures as "first -in- first out" flow pattern and affords many advantages to the industry. Mass flow helps to maintain uniform and controlled flow content and rates, reduce the radial segregation of the granules and prevent any stagnant zone formation (Jenike, 1964, Nedderman, 1992, Tüzün and Nedderman, 1982). According to Jenike and Johanson (1969), in the case of a mass flow trend, the transition zone is located at the connection of the hopper section to the vertical section of the silo. Transition zone is simply defined as the point of the intersection of the granular materials in the central plug flow with the bin boundaries. On the other hand, funnel flow trend which is also known also as "first -in- last out" is usually characterised either by shallow hopper geometry or flat bottoms (Tüzün and Nedderman, 1982). This type of flow has some advantages, especially the high capacity of the hopper or silo that may lead to lowering the operation cost. The main disadvantages of the funnel flow trend are segregation of the hopper content, powder flooding due to erratic flow, and stagnant zone formation (Holdich, 2002). In funnel flow cases, the transition zone cannot be generalised as in the cases of the mass flow trend. The height of the transition zone depends on the granular material characteristics, especially the internal angle of friction as well as the roughness of the boundaries (Muite et al., 2004).

Jenike (1964), Jenike and Johanson (1969) and Jenike et al. (1973) have reviewed the Janssen work and extended the work to include the silo hopper as well as the vertical part of the silo. They have published in detail stress states for both static and dynamic conditions. They have classified the stress state and wall pressure inside the vertical section and hopper section of the silo into two main stress states "active stress state" that develop during the filling phase and "passive stress state" occurring during discharging phase, see Figure 2.10.

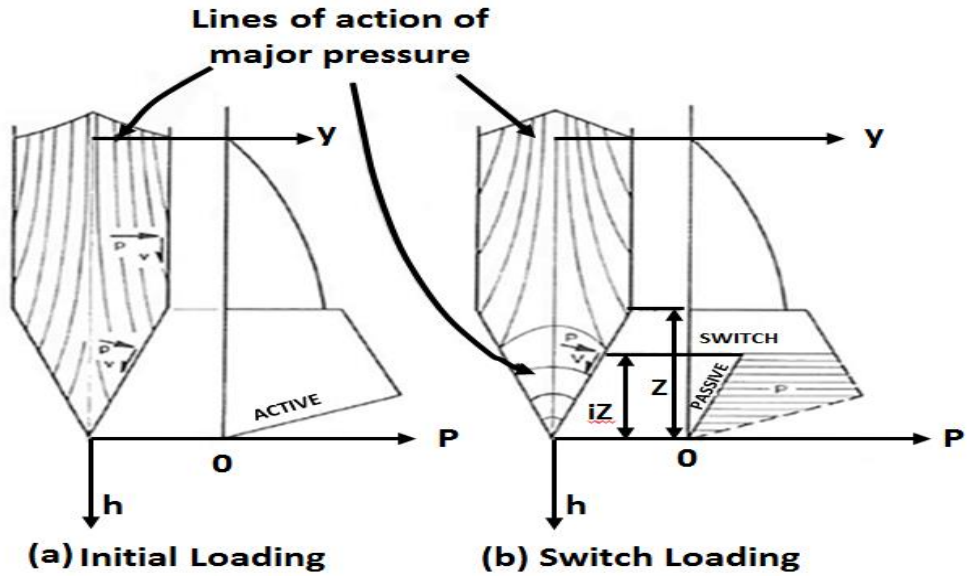


**Figure 2.10** Active and passive wall stress state and major pressure directions in vertical silo and hopper sections (Jenike and Johanson, 1969)

During the active stress state, as granular materials filled into the silo or storage bin, the bulky mass is built upward without showing any lateral deformations. This filling process creates an active pressure field, showing vertical to semi-vertical major principal pressure lines as illustrated in Figure (2.10a). At this stage, the granular materials exert a pressure ( $P$ ) on the hopper and vertical wall sections. By the time, the bulk solid settles and slightly slides along the bin boundaries and this partial movement creates frictional stress ( $v$ ) along the bin wall that can be equated as follows;

$$v = p \tan(\varphi) \quad \text{Eq. 2.12}$$

Where  $p$ , the pressure exerted on the walls and  $(\varphi)$  is the angle of friction against the wall. It is clear from (equation 2.12) that the measurements of shear stress on the bin wall ( $v$ ) are formulated by considering the balanced weight of the granular materials in the hopper according to the vertical pressure ( $p$ ) and the angle of friction between a bulk solid and the wall ( $\varphi$ ).

The passive stress state starts immediately after opening the storage bin outlet. At this stage, the initial flow process of the granular materials dilates the bulky mass located directly above the outlet. At the hopper section, granules slide radially and slip on hopper boundaries and imply a passive stress field having arched major

pressure lines as illustrated in Figure (2.10b). During the passive stress state, the vertical stresses acting within the granular materials bulk are almost proportional to the distance from hopper apex. The pressure increase linearly within the hopper section up to certain height below the transition point and then shifts to higher magnitudes dramatically. This shifting point is called the switch point as seen in Figure 2.10b. Obviously, a quick comparison between the magnitude of the two stress states, it is clear that the maximum stress magnitude in case of active stress status is much higher than the passive status. The deficiency of the stress magnitude is shown clearly by the dashed area.

### 2.2.1.3 Walter and Walker Method

Walker (1966) corrected the first assumption of Janssen that assumed the vertical and horizontal stresses as principal stresses by considering proper stress distribution in wall region (Nedderman, 1992). Janssen's analysis of cohesionless granular materials flow trend in silos or storage bins have been extended and deeply investigated by Walker and Walters and their co-workers (Walker, 1966, Walters, 1973a). Walker (1966) described the wall stress propagation and its distribution during the filling phase in the silo and hopper in multiple consequential steps. Initially, continuous filling of the bulk solids will raise the vertical pressure upward. According to Mohr's circle, this will increase the yield stress on the walls and inflates the circle till it exceeds the wall yield locus, see Figure 2.11.

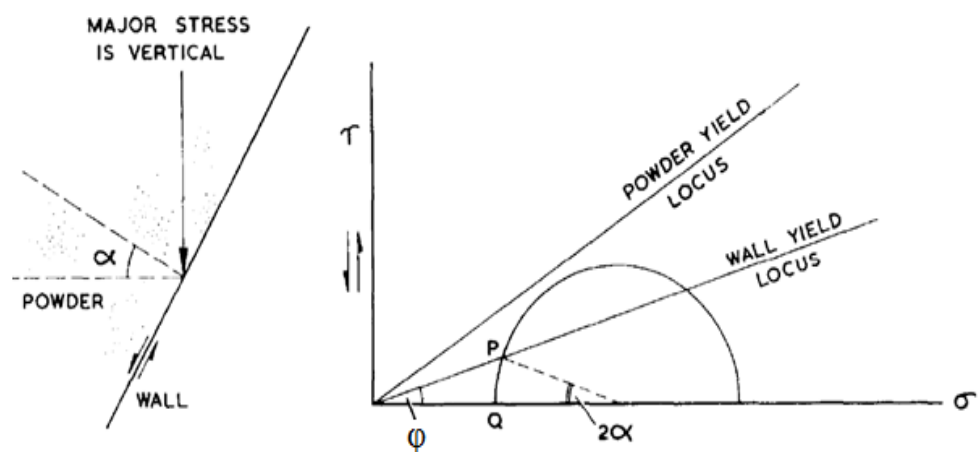


**Figure 2.11** Initial hopper wall pressure exerted by bulk solids at the filling phase (Walker, 1966)

As the bulk solid settle, it start to slid on the wall and raising gradually the horizontal stress until the wall stresses re-levelled on the wall yield locus (Nedderman, 1992).

Walker (1966) assumed that, at any level of the bulk solid bed, the hydrostatic pressure is equal to the vertical pressure. Mathematically, this means that the wall pressure is a constant multiplied by the exerted vertical pressure as follows:

$$W = V \frac{\sin 2\alpha \cos \varphi}{\sin(\varphi+2\alpha)+\sin \varphi} \quad \text{Eq. 2.13}$$

Where  $W$  is compressive stress normal to wall,  $V$  is vertical compressive stress and  $\alpha$  is hopper half apex angle and  $\varphi$  is the angle of wall friction.

Walker (1966), Walker and Blanchard (1967), Walters (1973a), (Walters, 1973b) investigated deeply the static and dynamic stress states inside hopper using slice element method according to various assumptions

In case of mass flow trend inside storage bin, Walker (1966 and 1973) investigated and analysed the stress distribution according to the following assumptions;

- The directions of both principal stresses are in the vertical plane normal to the nearest section of wall.
- The solid bulk materials within the bed and at the boundaries must be yielding within itself to discharge through the outlet.
- The mass flow trend is characterised by material sliding along the bin and hopper boundaries.
- The vertical stress acting on the horizontal plane is constant.

The main difference between Walters and Walker theories is the wedge effect. Walters used a frustum cone slice, while Walker used a cylindrical slice that touches the bulk only at one point and ignores that influence in the calculation. Figure 2.12 summarises the main difference in the assumption and calculation of both Walker and Walters. Stress component here is in reverse way compared to the vertical section.

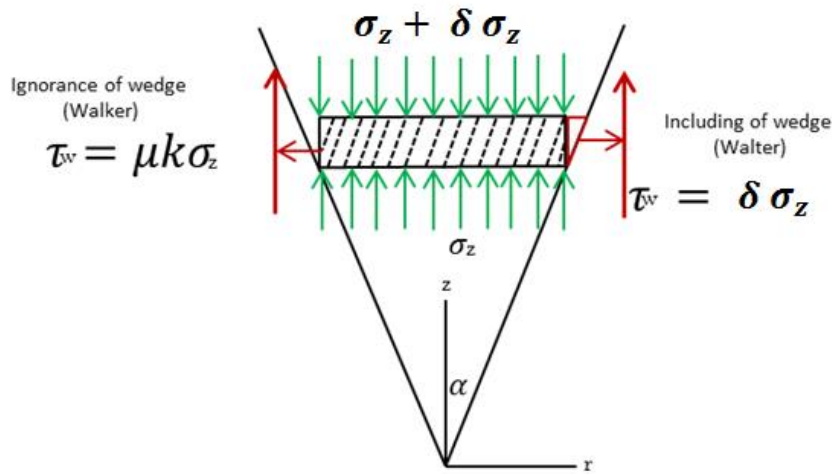


**Figure 2.12** Walker and Walters slice element method

The stresses acting on the slice are;

$\sigma_z$                   Acts on the lower zone of the element

$\sigma_z + \delta\sigma_z$       Acts on the upper zone of the element

$\tau_w = \delta\sigma_z$       Acts on the side of the element in case of Walter or

$\tau_w = \mu K \sigma_z$     Acts on the side of the element in case of Walker

### 2.2.2 Experimental Methods

Experimental approaches had been also conducted in addition to the analytical methods to measure and investigate the influence of the stress exerted by the granular materials on the walls of hoppers and silos. The experimental studies are crucial for realistic understanding of the influences of varying granular physio-mechanical properties on the storage bins wall pressures and stresses. This step is essential for multiple industries as storage bins are used for transporting granular materials and other processes. In addition, the experimental studies are useful to validate any analytical predictions for the calculation of the wall stress.

The pioneering experimental studies conducted by Walker (1966), Walker and Blanchard (1967) and Jenike et al. (1973) using coal granules and sand respectively are still considered as the main guideline and reference for researches investigating

the silo and hopper wall stress distribution. Jenike et al. (1973) reported from their experiments that for mass flow trend inside cylindrical hopper, the critical design stress has to be the maximum for both the initial loading (active stress) and flow loading (passive stress). Further details about Jenike and Walker experimental works are reported in sections 2.3.1.2 and 2.3.1.3.

Recently, many experimental researches rely on embedding multiple loading cells in both silo and hopper wall sides at different segments in order to measure the normal and shear stress exerted on bin walls (Chou and Chen, 2003, Bohrnse et al., 2004, Ostendorf and Schwedes, 2005, Ezz El-Arab, 2014). Such sensors help to evaluate and detect the stress fluctuation due to granular materials shifting from the shaft to the hopper section during the dynamic flow process (Bohrnse et al., 2004, Ostendorf and Schwedes, 2005).

Chou and Chen (2003) have evaluated the theoretical and experimental normal and shear stress in a 2D wedge shape hopper using embedded loading cells as shown in Figure 2.13. The hopper's internal angles evaluated in this research were  $20^\circ$  and  $40^\circ$ . The authors reported that the predicted theoretical stresses values were less than that obtained experimentally which attributed to the ability of wedge shape hopper walls to carry part of the granular materials weight due to both inter-particle and particle wall friction forces.

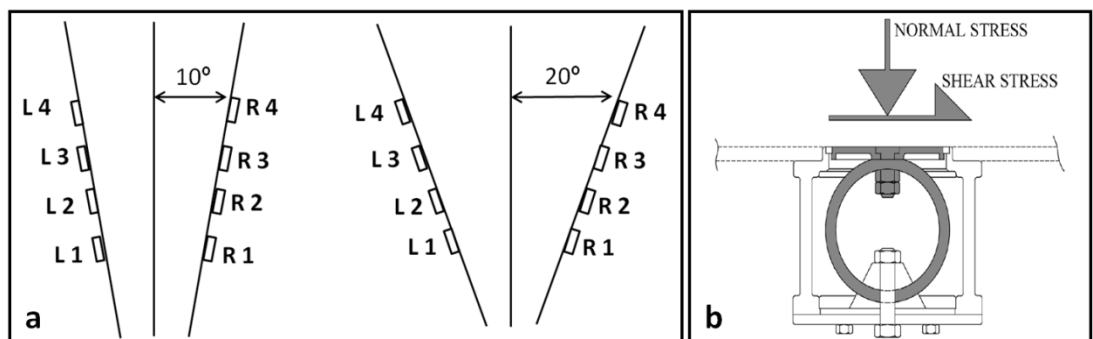


**Figure 2.13** Wall stress measurement method using embedded loading gauges on hopper walls; (a) location of gauges and hopper internal angles (b) drawing diagram of gauge (Chou and Chen, 2003)

Inside  $20^\circ$  internal angle hopper geometry, the flow trend was nearly mass flow and the dynamic stress on the hopper wall has a similar trend as the static stress, and shear stress values were less than the normal stress values. On the other hand,

hopper having 40° internal angle (nearly funnel flow geometry) showed clearly non-consistent stress measurements. Interestingly, the authors reported transit overpressure and under pressure during the dynamic granular materials flow process.

Ostendorf and Schwedes (2005) adapted the same embedded loading cell method with PIV technique to measure the wall stress and particles velocity inside the hopper geometry simultaneously. They have reported that the granular materials bulk density and radial stress values are decreased toward the hopper outlet as the particles velocity increased in this direction. They also reported that the stress values at the lower loading cells close to the hopper outlet are identical compared to the variable values at upper cells. Moreover, an early increase of wall stress at upper loading cells during the switch flow phase has been reported when the granules shift from shaft to hopper.

Ezz El-Arab (2014) conducted recently a concurrent experimental and numerical study using embedded loading cells and FEM to investigate cylindrical silo and hopper wall stress during the filling and discharging process. The author focused mainly on the influence of the filling method on granular materials flow and silo stress distribution. The study showed that the simulated discharging results are faster than the actual experimental results and any altering of the granular materials filling method crucially affects the flow and stress distribution. This is attributed to the granular bed dilation requirement to pass from its initial packing density inside the storage bin to the required critical density allowing smooth flow process. Interestingly, it has been reported that under mixed flow, high variation and noticeable asymmetry wall stress measurements have occurred during the discharging process. The reported asymmetry of the stress values are very high and may have great influences on overall stress magnitudes inside the silo. The author also reported the occurrence of two different categories of stress fluctuations during the dynamic flow process denoted as slower and momentary fluctuations. Slower fluctuations are created due to the developed shear bands as the granular materials shifting from shaft to hopper segment. Moreover, the momentary fluctuations developed as the macroscopic “steady state” flow in the hopper geometry is not real “steady state” flow trend where the magnitudes of the fluctuations are very

high. This can be considered as the main criticism of numerical simulations using FEM as it is very strong tool for simulation but cannot consider the microscopic influences of the materials on their macroscopic behaviour.

### **2.2.3 Simulation Methods**

Simulation or computational modelling methods such as FEM and DEM are considered powerful techniques to predict silo and hopper wall stress exerted by stored granular materials as well as the flow behaviour (Rotter et al., 1998, Baxter et al., 2000, Ding and Enstad, 2003, Landry et al., 2004, Zhang and Rosato, 2004, Ketterhagen et al., 2009a, Ding et al., 2011, Wang et al., 2013). Both FEM and DEM are widely used and adapted for granular flow assessment and stress predictions but certain limitations for both methods should be taken into consideration (Rotter et al., 1998, Ezz El-Arab, 2014). The capabilities of such methods to solve the problems of complex geometries make them suitable tools for assessment of both the filling and discharging process (Rotter et al., 1998, Ding et al., 2011, Wang et al., 2013). The main difference between FEM and DEM application for granular materials assembly assessments, is that FEM is based on the continuum approach while DEM is based on discrete approach (Cundall and Strack, 1980, Langston et al., 1995, Ding and Enstad, 2003, Ezz El-Arab, 2014). The continuum approach deals mainly with macroscopic scale characteristics that make it more applicable for large scale industrial manufacturing involving large amounts of bulk solids (Ding and Enstad, 2003). On the other hand, the discrete approach deals with microscopic scale characteristics and takes into consideration the physical characteristics of each discrete particle as separate entities for modelling (Cundall and Strack, 1979, Langston et al., 1995).

Langston et al. (1995) have developed and conducted a DEM based research project to evaluate the granular materials filling and discharging process using non-cohesive discs and spheres in two and three dimensional model hoppers respectively. The authors aimed to investigate the influence of the continuous and gradual hopper filling method on stress distributions. The obtained results showed that the gradual filling method improved the wall stress profile of the static status significantly. The authors also reported for the first time in DEM simulation in the case of the hoppers'

discharging process, the appearance of granular bed rupture zones and related wall stress peaks where the zones intersect with the hopper wall.

Ding and Enstad (2003) and Ding et al. (2011) developed the FEM study to model the development and the distribution of the hopper walls stress exerted by granular material during a filling process using multiple filling methods. Two different filling procedures have been applied in this study; switch-on procedure and layer by layer procedure, up to 8 layers. The aim was to investigate the influence of the filling procedures on the nature of stress distribution. The results reported that the maximum stress obtained at the end of the filling process does not occur at the bottom of the hopper but somewhat closer to layer 3 level. This area showed the best particle consolidation and has the lowest ratio of shear stress and normal stress. The maximum normal wall pressure at the hopper outlet during the filling process showed a marked deviation from that obtained by Walker as the pressure magnitude increased and moved progressively upwards. The authors also reported that the layer by layer filling procedure showed more stress values compared to switch-on procedure at the hopper bottom and less at higher levels.

Vidyapati and Subramaniam (2013) modelled the discharge dynamics of granular particles from a flat-bottomed silo using continuum modelling and three-dimensional DEM. Concurrent application of DEM with continuum modelling is due to the powerful capability of the DEM to investigate and quantify the influence of microscopic parameters such as interparticle friction coefficient, particle–wall friction coefficient and particle coefficient on the discharging rate. The DEM obtained results showed that the discharging rate in a flat bottomed silo are greatly influenced by interparticle friction coefficient and discharge outlet size alteration. However, the influence of the wall friction coefficient on the discharging rate is negligible. The obtained comparative quantitative results of discharge rates, solid velocities and solid stresses showed that the constitutive models over-predicted their values compared to DEM data.

Kondic (2014) adapted DEM to evaluate the influence of the ratio of hopper outlet size and the mean particle size on granular materials jamming inside the 2D silo geometry. The author was aiming to compare the 3D system ratio requirements to the 2D system. The obtained results reported significant influence of this ratio on the

particle jamming tendency. The small opening size showed the high jamming tendency close to the hopper opening regime and material parameters have strong influence. On the other hand, a larger opening size has less jamming tendency and the influence of material parameters, such as friction or coefficient of restitution is negligible.

Wang et al. (2013) and Wang and Ooi (2015) applied FEM and DEM for continuum and discrete assessment of granular material filling and discharging inside the conical hopper geometry respectively. The continuum modelling approach based on Arbitrary Langrangian-Eulerian (ALE) formulation in order to avoid any mesh alteration due high deformation possible of the materials. The results indicated that the combination of ALE and FEM effectively simulated the silo discharge under high deformation conditions. The obtained results of the discharge pressure distribution and mass flow rate are in a good level of agreement with those obtained from the theoretical models. The authors have reported very interesting phenomena through the analysis of the exerted pressure fluctuation which revealed two dominant frequencies. The origins of these frequency events are the propagation of the compression wave and development of intermittent shear zones within the granular bed during the discharging process, creating higher and lower frequency events respectively. This could provide a proper explanation for the coexistence of silo shaking and vibration during the discharging process. The predicted hopper wall stress distribution using FEM was much smoother than that obtained using DEM.

Xu et al. (2015) investigated the influence of both side and face wall friction coefficient of the hopper on the stress ratio during granular discharging, using DEM inside 3D system. The influence of the hopper wall thickness on stress ratio is also evaluated. The results indicated gradual increases of the side wall stress ratio due to side wall friction increment followed by a slightly decrease. At the same time, the face wall stress ratio showed slight early increases and then remained almost constant. On the other hand, increasing of the face wall friction coefficient, declines the side wall stress ratio in the thin hopper and remains constant in a dense one. Further analysis of the force network showed marked increases of relative density close to the wall as the wall friction coefficient increases, indicating more wall supported the particle load.

## 2.3 Powders and Granular Materials Subjected to Compression

In pharmaceutical science, the oral route of administration is the most favourite route for both patients and pharmaceutical product manufacturers. For example, in cases of systemic therapeutic actions, around 90% of the drugs are administered orally, and solid dosage forms such as tablets are the dominant form (Gilber and Neil, 1987). British pharmacopeia (B.Ph), defines the pharmaceutical tablet as a solid preparation contains a predetermined dose having one or more active ingredient with or without excipients obtained by compressing uniform assembly of particles. Compression of such assemblies takes place in confined compression die, having multiple geometries under either uniaxial or biaxial compression mechanisms. The final products must be elegant, strong enough to withstand mechanical agitation and must be chemically and physically stable (Gilber and Neil, 1987).

Figure 2.14 summarises the tablet manufacturing process from the pre-formulation phase through to the final solid product and shows the complexity of this process.

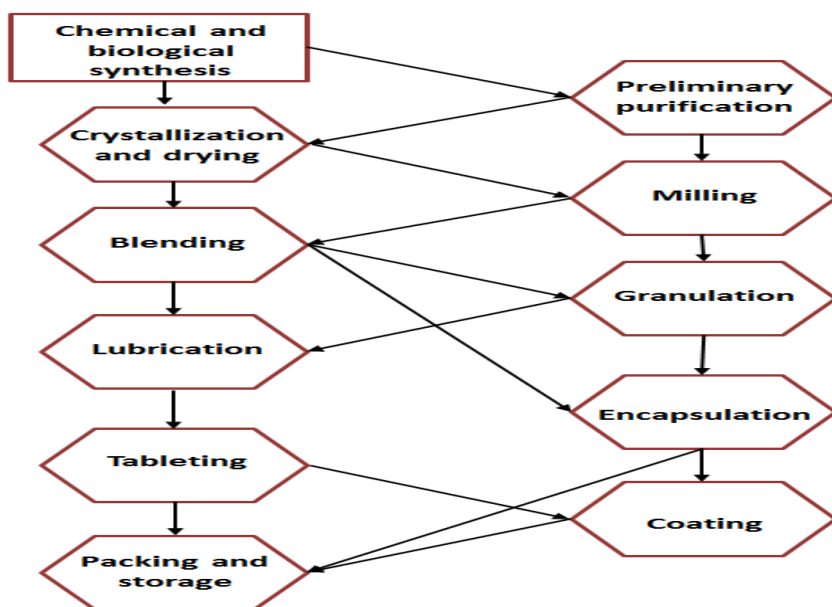


**Figure 2.14** Multiple stages involved in tablet manufacturing Modified from Muzzio et al. (2002)

Powder and granular material compression have been investigated extensively by many researchers during recent decades (Walker, 1923, Shapiro and Kolthoff, 1947, Kawakita, 1956, Heckel, 1961b, Kawakita and Lüdde, 1971, Hersey, 1974,

Carstensen and Toure, 1980, Denny, 2002, Sorensen et al., 2005, Mallick, 2014). In the pharmaceutical industry, there are many technical terminologies applied in the manufacturing processes, these terms are powder compaction, compression and consolidation (Marshall, 1987).

Compaction is generally applied when a sample of materials are subjected to certain levels of external mechanical force (Marshall, 1987, Odeku, 2007). The compression process describes the reduction in bulk material volume and the deformation nature of the powder sample under pressure, while consolidation reflects the increment in the material mechanical strength, resulting from particle-particle interaction (Marshall, 1987, Odeku, 2007).

The early pioneer who published mathematical equation describing powder compaction and consolidation characteristics is Walker (1923), where static load was applied to measure the changes in powder volumes and the resistance of the powder for the compression process. Such study is limited to the changes in powder porosity, densities and interparticle voids. Walker's equation directly reflects the impact of the applied pressure on the powder volume as his results shows the relationship of the powder's relative volume changes against the logarithmic applied pressure.

Another equation was reported latterly by Bal'shin (1938). He proposed and published a similar relationship to that observed by Walker using metallic powders with some justifications based on fluid mechanics. The most applicable mathematical modelling for powder compressibility and consolidation applied recently for multiple industry applications are those reported by Shapiro and Kolthoff (1947), Kawakita (1956), Heckel (1961b), (Heckel, 1961a) and Kawakita and Lüdde (1971). Although, these validated equations for powder compaction have received critical evaluations and criticisms regarding their constant values and their generalisation for both powders and granules (Celik, 1992, Shapiro, 1997, Sonnergaard, 1999, Denny, 2002).

Up to date, there is no available comprehensive mathematical equation that could be applied to a wide range of compaction in industry. Pharmaceutical industry mainly considers Heckel and Kawakita in most of their applications, as the pharmaceutical

powder may undergo elastic and/or plastic deformation. On the other hand, metallurgy industries prefer Heckel's equation due to plastic deformation nature of metals (Denny, 2002). Details on the nature of stress distribution within micron size particulates are still lacking.

During the compression process of powders in general, and pharmaceutical powders in particular, marked changes occur in the density profile distribution of compressed bed (Train, 1956, Heckel, 1961b, Kadiri et al., 2005, Wu et al., 2005, Sinka, 2007). These changes dramatically affect the mechanical properties of the final product such as tablet lamination and capping (Michrafy et al., 2002, Wu et al., 2005, Sinka, 2007, Akseli et al., 2014, Sarkar et al., 2015). Multiple investigations, including experimental and numerical methods have been used to explain these changes and their influences on the quality of the final products (Celik, 1992). The results showed that there are high influences of relative density distribution and shear stress profile propagation on the crack and lamination process, especially during tablet relaxation and ejection phases (Wu et al., 2005, Sinka, 2007).

In general, there are two common methods applied to investigate and probe the compression of powder and granule: mathematical method and numerical method.

### **2.3.1 Mathematical Methods**

An extensive review of literatures on powders and granules compaction and compression show the availability of a number of mathematical methods and equations based on experimental work applied at different stages of compression process (Carstensen and Toure, 1980, Celik, 1992, Odeku, 2007, Mallick et al., 2011, Mallick, 2014). The parameters of the mathematical equations are simply the applied pressure and the powder bed density, compressed bed volume and powder bed height.

### **2.3.2 Heckel's Equation**

Heckel derived his equation based on experiments using multiple compression of electrolytic iron powder and chemically precipitated copper powder at different compression pressures (Heckel, 1961b, Heckel, 1961a). Heckel's equation is one of the most commonly used equations in pharmaceutical science and his plot illustrated

in Figure 2.15 summarises the relationship between the applied compression pressure and porosity of the compressed bed.

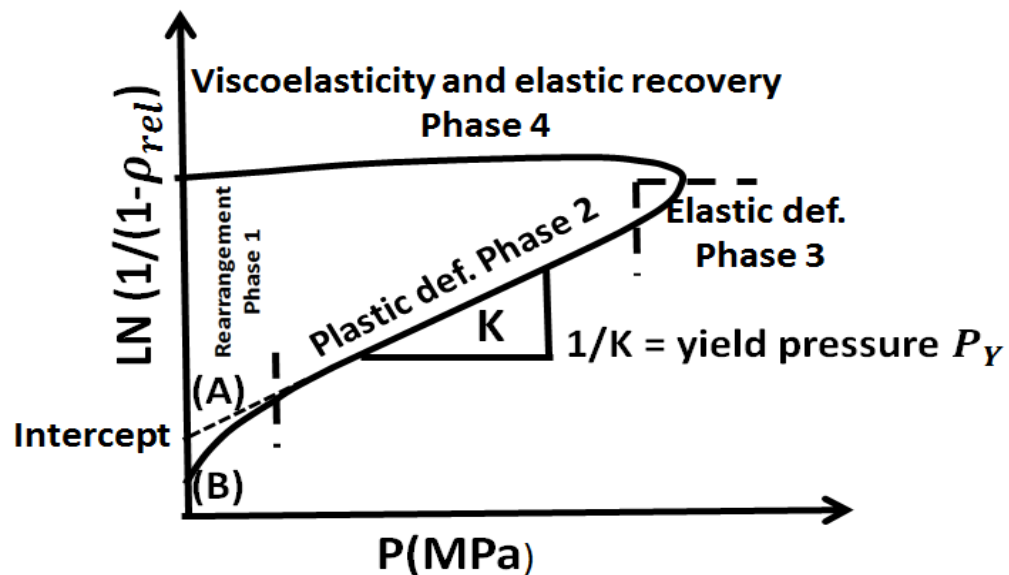


**Figure 2.15** Schematic plot of Heckel profile during compression and decompression process (Modified from (Comoglu, 2007)

Heckel equated this relationship as follows;

$$\ln\left(\frac{1}{1-D}\right) = kp + A \quad \text{Eq. 2.14}$$

Where  $D$  is the relative density of the powder,  $p$  is pressure,  $k$  is a constant,  $1-D$  is the pore fraction and  $A$  the intercept. Heckel assumed the powder compression rate is following the first order kinetics.

Heckel attributed the nonlinearity of the early phase of the compression (Phase one) to the effect of rearrangement processes in the powder bed and due to the discrete behaviour of the powder bed assembly (Heckel, 1961b). Denny (2002) provides another explanations for the phase (1) nonlinearity related to the ability of the powder to densify via brittle fracture mechanism or agglomeration, especially in the case of fine powders. He also criticised Heckel's equation and suggested that further modification and corrections are required.

Phase (2) represents the plastic deformation phase of the compressed powder, characterised by the clear linearity between the compression variables. At this stage the compacted state is achieved and the physiomechanical properties of the

compressed bed determine the extent of consolidation. Phase (3) is known as the elastic deformation phase and describes the elastic deformation of the compressed bed under high pressure (Sun and Grant, 2001). The last phase (4) is known as the viscoelastic and elastic recovery phase which occurs after compression, where some compacted materials may show this behaviour. Paronen (1986) and Sun and Grant (2001) discussed in detail the reliance of researchers on the Heckel equation to collect the required data for compression using well known methods; “out-of-die” method which occurs after compressed bed ejection at zero pressure load, and “in-die” or “at-pressure” which occurs during compaction under high loads. The vertical distance from point (A) to (B) is a measurement of the extent of rearrangement and fragmentation phase (Mallick, 2014).

### 2.3.2.1 Kawakita Equation

The second mathematical equation used commonly in powder compression is known as the Kawakita equation or Kawakita and Lüdde in some references (Kawakita and Lüdde, 1971). Kawakita equation shows the relationship between pressure and volume as follows;

$$C = \frac{v_0 - v}{v_0} = \frac{abp}{1+bp} \quad \text{Eq. 2.15}$$

Where  $C$  is the degree of volume reduction,  $v_0$  is the initial bulk volume,  $v$  is the volume of the compressed bulk and  $ab$  are constants. From equation 2.15, Kawakita equated the liner form of his equation as follows;

$$\frac{p_a}{c} = \frac{1}{ab} + \frac{p_a}{a} \quad \text{Eq. 2.16}$$

The linear relation between  $p_a/c$  and  $p$  is shown schematically in Figure 2.16.

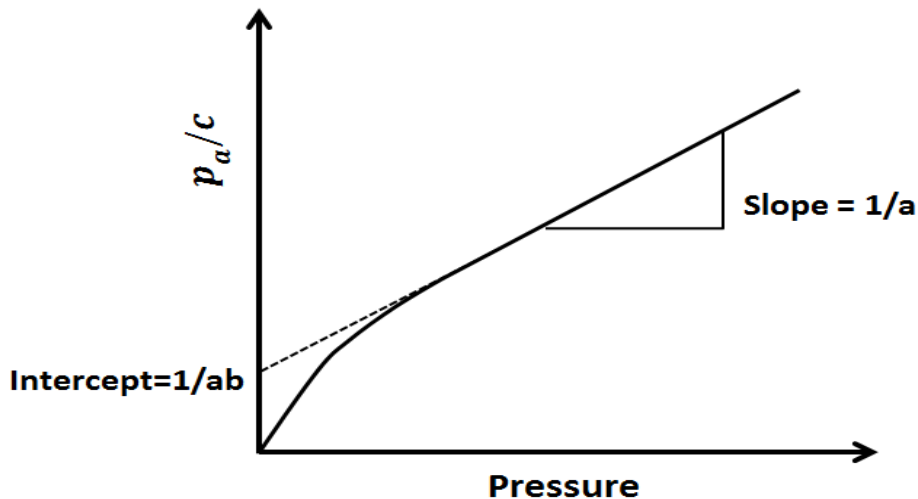


**Figure 2.16** Linear Kawakita plot for powder compression (Modified from Kawakita and Lüdde, 1971)

Kawakita and Lüdde (1971) have mentioned that the equation holds best results for soft fine “fluffy” pharmaceutical powders and more caution must be considered in the initial volume measurements to avoid any variation in the results. Similar to criticism over what has been reported in the case of Heckel, the initial curvature in Kawakita plot raises some arguments in the powder compression evaluation.

### 2.3.3 Computational Methods

Computational simulation of pharmaceutical powders and granules compression, stress distribution, densification and die filling has been of great interest in recent years (Michrafy et al., 2002, Hassanpour and Ghadiri, 2004, Antony et al., 2005, Wu et al., 2005, Kremer and Hancock, 2006, Wu and Cocks, 2006, Wu, 2008, Ketterhagen et al., 2009b, Frening, 2010).

Wu and Cocks (2006) and Wu (2008) developed and modelled the compression die filling using DEM, in order to investigate the influence of the particle physiomechanical properties such as particle shape and interparticle friction on the particle velocity and die filling trend. The obtained results indicate that spherical particles having low interparticle friction fill the die faster than irregular particle shapes that have high friction coefficient.

Hassanpour and Ghadiri (2004) modelled pharmaceutical powder compaction using DEM, in order to investigate the accuracy of using the Heckel equation parameters (applied pressure and powder deformation) to probe the yield stress of individual

particles. The authors reported that the Heckel approach cannot be generalised and the Heckel parameter is able to represent yield stress only at low ratios of Young's modulus to yield stress. The non-accuracy of the Heckel approach raised because it is almost impossible to subject all particles to the same compression load and any changes of the experimental condition or bed density would alter the values in the equation.

Frenning (2010) developed the combined DEM/FEM modelling approach, in order to investigate the micro and macro characteristics of sphere particles under compression conditions in a 3D system. Such combined method is able to investigate the influences of discrete particles properties such as yield stress and initial porosity using DEM on the macro behaviour of compressed bed via FEM result. This combination helps to focus on the mechanism of single particulate densification and deformation and its influence on the behaviour proceeded during the confined compression process. The author also reported that the Kawakita parameter  $1/ab$  reflects the (effective) yield stress of the granules.

Siiriä et al. (2011) computed the powder densification through a DEM approach to model the tabletting process. The authors aimed to probe and investigate the interparticle bonding under load in a confined chamber which helps to provide the basis and fundamentals to calculate internal strength distribution of the compressed tablet during the compaction process. The simulation results compared to that obtained experimentally and the compressed tablet strength have been calculated according to the number and strength of the bonds generated during the compression process. The accuracy of the simulation results was very high, as the magnitudes of both experimental and numerical forces are almost identical. The distribution of bond strength within the compressed table exhibited a similar trend to the density and pressure profile distribution available in the literature (Michrafy et al., 2004), except the centre of the tablet where some individual variations were reported.

Sinka et al. (2004) developed FEM to simulate the relative density distribution in curve-faced tablets and to investigate the influence of compression die lubrication on the density profile distribution. The obtained experimental and numerical results showed a dramatically different distribution trend of the density profiles and internal porosity of the lubricated and the non-lubricated tablet. The non-lubricated convex

tablet showed high dense regions at the die boundaries compared to the centre, while the lubricated tablet showed totally opposite results. Both numerical and experimental results showed good levels of agreement.

Michrafy et al. (2002) developed the FEM model in order to investigate the stress and density changes of powders based on the elastic–plastic theory under uniaxial compression at 50% of the compression cycle. The model takes into consideration the macroscopic features of powders such as cohesion and the interparticle friction. The obtained results showed marked increases in the axial displacement of compressed bed from the top to the bottom. These results have good levels of agreement with previous studies showing axial transmission of the load from the upper segment of the compressed bed to the lower segments (Train, 1956, Macleod and Marshall, 1977). The results also indicated that the pressure and the shear stress decreased at the die wall. On the other hand, the internal shear stress distribution profiles through the compressed bed increased from the top of the die to the bottom. During the unloading process, it behaves in a reverse way and increases the chance of tablet capping.

Wu et al. (2005) computed the mechanical characteristics of pharmaceutical powder as an elastic–plastic continuum material using FEM. The Drucker–Prager Cap (DPC) model was adapted in this study to reflect the failure and yield behaviours under uniaxial compression process. The obtained results showed non-uniform distribution of the relative density profiles under the compression, regardless of its initial uniformity before the compression. Through the compression process, highly dense zones were developed at the top section of the bed (below the upper punch) and relatively low dense zones were reported at the bottom. Density profile variation was directly attributed to the particle-wall friction coefficient that decreases the particle motion close to the wall as well as the very limited motion of the particles at the bottom, due to limited space. High stressed zones were reported at the top of the bed, especially at the upper wall edge. The bottom of the die and the boundaries showed relatively low stressed zones compared to the top segment. During the unloading process, the stress status inside the compressed bed reversed and the lower segment of the die showed higher effective stress values than the upper segment due to more bed relaxation. The authors reported that the occurrence of the

intensive shear band started from the top edge of the compressed bed to the mid-centre. This zone becomes very weak and tablet deformation can take place at this site. The numerical results have been validated by experimental results using X-ray tomography showing good levels of agreement.

Sinha et al. (2010) computed the compaction of pharmaceutical tablet using FEM. The authors investigated the accuracy and applicability of using relative density dependent DPC and a constant material parameter model for FEM applications. The results indicated that using a DPC material model through FEM application has more advantages than constant material parameter model. DPC was able to show clearly the incidence of material displacement as well as the vertical and radial deformations occurring at the boundaries compared to the constant property model. The experimental results were very close to the DPC results. The relative deviations of the constant property model from the experimental results were in a range of 5% and 6% for compression punch force and surface relative density measurements respectively. The main disadvantage of using DPC for computing powder compression, is the length of time required for both characterisation of the experiment parameters over a range of relative densities and performing the calculations.

Recently, there are significant developments in numerous qualitative and quantitative experimental visualising methods to probe the internal profile structure changes of powders and granular beds under certain external loads. These techniques include X-Ray micro-tomography (Fu et al., 2006, Hancock and Mullarney, 2005, Hall et al., 2010), positron emission particle tracking (Bridgwater et al., 2004), nuclear magnetic resonance imaging (Huan et al., 2004). Such techniques are powerful methods to show the powder and granular material density changes inside the compressed beds.

### **2.3.4 Compression Process Cycle**

Granules and powders compression process in pharmaceutical industry consists of four to five consequent stages (Carstensen and Toure, 1980, Denny, 2002). The difference between the previous classifications is whether to consider the die filling as single phase or not. The die filling process has been sought experimentally and numerically by numerous researchers who reported the crucial influence of this

phase on the integrity and quality of the final product (Wu et al., 2003, Guo et al., 2011, Riera et al., 2005). There are different opinions available in the literatures regarding the understanding of powder and granular material compression process, as it consists of several sequenced steps occurring in a very short time, and some overlaps are expected (Duberg and Nyström, 1986, Coube et al., 2005, Sinka, 2007, Nordstrom et al., 2009).

Accordingly a typical compression cycle is sub-classified into five stages as follow;

#### **2.3.4.1 Filling Stage**

During the filling stage, powders or granules are fed to the compression die from their storage bins using a suitable feeding hopper in loose packing (Coube et al., 2005). The physical properties of the particles such as particle sizes, size distribution and particle surface morphology have great influence on the initial packing density (Freeman and Fu, 2008). In addition to this, feeding hopper shape, compression die and tableting speed have noticeable influences on the packing density and integrity of the final product (Wu et al., 2005, Sinka, 2007). The common hopper shape feeding the die in the pharmaceutical industry is known as a horse shoe hopper that feeds the materials from the storage bins to the die and subsequently levels the granular assembly surface. This stage has a great impact on the quality, content uniformity and integrity of the final product (Sorensen et al., 2005).

#### **2.3.4.2 Particles Rearrangement Stage**

This stage starts immediately when the upper punch slips into the compression die at low pressure, causing rearrangement and sliding of the small particles between the large ones within the die chamber. Arch formation tendency and air entrapment within the compressed powder bed increased, especially in the cases of irregular particle shapes (Staniforth and Aulton, 2002). The nature of the changes at this stage is still ambiguous to the researchers and deep investigation on this stage of compression and stress distribution status is needed (Denny, 2002). According to the Heckel equation, this stage of the compression cycle is represented by the non-linear part (Figure 2.15). The nature of changes at this part needs further investigation, especially the stress status development. Unfortunately, experimental and numerical information and data at this stage are scarcely published. The limited available results through the literatures are limited to the changes in the volume of

compressed powders and density profiles (Sorensen et al., 2006, Sorensen et al., 2005).

#### **2.3.4.3 Elastic Deformation Stage**

This stage starts immediately after the rearrangement stage, the force of compression increases and the particles have more contact with each other. At this stage the particle size and final volume are reduced due to the elastic reversible deformation of the particles. Occurrence of the elastic deformation of the compressed particles depends on the applied load and the deformation nature of the particles. The elastic deformation stage must be exceeded to increase particle-particle bonding to obtain intact solid compressed mass (Carstensen and Toure, 1980). Some particles such as metal and ceramic do not show any elastic deformation behaviour as they are very rigid and start to fracture under high loads (Denny, 2002).

#### **2.3.4.4 Plastic Deformation Stage**

The plastic deformation stage is reached at very high external loading conditions. During this stage, particles exceed their elastic limit and start to fracture and compact. The maximum compression forces is exerted at this stage, where most modelling and experimental researches focused and concentrated to show the possible changes in the density distribution profiles, shearing band and stress status (Hewitt et al., 1974, Alexandrov et al., 1998, Hua et al., 2006). In the case of submicron particles compression, the particles mostly compact via plastic deformation as most particles pass a brittle stage to ductile transition and fragmentation (Atkins and Mai, 1986).

#### **2.3.4.5 Ejection and Bed Relaxation**

Releasing the compression load and ejection of the solid compacted particles is the last stage of the compression cycle. The compressed particles partially relax and the extent of relaxation depends on the nature of the particle deformation mechanism. Materials show elastic deformation, displays more bed relaxation than that deformed plastically (Rehula et al., 2012). The compressed bed relaxation and stress redistribution depends on the shape of the die and the lubrication of the granules (Han et al., 2008).

## 2.4 Photostress Measurements

Photoelasticity is non-destructive experimental technique used for qualitative and quantitative mapping of stresses and strains within machine component models that have complex structural geometries (Post, 1989). Photoelastic technology is widely used in engineering industries in which stress or strain information is crucial and required for further structural improvements of products or newly fabricated machines (Post, 1989, Aben et al., 2000, Smith Neto et al., 2006, Misseroni et al., 2014). Photoelastic technology is able to provide quantitative evidence of highly stressed areas and peak stresses at the surface plane as well as the internal structure that help the manufacturers for proper structure utilisation (Post, 1989).

Photoelastic technology is fundamentally based on “opto-mechanical” phenomenon known as material birefringence that is usually observed under polarised light (Post, 1989, Saad et al., 1996, Antony and Chapman, 2010). Birefringence may call a double refraction phenomenon due to its ability to divide the light into two components known as ordinary and extraordinary component (McKenzie and Hand, 1999). This birefringence is directly proportional to the difference between major and minor principal stresses at any point due to external applied forces or pressures. Birefringence is also possessed by many transparent polymers as well as a very few biological materials and tissues such as skeletal muscle fibres, the radula of a snail, and starch (McMahon, 2004). Human corneal eye tissue is also considered as one of the birefringent biological tissues due to highly organised internal lamellar structure (Hitzenberger et al., 2006, Antony, 2015). Highly ordered molecular structured crystals such as oxalic acid, and sucrose are considered as birefringent materials (Singh et al., 2012).

If the materials are not birefringent on their own, another method called birefringent coating method may be applied using a birefringent coating material (Andreyev, 1975, Akhmetzyanov and Albaut, 2004). This method is usually used for the measurement of surface stress and strains in opaque objects such as metals and wood using two and three dimensional models (Chang et al., 2009, Jankowski et al., 2010).

### **2.4.1 Background of Photoelasticity**

Thomas Johann Seebeck (1770 – 1831) is often known as the pioneer who discovered the thermoelectric effect at 1821 during the golden era of optic science applications (Aben, 2007). During (1822) he published his first paper that showed the magnetic polarisation of metals and minerals by temperature difference (Aben, 2007). It was the first opportunity to investigate systematically birefringence in glass specimens of different shapes using different thermal treatment. Since then, applications of polarised light facilitate and adapt new methods to investigate transparent objects, crystals and even solid objects using photoelastic coating materials (Andrushchak et al., 2004, Jankowski et al., 2010, Behringer et al., 2014).

Recently, modern photoelastic equipment is widely applied in the industrial field for qualitative and quantitative application, aiming for better insight, understanding and final product quality improvement (Calvert et al., 2002, Antony and Chapman, 2010, Ajovalasit et al., 2012, Albaraki and Antony, 2013, Antony et al., 2014b, Dora and Ramesh, 2014).

### **2.4.2 Light Principles and Physics**

Futterknecht et al. (2013), reported that the usage of polarised light by humans goes back to the Viking era, when they used a crystalline stone called “sun stone, as reported in many sagas” for navigation in cloudy conditions across the North Atlantic.

According to Maxwell’s theory, light, is an electromagnetic wave, which presents both an oscillating electric and magnetic field. The earlier wave oscillates at the same frequency as the latter, but with a perpendicular orientation. Only the electrical field is considered when determining the polarisation state of light (Berne and Pecora, 2000). The surrounding conditions may affect light’s nature and undergo two well-known phenomenon known reflection or refraction mechanisms. Reflection occurs when the light ray rebounds off a surface and the angle of the incident ray is equal to the angle of the reflected ray (Berne and Pecora, 2000). In contrast, refraction is characterised by the bending of light as it passes from one medium into another and alters the wave’s speed. According to that, light can be classified mainly as ordinary light and polarised light.

#### 2.4.2.1 Ordinary Light

In nature, light is non-polarised, light waves generated from the light source such as the sun, or a lamp and vibrates in all directions. Ordinary light waves as well as most waves (except sound waves) involve a vibration at right angles to their path (Berne and Pecora, 2000). Simply, ordinary light wave vibration can be described as a wiggled rope, where the waves fluctuate up and down and from one side to the other.

#### 2.4.2.2 Polarised Light

In the last few decades, the process of light polarisation is extensively accredited to be one of the most important properties of light due to its broad and extensive applications in several industrial and research fields (Goldstein, 2003). These fields include engineering, medicine, biology, pharmaceutical industry, optical devices industry and food processing. In nature, light polarisation may occur at multiple levels of earth atmosphere and utilised by some insects during their daily activities to determine the location of the sun, location of their nests and the flowers classes (Wehner, 2001).

Polarised light is quite simply light in which the waves all vibrate in one single and fixed direction. A polarising filter can easily convert ordinary light (non-polarised) into polarised light by allowing only a light wave oriented in a single plane with the transmitting axis to pass and block all other vibrational planes as shown in Figure 2.17.

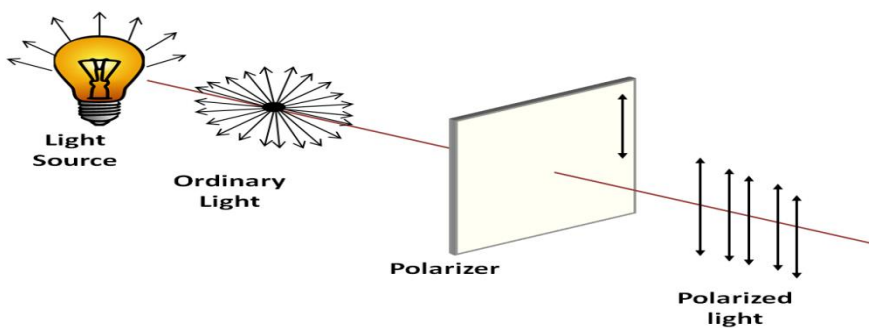


**Figure 2.17** Light propagation and polarisation using simple polariser

The most common method of light polarisation involves the use of polarising filters. Such filters are made of material that block one of the two planes of vibration in

each light wave due to their chemical composition. For example, a polaroid filter is produced commercially using a combination of long chains of polymers molecules aligned in the similar direction which creates an alignment axis. The horizontally aligned filter will allow only horizontal vibrations to be transmitted and absorb the vertical aligned vibrations.

Based on the previous fundamentals, polarised light movement can be sub-classified to three main classes; Linear polarised light, circularly polarised light and elliptically polarised light (McKenzie and Hand, 1999).

Recently, advanced technology developments have enabled the manufacture a wide range of polarisers, designed specially to produce polarised light of a specific state, independent of the incident state. It enables to changes electromagnetic energy, such as visible light, from a mixed or non-polarised wave into polarised one. Many optical devices such as cameras, telescopes, and microscopes have this technology either built in or a screw on function to examine specific materials for specific purposes.

### **2.4.3 Polariscopes**

Polariscopes can be simply described as instruments or devices that allow observation of photoelastic fringes in stressed photoelastic materials or coats. These fringe patterns are used to analyse the spatial and temporal stress magnitudes in mechanically stressed photoelastic materials.

Polariscopes are generally classified into two main groups; a) Plane polariscope and b) Circular polariscope.

#### **2.4.3.1 Plane Polariscope**

The plane polariscope setup consists of the light source and two linear, or sometimes called plane polarisers. The birefringent sample is placed between the two linear polarisers allowing the light to illuminate the specimen. The first polariser is placed in front of the light source to produce the linear polarised light and the second (may be called analyser) is located in the front of a viewing screen, the schematic arrangement is shown in Figure 2.18.

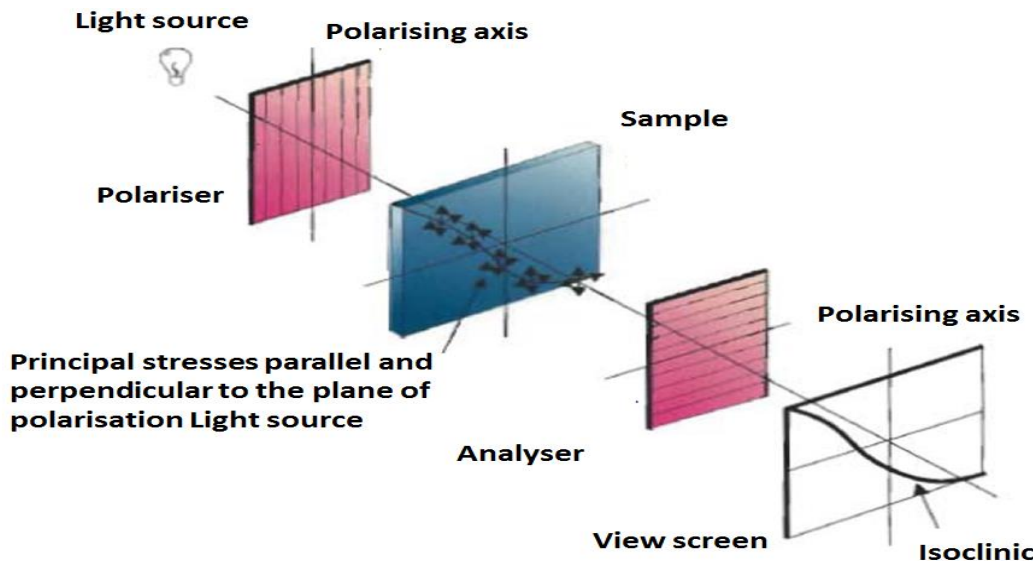


**Figure 2.18** Diagram illustrating the proper arrangement of plane polariscope (McKenzie and Hand, 1999)

The second polariser axis to the first analyser axis can be changed, according to the required case conditions. When a birefringent specimen is located in the setup, photoelastic fringes appear and they are called as isoclinic fringes. The key point of photoelastic theory in plane polariscope is the setup and arrangement of the components. If the polarising axis of the polariser and analyser are parallel to each, the photoelastic light-field is observed but if the two axes of polariser and analyser are perpendicular to each, only the photoelastic dark field is observed and obtained. Colours observed in the photoelastic stressed specimens represent magnitudes of principal stress difference and each colour fringe in the stressed specimen represents the retardation ( $\delta$ ) of the light between the major and minor axes.

#### 2.4.3.2 Circular Polariscope

The only main difference between the arrangement of the circular and plane polariscopes is involving two additional quarter wave plate in the optical setup (McKenzie and Hand, 1999). The first quarter wave plate is placed after the first polariser and before the stressed sample to convert the linear polarised light to a circular polarised light. The second quarter wave plate is kept before the analyser. When the polarised light passes through a quarter wave plate, the polarised light splits with  $1/4 \lambda$  retardation parallel to the direction of fast and slow axes of the quarter wave plate as shown in Figure 2.19.

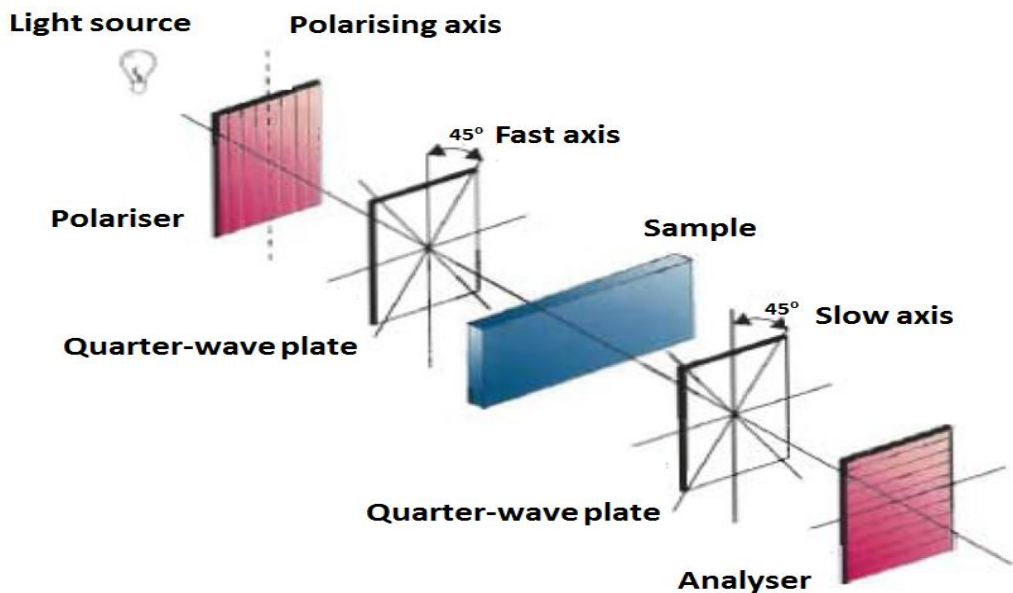


**Figure 2.19** Diagram illustrating the arrangement of circular polariscope (McKenzie and Hand, 1999)

Modern stress measurement methodologies such as PSAT employs circularly polarised light in its applications.

#### 2.4.4 Isoclinic and Isochromatic Fringes

There are two common terms used in optical stress analysis known as isoclinic and isochromatic fringes as shown in Figure 2.20. Under white light, the isoclinics are the black fringes which represent the centre of points having the same principal stress direction. The isochromatic fringes represent the same colour bands; represent the zone of equal principal stress difference. The only way to see and observe the full colour bands of the photoelastic fringes is by eliminating the isoclinic fringes. Isoclinic fringes are appeared when the direction of principal stress coincides with the polarisation axis of the polariser while isochromatic fringes are lines of constant principal stress difference (McKenzie and Hand, 1999). Plane polariscope enables the appearance of two different types of photoelastic fringes; isoclinic and isochromatic fringes. Image capturing and digital processing and post processing techniques allow the separation of the isoclinic and isochromatic fringe patterns.

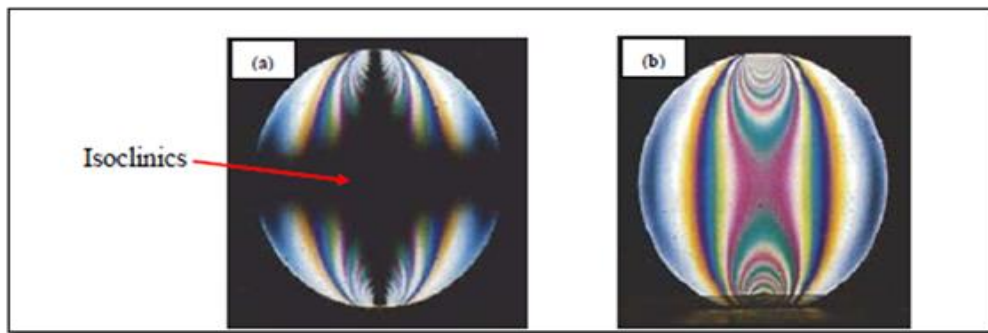


**Figure 2.20** Photoelastic fringes; a) isoclinic fringes, b) isochromatic fringes for a disk under axial compression (McKenzie and Hand, 1999)

Advanced circular polariscopes (such as PSAT) have the advantage over the plane polariscopes as they are able to eliminate the isoclinic fringes and show only the isochromatic fringes. The quarter wave plate in front of the rotatable linear polariser in the circular polariscope removes the isoclinic fringes, showing full multi-coloured bands of isochromatic fringes (McKenzie and Hand, 1999).

#### 2.4.5 Birefringence and Optical Anisotropy

During the 17th century, sailors who visited Iceland observed natural birefringent properties for the first time; they returned back to Europe with calcite crystals that showed double images of objects when light passes through the crystal (Madou, 2011). This phenomenon was explained later by (Christiaan Huygens 1629 - 1695, Dutch physicist) who called that a double refraction property due to ordinary and extraordinary light waves (Madou, 2011).

Mathematically birefringence is easily defined as the difference between the refractive indices  $\Delta n = n_1 - n_2$ . Many transparent solids are optically isotropic which means that the index of refraction  $n_1$  and  $n_2$  is equal throughout the matrix. On the other hand, some crystals are not and such crystals are known as optically anisotropic crystals, resulting in birefringence (Goldstein, 2011). The fast light component having lower index travels faster than the slower component having higher index, as a result, the two light components take different times to reach the internal structure of the sample.

The internal structure of any crystal showing birefringence property might be hexagonal, tetragonal, and trigonal (Heybey and Lee, 1967, Sajilata et al., 2006). Such crystals having different indices of refraction indexes within their internal

structures resulting in splitting of the entering light into two waves which will travel at different speeds. Birefringence might be an intrinsic property as in the natural birefringent crystal or tissues mentioned before or as an extrinsic property when any external load is applied to specimens. The extrinsic birefringence appears temporarily as the external load is acting on the sample enabling stress and strains spatial and temporal quantification through the produced fringes interference patterns (McKenzie and Hand, 1999, Majmudar et al., 2007, Antony and Chapman, 2010).

When the polarised light passes through a birefringent material it decomposes into two waves perpendicular to each other and correspond to the directions of major principal stress  $\sigma_1$  and minor principal stress  $\sigma_3$ . The two components of the light wave travel at different velocities, thereby developing further retardation ( $\delta$ ). The retardation of the light wave can be calculated by equation 2.17;

$$\delta = N\lambda \quad \text{Eq. 2.17}$$

Where:  $\delta$  = Retardation of light wave

$N$  = Fringe order

$\lambda$  = Light wavelength

The difference between major and minor principal stress components  $\sigma_1$  and  $\sigma_3$  can be related to the fringe orders displayed by birefringence specimen and hence to the maximum shear stress ( $\tau_{max}$ ) of the loaded material (Antony and Chapman, 2010, Antony et al., 2014b). According to the stress optic law, the difference in the magnitudes of major and minor stress components can be calculated using equation 2.18 and the maximum shear stress ( $\tau_{max}$ ) calculated using equation 2.19

$$\sigma_1 - \sigma_3 = \frac{nf}{t} \quad \text{Eq. 2.18}$$

$$\tau_{max} = \frac{\sigma_1 - \sigma_3}{2} \quad \text{Eq. 2.19}$$

Where:  $\sigma_1$  = Major principal stress

$\sigma_3$  = Minor principal stress

$n$  = Measured fringe order

$f$  = Material fringe coefficient

$t$  = Thickness of the model

Anisotropy is a term referring to inhomogeneous spatial distribution of the particle contacts which crucially alters the bulk mechanical properties of granular materials and forces transmission through granular assemblies (Cambou et al., 2004, Antony, 2007). When any object is said to be anisotropic, it means that its properties can vary depending on the direction of the measurement. The opposite of the anisotropic is isotropic, where the properties will be similar in all directions. Induced anisotropy due to application of external load has two distinct effects; the first one is directly related to the geometrical effect while the second is related to the mechanical behaviour (Majmudar and Behringer, 2005). Geometrical effect introduces anisotropy in the particulate contact network, while the mechanical effect creates an anisotropic force chain network and modifies the stress distribution within the system (Majmudar and Behringer, 2005, Antony, 2007). Hard granular media usually creates an anisotropic fabric network of strong force networks contacts carrying greater than the average normal contact force, which are significantly reduced in soft systems during granular material shearing process (Antony, 2007).

#### **2.4.6 Advanced Applications of Photoelasticity**

Latest advances in modern photoelasticity applications involve the use of digital PSAT that give good opportunity to evaluate real-time stress monitoring of devices or fabricated structures (Calvert et al., 2002, Antony and Chapman, 2010, Albaraki et al., 2013, Antony et al., 2014b). This advanced technology saved a lot of time consumed previously in manual operations. In such cases, a fully automated polariscope system linked to a high speed CCD camera is able to monitor changing stress patterns as it actually happens, see Figure 2.21a. Photonic stress application is employed in engineering fields for understanding stresses in continuum solid materials under loading conditions (Calvert et. al., 2002). Coating materials applied on opaque materials are usually transparent polymers which form a thin layer that is bonded integrally to flat or curved surfaces. Upon loading, the surface stresses are

transmitted to the coat and produced as a multicolour fringed in coating materials (Calvert et al., 2002).

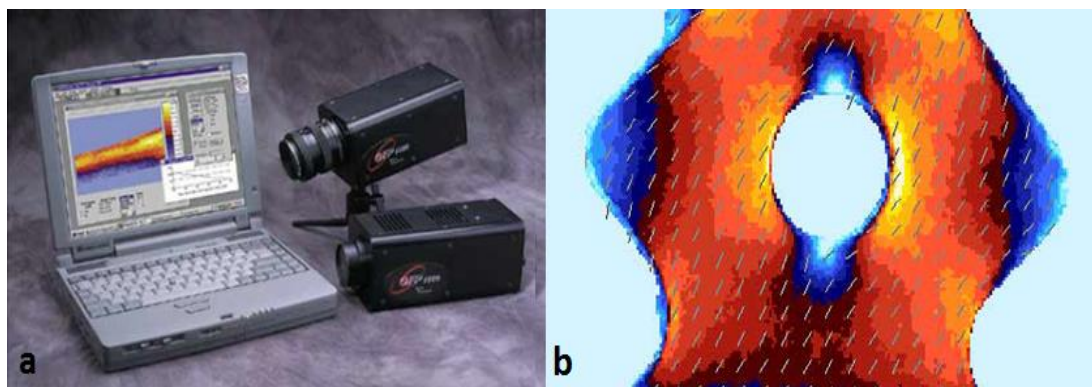


**Figure 2.21** Advanced Photo stress analysis system; a) Computer based photo stress system, b) Maximum shear stress profiles using coating materials (Calvert et al., 2002)

The advanced PSAT system consists of a projector unit illuminating circularly polarised light and a digital camera with a constantly rotating analyser. Within each analyser revolution, number of images are captured by the camera allowing proper measurement of the reflected light (Calvert et al., 2002). This technique is very sensitive and able to analyse the stress fringes (up to a maximum of  $\pm 0.002$  fringe). In cases of using a birefringent coat, it allows researchers to use a coat of a thickness between 0.1-0.4 mm and accurately measure fractions of a fringe order as shown in Figure 2.21b (Calvert et al., 2002).

#### 2.4.7 Application of Photoelasticity in Pharmaceutical Industry

The first published work on photoelastic technique application in the pharmaceutical industry was reported during the 1960s to assess pharmaceutical powder compression and die wall stress (Ridgway, 1966, Fedorchenko et al., 1968, Ridgway and Rosser, 1971). The principle of all studies based on compressing pharmaceutical powders under very high loading conditions reaching 12 (ton/in<sup>2</sup>), inside perspex die chamber. The radial stress in the compression die is measured and evaluated indirectly by using high speed cinematic photography having polarised light. The stress performed on the perspex sheet was analysed according to the fringes colour scale.

Latterly, a group of scientists in Duke University published novel studies using the photoelastic technique as powerful non-destructive method to evaluate granular material jamming inside hoppers, particles force networks and granular material shearing using transparent photo elastic disks in centimetre sizes (Majmudar and Behringer, 2005, Majmudar et al., 2007, Zhang et al., 2008, Behringer et al., 2014).

PSAT has been adapted and applied as a powerful visual imaging technique to measure and evaluate the influence of chamber boundaries and particle size of granular materials on shear stress distribution using photo elastic inclusion inside granular material (Antony and Chapman, 2010, Antony et al., 2014b). Recently novel PSAT setup has been effectively applied to map the distribution of maximum shear stress and major principal stress profiles within fabricated birefringent pharmaceutical excipient granules inside 2D hopper geometries (Antony et al., 2012, Albaraki et al., 2013).

## 2.5 Digital Particle Image Velocimetry

Velocity distribution in dynamic granular flows from the storage bins such as hoppers and silos has been of great interest during the last few decades in different industrial applications. Various efficient laboratory scale techniques have been applied to track and visualise the deformation and shearing zones of the granular beds. These include digital speckle radiography (Grantham and Forsberg, 2004) gamma-ray measurements (Tan and Fwa, 1991), electrical capacitance tomography (Grudzieñ et al., 2010), fast X-ray tomography (Baxter et al., 1990), stereophotogrammetry (Desrues and Viggiani, 2004), near infrared spectroscopy (Sarraguca et al., 2010) and digital particle image velocimetry (Ostendorf and Schwedes, 2005, Sielamowicza et al., 2006, Emery et al., 2009, Albaraki and Antony, 2014).

In the early 90s particle image velocimetry technique was known as (PIV) but recently emerged as digital particle image velocimetry (DPIV) using multiple ranges of digital cameras for measuring velocity fields in different applications (Holdich, 2002). This system may also be called digital tracking velocimetry (Adrian, 2005). Particle image velocimetry is one of the recent techniques adapted in the research field for multiple purposes and 2014 was considered the thirtieth anniversary of this

method (Adrian, 2005). DPIV was simply defined as a real, accurate and quantitative visual measurement of particle velocity vectors at specified area of interest (Adrian, 2005). Unlike the conventional particle tracking method, DPIV does not require individual tracking of the velocity profiles measurement as it is automated and able to provide sufficient temporal and spatial resolution in a defined area known as the interrogation area at multiple locations (Adrian, 1991, Adrian, 2005). A sufficient concentration of particles within the interrogation area and repetition of the process is able to obtain non biased results for the particle velocities from the digital records (Westerweel, 2000).

The DPIV technique is applicable for both three and two dimensional application for single and multiple particle flow tracking (Ovryn, 2000). The ability of DPIV technique to visualise and illustrate the velocity vectors and particle displacements in relatively large area, allows the researchers to use such techniques to track the granular flow behaviour in silo models. For example, Sielamowicza et al. (2006) applied DPIV to measure and evaluate the flow regions, velocity profiles, plug flow propagation, stagnant zones and shear zones of granular materials in 2D hopper geometry.

The early applications of this technique were successfully demonstrated in fluid dynamics (Santiago et al., 1998). The earliest applications for the granular matter flow was presented by Medina et al. (1998) and Lueptow et al. (2000), where the authors recommended such quantitative techniques to study granular flow behaviour using transparent wall apparatus (Medina et al., 1998, Lueptow et al., 2000). The early results obtained by Medina et al. (1998) and Lueptow et al. (2000) inspired many authors to apply this technology to similar trials for different purposes. The main objectives for those researchers were for accurate measurement of the temporal and spatial particle velocity and displacements (Waters and Drescher, 2000, Ostendorf and Schwedes, 2005, Slominski et al., 2007, Ulissi et al., 2009).

### **2.5.1 Application of DPIV and PIV: Granular Flows**

The first appearance of published research work using the PIV technique was reported during 1984 by Pickering and Halliwell (1984) and Adrian (1984) during the evaluation of the two phase particle flow (Adrian, 2005). Early application of

PIV based on recording multiple images of the experiment on a proper film, followed by computational analysis of the spatial correlation within a very limited area of interest to quantify the dynamic flow fields (Hesselink, 1988).

Willert and Gharib (1991) introduced digital particle image velocimetry (DPIV) as an alternative approach to resolve many problems associated with the conventional method such as image resolution and vector analysis. The new approach based mainly on recording digital video images uses a high resolution and high speed digital camera instead of conventional photographic images. The data analysis performed computationally which minimises any errors of photograph and eliminates any optical analysis complexity and data recovery. In contrast to gases and liquids, applying DPIV technique on granular materials does not require the addition of any tracers as the granular material itself acts as a tracer (Slominski et al., 2007).

The recent applications of DPIV for granular material flow behaviour analysis are generally implemented and adapted to evaluate the flow and discharge patterns of agricultural corps from silos having high storage capacity (Sielamowicz et al., 2005, Sielamowicz et al., 2011).

Sielamowicz et al. (2005) successfully applied the DPIV to evaluate and explore the flow nature of three densely packed granular materials: Amaranth, Flax-seed and Buckwheat in a flat bottom silo model. The results confirmed that the plug flow propagates in a vertical direction and starts directly above the outlet, broadening with the height. The experimental results of plug flow and the stagnant zone boundary measurement of the solid bulk using PIV as a function of time are in good agreement with that obtained by Nedderman (1995) using the kinematic method to predict the positions of the stagnant zones at boundaries. However, some differences were observed close to the silo orifice. The lines of the stagnant boundaries in this study were closer to each other in their vertical parts than those observed by Nedderman (1995) which gives an indication that the flowing region width does not increase greatly. The velocity profiles at different heights showed that the highest velocity was for those particles near the outlet, followed by the next region of particles at the next level of height from the opening in a consistent

manner. At the stagnant zones close to the boundaries, the magnitude of the velocity is very close to zero.

Similar research work has been conducted by Sielamowicza et al. (2006) for quantitative analysis of central plug flow zone evolution and propagation inside a 60° internal angle hopper using amaranth seeds as granular material. The authors evaluated quantitatively the generation of a flow channel at the central axis of the hopper which propagated upward during the discharge process. Also they have discussed and correlated that to the granular shear zones and discontinuities of vector fields. The results showed that granular materials at the outlet opening are in continuous motion and the plug flow zone is propagated upward and spread to the hopper walls. They also reported that the early granular materials discharging is not restricted to the materials in the plug flow region but the lateral region showed motion to some extent. The direction of the velocity vectors at the central flow region were in vertical direction while those in the boundaries showed some inclination to the walls.

Ulissi et al. (2009) evaluated the flow behaviour of multiple size glass beads, quartz and sand granules inside a 30° internal angle hopper geometry using PIV. The authors used this method as it is able to show and track velocity values for each spatial position within the hopper geometries. They have inserted a congregate of dyed particles known as “markers” and traced them using a CCD camera. The results indicated that the whole hopper showed vertical direction of the velocity vectors and the maximum velocity across the granular bed was obtained at the central axis of the hopper.

Bohrnsen et al. (2004) evaluated the stress states and the dynamic flow trends from the silo having a 30° internal angle hopper experimentally and computationally using granulated polyethyleneterephthalate (PET) placed under a steady state flow condition. For normal and shear wall stress measurements, special load cells were fixed to both silo walls. Finite element method (FEM) and PIV were used to evaluate the experimental dynamic flow. The authors reported the changes in the stress state inside the silo and the hopper during the dynamic discharge phase. In static condition, the direction of the major principal stress direction was in the vertical direction and known as active stress state. At the early stage of discharge,

the major principal stress altered to the horizontal direction immediately above the hopper outlet and this phase is called the transition phase. The authors attributed the wall stress increases during the flow process to the instant dilation of the initial granular void directly above the hopper outlet without any changes at the upper layers. This leads to dramatic changes in the bulk density of the granular material that compensated to the equilibrium state by the increasing the normal and shear stress on the walls. The maximum change in the magnitude of stress has been reported at the junction of the hopper to the vertical walls of the silo and called the transition position. In general, the results showed good agreement between experimental and simulation findings.

Ostendorf and Schwedes (2005) have expanded the application of PIV to evaluate the dynamic effect and the bulk solid flow profiles inside multiple silo geometries. The authors used Polyethylenetherephthalate (PET) cylindrical shape pellets as a model of free flowing granules. The silo walls were fabricated using perspex sheets and similar loading cell positions to the previous study have been used, and their numbers and locations depend on the internal hopper angle value. The higher hopper's internal angle, the lower the load cell numbers. These embedded special loading cells were allowing the measurement of both the wall normal and shear stress fluctuation during the dynamic flow (Bohrnsen et al., 2004). The results of the velocity profiles inside the 30° internal hopper angle, clearly indicate that the nature of the flow inside the hopper is identical to mass flow behaviour, as all particulates are in a motion inside the hopper. The particle velocity magnitude was the highest at the hopper outlet and the central axis of the hopper and the magnitude decreased towards the hopper top and toward the boundaries. The experimental results were compared with those obtained by simulation using FEM for correlation. The simulation results showed that the decrease in the velocity vector towards the hopper top is higher than that obtained experimentally. The authors attributed this to not considering internal friction of particles during the numerical simulation. The authors also reported two different kinds of fluctuation occurring during the discharging process; slower and momentary fluctuation. The slower fluctuations are caused by shear bands which develop at the transition from shaft to hopper and the momentary fluctuations are due to the fact that the macroscopic "steady state" flow in the hopper is not "steady state" at the microscopic scale. These fluctuations

cannot be found in numerical FEM simulation results because the macroscopic approach of the FEM is unable to consider the microscopic effect of particles in details.

### **2.5.2 Application of DPIV and PIV: Granular Materials Subjected to Compression**

Application of DPIV technique to visualise and investigate the deformation of granular materials during compaction process is scarcely published and the available ones have been applied for specific and limited purpose (Beckett and Augarde, 2011, Krok et al., 2014, Pietrzak and Leśniewska, 2012, Xu et al., 2011, Cheng et al., 2001, Senatore et al., 2012). All these studies did not represent the actual compression of the granular materials within confined geometries similar to that used in the pharmaceutical industry for tableting or ceramic manufacturing in engineering industry. The work conducted by Beckett and Augarde (2011), reported the impact of the compaction process as non-confined method on two soil layers to investigate and identify the influence of compaction on macro and microstructure soil properties. The fabricated rig used in this study is able to impact the outer soil layer in non-confined compression trend, as the punch dimensions is much less than the die chamber dimensions. The study shows that the artificial compaction of the soil is applicable for qualitative analysis of soil deformation and applicable to observe the geological changes using less-expensive and non-destructive method.

Recently Krok et al. (2014) investigated the influence of stress produced by the rollers of a roll compactor on the vertical velocity of a powder materials. The nature of the compaction stress produced by such an instrument is similar to that applied during the dry granulation process in pharmaceutical industries but not the tableting process (Sonam et al., 2013). The compaction mechanism is different to what occurs in granular material compression within tableting dies. The study showed that the influence of the particles internal friction on particle velocity is more than that of the particle wall friction. This leads to less momentum transfer from the wall side to the centre region of consolidation. In addition to that, the feeding speed has a strong influence on the magnitudes of particle velocity.

Granular soil material subjected to slow indentation and deformation have been investigated using the high speed imaging technique and a hybrid particle image velocimetry (Murthy et al., 2012). The results indicate that there is a rigid triangular dead zone generated directly below the punch and the boundary granules move obviously in a systemic manner with respect to the indenter midline. The granular bed deformation is diffused and highly stressed zone is localised at the punch corner due to particle rotational motion at this site.

Pietrzak and Leśniewska (2012), applied the geo PIV software to investigate the evolution of granular glass bead failure in a 2D setup. The results reported that the granular material under compression can show some cyclic changes. The authors did not provide any proper explanation for the nature of the cyclic changes but they linked that to the micromechanical properties of the granular materials. They have recommended continuous deep investigation to clarify the nature of the cyclic changes that may help, and provide proper explanation for the earth thrust on retaining walls.

Xu et al. (2011) have adapted PIV to investigate the limestone failure, deformation and strain propagation under uniaxial compression. The results indicated that the resultant normal strains are totally dependent on the positions of the crack and its mechanism of propagation. Cheng et al. (2001) applied PIV to observe the rotation of soil grains under external load. The results enrich the soil mechanics as key features of soil microscopic fracturing and particles rotation have been reported. Soil grain plastic deformation has been correlated to both the stress and shear strain. Senatore et al. (2012) investigated the soil granular deformation under low weight wheel motion as clear understanding of such mechanism helps to enrich the properties of soil fundamentals. The results supported that the PIV was able to show the deformation, trajectories and stress fields of granular soil under the wheel motion.

## 2.6 Conclusions

In this chapter, extensive literature reviews have been conducted to show the complex behaviours of the granular materials and the main issues related to their micromechanics during the flow and compression processes. Static and dynamic

granular materials stress status in silos and hoppers and the methods applied for stress assessment have been presented in detail.

The review shows that there is no available experimental method to visualise the initial packing shear stress profile distribution and direction within actual granular material assembly during the static conditions. Clearly such details are lacking for micron size particles. Applying advanced Photostress tomographic technique in such a research project is valuable to shed light on the possible influences of the static stress distribution on the nature of the subsequent dynamic flow of granular material. The dynamic flow assessment can be evaluated quantitatively using DPIV as a visualising technique, able to measure the spatial and temporal velocity gradient in particulates. The flow trajectories, plug flow and stagnant zone can be evaluated qualitatively using CCT.

In addition, application of such a method to probe the stress profile propagation within granular assembly during confined compression under relatively low compression forces is scarce and requires great attention. This will help to understand the influence of particle scale properties and the die wall characteristics in the stress propagation process during the rearrangement stage of compression cycle.

Development of this type of experimental works needs to fabricate actual pharmaceutical micro-granules having a good level of birefringence and easily coloured to be suitable for PSAT, CCT and DPIV applications. These challenges have been addressed in the following chapters.

## **Chapter 3 : Fabrication and Characterisation of Pharmaceutical Granules for PSAT and DPIV Applications**

The aim of this part of the work is to experimentally develop birefringent granules in micron size for the first time. Subsequently, their particle scale properties are characterised comprehensively. Also granules are colour coded for conducting qualitative experimental flow assessment at later stage. The chapter discusses in detail the features of native starch powder which make it a suitable raw material for making birefringent particles and colour coded granule fabrication for PSAT, CCT and DPIV applications respectively. General back ground about the granulation techniques and wet granulation method in particular has been presented. The main reasons for applying wet granulation method to fabricate granules have been underlined. The chapter also mentions the materials and methodologies applied to the fabrication processes for both stress responsive granules for PSAT application and colour coded fabricated granules for CCT and DPIV studies. The last two sections of this chapter describe the most relevant characteristics and physiomechanical properties of the fabricated granules as well as the standard methods applied for characterising the granules.

### **3.1 Introduction**

The key step for using PSAT to study the micromechanical properties of granules is their birefringent property. Highly ordered molecular structure crystals such as oxalic acid and sucrose are naturally birefringent (Singh et al., 2012). Many transparent polymers and very few biological materials and tissues are able to display birefringence property when they are exposed to polarised light (McMahon, 2004). For example, human corneal eye tissue (Hitzenberger et al., 2006, Antony, 2015), human skeletal muscle fibre and starch are common example of natural birefringent materials (McMahon, 2004).

#### **3.1.1 Starch**

Starch and cellulose are considered as the most abundant carbohydrate produced from plant as raw materials for many industrial applications (Singh, 2011). They are commonly involved in food, pharmaceutical, cosmetics and paper industries. Starch

is a natural polymer, build-up basically of multiple glucose units. Globally, the production of starch almost exceeds a hundred megatons obtained mainly from maize, wheat and potatoes. Starch is a natural product of photosynthesis and can be found in all organs of higher level plants (Shannon et al., 2009).

### 3.1.1.1 Chemical Structure of Starch

The chemical structure of starch as a carbohydrate polymer is very complex, it is mainly composed of a mixture of two building units or isomers. These isomers are called amylose which is mainly a linear polysaccharide moiety and amylopectin as a highly branched polysaccharide moiety (Shannon et al., 2009). Amylose molecules in a starch structure may consist of a collection of 200 to 20, 000 glucose units forming a helix like structure. In contrast, an amylopectin structure is more complicated than amylose due to its multiple branching nature and may contain up to two million units of glucose (Shannon et al., 2009)..

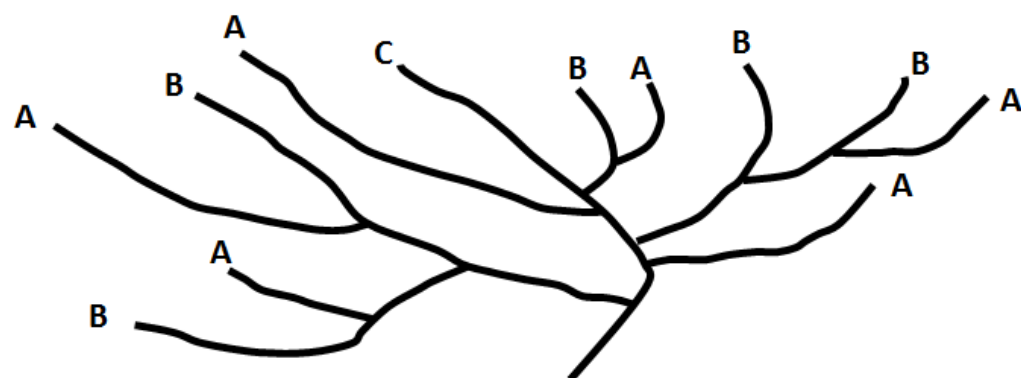


**Figure 3.1** Meyer Bernfeld tree structure for amylopectin

Amylopectin molecules contain different chains denoted as A, B, and C chains and are also known as Meyer Bernfeld tree, see Figure 3.1. Chain A branches on B or C chains and contains no branches, while B chain branches on B or C chains and contains branches with A or B. Finally, C chain contains A and B branches together with only the reducing end of the molecule (Shannon et al., 2009).

### **3.1.1.2 Starch Granule Morphology and Porosity**

Starch granule morphology has been investigated well for multiple food applications and it is totally dependent on the plant origin and generally varied from spherical, ovoid and angular shapes (Smith et al., 1995, Chen et al., 2006, Shannon et al., 2009). Maize starch granules morphology and microstructure depend mainly on the amylose to amylopectin ratio. Chen et al. (2006) studied the morphology of different maize starches, including waxy starch (contain zero amylose), Native maize (contains 26% amylose), G 50 (contains 50% amylose) and G 80 (contains 80% amylose). The microscopical results showed a mixture of rounded granules from the floury endosperm and angular granules from the horny endosperm. They also reported that, the granules shape of the amylopectin rich starches were more regular in shape than those of the amylose rich starches.

Native starch is a well-known porous raw material in industry (Fortuna et al., 2000, Huber and BeMiller, 2000, Sujka and Jamroz, 2010). Starch surface pores are simply defined as the ratio volumes of the pores to the solid state volume (Sujka and Jamroz, 2007). In the food industry, this natural porous feature can be modified or altered using multiple approaches such enzymatic hydrolysis and drying process (Sujka and Jamroz, 2007, Sujka and Jamroz, 2010). Starch porosity can be classified into three main groups; (i) macropores, if the pore diameter is more than 50 nm, (ii) mesopores if the pore diameter is in range of 2 to 50 nm and (iii) micropores, if the diameter is less than 2 nm (Sujka and Jamroz, 2007). In addition to this porosity, starch granule agglomeration can create more inter-particle void as they have relatively high surface energy (Karathanos and Saravacos, 1993).

Corn starch in particular, characterised by a channel like structure and cavities within their internal structure (Huber and BeMiller, 2000, Kim and Huber, 2008). The channels start from the outer surface to the interior part of the granule in a serpentine way (Fannon et al., 1993). The depth of these channels varies and depends on the location of the cavity (Huber and BeMiller, 2000). Mostly the channels reach the central lamella of the granule and their size can be enlarged by the drying process (Huber and BeMiller, 1997).

### 3.1.1.3 Birefringence of Starch Granules

Native starch is an example of a few natural and biological materials that exhibit birefringence and have the ability to polarise the light (McMahon, 2004). The internal structure of these biological materials show a highly ordered internal arrangement and alignment approaching a crystalline or semi-crystalline orientation (Zobel, 1988, Frost et al., 2009). Native starch exists as a crystalline structure with low and imperfect crystalline granules consisting mainly of a high content of highly branched amylopectin and essentially linear amylose (Pérez et al., 2009). A crystalline core in starch granules is formed due to hexagonal array packing of amylopectin in helical coil like structures (Zobel, 1988, Sajilata et al., 2006). Amorphous regions of starch granules consist of linear amylose and low branched amylopectin which are responsible for starch granule anisotropy (Imberty et al., 1991, Jane, 2006).

Birefringence characteristics of starch were reported and attributed to the crystalline structure of the granules (Baker and Whelan, 1950). In polarised light, starch granules show strong birefringence, resulting in the “maltese cross” pattern (Pérez et al., 2009), as shown in Figure 3.2.

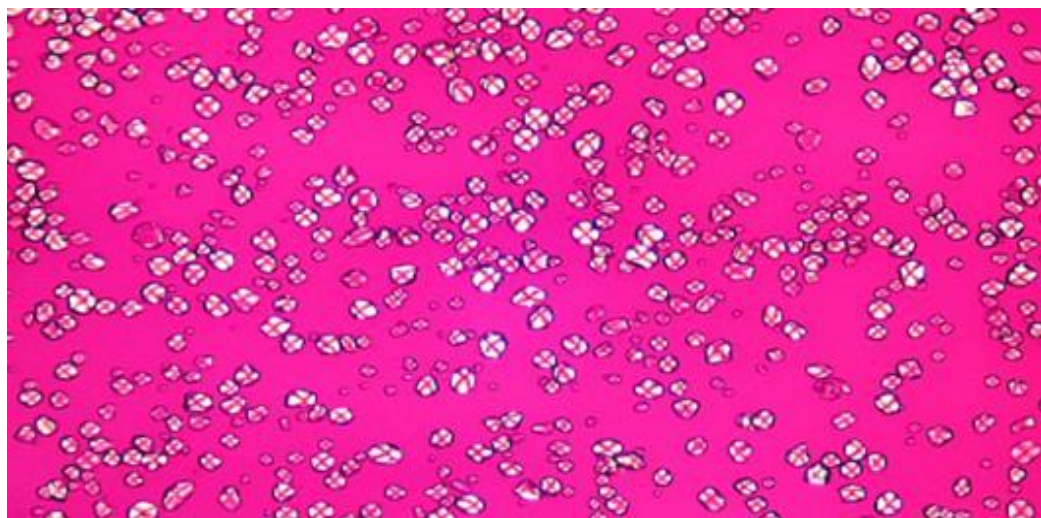


**Figure 3.2** Birefringence of stained starch granules under polarised light microscope as Maltese Cross (Starches, 2015)

Iodine staining of starch powders has been used to differentiate multiple genotypes, it is particularly effective to distinguish native and waxy starch granules (Baker and Whelan, 1950, Evans et al., 2003). It has been reported that native starch granules

are able to show strong birefringence in the presence or absence of iodine (Evans et al., 2003).

The early results of the research project obtained in order to evaluate the birefringence of the fabricated granules, showed obvious isochromatic fringes in cases of the stained granules, further details are available in section 3.2.2.1. The influence of iodine on the granule birefringence may need further investigation on the crystal level using advanced technologies. It has been reported that iodine staining is able to modify some fibre internal structure and its optical properties including refractive indices and birefringence (Shabana, 2006).

High temperature alters the birefringence of starch granules. In the food industry, starch gelatinization temperature is predicted when a starch sample loses 98% of its birefringence characteristic (Goering et al., 1974, Coral et al., 2009). Starch granules' loss of birefringence is considered as one of the most common and accurate methods to determine the gelatinisation temperature range of all starch genotypes (Goering et al., 1974, Lund and Lorenz, 1984). The loss of birefringence occurs over a broader temperature interval (Lund and Lorenz, 1984). Goering et al. (1974) studied the birefringence end point temperature (BEPT) of several starch types and the results indicated that the loss of birefringence for all granules sizes occurred simultaneously and not in sequence according to their sizes.

### **3.1.1.4 Starch Crystallisation and Re-crystallisation.**

Starch granules are basically composed of alternating amorphous and crystalline lamellae at the peripheral and the centre of the granule respectively (Whistler and BeMiller, 1997). X-ray differential scanning technique (XRDS) is commonly used to show starch crystallinity and to detect any changes in native starch crystallinity as well as other starch genotypes in processes (Zobel, 1988, Shamai et al., 2003, Frost et al., 2009). Generally two polymorphs are detected in native starch, (A) type in grain starch and (B) type in tuber derived starch. The polymorphism, thermal stability and recrystallisation of maize starch have been studied in detail by (Shamai et al., 2003). They have used XRDS to compare the starch crystallinity changes of heated and non-heated maize starch at a high temperature (95°C for 24 h, HT) and a relatively low temperature (40°C for 24 h, LT). They reported that, the diffraction patterns of the native maize starch is a typical A-type polymorph, while low

temperature incubated starch resulted in a formation of B-type pattern and indicated by pronounced peaks. High temperature incubated maize starch led to the formation of a mixture of V- and A-type structure denoted as C-type, as illustrated from the peak diagram as shown in Figure 3.3.

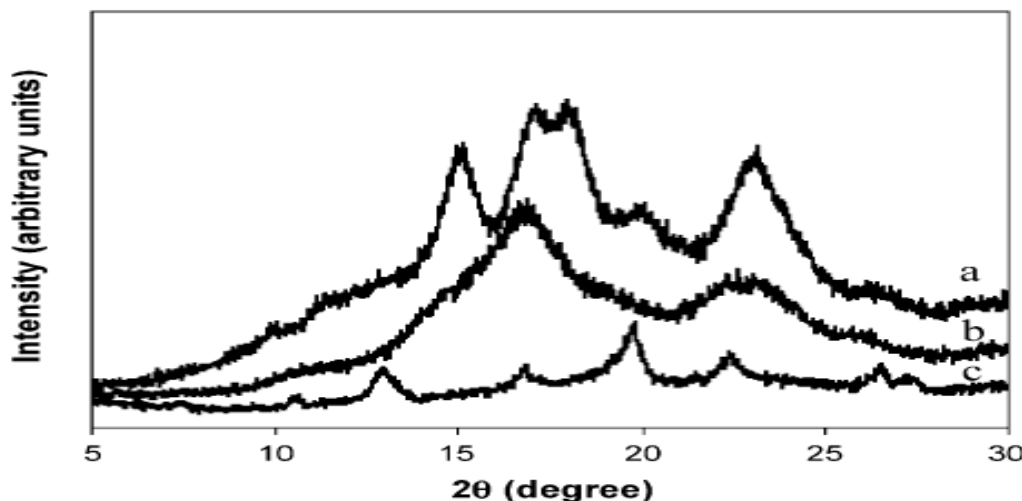


**Figure 3.3** X-Ray diffraction patterns of (a) native maize starch and (b) low temp incubated maize starch (LT) and (c) high incubated maize starch (HT) (Shamai et al., 2003)

Arrangement of amylopectin molecules within the granules is responsible for the crystalline structure of starch granules (Huang et al., 2007) and consequently the birefringence of starch granules (Baker and Whelan, 1950), see Figure 3.4

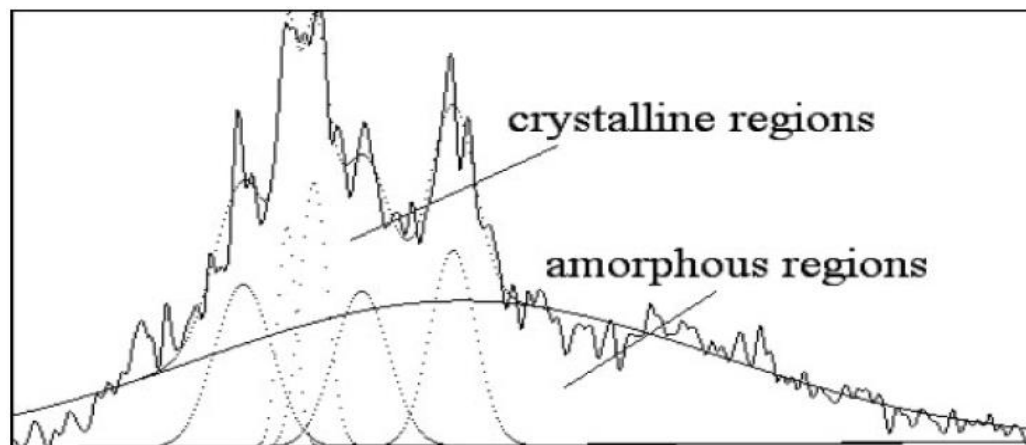


**Figure 3.4** The crystalline and amorphous regions in native starch (Huang et.al., 2007)

Many studies suggested that amylose is mainly located in the amorphous areas of the granule while amylopectin is located at the crystalline region (Jenkins and

Donald, 1995, Huang et al., 2007, Frost et al., 2009). Recent studies conducted by Jane (2006) and Huang et al. (2007) reported that the location of amylose molecule as well as low branched amylopectin are mainly located in peripheries while highly branched amylopectin is more concentrated at the centre of the granules.

### **3.1.2 Granulation Technique**

Granulation is a process of size enlargement, particles agglomerate together and suitably form larger and multi-particle entities called granules (Parikh, 2009). In pharmaceutical science, it has been reported that the word granulation comes from Latin term known as “granulatum,” which means grained (Parikh, 2009).

In general, granulation technique is classified to dry and wet methods, based on the process involved in granules preparation. Recently, and due to advanced technologies involved and adapted for granulation process, it is classified as conventional and novel methods (Saikh, 2013). The conventional methods involve dry and wet granulation techniques, using roll granulator or high and low shear mixers (Dhumal et al., 2010). In the other hand, the novel methods involve the recent techniques, adapted and modified to granulate powder mixtures for multiple industrial purposes. For example, fluidised bed and freeze granulation methods (Srivastava and Mishra, 2010) and seeded granulation (Rahmanian et al., 2011, Hassanpour et al., 2013, Rahmanian and Ghadiri, 2013) .

The inter-particle bonds are usually formed by the applied compression forces or by using a suitable binding agent or granulating agent that make this agglomerate physically stable (Tousey, 2002, Solanki et al., 2010, Agrawal and Naveen, 2011, Sakr et al., 2012). The major linkage forces between particles can be attributed to the attractive forces between solid particles or van der Waals forces, capillary forces mechanical interlocking, solid bridges after solvent evaporation, and adhesion/cohesion forces in the immobile liquid films between discrete powder particles (Litster et al., 2004, Agrawal and Naveen, 2011). Variable factors alter the granulation process and the effectiveness of granulation depends on many important factors such as particle size of the drug and excipients, type of binder, volume of binder, massing time, amount of applied shear, and drying rate and industrial scaling up (Hassanpour et al., 2009, Leuenberger et al., 2009, Solanki et al., 2010).

Among all existing granulation techniques and size enlargement processes, wet granulation and thermal (melt) granulation are particularly interesting as they obtain regular dense shaped and free-flowing granules and a high degree of compaction and kinetically modified release granules for drug delivery (Al-Suwayeh et al., 2009, Agrawal and Naveen, 2011, Dhumal et al., 2010). In addition to this, such granulation techniques allow the manufacturer to modify many crucial characteristics of active ingredients such as drug release and solubility (Al-Suwayeh et al., 2009, Dhumal et al., 2010).

### **3.1.2.1 Wet Granulation Technique**

The history of wet granulation technique has been well-known since the 1950s, when the novel works of Newitt and Conway-Jones (1958) and Capes and Danckwerts (1965) were published (Sakr et al., 2012). Since that time, wet granulation has been a subject of fundamental and applied research and considered as one the most widely used processes of granulation in the pharmaceutical industry (Kristensen and Schaefer, 1987, Agrawal and Naveen, 2011, Shi et al., 2011, Osei-Yeboah et al., 2014). Variable factors control the granulation process and make it a simple or very complex process. Such factors include, powder's physical and mechanical characteristics, formulation process, aim of granules or tablets, scaling up the manufacturing and design process, and the available instruments for granulation (Kristensen and Schaefer, 1987, Al-Suwayeh et al., 2009, Hassanpour et al., 2009, Leuenberger et al., 2009, Agrawal and Naveen, 2011, Sakr et al., 2012).

Wet granulation process involves the addition of a liquid solution to agitated powder assembly with continuous mixing to form a solid mass. The added liquid solution can be either aqueous based or a solvent based solution with or without binder (Agrawal and Naveen, 2011). The manufacturers prefer to use aqueous solutions more than solvents, due to having to deal with high safety margins. (Tousey, 2002, Litster et al., 2004, Agrawal and Naveen, 2011). Although some granulation processes may only require the addition of aqueous solvents to create granules with sufficient physical strength, some active ingredient or excipient may not be compatible with water, leading to a change in the solvent or using another granulation technique (Tousey, 2002, Agrawal and Naveen, 2011). Agitation and continuous mixing of water with active pharmaceutical ingredients and other

excipients, form multiple strong bonds between powder particles that held them together (Iveson et al., 2001, Tousey, 2002, Agrawal and Naveen, 2011).

In general, if granules are created only by using water as aqueous solvent or steam drops, the resultant granules will not be strong enough to tolerate further mechanical agitation and fall apart (Tousey, 2002, Litster et al., 2004, Agrawal and Naveen, 2011). In such conditions, another aid ingredient known as a binder (pharmaceutical glue or granulating agent) may be added to the powder mixture as a dry powder or as a dissolved binder in the solution. The most common pharmaceutical binders and adhesive ingredients used in pharmaceutical industries are starch powder (Kottke et al., 1992, Alanazi et al., 2008 ), polyvinyl pyrrolidone (PVP) (Tousey, 2002), Tragacanth (Tekade Bharat et al.), sodium alginate (Singh, 2011), polyethylene glycols (Al-Suwayeh et al., 2009).

According to Iveson et al. (2001), there are three fundamental stages govern the modern wet granulation process as summarised in Figure 3.5. These steps determine the wet agglomeration behaviour and include;

- Wetting and nucleation stage
- Consolidation and coalescence stage
- Attrition and breakage stage.

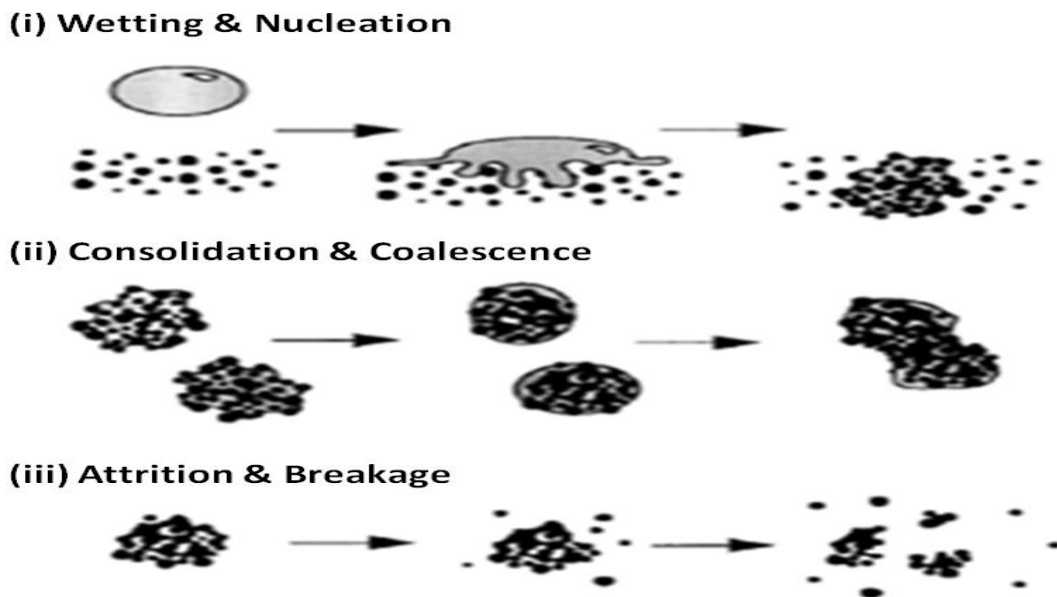


**Figure 3.5** Modern approach in wet granulation (Iveson et al., 2001)

Moreover, Hapgood et al. (2002) classified the complex wet granulation process to three main phases (i) Granule nucleation and binder distribution (ii) Granule consolidation and growth (iii) Granule attrition and breakage. He considered the wetting phase as the most critical phase for the nucleation step and is governed by the kinetics of the binder droplet penetration to the powder mixture and the fluctuation of drops onto the powder surface during the manufacturing process (Hapgood et al., 2002).

The main motivations to use the wet granulation technique for stress responsive granules fabrication in this research project are summarised as follows; (i) Relatively short processing time compared to other techniques and easy to control on lab scale (ii) High efficiency in case of cohesive powders (iii) Using of starch powder as raw material and granulating agent (iv) Applying of wet screening granulation method is possible (cold conditions).

## **3.2 Fabrication of Stress Responsive Granules for PSAT Applications**

### **3.2.1 Materials and Methodology**

#### **3.2.1.1 Materials**

Corn starch was obtained from (Sigma Aldrich, UK) and potassium iodide solution (2.5% w/v) was obtained from the local pharmacy. Both ingredients were used as raw materials to fabricate self-responsive birefringent granules. Starch is commonly used in pharmaceutical industries as a binder, disintegrant, lubricant and bulking agent in solid pharmaceutical dosage form manufacturing. Potassium iodide solution was used to improve the starch granules birefringence under polarised light. Native starch raw powder showed very poor flow properties due to its very fine nature, the powder particles are agglomerated and the angle of repose was 48°, see Figure 3.6.

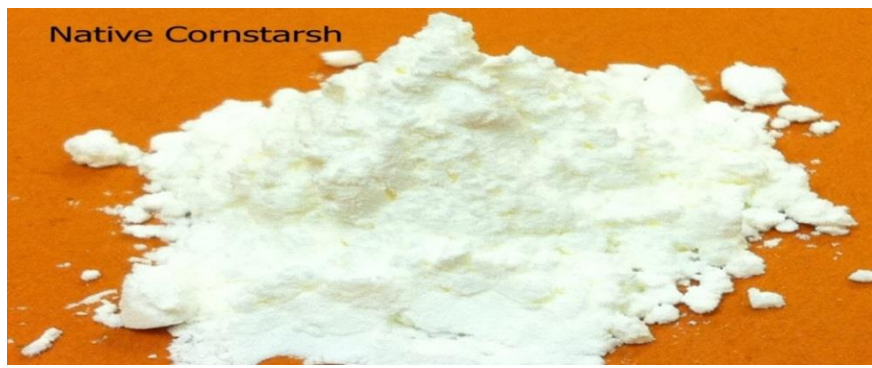


**Figure 3.6** Very fine native starch powder used for stress responsive granules fabrication

### **3.2.1.2 Method of Fabrication: Granulating Fine Starch**

#### **3.2.1.2.1 Starch Paste Preparation.**

Starch (5% w/v) paste was prepared as a granulating agent (binder) by carefully weighting 5 gm of the starch powder and dispersing it in 30 ml of cold distilled water. Continuous manual mixing of the mixture was applied until a white colour colloidal suspension developed. Concurrently in a separate container, 60 ml of water was boiled and the white colour suspension was then added to the boiled water in small portions. The remaining 10 ml of cold water was used to clean and wash any residual of the white colour suspension and added to the boiled portion. Continuous mixing was performed until a clear paste developed. The container with the whitish paste was transferred to a cold water bath and continuously stirred until a thick white paste was obtained.

#### **3.2.1.2.2 Iodization of Starch Paste**

5 ml of potassium iodide solution was added to each 100 gm of starch (5% v/w) paste. Continuous stirring was applied to homogenise the paste with the added iodine dye until a homogenous past colour was obtained.

#### **3.2.1.2.3 Fabrication of Stress Responsive Granules**

Manual wet granulation method of massing and screening was applied as the granules were prepared on lab scale to avoid any source of heat during the

granulation process. Possible heat source during the granulation process comes from using low or high shear mixers or heat during the drying process. This step has been done as the temperature increase during the granulation process may result loss of granules birefringence (Goering et al., 1974). Moreover, manual granulation method is able to produce less dense granules with sufficient mechanical strength which enhance the intergranular spaces.

The required amount of starch powder to be granulated was placed in a stainless steel tray. Iodised starch paste was added to the powder portion by portion with continuous kneading of the mixture by hand. Continuous mixing is essential to ensure uniform colour and paste distribution through the powder. Addition of iodised starch paste was continued in small portions until a damp mass developed. At this stage, addition of starch paste should be in caution to avoid powder over wetting. The ratio of the iodised paste to the raw powder for granulation was optimised at 38% (w/w). The final wet mass is subsequently forced through a 10-mesh screen to form the granules. The obtained granules were spread in a cleaned stainless steel tray lined with a large piece of clean and dry paper and left to dry up to 72 hrs at room temperature. The prepared granules were sieved using standard serial sieves and free flowing granules in the size range of 300 to 1000 $\mu$ m (average diameter  $d = 650\mu$ m) were selected for the PSAT experiment work reported here in this research project, see Figure3.7. The obtained solid dry granules were stored in air-tight container and kept for further characterisation and evaluation.



**Figure 3.7** Image of stress responsive granules using iodised corn starch paste

The same granulation procedure was repeated using a non-iodised starch paste as illustrated in Figure 3.8. The aim of this procedure is to evaluate the performance of the birefringence and the effect of iodine staining on isochromatic fringes.



**Figure 3.8** Image of stress responsive granules using non iodised corn starch paste

### **3.2.2 Characterisation and Physiomechanical Properties of the Stress Responsive Granules**

The fabricated granules were characterised using a number of standard methods. These features include birefringence intensity, crystallinity of granules, internal angle of friction, static angle of repose, true density, bulk and tapped densities, Hausner and Carr's indices.

The granules birefringence intensity was evaluated using PSAT equipment while granules crystallinity was assessed using XRDS. The granules' true density was obtained by using the Helium Gas Pycnometer (AccuPyc 1330). The bulk and tapped densities were obtained using a tapped density tester (model AS-100). The static angle of repose was measured by using the conventional fixed angle method while the angle of internal friction, angle of wall friction, and flow factors were obtained by using the ring shear cell tester (RST-XS at 5 kPa). Carr's index and the Hausner ratio were calculated using the standard equations. The methods of characterisation and the obtained outcomes are discussed in details as follows;

#### **3.2.2.1 Birefringence intensity of Fabricated granules**

The birefringence intensity of the prepared iodised and non-iodised granules has been tested using the PSAT technique to evaluate the intensity of isochromatic

fringes. This will help to indicate the influences of iodine dye on the birefringence intensity. The fabricated birefringent granules were feed in static layers into hopper geometry held between two transparent sheets and mounted on suitably aligned balanced rig. The 2D PSAT setup was optimised and circular polarised light illuminated the fabricated birefringent granules and multiple digital images captured by the camera and analysed using proper PSAT for stress distribution profiles. More details about the procedure and the methodology are available in section 4.2.2. The result displayed in Figure 3.9 indicates that the iodised granules illustrated in Figure 3.9 (a) are able to show better birefringence than the non-iodised granules as seen in Figure 3.9 (b). This improvement appears as high resolution and sharpness of the isochromatic fringes pattern for the iodised granules assembly inside the hopper geometry.

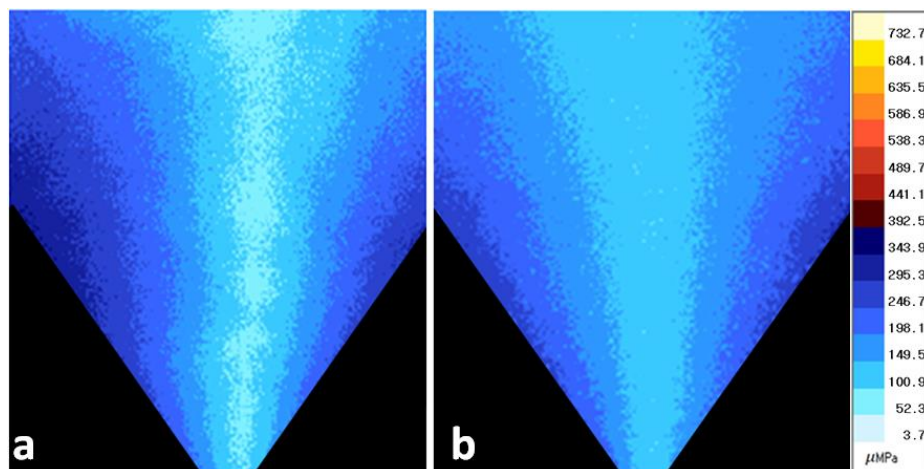


**Figure 3.9** Comparison of birefringence intensity of the prepared granules, (a) Isochromatic fringes of iodised granules and (b) Isochromatic fringes of non-iodised granules

The mechanism of birefringence enhancement is unknown to occur at single crystal level. It has been reported that Iodine staining is able to modify some fibre internal structure and its optical properties measured using polarising interference technique, these properties include refractive indices and birefringence (Shabana, 2006). The influence and effect of iodine on the granule birefringence is an interesting area for future work and needs further investigation on crystal level using advanced technologies. In the present case, as the iodised granules gave a good level of

birefringence response, the iodised granules have been selected and subjected to further characterisation tests as shown in the following sections.

### **3.2.2.2 Evaluation of Granules Flowability Using Ring Shear Cell Tester**

The stress responsive granules were evaluated for their flowability and wall friction using the Schulze ring shear tester, this recent automated technique has many advantages over the other technique (Schulze, 2008). Flowability, cohesivity, flow function ( $ff_c$ ) and internal angle of friction ( $\phi$ ) assessments are conducted by measuring granular materials yield locus while wall yield locus is applied to measure the angle of wall friction( $\varphi$ ).

The flowability assessment was conducted using the RST-XS fully automated ring shear tester connected to PC with RST- Control 95, using a  $30\text{ cm}^3$  annular cell. Excess granules were poured gently into the annular cell to overfill the cell. The extra granular materials were gently removed and the granular bed levelled. The filled annular cell was weighted and recorded before the test. The test was conducted using 5 kPa normal load and sheared at 4, 3, 2 and 1 kPa. At the first normal load (Preshear load) the granular assembly is consolidated and maintained at a steady state. Shearing of the granular assembly occurred at the other four force levels. The results are summarised in Table 3.1.

### **3.2.2.3 True Density Measurement**

The true density of the stress responsive granules was evaluated using Micrometrics Helium Gas Pycnometer (AccuPyc 1330). Helium Pycnometer measures the bulk solid density by measuring the changes of helium pressure in the calibrated chamber. The procedure is automated and the limiting step in true density measurement is the standard deviation (SD) value in the calibration step which should be not more than 0.0001%. Once the system is calibrated, the dry empty sample cup weighted and recorded as the first weight. The granules poured gently to fill one third of the cup and reweighted as second weight. The filled cup was inserted into the cell chamber and the chamber cap covered. The system was run under the recommended gas pressure according to the manual and the system stop automatically if five consequent readings are recorded with the SD less than 0.0001% obtained. The result is reported in Table 3.1.

### **3.2.2.4 Bulk and Tapped Densities**

Tapped density tester (model AS-100) was used to measure both bulk and tapped densities. A sample of 30 gm of granules was gently and slowly poured through a short stemmed glass funnel into a 100 ml graduated cylinder. The volume occupied by the powder was measured to the nearest 0.5 ml and the bulk density ( $V_b$ ) calculated in (gm/ml) via dividing the weight by the initial volume obtained. The bulk density recorded is the average of five determinations and the result is illustrated in Table 3.1.

The same cylinder, containing the powder was then tapped for 500 taps using the density tester. Some preliminary tests have been conducted to ascertain the number of taps able to give constant granule height. Sufficient tapping are able to eliminate any air voids between the granules and provide fixed volume. The occupied volume was measured to the nearest 0.5 ml and the tapped density ( $V_t$ ) calculated in (gm/ml) through dividing the weight by the final constant volume. The tapped density recorded is the average of five readings. The result is shown in Table 3.1.

### **3.2.2.5 Carr's Index**

The changes occurring in packing arrangement during the tapping procedure are expressed as Carr's index (I); the result is shown in Table 3.1. Carr's index is considered as an indirect parameter for powder flowability evaluation. The smaller the Carr's Index the better the flow (Shah et al., 2008). It is easily calculated using the following equation;

$$\text{Carrs Index } (I) = \left( 1 - \frac{V_b}{V_t} \right) \times 100 \quad \text{Eq. 3.1}$$

Where:

I = Carr's Index.

$V_b$  = Bulk density.

$V_t$  = Tapped density

### **3.2.2.6 Hausner Ratio**

Hausner ratio is another indirect tool for powder flowability assessment. In general, if the Hausner ratio is less than 1.25, this indicates a free flowing powder, but if its

value is greater than 1.25, it indicates poor powder flow (Shah et al., 2008). The value of the Hausner ratio obtained by using the following equation:

$$\text{Hausner Ratio} = \frac{\text{Tapped Density}}{\text{Bulk Density}} \quad \text{Eq. 3.2}$$

The calculated value was calculated using the average readings of bulk and tapped densities and the result is reported in Table 3.1.

### 3.2.2.7 Static Angle of Repose

Static angle of repose of the granules was measured according to the fixed funnel and free standing cone method. The granules were carefully poured through the funnel with its tip 3 cm height ( H) until the apex of the formed inverted conical pile just reached the tip of the funnel. The mean diameter of the base for the powder cone was determined and the tangent for the angle of repose was given as:

$$\tan(\theta) = \frac{\text{Height}}{0.5 \text{ Base}} \quad \text{Eq. 3.3}$$

The calculated angle of repose is the average of five readings and the result is shown in Table 3.1.

**Table 3.1** Experimental results of the physical and mechanical properties of the birefringent granules used in PSAT study

Parameter	Value
True Density (g/cm3)	$1.5014 \pm 0.0001$
Tapped Density (g/cm3)	$0.529 \pm 0.0027$
Bulk Density (g/cm3)	$0.439 \pm 0.0042$
Hausner Ratio	1.18
Carr's Index	15.41
Static angle of repose (°)	$37.85^\circ \pm 0.53$
Angle of internal friction ( $\phi$ )	$40^\circ$
Angel of wall friction ( $\varphi$ ).	$17.7^\circ$
Flow factor ( $ffc$ )	4.60

### 3.2.2.8 Particle Size Distribution Analysis

Particle size distribution of the stress responsive granules was obtained using the sieve analysis method. Around 400 g of the prepared granules were sieved using a series of US standard sieves ranging in screen opening from 300 to 1000  $\mu\text{m}$ . The sieve sets used are 1000, 850, 710, 600, 425 and 300  $\mu\text{m}$ . The largest particles are those passed through the (1000  $\mu\text{m}$ ) sieve and the smallest particles sizes are those retained on (300  $\mu\text{m}$ ) sieve. Any size below 300  $\mu\text{m}$  is excluded. The test was conducted using US sieve and shaker (Model Haver EML Digital plus) in multiple runs, and the maximum weight sieved in each run is 50gm. The granules were placed on the top sieve (1000  $\mu\text{m}$ ) and automatically shaken for 5 cycles, each cycle is 60 sec at amplitude 1.5. The fractions retained on each sieve were weighed and the percentages retained were obtained as shown in Figure 3.10.

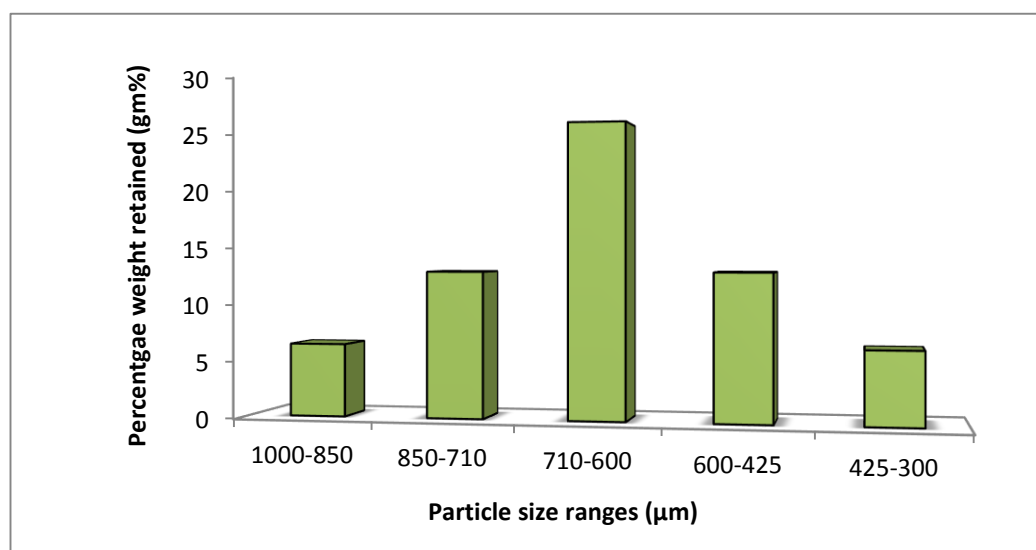


**Figure 3.10** Particle size distribution of stress responsive granules used in the experimental work for PSAT study

### 3.2.2.9 X-Ray Differential Scanning Test (XRDS)

X-ray diffraction analysis of both raw corn starch and the fabricated stress responsive granules were performed, using D8 Advance Bruker X-ray powder diffractometer (Bruker AXS, Rheinfelden, Germany) equipped with Cu K $\alpha$  radiation ( $\lambda=0.15406 \text{ nm}$ ) and operating at 40 kV and 40 mA. The scattering angle ( $2\theta$ ) covered the range from  $0^\circ$  to  $60^\circ$  with a step of  $0.02^\circ$  and a sampling interval of 10s.

The crystalline and amorphous states of native corn starch checked by XRDS, and the results showed A-Type crystalline pattern as shown in Figure 3.11.

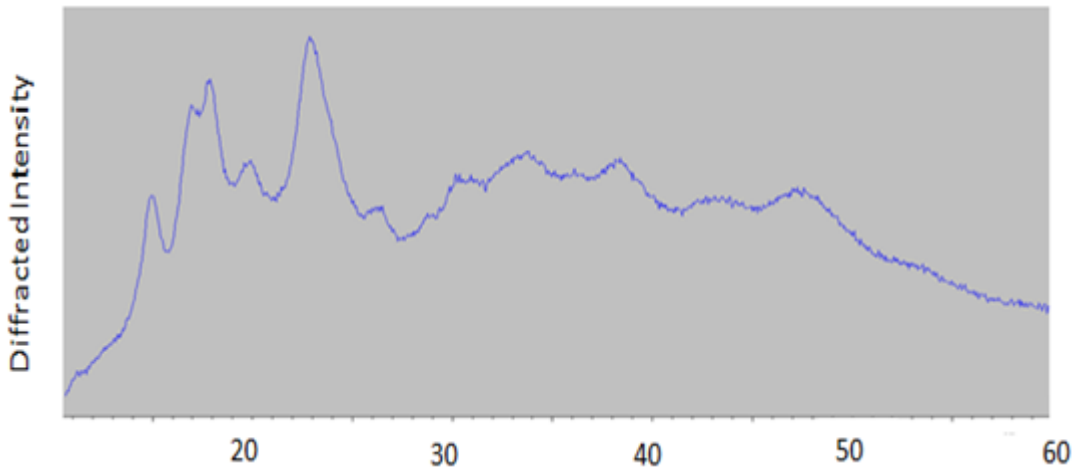


**Figure 3.11** X-Ray diffraction patterns of semi-crystalline native corn starch

A-Type crystalline pattern is an indication of very compacted hexagonal arrays of amylopectin in helical coils in addition to amylose double helix. This result is in full agreement with that obtained by (Zobel et. al., 1988, Shamaia et.al., 2003, Huang et.al., 2007, Jane 2006, Frost et.al., 2009). The three broad peaks at the diffracted angles around 14, 17 and 23 represent the crystalline portion of an A-pattern starch and the area below these peaks represents the amorphous portion.

The X-ray diffraction pattern of the fabricated stress responsive granules is shown in Figures 3.12.

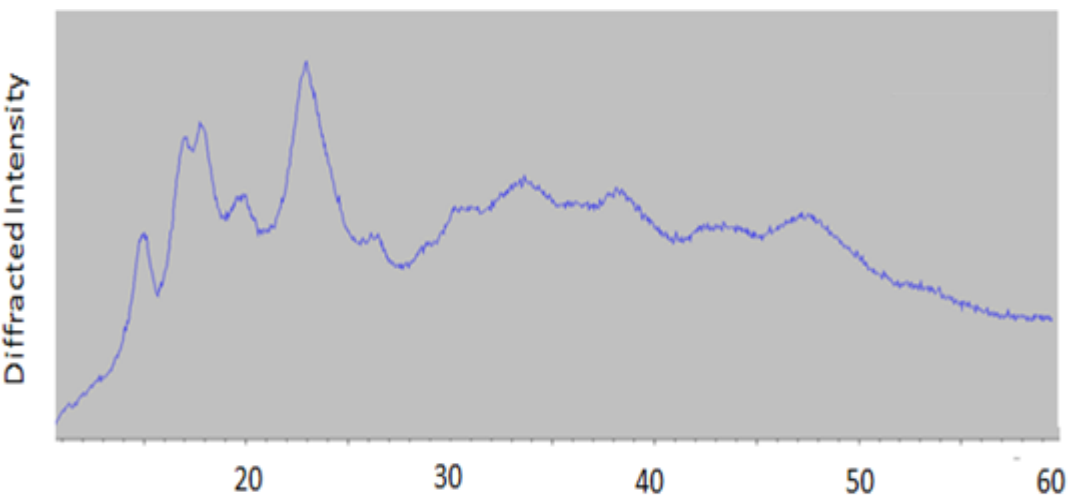


**Figure 3.12** X-Ray diffraction patterns of the fabricated stress responsive granules

The XRDS result is similar to that observed in case of native raw powders and no reported altering of the scattering angles or appearance of new peaks. However, the crystalline portion peaks intensity show slight decreases compared to raw material. The broad peaks at the diffracted angles around 14, 17 and 23 decreased from 26500 to 24000, 35000 to 31500 and 38000 to 35500 respectively. This might be attributed to the influence of the gelatinised paste used during the granulation process.

### **3.2.2.10 Scanning Electron Microscope (SEM)**

A scanning electron microscope was used to show the appearance, morphology, pores and surface details of the corn starch granules in both native starch raw material and the fabricated granules. Another aim of SEM is to observe any changes in the granule morphology due to the granulation process. Scanning electron micrograph results are shown in Figure 3.13 and Figure 3.14.

The morphology of native corn starch granules is similar to that reported in the literature (Chen et al., 2006). The granules are round, regular in shape and showing a non-smooth surface. These morphology characteristics indicate high amylopectin content. Usually high amylose starch shows elongated and irregular granules shape. The native fine starch powder images show granule lumps and dense aggregate of the granules due to very low particle size. In such cases, the high surface energy of the starch powder will enhance the agglomeration and particles attract and adhere due to Van der Waals forces.

The fabricated stress responsive granule morphology shows some improvement in the shape of the granules which become more rounded in shape. The inter-particles voids become bigger in size and more obvious in the fabricated granules compared to the dense raw starch powder.

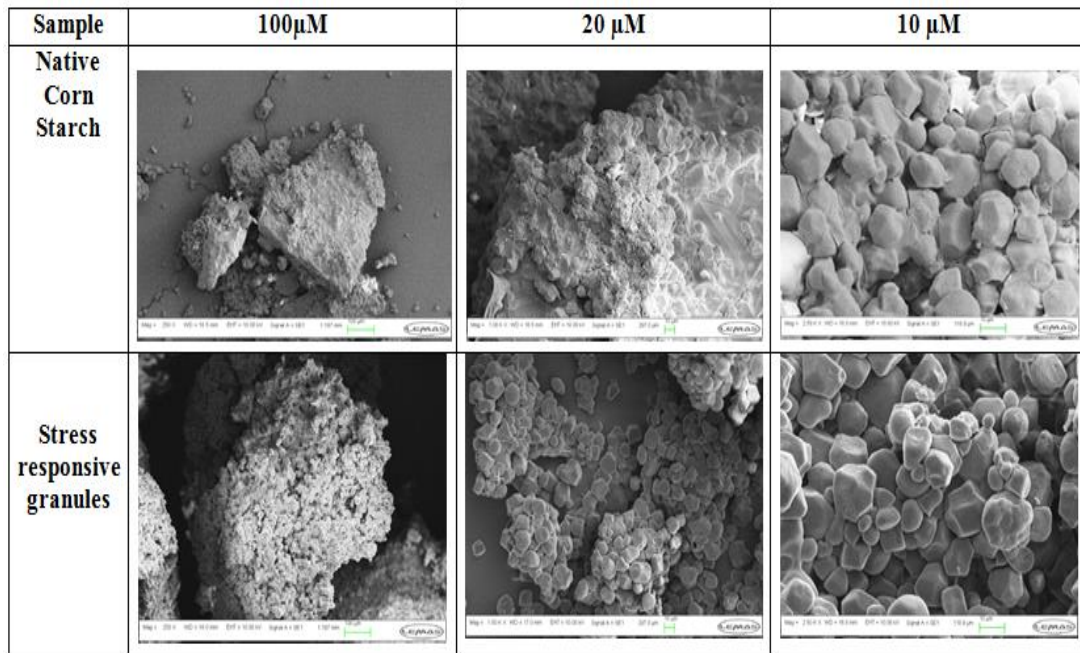


**Figure 3.13** SEM image of native corn starch and stress responsive granules at different magnification powers

Pores and cavities were reported obviously on the surface of both native starch granules and stress responsive granules as clearly illustrated in Figure 3.14. Inter and intra granular channels and surface pores are well known characteristics for starch granules as reported earlier in literatures (Karathanos and Saravacos, 1993, Huber and BeMiller, 2000, Sujka and Jamroz, 2010) .

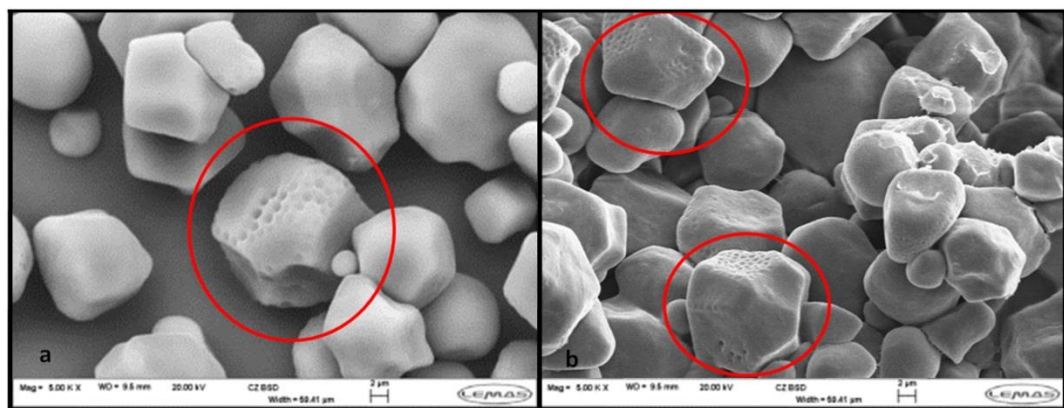


**Figure 3.14** Surface pores on both (a) native starch granules and (b) stress responsive granules

### **3.3 Fabrication of Colour Coded Granules for Qualitative Dynamic Flow Analysis and DPIV Applications**

#### **3.3.1 Materials and Methodology**

#### **3.3.2 Materials**

Corn starch was obtained from (Sigma Aldrich, UK) and multiple colouring agents (blue and yellow) have been obtained locally.

#### **3.3.3 Method of Fabrication**

##### **3.3.3.1 Starch Paste Preparation**

Sufficient quantity of starch paste (5%w/v) was prepared using the same methodology mentioned previously in section 3.2.1.2.1.

##### **3.3.3.2 Colouring of the Starch Paste**

The prepared starch was divided into two portions; each portion was weighing 100gm. For the paste colouring procedure, 5 ml of each colouring agent was added to each paste portion with continuous stirring to homogenise the paste with the added colouring agent.

##### **3.3.3.3 Fabrication of the Colour Coded Granules**

The same methodology mentioned previously in section 3.2.1.2.3 and Albaraki and Antony (2014) has been applied here using the coloured starch paste.

#### **3.3.4 Physiomechanical Properties of the Fabricated Granules**

The physical and mechanical properties of the fabricated granules for DPIV application were measured using the same methodologies mentioned in section 3.2.2. and the results are summarised in Table 3.2.

**Table 3.2** Experimental results of the physical and mechanical properties of the granules used in colour coding and DPIV study (Albaraki and Antony, 2014)

Parameter	Value
True Density (g/cm3)	$1.5014 \pm 0.0001$
Tapped Density (g/cm3)	$0.537 \pm 0.005$
Bulk Density (g/cm3)	$0.443 \pm 0.004$
Hausner Ratio	1.212
Carr's Index	17.50
Static angle of repose ( $^{\circ}$ )	$38.12^{\circ} \pm 0.41$
Angle of internal friction ( $\emptyset$ )	$39^{\circ}$
Angel of wall friction ( $\phi$ )	$17.9^{\circ}$
Flow factor ( $ffc$ )	4.80

### 3.4 Conclusions

The characteristics of native corn starch powder; such as natural birefringence feature, porosity, high adsorption capability and ease of modifying and fabrication have been utilised properly to fabricate stress responsive and colour coded granules. The manual wet granulation technique has been applied for fabricating micronizes granules to avoid any heat production sources during the granulation process that alters the birefringence nature of corn starch granules. Additionally, this technique is commonly used in the pharmaceutical industry, applicable for laboratory scale production and ease for modifying pharmaceutical powders for multiple purposes. It has been noticed that iodine has a positive influence on the fabricated stress responsive granules birefringence. Similar granulation conditions have been applied in case of colour coded granule fabrication to unify the fabrication condition and benchmarking. The selected particle size range for PSAT, CCT, and DPIV studies (300-1000 $\mu$ m) was characterized using both conventional and advanced automated evaluation methods. The physical and mechanical results indicate free-flowing characteristics for the prepared granules and the influence of cohesivity is minimal as intended in the current study.

## **Chapter 4 : Experimental Visualising and Analysis of Maximum Shear Stress Distribution and Direction of Principal stresses inside particulate packing at Static Condition**

The aim of this chapter is to report about research on the application of PSAT as a recent non-invasive visualising technique to understand the stress distribution characteristics of micron size particulates systems for the first time. The outputs include the maximum shear stress profiles distribution and direction of principal stresses inside multiple internal angular hopper geometries ( $30^\circ$ ,  $60^\circ$  and  $90^\circ$ ). The work emphasises the influence of hopper internal angle on the maximum shear stress profiles distribution and principal stress directions under a static condition. The hoppers were filled in multiple layers of free flowing stress responsive granules in range of a  $300 - 1000 \mu\text{m}$  as detailed in Chapter 3. The stress distribution profiles were quantified using proper PSAT software. The stress distribution profile was evaluated across the hopper's width at three different heights; orifice, one forth and middle section levels. The experimental and numerical results obtained using DEM showed a good level of agreement of nonhomogeneous distribution of the maximum shear stress due to the internal hopper angle influence, and the results have been published jointly with a member of our research group. The results prompted investigation of how such microscale characteristics may potentially influence the nature of the dynamic flow process and will help to predict the related flow hypothesis through the each hopper geometry. Some of the results reported here were presented at Powder and Grains 2013 in Sydney and published as proceedings in AIP 2013 (Albaraki et al., 2013), as well as two other conferences (Antony et al., 2012) and (Antony et al., 2013), although journal manuscripts are currently being prepared.

### **4.1 Introduction**

Flowability of granular material and sliding characteristics on their storage bin walls are practically ranked from free flowing to non-flowing and their flow behaviour is very complex in multi-dimensional aspects (Prescott and Barnum, 2000, Schulze, 2008). The filling process of granular materials in their storage bins and bunkers are

characterised by gradual forming of a growing heap of the bulk solid against the fixed bin walls under elevated pressure conditions. Clear understanding of stress distribution profiles and direction of principal stresses within granular materials inside their storage bins, such as silos and hoppers is essential to understand the fundamentals of granular flow behaviour and also crucial for the proper design of the storage bins (Ooi and She, 1997, Chen et al., 1998, Ooi et al., 1996, Teng et al., 2001, Zhao and Teng, 2004). Miscalculation or underestimation of internal stress influences on storage bin walls may lead to serious and catastrophic failure in the storage bins (Carson, 2001, Schulze, 2008).

For more than a century, and since Janssen (1895), the prediction of the stress exerted by granular material on the walls of their storage bunkers was subjected to a great deal of attention (Walker and Blanchard, 1967, Walters, 1973a, Chen et al., 1998, Schulze, 2008). The early work conducted by Janssen (1895), has been reviewed, criticised and expanded by other authors such as Jenike (1967) , Walker (1966 and 1967) and Walter (1973) who involved the inclined part of the silo (hopper section) in their researches. The stress distribution and the direction of the principal stress during the filling and discharging process have been calculated using many mathematical models and generally classified into two states; active stress state during the filling process and passive stress state during the discharging process.

The first appearance of the stress terminologies “active” and “passive” stress states goes back to Rankine (1857) for earth pressure calculation (Schulze, 2008). His method was applied to measure the maximum compressive stress acting on the granular material surface and known recently as unconfined yield stress ( $\sigma_c$ ). Stress ratio that reflects the ratio of the vertical and horizontal stresses, plays a crucial role in granular material assembly stress status and flowability. Theoretical calculations of stress distribution mainly depend on the theory assumptions regarding the vertical and horizontal stresses (Nedderman, 1992, Schulze, 2008). If the vertical stress is the major principal stress, the stress status is denoted as active stress state. However, if the horizontal stress is the major principal stress, the stress status inside the storage bin is denoted as passive stress state. The theoretical assumption by denoting the vertical and horizontal stresses as major and minor principal stresses has been proved to be incorrect (Nedderman, 1992, Schulze, 2008).

The literature did not clearly report any experimental results on the influence of the hopper internal angle on the nature of the stress distribution and its direction within granular materials of micron size under both static and dynamic conditions. Moreover, no consequential experimental method reported the stress distribution and direction inside flow chambers using actual micronised granular assembly in static condition and any possible influences on the dynamic flow process. Such features are essential and sought in many industries to optimise various manufacturing processes involving particulates.

This aspect is addressed in this chapter, i.e., quantifying stresses and their directions within particulate packing containing micron size granules.

## 4.2 Material and Methodology

### 4.2.1 Material

The fabricated stress responsive granules (as described in Section 3.2) have a particle size distribution ranging from 300 to 1000  $\mu\text{m}$  were selected to visualise and probe the maximum shear stress distribution and its direction inside constrained geometries using PSAT. Different internal angle ( $30^\circ$ ,  $60^\circ$  and  $90^\circ$ ) 2D hoppers were fabricated in mechanical engineering workshop in Leeds using perspex sheets. The dimensions of the hoppers used in this research project for both studies are as follows; the height ( $H$ ) is 8 cm ( $\approx 123d$ ), orifice width ( $w$ ) is 7mm ( $\approx 11d$ ), nozzle length is 20 mm ( $\approx 31d$ ) and the hopper thickness (perpendicular to the plane of hopper) is 4mm ( $\approx 6d$ ), see Figure 4.1. The hopper internal surfaces and edges were finely polished to minimise wall friction.

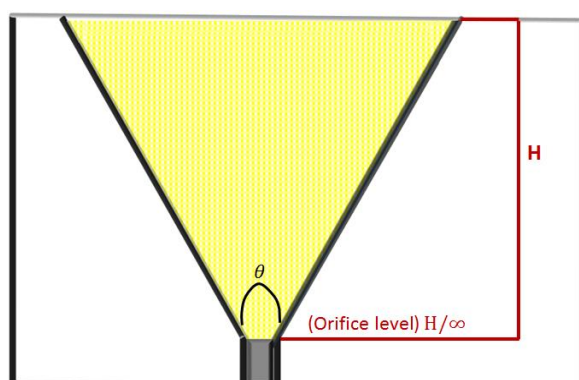


**Figure 4.1** Schematic diagram of 2D hopper geometry internal angle filled by stress responsive granules used in the PSAT study

#### 4.2.2 Methodology

The PSAT study was conducted to investigate how the hopper internal angles influences the maximum shear stress distribution inside granular pharmaceutical beds within different hopper geometries under self-weight. The heights of the granular bed were kept constant among the three selected hoppers.

Before the filling process, the hopper nozzle was closed by using a suitable fit spacer to allow for filling the hopper in static layers. The stress responsive granules were fed into the Perspex hopper geometry held between two transparent Perspex sheets, as shown in Figure 4.1. The filling process was conducted using a conical funnel, which was initially aligned along the central axis of the hopper. The funnel had a long, flexible nozzle to build up the granular layers and to minimise any segregation of the particles during the filling process. It also helps to level the granular bed. The filled hopper geometry was mounted on a suitably aligned balanced rig and fitted within the required 2D PSAT setup, as shown in Figure 4.2.

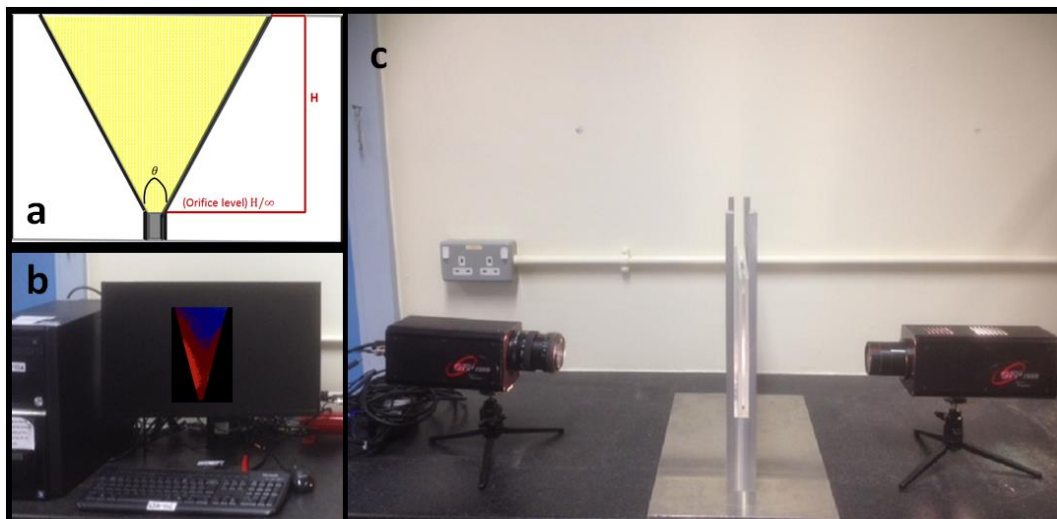


**Figure 4.2** Experimental setup of the PSAT system for maximum shear stress measurement within granular materials inside hopper geometries; (a) hopper geometry, (b) PSAT software, and (c) PSAT 2D setup

The conducted preliminary studies proved that the selected hopper dimensions and the ratios of the hopper dimensions to the average particle size ( $d$ ) are adequate to secure continuous flow during the dynamic flow experiments. The filling procedure for each hopper angle had been repeated at least 15 times to ensure that the initial packing of granules is homogenous. To conduct this, the mean weight of the granules from the different runs was calculated and the variations verified to be

within an acceptable range ( $4.511 \pm 0.232$ ,  $10.464 \pm 0.276$  and  $13.364 \pm 0.220$  g) for the  $30^\circ$ ,  $60^\circ$  and  $90^\circ$  hoppers respectively.

The major components in the PSAT system are the circular polarised light projector, stress responsive granules, balanced mounting rig and a digital PSAT camera connected to PSAT software, as shown in Figure 4.2. The camera is supplied with a constantly rotating analyser working at multiple revolutions, and for each revolution, a series of images are taken, allowing the best light intensity to be measured. Once the PSAT setup starts, the emitted circular polarised light illuminated the stress responsive granules and multiple digital images were captured by the camera and analysed by the PSAT software for stress profiles distribution using proper PSAT software.

#### 4.2.3 PSAT System Limitations

A number of trial experiments were conducted at the beginning of this research project to optimise the experimental work conditions, aiming to obtain the best results using PSAT. A high resolution of captured images depends on sufficient illumination of the stress responsive granules. The reproducibility of the PSAT 2D setup system was checked and tested for multiple samples that provide identical stress profiles distribution under similar experimental conditions. However, the main limitations of 2D PSAT setup for best image resolution are summarised as follow;

- The light intensity within the stress responsive granules must be maintained during the experimental work in a range of 180 to 250 light units from camera.
- The best sample thickness for any storage bin section able to maintain uniform light intensity is not more than 6mm.
- The distance between the light source and the stress responsive granules assembly must be in range of 45 to 65 cm to give the best granular bed illumination and high resolution of the images.
- The best PSAT image resolution was obtained at five revolutions/second of the analyser.

### 4.3 Results and Discussions

All captured images by PSAT were calibrated and scaled using built in software in order to simplify the comparison of the fringe images. The magnitude of the maximum shear stress profiles and the direction of major principal stress within the stress responsive granular beds were evaluated within the entire hopper geometries at static condition. The images were colour-coded in relation to the magnitude of maximum shear stress within the hopper. The distribution of stress profiles was evaluated across the granular bed for all internal angles of hopper geometries at three different heights,  $H/\infty$ ,  $H/4$  and  $H/2$  as shown in Figure 4.3. Level  $H/\infty$  represents the hopper orifice level and denoted also as level zero. The software is adapted to measure the stress magnitude at every single pixel point that can be converted later to a metric unit.

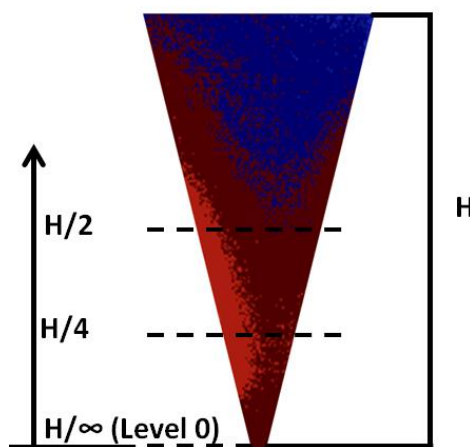


**Figure 4.3** Selected heights for maximum shear stress analysis across the width of the stress responsive granules

#### 4.3.1 Hopper Geometry Having a 30° Internal Angle

At a 30° internal hopper angle, high magnitude in the maximum shear stress distribution has been observed within the stress responsive granular assembly inside the whole hopper, especially below the mid-half of the hopper; see Figure 4.4 (a). The direction of the major principal stress within the whole hopper tends to be aligned in the vertical direction (along the direction of gravity), as illustrated in Figure 4.4 (b). The vertical direction of the major principal stress indicates that if the particles were allowed to flow, they would flow freely without any hindrance within

all hopper segments. The flow behaviour inside this geometry will be evaluated experimentally in Chapter 6 using DPIV and the influences of the stress status will be discussed in details.

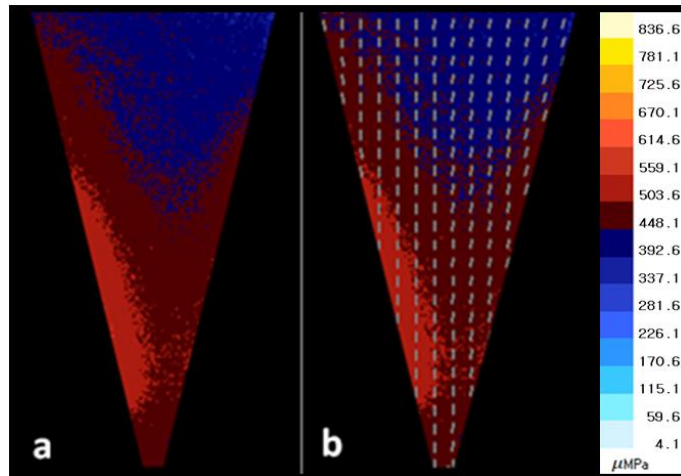


**Figure 4.4** Experimental 2D PSAT setup results: (a) maximum shear stress profiles distribution and (b) major principal stress direction inside stress responsive granules at  $30^\circ$  internal angle hopper geometry

The normalised maximum shear stress magnitudes across three different hopper heights;  $H/\infty$ ,  $H/4$  and  $H/2$  were evaluated and the result is shown in Figure 4.5. The normalisation is done with respect to the maximum shear stress acting on the wall at the level of the selected heights.

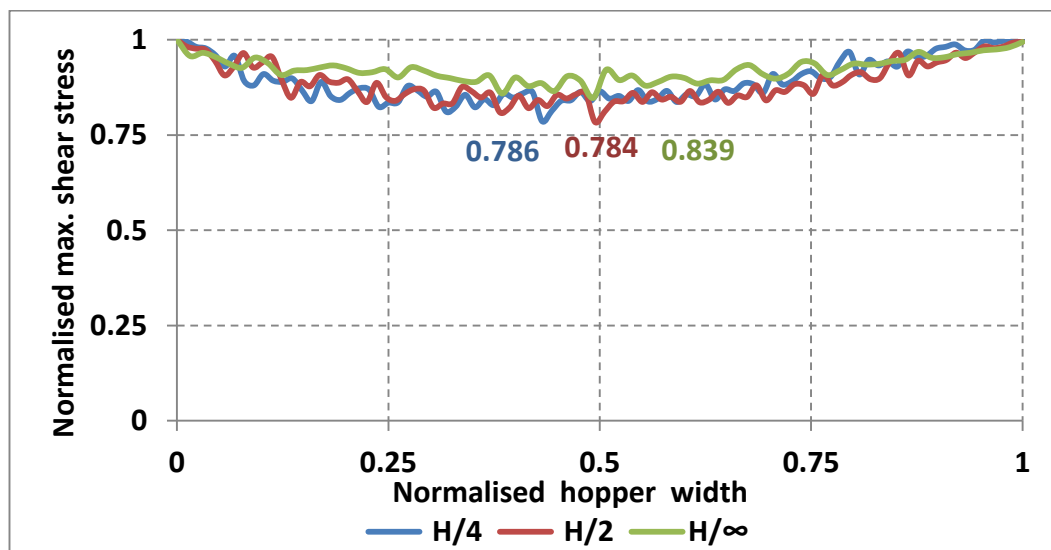


**Figure 4.5** Normalised maximum shear stress distribution profiles inside  $30^\circ$  internal angle hopper at multiple heights;  $H/\infty$ ,  $H/4$  and  $H/2$

The aim of this analysis across the granular assembly is to investigate the extent of the non-homogeneity in shear stress distribution within the granular bed across the horizontal sections and to explore the stress deviation between the boundaries to the central axis. This will give an idea of the influence of the bin geometry, inter-granular friction, particles location and bin boundaries on the maximum shear stress distribution. The plot in Figure 4.5 shows relatively low stress profile deviation between the hopper boundaries and the central hopper axis. Marked overlapping of the normalised maximum shear stress profiles across the hopper width has been reported at all three levels. This indicates a good level of homogeneity for stress distribution across the hopper width at this geometry at all heights. The previous observations were confirmed using the average normalised maximum shear stress values across the whole section of the hopper width at all three heights as shown in Figure 4.6.

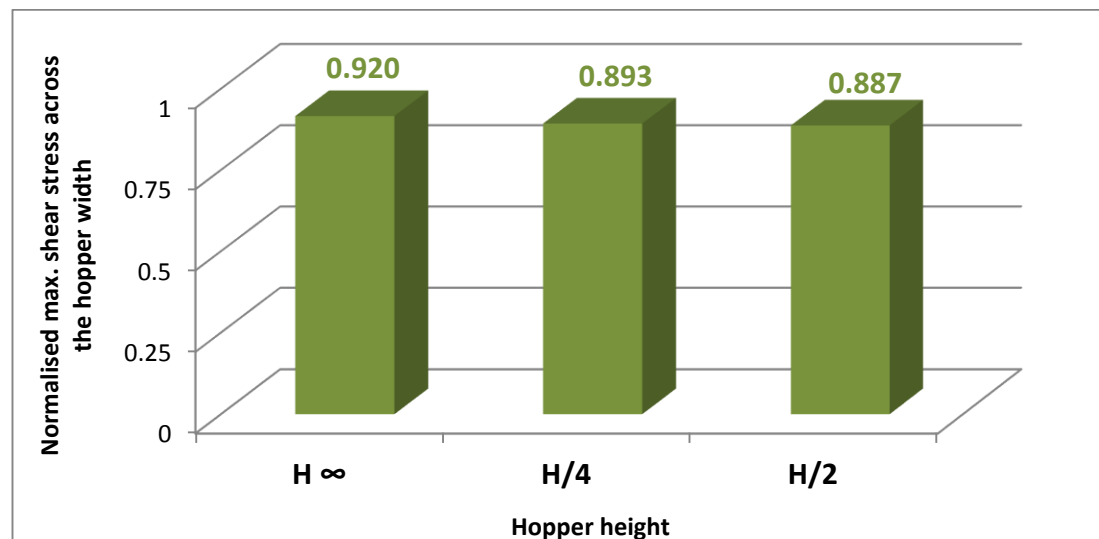


**Figure 4.6** Normalised average maximum shear stress magnitudes inside 30° internal angle hopper at multiple heights;  $H/\infty$ ,  $H/4$  and  $H/2$

The average values are 0.920, 0.893 and 0.887 at  $H/\infty$ ,  $H/4$  and  $H/2$  respectively and the overall average stress differences are less than 4%. This result confirms the homogeneity of shear stress distribution across the hopper width at all selected heights.

The minimum normalised values of the stress at the three hopper heights are 0.839, 0.786 and 0.784 at  $H/\infty$ ,  $H/4$  and  $H/2$  respectively as shown in Figure 4.5 and Table 4.1. The relative stress deviations at the central zone to that obtained at the hopper

boundaries at H/ $\infty$ , H/4 and H/2 are less by 16.1%, 21.4% and 21.6% respectively as shown in Table 4.1.

The analysis has been also repeated using the average normalised maximum shear stress values at the central axis and the boundaries. To conduct these calculations, the average normalised maximum shear stress values were calculated at both boundaries and the central zone as an average of five points along each level. The average normalised values of the stress at the central axis and the boundaries at H/ $\infty$ , H/4 and H/2 are 0.890, 0.840, 0.833 and 0.957, 0.968, 0.960, respectively. The relative average stress ratio at the hopper central zone to that obtained at the boundaries at H/ $\infty$ , H/4 and H/2 is less by 7%, 13.22% and 13.23% respectively as seen in Table 4.1. Both measurements using the minimum normalised maximum shear stress values and average normalised maximum shear stress values confirm the stress homogeneity across the hopper width.

**Table 4.1** Normalised maximum shear stress findings and comparisons inside the 30° internal angle hopper geometry

	H/ $\infty$	H/4	H/2
Minimum normalised ( $\tau_{max}$ ) at (CZ)	0.839	0.786	0.784
Normalised ( $\tau_{max}$ ) at (HB)	1	1	1
Stress Ratio (CZ) < (HB)	16.1%	21.4%	21.6%
Average normalised ( $\tau_{max}$ ) across the bed	0.922	0.894	0.887
Average normalised ( $\tau_{max}$ ) at (CZ)	0.890	0.840	0.833
Average normalised ( $\tau_{max}$ ) at (HB)	0.957	0.968	0.960
Average stress ratio (CZ) < (HB)	7%	13.22%	13.23%
* (CZ) is Hopper central zone			
*(HB) is Hopper boundary			

The maximum shear stress magnitudes exerted by granular materials on the hopper walls at the end of the filling process were evaluated using the slice method. The method relies on dividing the hopper geometry to eight equal slices, each slice representing 1cm height and the stress magnitude is measured at the centre of each layer close to the boundary as seen in Figure 4.7. A similar method was applied by Ding and Enstad (2003) and Ding et al. (2011) and the aim of this analysis is to investigate the location of the maximum shear stress exerted by the granular materials on the hopper wall. The shear stress measurement was conducted as the

average of five stressed points close to the hopper boundary, not as a single stressed point calculation where the area of measurements is 5x5pixel.

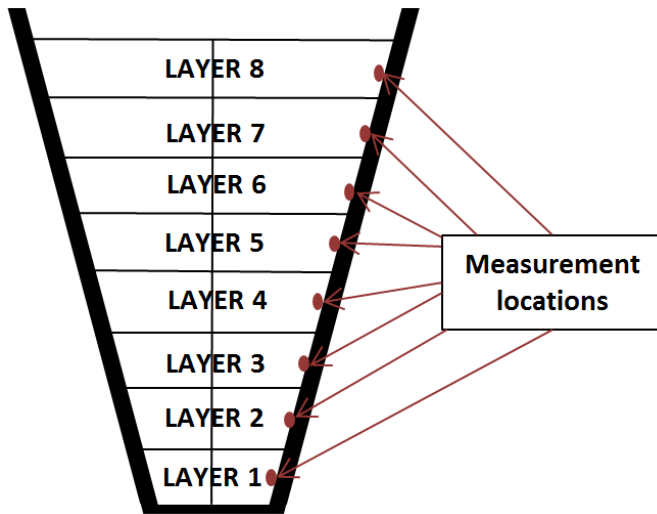


**Figure 4.7** Granular materials equal slices inside 30° internal angle hopper geometry and the point of stress measurement

The results indicate that the highest average maximum shear stress was reported at the level of layer 3 as shown in Figure 4.8. A similar shear stress distribution trend exerted by granular materials on the hopper walls has been reported by Ding and Enstad (2003), Ding et al. (2011), Wang et al. (2013) using the numerical methods, FEM and DEM.

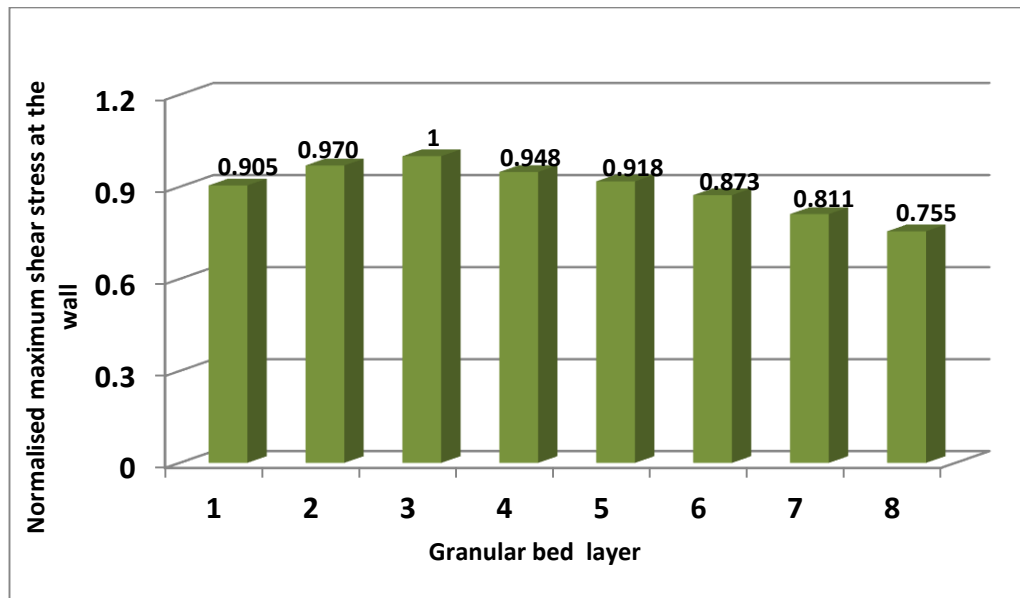


**Figure 4.8** Normalised maximum shear stress exerted on the hopper wall at the end of the filling process inside 30° hopper geometry

In general, the results show that the maximum shear stress values at all three heights are close to each other. The average percentage of maximum shear stress across the whole section at  $H/\infty$  to  $H/4$  and  $H/2$  was very close to each and the percentage of the variation was in range of 3-4%. This indicates that the granular assembly within the hopper is highly stressed at the three levels and shows relative spatial homogenous distribution of the maximum shear stress across all three heights. The highest magnitudes of the maximum shear stress were always obtained close to the hopper boundaries while the lowest values are reported at the central region of the hopper, as illustrated clearly in Figure 4.6. The zigzag shapes of the plots prove the quantitative ability of PSAT to accurately measure the spatial distribution and magnitudes of the shear stress at any single points across the granular assembly.

Based on the relative uniformity of the maximum shear stress distribution profiles across this hopper width, as well as the vertical direction of the major principal stress within the whole hopper geometry, the flow behaviour inside this hopper geometry thought to be in mass flow trend. The granular flow could proceed through the whole bed including particulates residing close to the hopper boundaries. Accordingly, no solid bulk segregation or stagnant zone formation are expected in such geometry during the dynamic flow process. These predictions will be assessed qualitatively in Chapter 5 using CCT and quantitatively in Chapter 6 using the DPIV method.

#### **4.3.2 Hopper Geometry Having a 60° Internal Angle**

The maximum shear stress distribution profiles and the major principal stress direction within 60° internal angle hopper geometry are shown in Figure 4.9. In general, the magnitude of the maximum shear stress profiles is less than that obtained in the case of the 30° hopper geometry. This is obviously noticed through the calibrated stress colour scale of the profiles. The central axis of the hopper geometry shows relatively less stressed zone compared to the hopper boundaries. This low stress zone appears as the light blue region in the central axis of the hopper compared to the dark blue at the boundaries as shown in Figure 4.9 (a). The low stressed zone in the light blue colour starts directly above the hopper outlet and propagates upward to higher hopper boundaries and the outer layer of the stress responsive granules. Outside the central zone, higher stressed zones are

symmetrically distributed in ascending order until it reclines on both hopper boundaries. High layers of the stress responsive granules show large, low stressed zone, forming a V shape; this zone starts at the middle height of the central zone and expands to the outer layer of the granular material.

The directions of the major principal stress within the hopper geometry show a vertical to semi-vertical direction within the low stressed central zone and its close surrounding zones, as shown in Figure 4.9 (b). Outside this region, the direction of the major principal stress is inclined or deviated from the vertical route. Deviations have been noticed to be parallel to the hopper boundaries and extended from the hopper outlet zone parallel to the walls and upward to the top zone of the granular bed. The regions close to the hopper boundaries show more inclination in the direction of the major principal stress parallel to the hopper walls.

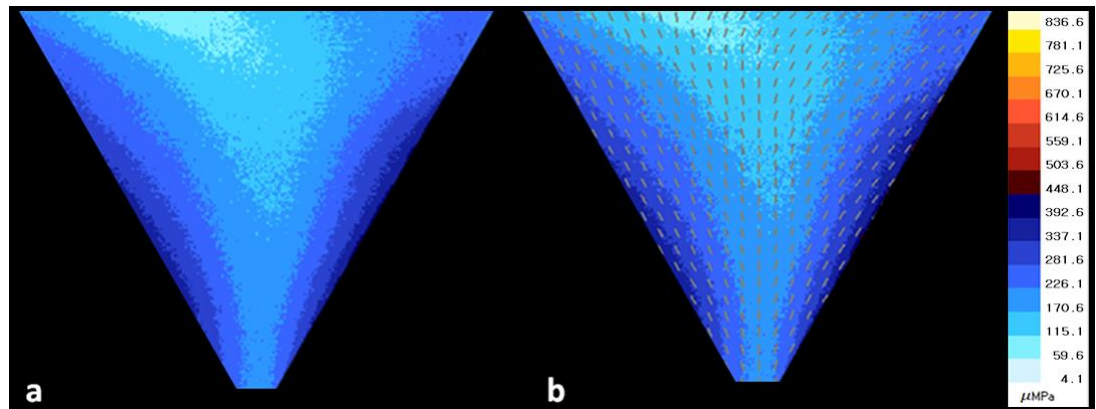


**Figure 4.9** Experimental 2D PSAT setup results: (a) maximum shear stress profiles distributions, and (b) major principal stress directions inside stress responsive granules at  $60^\circ$  internal angle hopper geometry

Similar to what was conducted in the case of the  $30^\circ$  internal angle hopper geometry, the maximum normalised shear stress magnitudes across the three different hopper heights  $H/\infty$ ,  $H/4$  and  $H/2$ , were analysed and the results are shown in Figure 4.10. It is clear from Figure 4.10 that the maximum shear stress distribution is non-homogenous across all three heights. The central axis of the lower hopper segment at  $H/\infty$  that locates directly above the hopper outlet, shows relatively high stress magnitude compared to that at  $H/2$  and  $H/4$ . The plot obviously shows a high difference in the stress magnitude between the hopper central zone and the boundaries, indicating a high degree of stress deviation. The average normalised maximum shear stress across the entire hopper width at all three heights was

calculated as shown in Figure 4.10. The average values are 0.690, 0.675 and 0.613 at  $H/\infty$ ,  $H/4$  and  $H/2$  respectively. Similar to what has been observed in the case of the  $30^\circ$  hopper geometry, the lower hopper segment is more stressed than the other two heights, but the stress deviation between the central region and the wall is higher in the case of the  $60^\circ$  geometry.

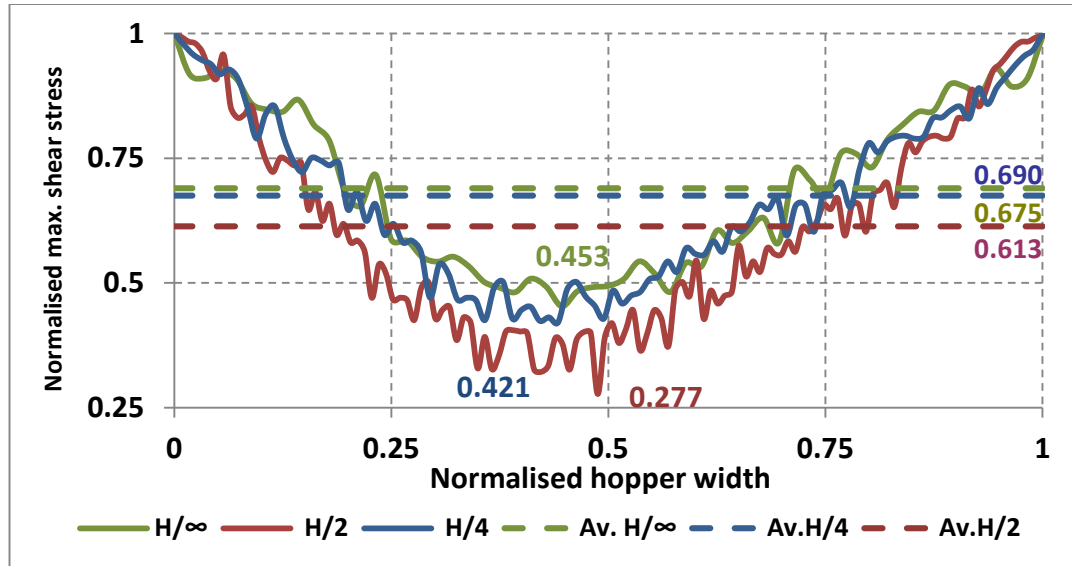


**Figure 4.10** Normalised maximum shear stress value distribution and its average magnitudes inside  $60^\circ$  internal angle hopper at multiple heights;  $H/\infty$ ,  $H/4$  and  $H/2$

The minimum normalised shear stress across the three heights is reported at the central hopper region and the values are 0.453, 0.421 and 0.277 at  $H/\infty$ ,  $H/4$  and  $H/2$  respectively as shown in Figure 4.10. The relative stresses at the hopper central zone to that at the boundaries at  $H/\infty$ ,  $H/4$  and  $H/2$  is less by 54.70%, 57.90% and 72.3% respectively, as shown in Table 4.2. The results report higher stress deviation at level  $H/2$  compared to  $H/\infty$  and this could be attributed to the low stressed central zone forming a (V) shape, starting at around  $H/2$  level and expanded to the outer granular layer; see Figure 4.9.

The normalised shear stress calculations were repeated using the average values at the central hopper zone and boundaries using the same principles as used in the case of  $30^\circ$  hopper geometry. The average values of the normalised stress at the central region and the boundaries at  $H/\infty$ ,  $H/4$  and  $H/2$  are 0.490, 0.481, 0.373 and 0.912, 0.954, 0.978 respectively, as summarised in Table 4.2. The relative average stresses

ratios at the hopper central zone to that obtained at the hopper boundaries at  $H/\infty$ ,  $H/4$  and  $H/2$  are less by 46.27%, 49.58% and 61.86% respectively. Both stress measurements using the minimum normalised maximum shear stress values and average normalised maximum shear stress values show non homogenous stress distribution and the highest deviation was obtained at  $H/2$ . The results in Table 4.2 summarise the previous stress calculations and comparisons.

**Table 4.2** Normalised maximum shear stress findings and comparisons inside the  $60^\circ$  internal angle hopper geometry

	$H/\infty$	$H/4$	$H/2$
Minimum normalised ( $\tau_{max}$ ) at (CZ)	0.453	0.421	0.277
Normalised ( $\tau_{max}$ ) at (HB)	1	1	1
Stress Ratio (CZ) < (HB)	54.70%	57.90%	72.30%
Average normalised ( $\tau_{max}$ ) across the bed	0.690	0.675	0.613
Average normalised ( $\tau_{max}$ ) at (CZ)	0.490	0.481	0.373
Average normalised ( $\tau_{max}$ ) at (HB)	0.912	0.954	0.978
Average stress ratio (CZ) < (HB)	46.27%	49.58%	61.86%
* (CZ) is Hopper central zone			
*(HB) is Hopper boundary			

All the previous calculations indicate that the stress distribution across the horizontal hopper sections is non-homogenous across all three heights. The results also indicate that the central axis of the hopper at all three heights is the least stressed zone. The stress deviation from the walls to the central hopper axis is relatively low at  $H/\infty$  compared to the other two heights, indicating low extent of granular stagnation at this segment within this geometry. Moreover, these findings give an indication that the granular portion close to the outlet region could show good extent of flow due to relative homogenous stress distribution and major principal stress direction toward the outlet. The relatively high stress deviations suggest a high possibility of central plug flow generation at the central axis of this hopper geometry.

The shear stress exerted by granular materials on the hopper wall at the end of the filling process was evaluated using the slice method and the same measurement principles as used in the case of the  $30^\circ$  geometry. The results indicate that the general stress distribution trend is similar to what has been obtained in cases of  $30^\circ$  hopper geometry; the only exception is that the maximum shear stress value is reported at the level of Layer 4 not Layer 3, as shown in Figure 4.11.

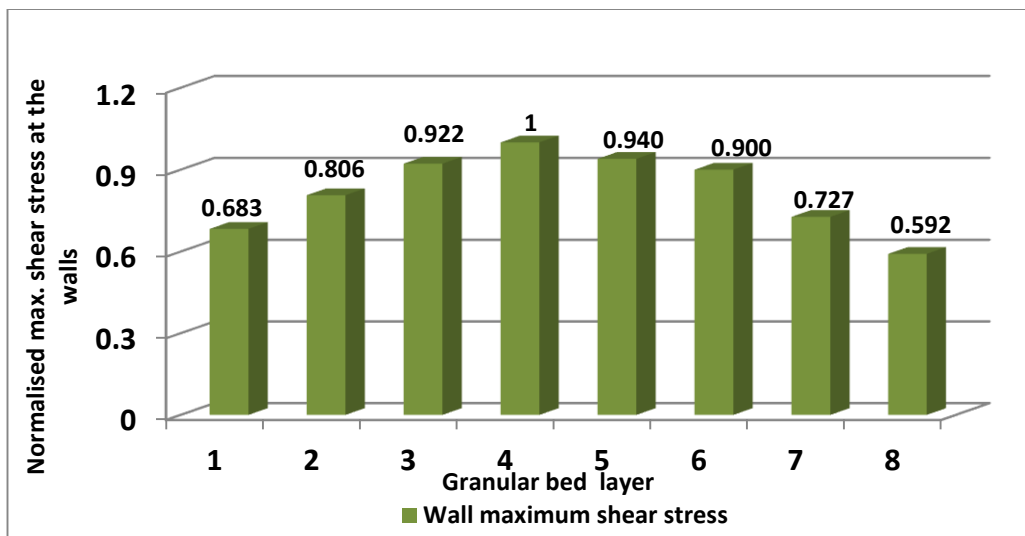


**Figure 4.11** Normalised maximum shear stress exerted on the hopper wall at the end of the filling process inside 60° hopper geometry

The previously obtained microscopic characteristics of the granular bed inside such hopper geometry could greatly influence the granular macroscopic flow behaviour and this will be validated qualitatively and quantitatively in Chapters 5 and 6, respectively. Based on the non-uniformity of the maximum shear stress distribution profiles across this hopper width and the non-vertical direction of the major principal stress outside the central zone of this hopper geometry, the flow behaviour inside this geometry thought to be in funnel flow trend and subdivided into three main flow zones, as illustrated in Figure 4.12.

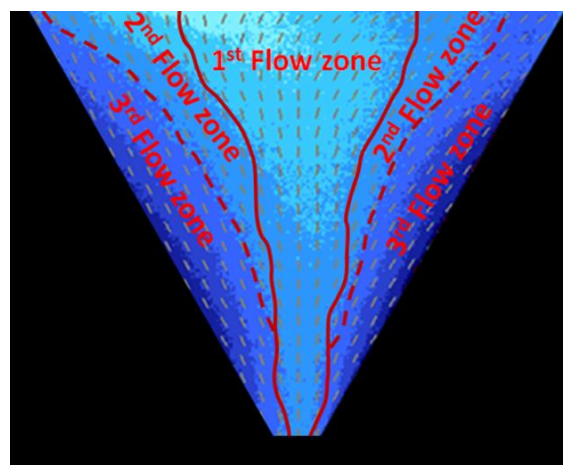


**Figure 4.12** Potential flow zones according to the stress magnitudes and the directions of the major principal stresses inside 60° internal angle hopper geometry

This subdivision is based on the stress magnitudes as well as the directions of the major principal stress within each zone. The first zone starts directly above the hopper outlet region and expands upward to reach the outer layer of the granular material and does not reach the hopper boundaries at any region. The second zone comes next where the stress magnitude is higher than that observed at the first zone and the direction of major principal stress is inclined. This zone started at around ( $H/4$ ) and expanded vertically to reach the outer granular layer in a position close to the hopper boundaries. This zone almost enveloped the first flow zone. According to these findings, this zone will flow next to the first zone. Simultaneous flow at the borders of both zones are expected (Nedderman, 1992). The third zone involves the remaining hopper geometry, especially those close to the boundaries. The third zone is the highest stressed zone of this geometry and the direction of the major principal stress is totally inclined, parallel to the hopper wall. Those closest to the wall are the more inclined in direction and expected to be the last flowing zone, and granular stagnation during the dynamic flow process is expected.

#### 4.3.3 Hopper Geometry Having a 90° Internal Angle

The PSAT results of the maximum shear stress profile distribution and the major principal stress directions within 90° internal angle hopper geometries are illustrated in Figure 4.13.

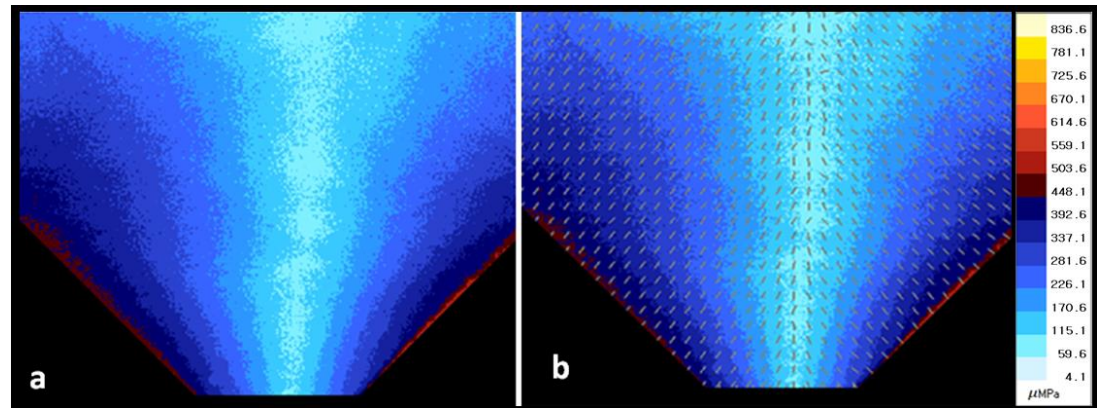


**Figure 4.13** Experimental 2D PSAT setup results: (a) maximum shear stress profiles distributions, and (b) major principal stress direction inside stress responsive granules at 90° internal angle hopper geometry

The calibrated image of the maximum shear stress distribution profile shows generally lower magnitudes than the 30° hopper and an almost similar distribution

trend to that obtained in the case of the 60° internal angle hopper geometry. The central axis of the hopper shows a relatively low stressed zone compared to the surrounding boundaries. This low stressed zone appears as the very light blue region in the central axis of the hopper, compared to the dark blue fringe colours and few red fringes at the hopper boundaries, as shown in Figure 4.13 (a). The low stressed zone is located exactly above the hopper outlet and propagates upward to the outer layer of the stress responsive granules. Opposite to what has been reported in the case of the 60° internal angle hopper, this zone is less in both magnitude and dimension. Outside the central zone, the fringes are generally in the blue fringe and minor high stressed zones in the red fringe were reported at the boundaries.

In general, the low stressed central zone splits the 90° internal angle hopper geometry into two identical stressed regions located on its right and left sides. Both hopper boundaries' sides showed relatively high stressed zones compared to the central axis, and the closer to the boundaries is the more stressed zone. All stress profiles inside the hopper are in a clear V shape beginning at the hopper base and extend to the outer granular layer. The direction of the major principal stress within the hopper geometry shows an almost vertical direction in the narrow central low stressed zone. Outside the central zone, the direction is diverted perpendicularly toward the hopper walls, as illustrated in Figure 4.13(b).

Similar to the previous hopper geometries, the maximum shear stress distributions and magnitudes across the three different hopper heights, H $\infty$ , H/4 and H/2 were analysed and the result is shown in Figure 4.14. The results show clearly that the stress ratio at the wall side to the central axis is very high compared to the previous two hopper angles at all three heights. At the hopper central axis, the normalised stress magnitudes were very close to zero at all three heights, as visibly illustrated in Figure 4.14. It is clear that maximum shear stress distribution within this hopper geometry is strongly non-homogenous across all three heights. Moreover, the non-homogenous stress distribution inside this hopper geometry is the highest case compared to the previous two geometries. In general, the stress magnitudes at all three heights are very close to each and the distribution profiles overlap at many points. The plot clearly shows a very high difference in the stress magnitude between the hopper central zone and the boundaries.

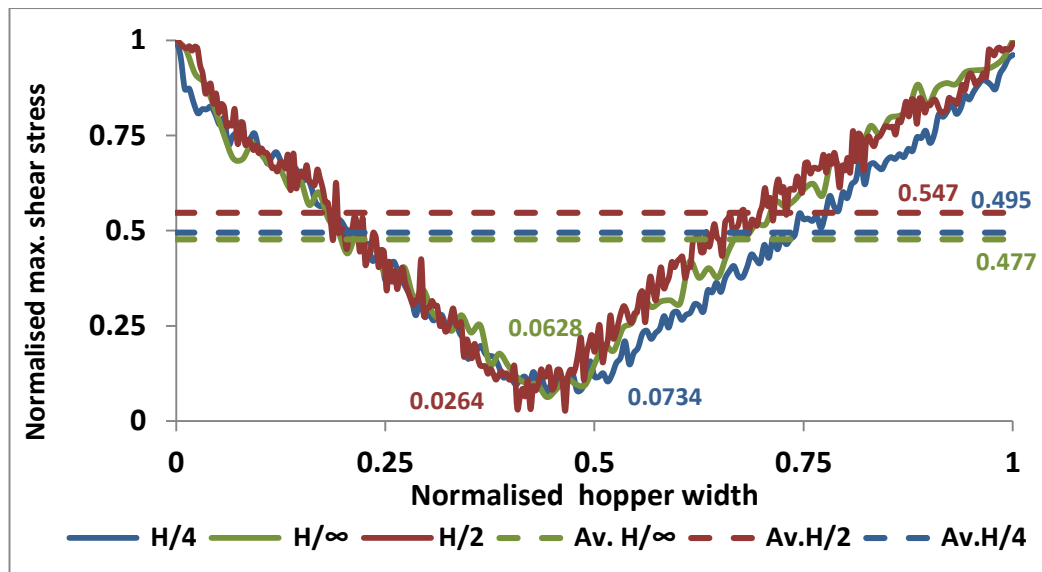


**Figure 4.14** Normalised maximum shear stress profiles distribution and its average values inside 90° internal angle hopper at multiple heights; H/∞, H/4 and H/2

The average normalised maximum shear stress across the entire three heights was calculated and the average values are 0.477, 0.495 and 0.547 at H/∞, H/4 and H/2 respectively, as shown in Figure 4.14. Opposite to what has been reported in the previous two hopper geometries, the middle hopper segment at H/2 shows a higher average normalised stress than that at H/4 and H/∞, which indicates a strong non-homogeneous distribution of the maximum shear stress profiles inside this hopper geometry.

The minimum normalised shear stress values at the three heights are 0.0628, 0.0743 and 0.0264 at H/∞, H/4 and H/2 respectively. The relative stresses at the hopper central zone to that obtained at the hopper boundaries at H/∞, H/4 and H/2 is less by 93.72%, 92.57% and 97.36% respectively as shown in Table 4.3. The stress ratio analysis was repeated using the average maximum shear stress values at the boundaries and central region. The average values of the normalised stress at the central axis and the boundaries at H/∞, H/4 and H/2 are 0.103, 0.0902, 0.074 and 0.931, 0.913, 0.982 respectively. The average relative normalised stresses at the hopper central zone compared to that obtained at the boundaries at H/∞, H/4 and H/2 are less by 88.94%, 90.12% and 92.46% respectively, as shown in Table 4.3.

**Table 4.3** Normalised maximum shear stress findings and comparisons inside the 90° internal angle hopper geometry

	H/ $\infty$	H/4	H/2
Minimum normalised ( $\tau_{max}$ ) At (CZ)	0.0628	0.0743	0.0264
Normalised ( $\tau_{max}$ ) At (HB)	1	1	1
Stress Ratio (CZ) < (HB)	93.72%	92.57%	97.36%
Average normalised ( $\tau_{max}$ ) across the bed	0.477	0.495	0.547
Average normalised ( $\tau_{max}$ ) at (CZ)	0.103	0.0902	0.074
Average normalised ( $\tau_{max}$ ) at (HB)	0.913	0.931	0.978
Average stress ratio (CZ)<(HB)	88.72%	90.31%	92.46%
* (CZ) is Hopper central zone			
*(HB) is Hopper boundary			

Although single stressed point calculation shows lower stress ratio at H/4 compared to that at H/ $\infty$ , the calculations using the average stress values of five points at the central region and boundaries show that the H/ $\infty$  level is less stressed than the H/4 and H/2 levels. The previous calculations show a complex strong non-homogenous stress distribution within this hopper geometry and the high stress deviation between the hopper central zone and its corresponding boundaries

The shear stress exerted by granular material on the hopper wall at the end of the filling process was evaluated using the slice method. The results indicate that the maximum shear stress value is reported at the level of Layer 4 and is similar to what has been reported in case of the 60° hopper geometry as seen in Figure 4.15.

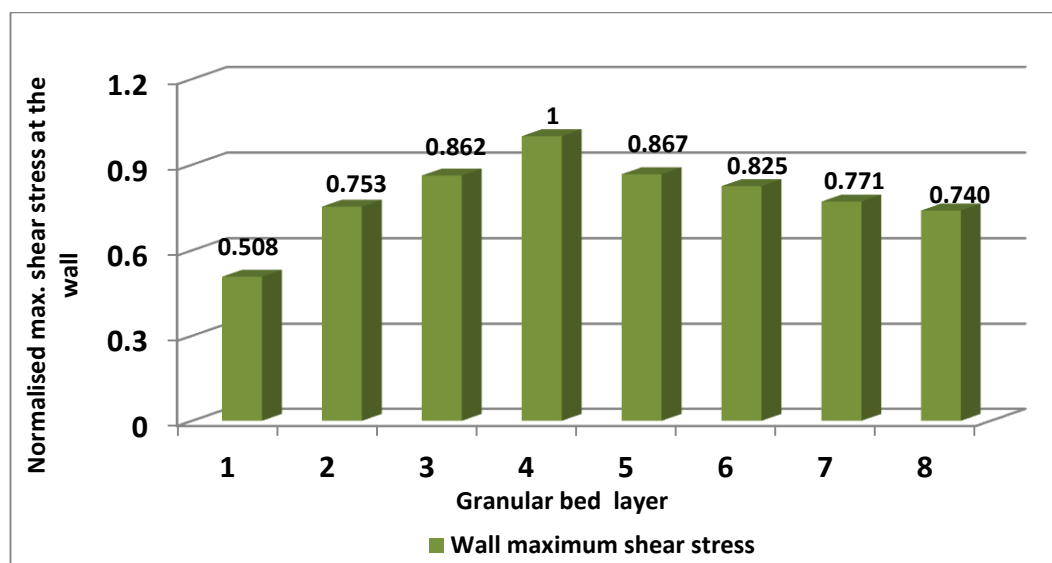


**Figure 4.15** Normalised maximum shear stress exerted on the hopper wall at the end of the filling process inside 90° hopper geometry

Generally, the previously obtained microscale analysis showed clearly that the maximum shear stress profile distribution is strongly non-homogeneous across the granular bed at all three heights and such characteristics could potentially influence the macroscale behaviour. High stress deviation between the hopper central axis and the walls at all three heights would increase the incidence of the generation of narrow plug flow at hopper central axis and, as well stagnant granular zones close to the boundaries at all heights. All the previous analyses are supported by the direction of the major principal stress inside the hopper geometry. The low stressed central zone of the hopper is characterised by an almost vertical direction of major principal stress indicating initial flow at the central region. The perpendicular direction of the major principal stress outside the central zone is supporting the anticipation of stagnant zone formation at hopper boundaries.

Based on the previous analysis of the maximum shear stress distribution profiles and direction of major principal stress, the flow behaviour inside this geometry thought to be in funnel flow trend and subdivided to three main flow zones as illustrated in Figure 4.16. The first zone is a very narrow zone, starting directly above the hopper outlet region and propagating upward to reach the outer layer of the granular materials. This zone is very narrow compared to that obtained in the case of the 60° internal angle hopper geometry. The direction of major principal stress in this zone is almost vertical. The second zone comes next to the first zone where the stress magnitudes are higher than that at the central zone and the direction of major principal stress is perpendicular to the hopper walls. This zone starts close to the outlet region and expands vertically to reach the outer granular layer close to the hopper boundaries. According to these analyses, this zone will flow next to the first zone and the stagnation tendency is high. The third zone involves the remaining part of the hopper geometry outside the previous two regions. The stress values in this zone are the highest within the hopper geometry and the major principal stress directions are totally perpendicular to the hopper walls. Accordingly, this zone will be the last flowing zone and will show more stagnation tendency during the flow process. It is expected that granular material close to the hopper walls show sliding on the hopper wall at a late flow stage due to high stress magnitudes close to the boundaries. The previous anticipated macroscopic behaviours will be analysed

qualitatively and quantitatively using CCT and DPIV in Chapters 5 and 6, respectively.

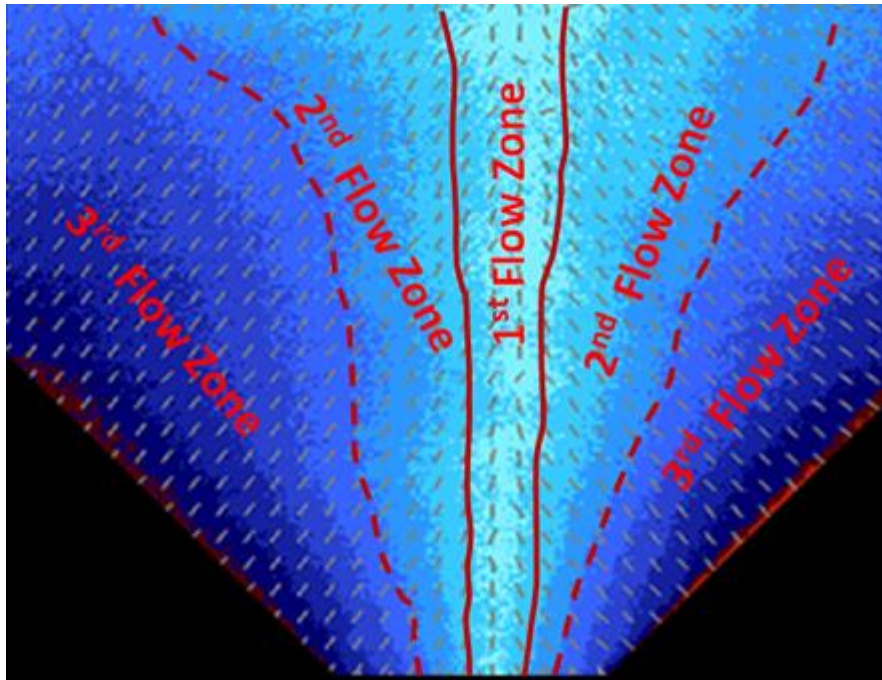


**Figure 4.16** Expected flow zones according to the stress magnitudes and the directions of the major principal stresses inside 90° internal angle hopper geometry

#### 4.3.4 General Remarks for the Experimental Results and Numerical Validation of the Stress Profiles Distribution.

The quantitative analysis of maximum shear stress distribution across the hopper width at three different levels,  $H/\infty$ ,  $H/4$  and  $H/2$ , was able to provide a clear indication about the influence of hopper geometry on the nature of the distribution. Further analysis was conducted at each level for all three geometries separately as illustrated in Figure 4.17. The graphs are in polynomial plot 2<sup>nd</sup> order to smooth the plot and show clearly the stress distribution differences and ( $R^2$ ) was in range of 0.8028 to 0.9479 in all cases.

At the 30° hopper geometry and across all hopper levels,  $H/\infty$ ,  $H/4$  and  $H/2$ , the normalised maximum shear stress profiles show more homogeneous distribution than those reported in the 60° and 90° hopper geometries at the same height and

stress deviations toward the hopper walls are minor. These were confirmed by low values of stress ratio at the hopper walls to the central region at all heights.

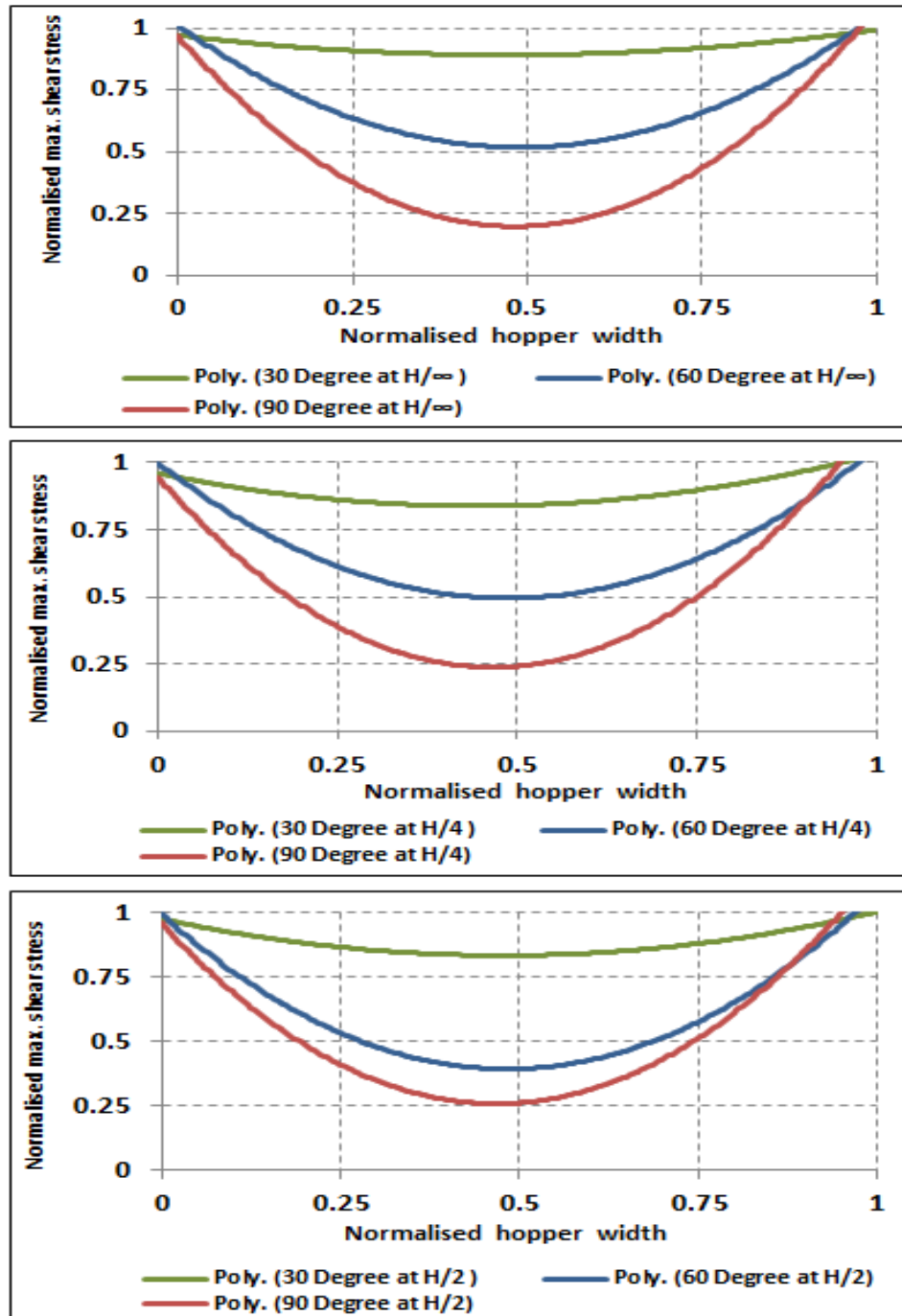


**Figure 4.17** Normalised magnitude of maximum shear stress distribution across the width of the hopper at  $H/\infty$ ,  $H/4$  and  $H/2$  within the selected hopper geometries

On the other hand, hopper geometry having a  $60^\circ$  internal angle shows obvious non-homogenous stress distribution across all hopper heights. The extent of non-

homogeneity at all heights is less than that reported in the cases of the 90° hopper geometry and more than the 30° hopper geometry. In such hopper geometry the stress is deviated toward the hopper wall outside the central hopper region and could increase the chance of granular stagnation.

Finally, hopper geometry having a 90° internal angle shows the strongest non-homogeneity stress distribution at all heights. The stress deviation to the wall is the maximum among all hopper geometries. It is very clear through the plots, that the stress magnitudes at the central axis of such hopper geometries are the lowest among all hopper geometries at all selected heights.

Further validation of the PSAT experimental maximum shear stress distribution results was conducted using the DEM and reported in a joint publication in collaboration with the research group colleague (Albaraki et al., 2013). DEM has been applied here, as it is a strongly recommended method for studying the mechanical behaviour of particulate assemblies and assessment of microscopic features (Cundall and Strack, 1980, Cleary and Sawley, 2002, Antony, 2007, Kozicki and Tejchman, 2011). The contact model used in this study is the linear contact model and it is defined by the normal and shear stiffness (force/displacement) of the two contacting units (particle-to-particle or particle-to-wall). The linear contact model has been extensively adopted in DEM numerical applications especially for dry granular material assemblies. Maximum shear stress distribution within conical hopper geometries identical to the case of PSAT experiments is obtained using PFC3D. The particle-scale properties used are shown in Table 4.4, and the hopper width ( $d$ ) = 0.005m, as illustrated in Figure 4.18.

**Table 4.4** Properties of particles used in DEM simulations

Parameter	Value	Parameter	Value
Gravity (m/s <sup>2</sup> )	9.8	Particle average radius ( $\mu m$ )	650
Density (kg/m <sup>3</sup> )	708	Particle radius ratio ( $\frac{D_{max}}{D_{min}}$ )	3.3
Initial porosity	0.169	Friction coefficient	0.3
Minimum radius ( $\mu m$ )	300	Stiffness (N/m)	1e7

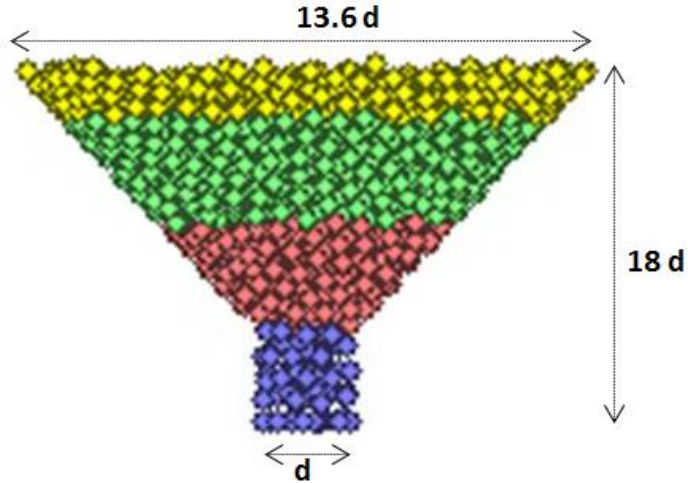


**Figure 4.18** Cross section of the hopper (schematic) and the confinement of particles

The simulations were performed for all cases of hopper angles ( $30^\circ$ ,  $60^\circ$  and  $90^\circ$ ) as in the case of the experiment reported earlier. The density value used here is the value of the envelope density, not the true density. Granular samples are created randomly and consistently in all the runs. The benchmarking of the results was conducted at height ( $H/2$ ). The created spherical particles were allowed to reach equilibrium after which the maximum shear stress was tracked along different scanning points at the selected height and the result is presented in Figure 4.19. The obtained DEM based results were compared with experimental results obtained from PSAT for all hopper geometries,  $30^\circ$ ,  $60^\circ$  and  $90^\circ$  internal angles. The simulation results are illustrated in Figure 4.19 with the experimental results. They show that normalised shear stress is higher along the hopper boundaries and tends to decrease towards the central region of the hopper for all hopper geometries. High shear stress magnitudes are reported in hoppers having smaller internal angles across the horizontal section of the granular material bed.

This trend of shear stress distribution across the granular material bed obtained from DEM is similar to what was obtained using PSAT. The PSAT experimental data are plotted in solid lines while DEM data are plotted in dashed lines. The numerical and experimental results show a good level of agreement at this height level across all hopper geometries.

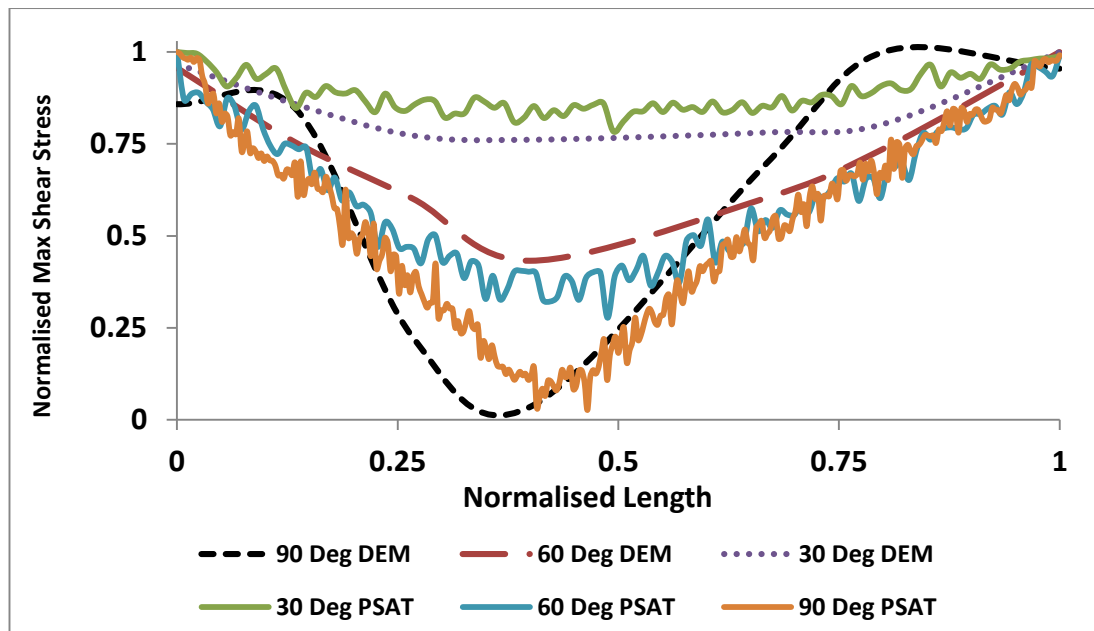


**Figure 4.19** Maximum shear stress distribution for granular bed using DEM simulation (dashed lines) and PSAT experimental work (solid lines) at H/2 across all hoppers geometries

This good level of agreement between the two methods validates the accuracy of the quantitative experimental maximum shear stress analysis results, obtained by applying PSAT at static condition.

#### 4.4 Conclusions

The maximum shear stress distribution profiles and direction are analysed using PSAT at three hopper geometries having 30°, 60° and 90° internal angles. The maximum shear stress distributions across all hopper widths were analysed at three different levels, H/ $\infty$ , H/4 and H/2. The results indicate that hopper internal angle has great influence on the magnitudes and directions of the maximum shear stress profiles that may potentially influence the flow behaviour. Accordingly, three anticipated hypotheses for granular material flow are suggested, based on the stress status findings within each hopper geometry. The hypothesis on dynamic flow characteristics of granules will be verified in subsequent Chapters 5 and 6.

The stress profile distribution shows a good level of homogeneity across the hopper width for the 30° internal angle hopper geometry across all heights. The entire

hopper geometry shows relatively high levels of stress at the bottom and middle sections and the low stressed zone at the top section of the hopper. The direction of the major principal stress inside the hopper geometry was vertical at all hopper segments. These microscopic characteristics of the granular material inside this geometry suggest that the flow hypothesis will be in mass flow trend.

The hopper having  $60^\circ$  internal angle hopper geometry shows a slightly different behaviour compared to the  $30^\circ$  hopper geometry. The maximum shear stress distribution profiles inside the hopper at all three levels show relatively high non-homogeneous distribution. The results showed a relatively low stressed central region along the axisymmetric axis of the hopper locates directly above the hopper outlet and propagates vertically to the outer layer of the granular materials. Relatively high stressed zones are reported outside this region, toward the hopper boundaries. The direction of the major principal stress inside the central zone is in a vertical to almost vertical direction. Apart from this zone, the direction inclined parallel to the hopper walls and the closer to the wall are the most inclined. According to the previous findings, the hypothesis of the flow trend inside such hopper geometry thought to be in funnel flow trend and this will be verified in Chapters 5 and 6. The flow would start at the low stressed central zones, creating axisymmetric plug flow and the boundaries will flow next to that according to the shear stress profile magnitude within each segment. The extent of stagnation at the boundaries is relatively high, especially at higher segments close to the boundaries. Lower hopper segment might show some extent of granular motion, especially at an early stage of the flow process.

The hopper having a  $90^\circ$  internal angle hopper geometry showed a very complex stress distribution trend. The maximum shear stress distribution profiles inside the hopper geometry shows a strongly non-homogeneous trend at all hopper segments and among all other hoppers geometries. The PSAT image shows very narrow low stressed zone at the axisymmetric axis of the hopper, enveloped by relatively high stressed zones expanding to the hopper boundaries. The narrow low stressed zone locates directly above the hopper outlet in the axisymmetric axis of the hopper and propagates upward to the outer layers. The extent of this region is less than that reported in the case of  $60^\circ$  internal angle hopper geometry and the direction of the

major principal stress is almost vertical. Apart of this zone, the direction is perpendicular to the hopper walls. Based on the previous analysis, the flow hypothesis inside such geometry showing this microscopic characteristic seems to be in obvious funnel flow trend. The early flow stage would take place at the location of narrow central zone, creating central plug flow. The flow of the boundaries will be next to that, based on the stress magnitudes and direction. The extent of stagnation inside this geometry might be higher than that expected in the case of 60° geometry.

The experimental PSAT results and the DEM numerical results show a good level of agreement of non-homogeneous distribution of the maximum shear stress profiles inside granular material stored in different hopper geometries. Both methods reported that smaller internal angle hopper results in a more uniform profile of maximum stress distribution and the central zone is less stressed than the boundaries.

Overall, this chapter has illustrated information on how shear stress distribution occurs inside particulates stored inside hopper geometries. Based on the static stress distribution of the filling, hypothesis of flow have been suggested on the potential dynamic flow trajectories of particulates. Indeed such strong correlations are seen in Chapter 5 and 6 of the thesis.

## **Chapter 5 Analysis of Bulk Dynamic Flow characteristics of grains inside 2D Converging Hopper Geometries Using Colour Coding Technique**

The aim of this chapter is to focus on the qualitative dynamic flow properties of grains using a simple colour coding technique. This will help to understand qualitatively the links between their stress distribution characteristics at static state as presented in Chapter 4 to the subsequent dynamic flow behaviour. The focus will be mainly on flow trajectories, tracking of the central plug flow generation and propagation, as well as the extent of stagnation within the granular bed, inside hopper geometries during the flow process. To achieve this, qualitative colour coding technique (CCT) will be applied, based on filling coloured granules in multiple layers inside hopper geometries, with each layer having a separate colour. Wet granulation technique applied to prepare coloured granules, similar to the stress responsive granules used for stress visualisation and same granules size range ( $300 - 1000 \mu m$ ) are used. Each coloured layer has a size range of ( $300 - 1000 \mu m$ ) and similar size distribution. Some of the results reported here have been presented in two conferences (Albaraki and Antony, 2013) and (Antony et al., 2014a)

### **5.1 Introduction**

Colour coding technique can be defined as a very simple, repeatable and relatively low cost qualitative visualising technique for granular material flow assessment. Such technique is able to demonstrate the characteristics of granular material behaviour under different flow, filling and compaction conditions. This technique depends on applying different colours to the fabricated granules in different particle sizes. The coloured granular material then can be used to visualise the behaviour during any particular process. A similar technique has been applied by Aole et al. (2012) for the quantitative evaluation of powder density distribution within confined die geometry as a function of process parameters (Aole et al., 2012). Application of such coloured layers method to investigate the influence of the feed shoe hopper on the die filling process makes the investigation more insightful and informative. Applying such a technique to this research project is beneficial to build a clear

understanding of the flow process of pharmaceutical excipients granules based on visual tracking of the flow trajectories and the extent of stagnation inside multiple hopper geometries. This technique was essential especially at early stage of the project when access to more advanced DPIV was limited.

## 5.2 Material and Methodology

### 5.2.1 Material

The fabricated coloured granules mentioned in Section 3.3 having a particle size ranging ( $300 - 1000 \mu\text{m}$ ) have been used to visualise and analyse the flow trajectories and extent of stagnation during the dynamic flow process. Each coloured layer has a size range of ( $300 - 1000 \mu\text{m}$ ) and similar size distribution to that used in PSAT study in Chapter 4 and the same hopper geometries having ( $30^\circ$ ,  $60^\circ$  and  $90^\circ$ ) internal angles were used. The dynamic flow process was performed under the same laboratory conditions. The hoppers dimensions were also the same as mentioned in Section 4.2.1. Characterisation of the physical and mechanical properties of fabricated coloured granules has been mentioned in Section 3.3.2.

### 5.2.2 Methodology

The experimental assessment of dynamic flow behaviour of the coloured granules have been conducted under normal gravity condition and initially packed as multiple coloured layers as illustrated in Figure 5.1.

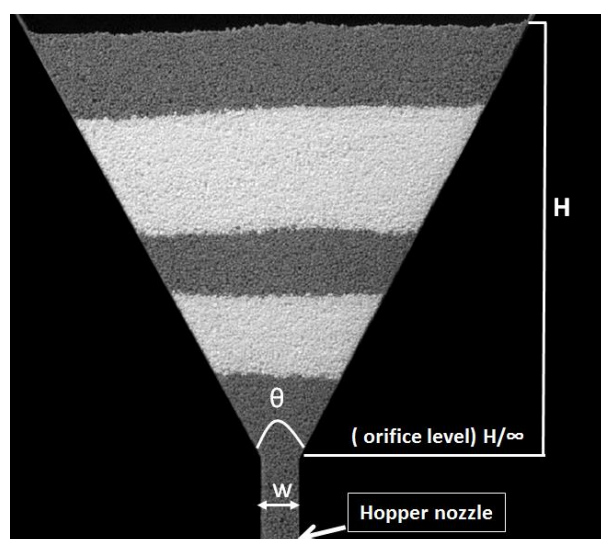


**Figure 5.1** A typical image of granular layers filled inside the hopper ( $\theta = 60^\circ$ )

Colouring in layers would simply help to track the motion of the grains without any bias. The filling process of the coloured granular materials into multiple hopper geometries was conducted similar to the case of stress responsive granules mentioned in Section 4.2.2. The fabricated hopper geometries were held between two perspex sheets and mounted on a balanced and aligned rig. Before hopper filling, the hopper nozzle was closed, using a suitable closure, which allowed the grains to be fed in layer trend. The filling process was conducted using a conical funnel, which was initially aligned along the central axis of the hopper. The funnel had a long flexible nozzle to build up granular layers and to minimise any segregation of the grains during filling and to help level the granular bed (Albaraki and Antony, 2014). Once the required height was achieved, the funnel sloped to both sides and the top surface was levelled slowly. No tools were used during this procedure to avoid any external loads that may alter the initial packing density. Similar to what has been conducted in the case of PSAT, the height of the granular bed was kept constant among all hoppers geometries at about 8 cm from the centre of the hopper outlet. To ensure the initial packing density of the granular assemblies, the mean weight of the coloured granules from the different runs was calculated, and the variations are within acceptable ranges ( $4.503 \pm 0.191$ ,  $10.471 \pm 0.247$  and  $13.386 \pm 0.209$  gm) for the  $30^\circ$ ,  $60^\circ$  and  $90^\circ$  hoppers respectively. The dynamic flow of the granular materials was recorded using a high speed digital camera (Photron fastcam viewer PFV, model SA5, the speed was 1000 frame/ second, the resolution was  $1024 \times 1024$  pixels and the maximum shutter speed is  $1\mu\text{s}$ ).

The experimental set up of the dynamic flow process assessment consists of two lamps, a high speed camera and the hopper geometry mounted on the rig as illustrated in Figure 5.2. The light sources have to be in positions to allow sufficient illumination of the coloured layered granular bed. The intensity of the emitted light contrast was optimised to obtain the high resolution for the captured images. The high speed camera shading procedure must be activated and adjusted before any recording. As the hopper outlet closure was removed, the flow of granular materials was initiated and the entire flow process was recorded until all the granules were fully discharged from the hopper. The length of the captured records can be resized to include the actual flow time and exclude the extra time intervals.



**Figure 5.2** Diagram of experimental 2D setup of the dynamic flow assessment using coloured granules and high speed camera

### 5.3 Results and Discussions

#### 5.3.1 Hopper Geometry Having a 30° Internal Angle

Early stage flow results obtained during the dynamic flow behaviour for the case of 30° internal angle hopper are illustrated in Figure 5.3

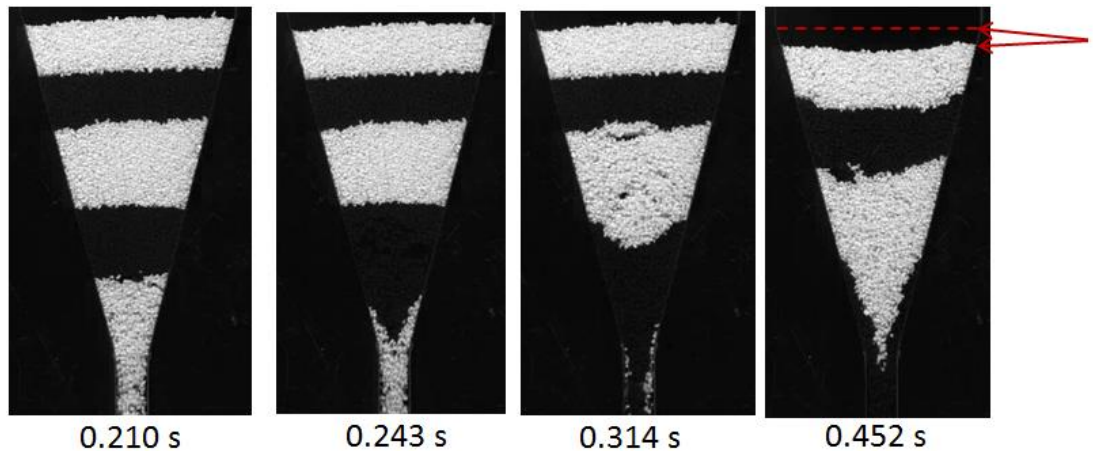


**Figure 5.3** Early stage of the dynamic flow process at 30° internal hopper angle

The images show clearly that after releasing the hopper opening at 0.210 second, the granular bed portion in the white colour, located directly above the hopper outlet, is dilated, and shows continuous motion and discharged first. This motion is experienced by the granules close to the hopper boundaries as well as those located in the central axis of the hopper geometry. According to the PSAT results reported in Section 4.3.1, this hopper segment showed a good level of homogenous stress distribution that allowed the solid bulk to flow without any hindrance. It is worth

remembering from Section 4.3.1 that initially the direction of the major principal stress for this hopper geometry was in vertical direction that helps to induce uniform, mass flow trend. The first discharged portion of the granular material dilates the granular assembly leading to dramatic lowering of the granular bed density. Further, at time 0.243 seconds and 0.314 seconds respectively, the first coloured layer of the granules were totally discharged as one layer, without generating any stagnant zone at the hopper boundaries. The upper layers within the hopper geometry continue to dilate uniformly in a consistent manner as obviously seen at the image of 0.314 seconds. At 0.452 seconds the second layer of the granules are also discharged through the outlet, and the level of all the hopper granules dropped once as one layer without producing any plug flow zone or stagnant zones. The drop of the entire granular bed inside the hopper geometry may increase the magnitude of the normal wall and shear stress inside the hopper as compensatory mechanism to fulfil the equilibrium forces in the upper layers (Bohrnsen et al., 2004).

The time intervals from 0.658 seconds to 1.528 seconds respectively are shown in Figure 5.4. The granular flow pattern from the hopper is consistently taking place, layer by layer. This flow trend has been denoted in solid bulk dynamics as “first in first out” which means the first occupied portion discharged first (Nedderman, 1992).

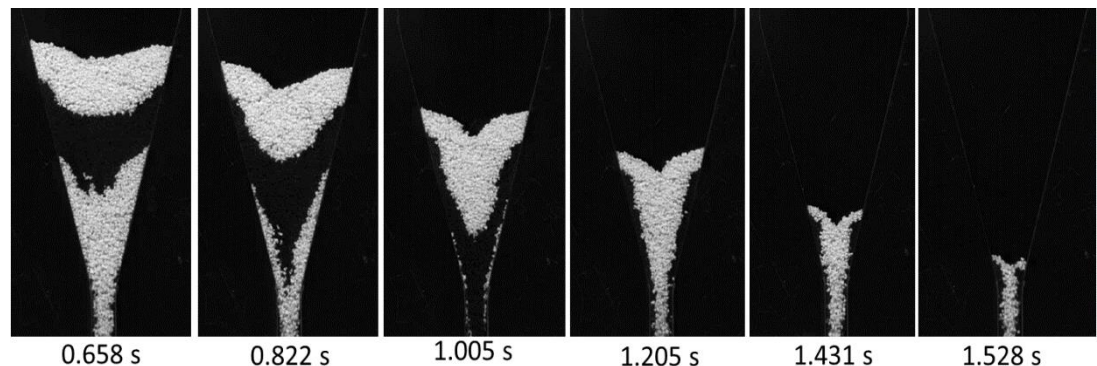


**Figure 5.4** Serial of images show the flow process at late stages of the flow process inside 30° internal angle hopper

The reduction in the bed height is proportional to the granular material discharged from the hopper and no dead or stagnant zones have been developed inside the hopper geometry. At 1.005 seconds, the granules within the hopper rearrange and

clearly become more condensed, compared to the dilated layers at an earlier time. The flow from the central axis is relatively faster than that obtained at the hopper boundaries.

All the previous qualitative observations of granular flow trend at 30° internal angle hopper are indeed clear evidences that the flow of the granules at this particular geometry is in mass flow behaviour. This behaviour is characterised by continuous particulate motions inside the hopper geometry (Castellanos et al., 1999, Holdich, 2002, Watson and Rotter, 1996). Mass flow pattern is also characterised by controlled and uniform flow trend as well as less segregation and high stress magnitude (Holdich, 2002). The nature of the flow at the end stage of the flow and the fast flow of the central axis is in agreement with the results obtained by Ulissi et al. (2009) where the maximum particle velocity is reported in the centre of the outlet region hopper.

The obtained results here are in a good level of agreement with PSAT results and anticipated flow hypothesis reported in Section 4.3.1. The granular assembly high vertical anisotropy as well as the homogenous distribution of the stress within all hopper geometry, allow the granular material to flow without any hindrance in mass flow trend along the whole hopper. These results confirm the anticipated hypothesis of the flow presented in Chapter 4 and obviously show how the initial stress packing status influences the dynamic flow trend. Further quantitative analysis of the flow behaviour at this hopper geometry using the same granular material will be presented in Chapter 6 using DPIV method.

### **5.3.2 Hopper Geometry Having a 60° Internal Angle**

The early stage of the granular material flow process is illustrated in Figure 5.5. The early stage of the flow is characterised by the generation of axisymmetric central plug flow zone. Images in Figure 5.5 track the formation and progression of this zone from early stage until 0.565 seconds, where this zone reaches the maximum height at the top layer of the bed. Once the hopper outlet is released, the first portion of the granular bed in dark colour directly above the hopper outlet starts to flow. The discharged granules in general, are those located at the central axis of the hopper and at the lower hopper section close to the outlet region.

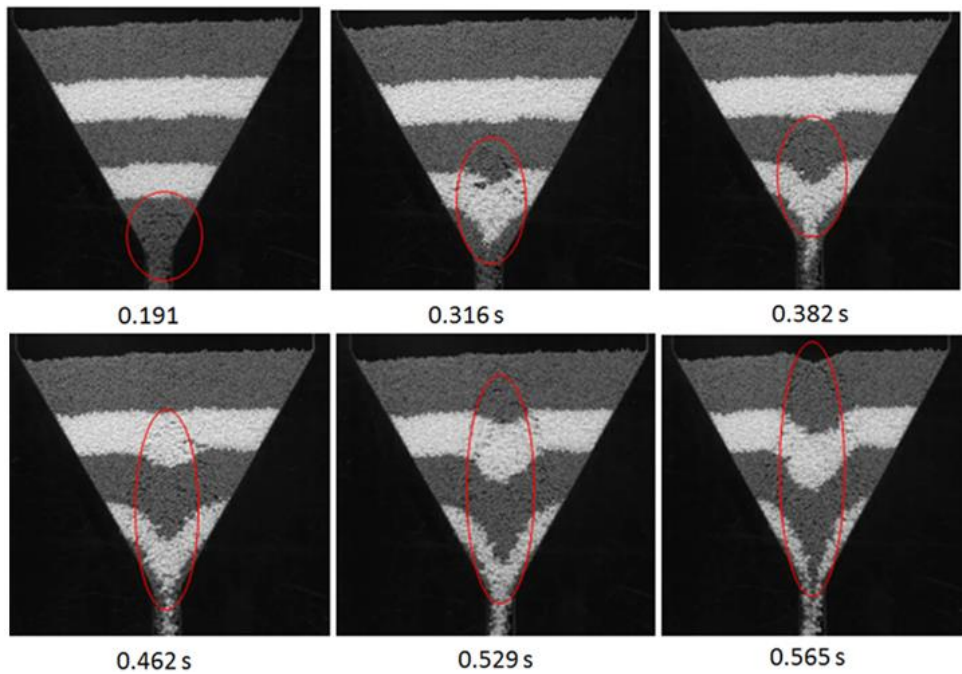


**Figure 5.5** Generation of plug flow zone (first flow zone) at  $60^\circ$  internal hopper angle at axisymmetric axis during the early stage of the flow

At 0.316 and 0.382 seconds the second layer of the granular bed starts to flow at the centre of the bed. The granules close to the hopper wall show almost no flow, compared to the region close to the plug flow zone, especially at the upper layers. Stagnation tendency at the boundaries is very obvious at these layer heights. This stage is also characterised by the appearance of a parabolic stagnant zone at the bottom section of the hopper geometry. The same flow behaviour and trend continued at 0.462 and 0.529 seconds and more obvious parabolic zones formed at the lower granular layers. At 0.565 seconds the generation of the plug flow zone is completed and reaches the top of the granular assembly. The flow zone directly starts above the hopper outlet and propagates upward to the top of the granular bed in symmetric trend that divides the hopper into two equal sides. According to the initial packing stress status analysis, reported in Section 4.3.2, this flow zone locates exactly at the central low stressed zone, showing almost vertical direction of the major principal stress, denoted as first flow zone in Figure 4.12. The parabolic zones at lower granular layers are clear, and the main flow region at this stage is performed mainly through the central zone and partially through the peripheral sides. These results are in a good level of agreement with that obtained experimentally by (Sielamowicza et al., 2006).

Further tracking of the bulk solid flow process at the second flow zone is illustrated in Figure 5.6. This figure also shows the horizontal spread of the plug flow zone toward the hopper boundaries, as well as the plug height changes during this stage of flow.

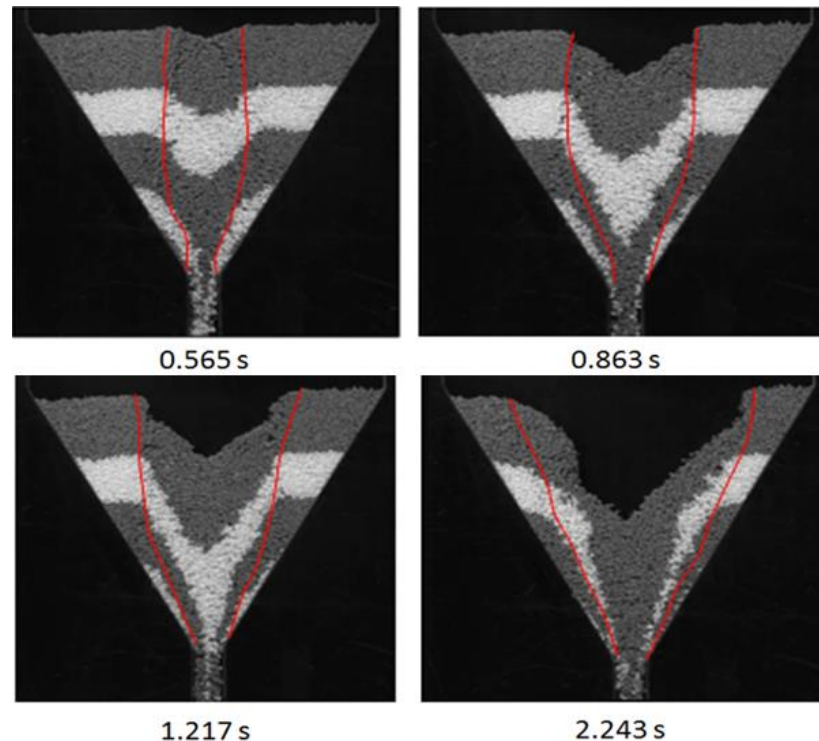


**Figure 5.6** Tracking of the expansions and changes of the flow zone (second flow zone) at 60° internal hopper angle at second stage of the flow process

Once the plug flow reaches the top of the granular bed, the first granular layer is discharged completely from the hopper and the upper layers take the clear parallelogram or parabolic shape toward the outlet direction. At higher coloured granular layers, the width of the plug flow starts to increase on both right and left sides, until it reaches the hopper boundaries at a later stage. In such cases, granular flow comes mainly from the upper layers as the flow zone width expands to reach the boundaries. The stagnant zones close to the hopper walls are now obvious through the coloured layers and the incidences of stagnation are more at higher layers. The flow zone width is increased dramatically through the granular bed, particularly at the top section. At this stage of the flow process, the flow zone doesn't reach the boundaries but very close to them. The flow mechanism at this stage of the flow is a mixture of central and radial flow trends via the central zone

and from the boundaries toward the central flow region respectively. The PSAT results showed that this zone (2<sup>nd</sup> flow zone) is more stressed than the central zone and less than the boundaries and the direction of the major principal stress in this region was inclined parallel to the boundaries as seen in Figure 4.12.

Additional tracking of the third flow zone is summarised in Figure 5.7. At this stage the central flow zone reaches the hopper boundaries and the main route of the flow is the radial flow trend from the boundaries towards the central flow region. At 4.028 seconds the bulk solid near the hopper boundaries started to flow and slide over the walls, indicating the maximum width for the central flow region. This stage is characterised by avalanche flow trend of the granular material from the boundaries towards the central flow region. The granules at the boundaries also slid over the walls in a slower motion than that flow toward the central zone. The flow boundaries between the flowable layers are showing continuous flow regions of mixed coloured granules. The end of this flow phase shows continuous motion of the remaining granules inside the hopper, and the particulates motion is a mixture of both sliding on the hopper walls and freely flowing through the central zone as seen at 4.628 second.

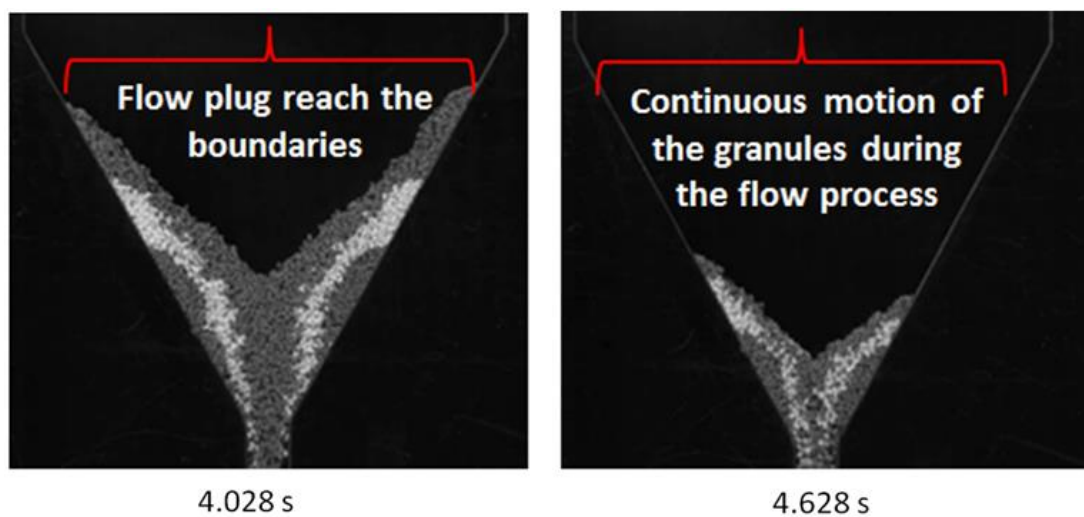


**Figure 5.7** Flow process tracking and changes of the flow zone (third flow zone) inside 60° internal hopper angle at the third stage of the flow process

The reported stress profiles distribution using PSAT at this zone (3<sup>rd</sup> flow zone), showed high shear stress profiles comparing to the 1<sup>st</sup> and 2<sup>nd</sup> zones and the

direction of the major principal stress was totally inclined parallel to the direction of the hopper wall as seen in Figure 4.12.

In general, the flow nature during this late stage of the flow is mainly through the radial flow trend. This will be quantitatively validated in Chapter 6 using DPIV technique and analysing the direction of the mean velocity vectors in these regions.

The evolution of the central plug flow height (from orifice level) against flow time at  $60^\circ$  internal hopper angles was measured, starting from the top of the granular bed downward to the outlet region and the result is illustrated in Figure 5.8.

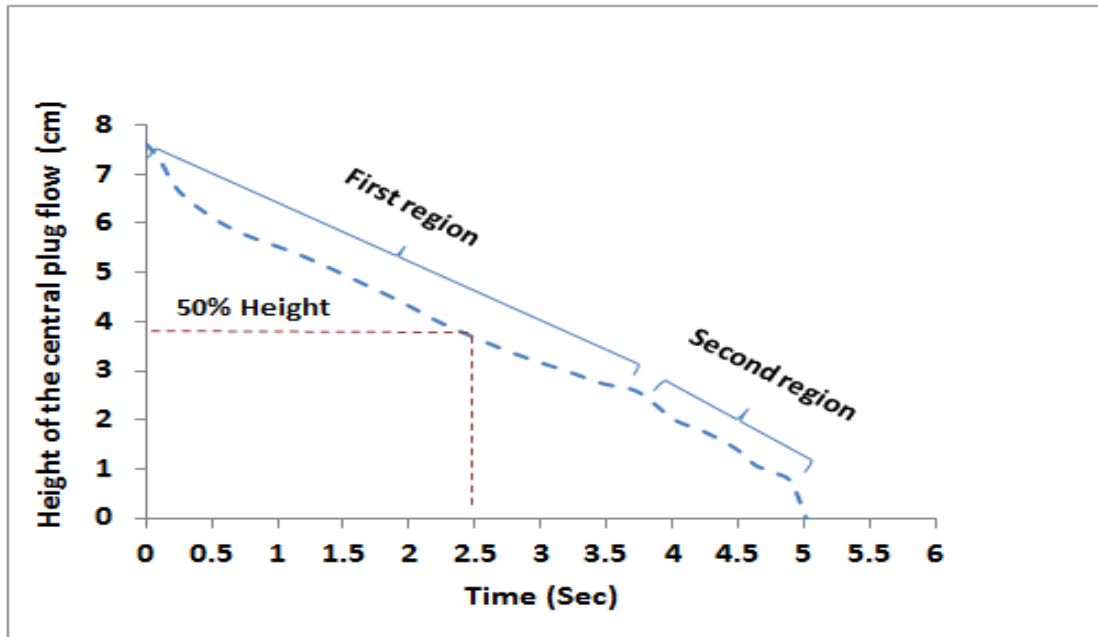


**Figure 5.8** Evolution of the of plug flow zone height measured in the symmetry axis at  $60^\circ$  internal angle hopper geometry

The changes in the central plug flow height are measured in the symmetry axis of the hopper, by measuring the changes in the height of the zone at the centre in centimetres, as a function of time in seconds. The maximum plug flow height is achieved at 0.435seconds when the central plug flow reached its maximum height propagation within the granular bed after the opening of the outlet, as seen in Figure 5.5. This time is considered as the zero time for any measurement changes.

Figure 5.8 clearly shows that the plug flow zone changes simply subdivide to two main regions. Throughout the first region, there is a dramatic decrease in the flow

zone height until around 3.7 seconds. The decreasing trend is characterised by a slightly concave line. The plug flow height reaches 50% of its original height around 2.5 seconds and the flow zone height is terminated at around 5 seconds. The measurement of the plug height at late flow stage is very difficult, as the radial flow trend dominates and no clear location was observed. At the second region of the plot, the descending extent of the plug flow height tends to be less than that observed in the first region and becomes almost linear. This could be due to the steady avalanche flow trend from the granular region close to the hopper boundaries in the plug flow zone. These results and trends of the flow zone are in general in a good level of agreement to that reported by (Sielamowicza et al., 2006) at the same hopper internal angle geometries, using amaranth seeds of higher particle size.

Tracking of the stagnant zone generations and their changes during the dynamic flow process is shown in Figure 5.9 Stagnant zones are formed at both sides of the central plug flow zone and close to the hopper boundaries.

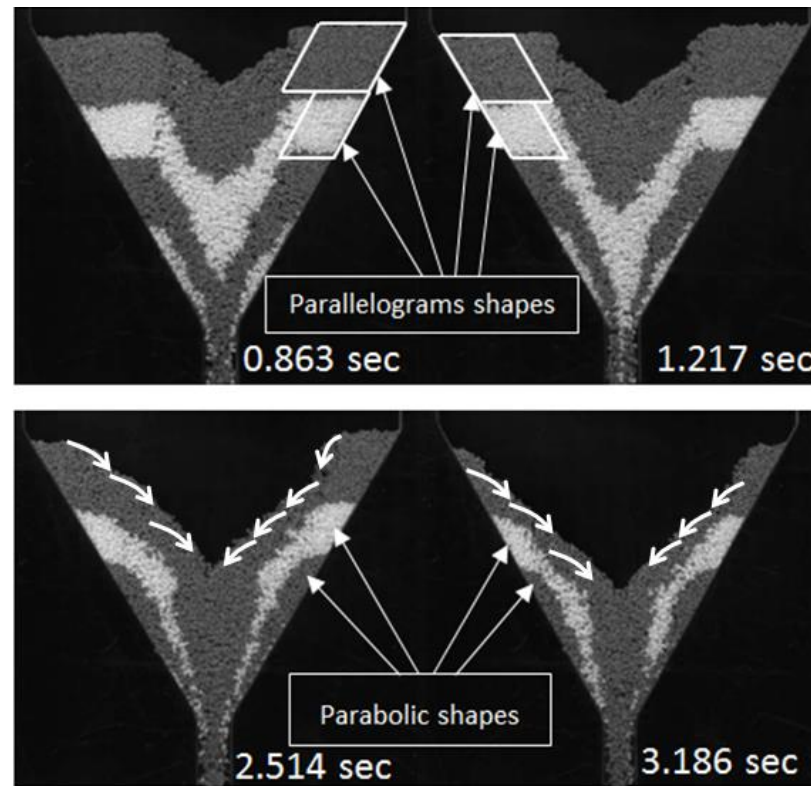


**Figure 5.9** Stagnant zones shapes at the middle and top granular layers at two stages of the flow process

These stagnant zones are mainly formed at the top and middle sections of the hopper taking two main shapes; parallelogram and parabolic shapes. The parabolic shapes

form as a result of high avalanche flow trend of the outer layers of the granules toward the flow zone during the second and third stages of the flow process.

Furthermore, graphical analysis has been conducted to measure the changes of the stagnant zone dimensions at the top and middle hopper, the results are illustrated in Figure 5.10.

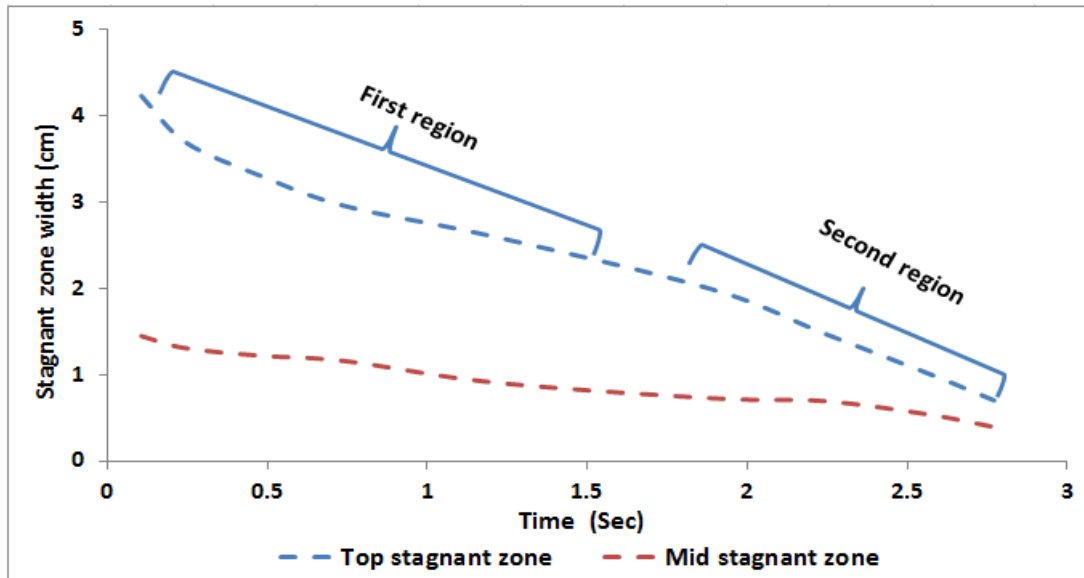


**Figure 5.10** Measurements of stagnant zone dimension changes at the top and middle of 60° internal angle hopper geometry

The changes of the stagnant zone at the top section can be divided to two regions, first and second region. At the first region, the granular bed dimensions decrease dramatically until around 1.75 seconds. This indicates a high radial flow trend at this stage from the upper layers towards the central plug flow. The second region after 1.75 seconds until the end of the process is almost linear, indicating a more uniform and stable gliding of the top layer toward the flow zone. The changes at the whole middle stagnant section dimension are more linear than that at the top section, indicating a uniform steady flow of the grains within the flow stream. At a 50% time interval, the top section dimension changed by around 43.26%, compared to 38.6% at the middle section.

In general, the obtained results here and the PSAT results for maximum shear stress distribution and direction in Section 4.3.2 and Figure 4.12 are showing good levels of agreement. The anticipated hypothesis of the flow behaviour suggesting three

flow zones are clearly proved here qualitatively using the colour coding technique, see Figure 4.12. The central plug flow generated at the early stage of the flow is located exactly at the low stressed central zone reported earlier using PSAT showing vertical direction of the major principal stress, 1<sup>st</sup> flow zone. The second flow zone, which has higher stress magnitudes than the central zone, flows second to the central zone, due to stress magnitudes and inclination of the major stress principal direction. The third flow zone is close to the hopper boundaries that have the highest stress magnitudes and the most inclined directions of the major principal stress. The stagnant zones are reported clearly inside this hopper geometry, particularly at the end stage of central plug flow propagation. The stagnation tendency is increased at the higher hopper segment boundaries. Lower hopper segments close to the outlet showed good extent of particulates motion, which could be attributed to the low stress magnitudes at this zone, as well as the direction of major principal stress toward the outlet region.

These dynamic results using CCT confirm qualitatively the anticipated hypothesis of the flow based on the initial stress packing status. Further quantitative analysis of the flow behaviour at this hopper geometry using the same granular materials will be conducted in Chapter 6 using DPIV method.

### **5.3.3 Hopper Geometry Having a 90° Internal Angle**

Based on the obtained PSAT results in Section 4.3.3 and Figure 4.16, it is expected that the central axis of the hopper will flow first based on the stress magnitudes and direction followed by the surrounding regions. This expected flow trend will create a narrow central plug flow at the central axis of the hopper due to low stress magnitudes and the vertical to almost vertical direction of the major principal stress at this region. The anticipated granular flow trend inside the 1<sup>st</sup> flow zone reported in Figure 4.16 is clearly illustrated here in Figure 5.11. The images clearly show the generation and propagation of the narrow axisymmetric central plug flow zone located at the central hopper axis. The time interval of axisymmetric flow zone generation starts immediately after opening the hopper outlet and ends by reaching the outer layer of the granular bed at 0.874 seconds. The plug flow zone locates exactly at the expected site of the first flow zone, illustrated in Figure 4.13. This

location is a relatively low stressed zone with almost vertical direction of the major principal stress.

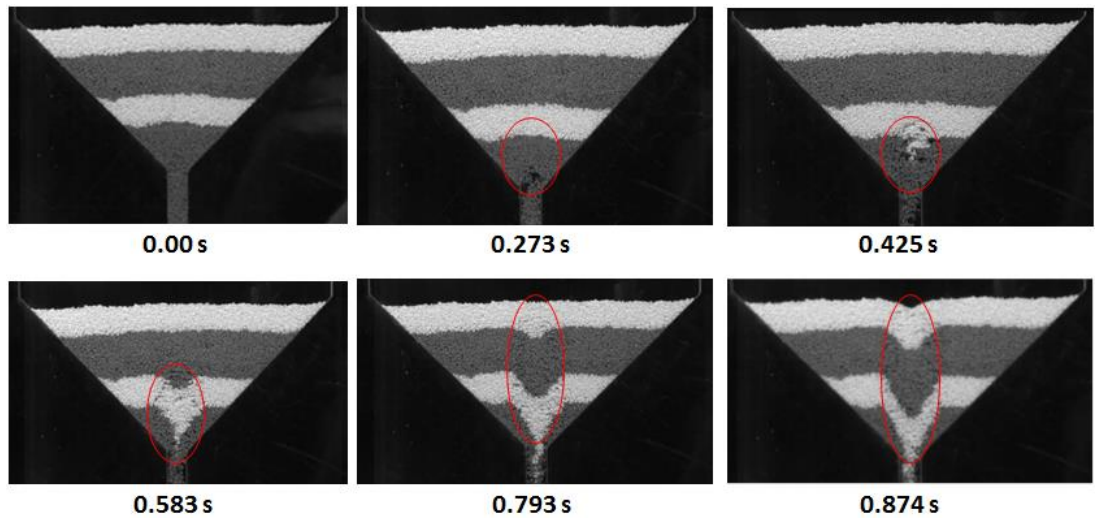


**Figure 5.11** Generation of plug flow zone (first flow zone) at  $9\text{ }0^\circ$  internal hopper angle at axisymmetric axis during the early stage of the flow

After releasing the hopper outlet, the first discharged portion is the grains at the central axis of the first granular layer located directly above the hopper outlet. The central plug flow continued to propagate upward in a vertical trend until it reached the outer granular bed layer. At 0.425 the second granular layer started to flow at the central line. Opposite to what has been observed at  $60^\circ$  hopper geometry, the granular material boundaries close to the outlet region show very limited flow and the shape of the boundaries take the parallelogram shapes. The flow at each granular layer starts exactly at the axisymmetric axis of the hopper and expands upward to the next slice. The horizontal expansion of the plug flow is much less than that reported in cases of  $60^\circ$  internal angle hopper geometry. Starting from 0.793 seconds to 0.874 seconds, it is clear that the stagnant zones shapes take the parallelogram shape at all slices levels. The extent of the central plug flow expansion is much less than that observed at  $60^\circ$  hopper geometry and this is due to the perpendicular direction of the major principal stress toward the hopper wall, compared to the parallel directions observed in cases of  $60^\circ$  hopper geometry. At 0.874 seconds the generation of the plug flow zone is optimised and reaches the top of the granular assembly. Granular bed dilation is clearly reported at this stage of the flow process

at the central zone and starts immediately at 0.273 seconds and continues until the full propagation of the central flow zone is achieved at 0.874 seconds.

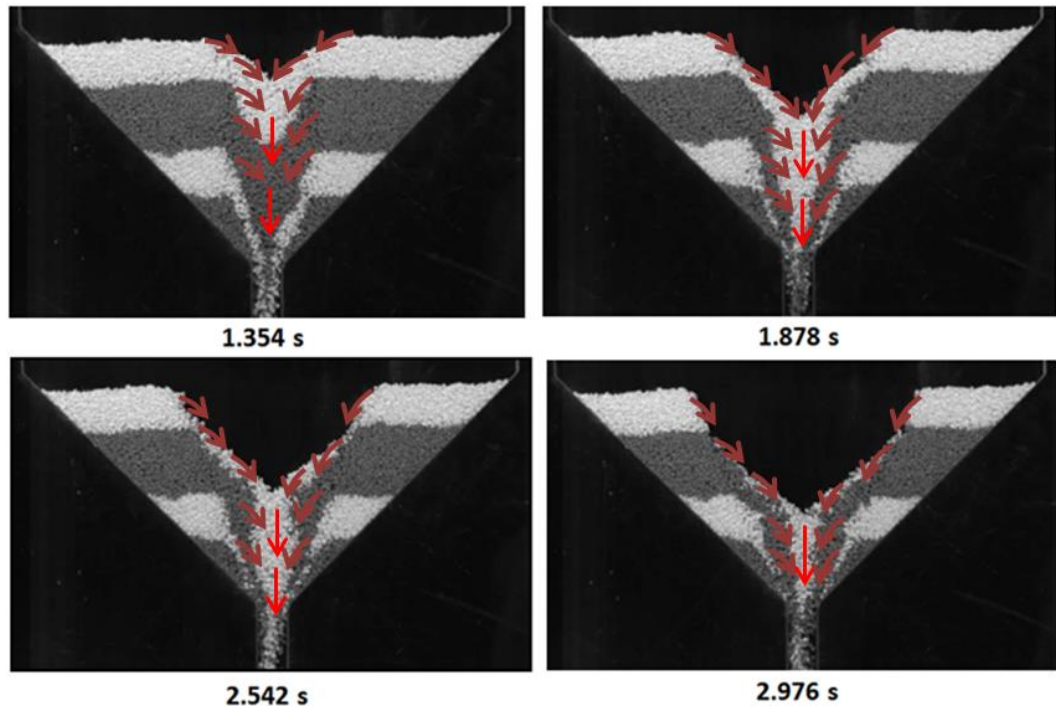


**Figure 5.12** Tracking of the expansions and changes of the flow zone (second flow zone) at 90° internal hopper angle at the second stage of the flow process

Further analysis and tracking of the dynamic flow process at the second flow zone based on stress status presented in Figure 4.16 is illustrated here in Figure 5.12. According to the stress profile magnitude and direction, this zone is the moderately stressed zone and the direction of the major stress principal is perpendicular to the direction of the hopper walls. The results in Figure 5.12 show clearly the horizontal expansion of the central flow zone toward hopper boundaries, flow trajectories through all layers, avalanche flow trend and plug height changes during this stage. Differently from what has been reported in cases of 60° internal angle hopper geometry, no whole granular layer has been fully discharged from the hopper up to the end of this stage. The shape of the stagnant zone in the boundaries is taking the parallelogram shapes across all granular layers. Above the central plug height, flow from the boundaries to the central zone takes a steady avalanche trend, while the parts below that show sliding of the granules along the flow zone boundaries. The stagnant zones are obviously reported through all layers and start directly outside the central flow zone boundaries until the hopper walls. The central flow zone

dimensions are increased dramatically at the higher layer toward the boundaries due to high radial flow tendency in an avalanche trend as shown in Figure 5.12.

In general, the flow nature at this stage is a mixture of both radial and central flow trends and stagnant zones are highly persistent. Clear granular bed shearing points are reported at all levels very close to the flow zone boundaries. At these shearing points, the granules start to flow from the stagnant zones towards the plug flow.

The analysis and tracking of the last phase of the flow process through the third flow zone based on PSAT findings at section 4.3.3 and Figure 4.16 is illustrated here in Figure 5.13. This flow zone showed the highest stress magnitudes within this hopper geometry and the direction of the major principal stress is totally perpendicular on the hopper walls. At this stage of the flow process, the central flow zone continues to spread horizontally until it reaches the hopper walls. Radial flow trend is the main route of granular flow during this phase as shown in Figure 5.13, where granular materials flow in avalanche trend from the hopper boundaries towards the central flow zone. As the particles reach the central flow zone, the flow mechanism at this plug tends to be central flow trend.

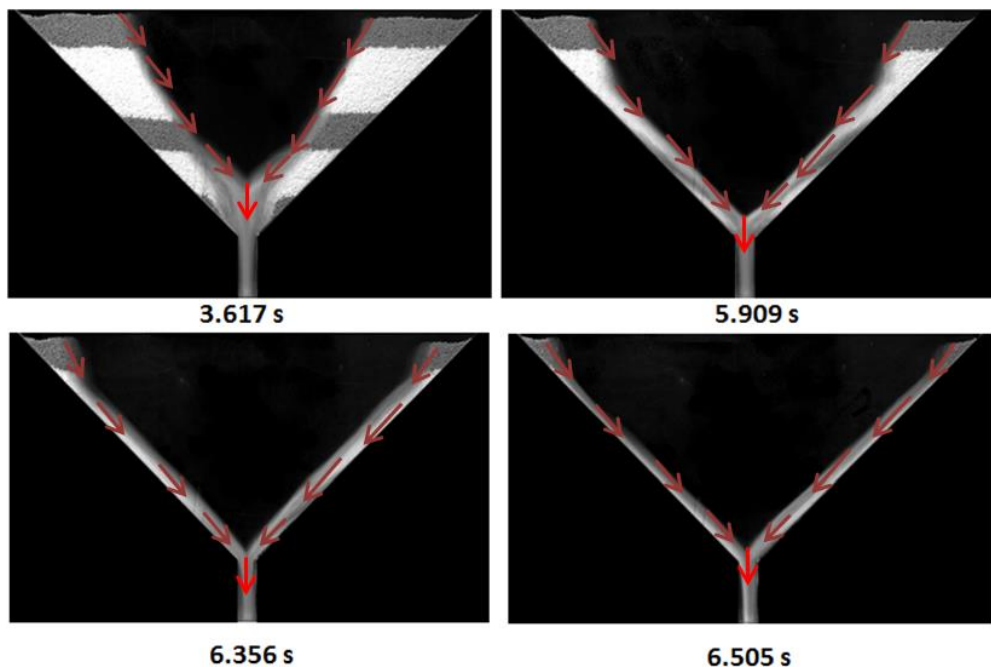


**Figure 5.13** Tracking of the expansions and changes of the flow zone (third flow zone) at 90° internal hopper angle at third stage of the flow process

The avalanche flow trend occurs through the external surface of each layer toward the plug flow zone. Increasing the angle of the plug toward the hopper walls slows the granular flow toward the flow zone. This is due to increasing the angle of sliding which negatively decreases the strength of the avalanche (Amorós et al., 2000). At 6.356 and 6.505 seconds the main flow route comes sliding through the granules on the hopper walls until the end of the flow process. Differently from what has been observed in cases of 60° hopper geometry, stagnation tendency at this geometry persists until late flow stage.

In general, this stage of the flow is characterised by domination of radial granular flow trend toward the central flow zone in an avalanche trend and stagnant zones are highly persistent.. The strength of the avalanche flow depends mainly on the sliding angle of the granules toward the central flow zone. The higher sliding angle is the slowest avalanche trend. Granular bed shearing points are clear across all layers close to the flow zone boundaries. When the central flow zone reaches the hopper boundaries, sliding mechanism becomes predominant and shearing points disappear.

Further analysis has been conducted to measure the evolution of the central plug flow height against flow time in the axisymmetric axis of the hopper. The zero time for the measurement is the time of reaching the plug flow the outer granular bed layer, the measurements are in a downward manner to the outlet region, and the result is illustrated in Figure 5.14.

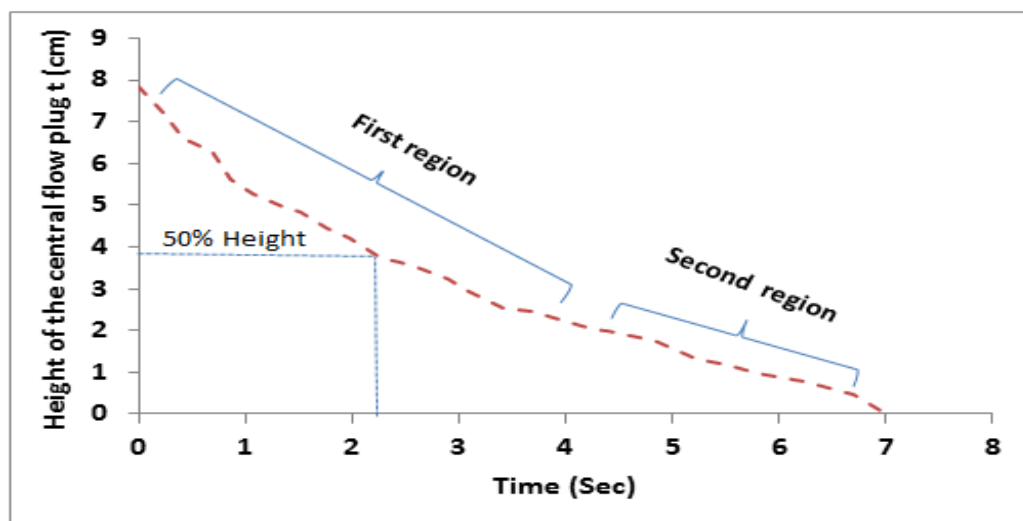


**Figure 5.14** Evolution of the height of plug flow zone measured in the symmetry axis at 90° internal angle hopper

Similar to what has been reported in cases of 60° internal angle hopper geometry, the evolution of the central plug flow is divided into two main regions. In the first region, there is a dramatic decline of the plug height up to around 4 seconds due to heavy flow of the central upper layers through the central flow zone. In the second region, the decline of the plug flow height tends to be less than that observed in the first region and becomes almost linear. This could be attributed to the steady avalanche flow from the boundaries toward the plug flow zone (Amorós et al., 2000).

At a later stage, analysis of the granular bed stagnation inside 90° internal angle hopper was conducted during the dynamic flow process. It has been noticed that the stagnation tendency inside such hopper geometry is more than that observed in cases of 60° hopper geometry and started at an early stage of the flow process and almost persisted throughout the entire flow process. The results illustrated in Figure 5.15 show the created stagnant zones during the flow stages reported in this chapter.

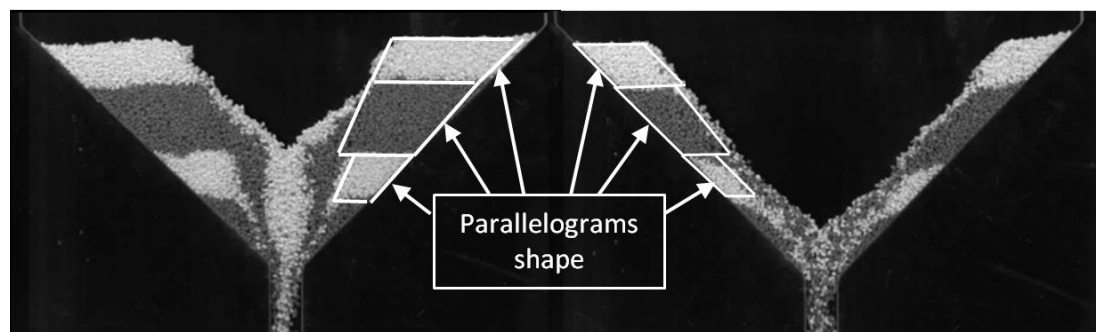


**Figure 5.15** Stagnant zones at different hopper segments inside 90° internal angle hopper geometry

Stagnant zones were formed at both sides of the central plug flow zone and diminished toward the hopper boundaries. The parallelogram shaped stagnant zones inside the granular bed layers persisted to the late stage of the flow especially at higher levels as seen in Figure 5.15. The changes of the stagnant zone dimensions in the top and middle height of the hopper were graphically analysed and the results are illustrated in Figure 5.16. The graph shows that there is a dramatic decrease in the first segment of the stagnant zone at the top section especially at early flow stage. This is due to the fact that the main flow process comes through the fast radial flow of the top layer into the central flow zone in an avalanche trend.

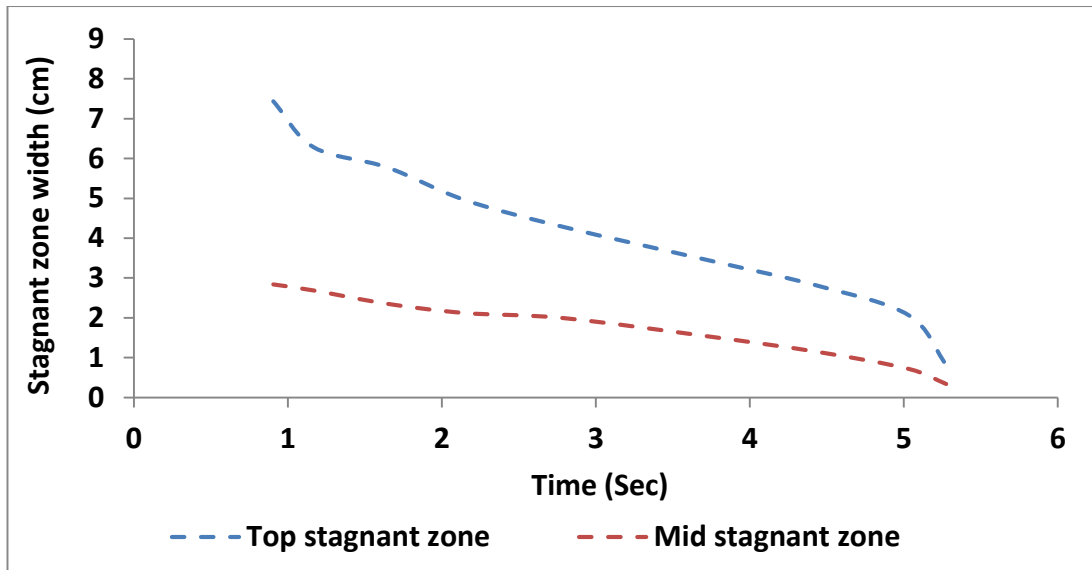


**Figure 5.16** Measurements of stagnant zone dimension changes at the top and middle of 90° internal angle hopper geometry

At this stage of the flow, the particle sliding angle towards the plug flow is low and speeds up the avalanche flow. By the time, the graph tends to be more linear until the last stage of the flow and this is due to the uniform steady gliding of the granules as an avalanche flow trend (Amorós et al., 2000).

The change at the middle stagnant section is almost linear from the early stage of the flow until the end. This is an indication of a uniform and steady flow of this region. At a 50% time interval, the top section changes is around 39.18%, compared to around 26.05% at the middle section. This indicates that the flow through the upper layer is more than that performed from middle layers.

## 5.4 Conclusions

The qualitative colour coding analysis of the granular material flow process from multiple hopper geometries is successfully applied here and showed interesting results. Hoppers having 30° internal angle hopper geometry showed mass flow trend throughout the whole flow process, and the granular material inside the hopper showed continuous motion at all hopper segments. The granular bed dilation during the flow process is clearly reported, especially at the early stage of the flow. The obtained qualitative results are in good agreement with the trends displayed by the maximum shear stress distribution results inside such hopper geometry, showing

homogeneous stress distribution and vertical direction of the major principal stress, (Section 4.3.1). No progression of any central plug flow or stagnant zones at the hopper boundaries are found inside this particulate geometry. The solid bulk granular material discharge, follow a first in first out regime and the mechanism of the flow is performed through the central flow route.

The flow behaviour in cases of  $60^\circ$  and  $90^\circ$  internal angle hopper geometries develop in more stages than those reported in cases of  $30^\circ$  internal angle hopper geometry. In general, the behaviour of the granular material flow inside both geometries was in funnel flow trend performed through three flow zones, and the granular discharge mechanism is a mixture of both radial and central flow route. The first flow zone initially performed through the propagated central plug flow zone at the axisymmetric axis of the hopper geometries and above the hopper outlet. The central plug flow spread was higher in cases of  $60^\circ$  hopper geometry than that obtained in cases of  $90^\circ$  hopper geometry. This is mainly due to relatively wide low stressed central zone, showing almost vertical direction of the major principal in cases of  $60^\circ$  hopper geometry. The second and third flow zones come next to those pertaining to the stress magnitude and direction in each zone as shown in Figure 4.12 and Figure 4.16. Granular bed stagnation inside the hopper geometries was reported in both cases but the incidences and extent were more in cases of  $90^\circ$  internal angle hopper geometry. This is attributed to the perpendicular direction of the major principal stress to the hopper walls in case of the  $90^\circ$  hopper geometry, compared to the parallel direction to hopper walls reported in cases of  $60^\circ$  hopper geometry. Generally, the obtained qualitative results for  $60^\circ$  and  $90^\circ$  hopper geometries are in good agreement with the non-homogenous maximum shear stress distribution profile and direction showing more deviation toward the hopper walls.

Though technologies for dynamic tracking of stress in granular materials is not yet available easily, the current study shows that the nature of shear stress distribution in granular materials even at static state provides many interesting information on their dynamic flow trajectories.

## **Chapter 6 Analysis of the Granular Materials Dynamic Flow trend inside 2D Converging Hopper Geometries Using Digital Particle Image Velocimetry (DPIV)**

The aim of this chapter is to explore quantitatively the influence of hoppers geometries on the dynamic flow process of granular material using digital particle image velocimetry (DPIV). The analysis based on quantitative measurement of the mean velocity vectors at different segments of the hoppers geometries. The results will emphasise and link that to the influence of initial packing stress profile distribution and direction inside hoppers geometry at static condition. The analysis focused mainly on the general flow trend, generation of central plug flow, stagnation tendency of the granular materials inside multiple hopper geometries. Multiple variable factors influencing the granular material flow process such as outlet size, bed lubrications and hopper wall roughness have been presented here for all selected hoppers geometries. Most of the results reported here have been published in the Journal of Power Technology (Albaraki and Antony 2014).

### **6.1 Introduction**

Particle image velocimetry (PIV) has been applied in research fields for spatial and temporal measurement of particle mean velocity in fluid dynamics (Adrian, 1991, Adrian, 2005). Digital image velocimetry (DPIV) is the digital equivalent method of the conventional particle image velocimetry (PIV) and laser speckle velocimetry (LSV) based on using a highly sensitive digital camera with high resolution capacity (Willert and Gharib, 1991). Analysis of the results performed computationally instead of manual data processing significantly reduce any potential PIV errors (Willert and Gharib, 1991). Recently, DPIV has been adapted for spatial and temporal analysis of solid bulk discharge from storage bunkers such as silos and hoppers, having different outlet orientations and multiple geometries (Sielamowicz et al., 2005, Sielamowicza et al., 2006, Sielamowicz et al., 2011).

The adaptive DPIV applied in this research project is non-invasive, real time, a whole-flow-field optical measurement technique. The software is able to provide mean velocity vectors of particles within the whole area of interest, as well the

vertical velocity components across the hopper width at any required level. This will help to link the trend of maximum shear stress results obtained using PSAT method reported in Chapter 4 to the DPIV results obtained here. The height of the velocity measurements are identical to those used in cases of PSAT study,  $H/\infty$ ,  $H/4$  and  $H/2$ . This will help to investigate thoroughly and quantitatively, the influence of shear stress profile distribution and major principal stress direction on the particles spatial and temporal flow behaviour and velocity gradients.

## **6.2 Material and Methodology**

### **6.2.1 Material**

Materials used in this chapter are the fabricated coloured granules described in Section 3.3, having a particle size range of 300 to 1000  $\mu\text{m}$ . Identical hopper geometries and dimensions having ( $30^\circ$ ,  $60^\circ$  and  $90^\circ$ ) internal angles were used, similar to those used in Chapter 4 and 5. Magnesium stearate powder was obtained from (Sigma Aldrich, UK) for granular bed lubrication. Sandpaper was obtained from the local market for altering hopper wall roughness. Characterisation of the physical and mechanical properties of fabricated coloured granules has been presented in Section 3.3.2. The roughness of the walls was characterised and evaluated in a mechanical engineering laboratory and the results are also presented in this Chapter.

### **6.2.2 Methodology**

Filling of coloured granular material in multiple layer style, image capturing and experimental setup are identical to those reported in details in Chapter 5 (Section 5.2.2). The dynamic flow process was performed under the same ambient laboratory conditions. The temperature was measured during the lab work and was in range 17-19°C. Similar to conditions in cases of the PSAT and colour coding method, the height of the granular material inside the hopper geometries was kept constant across all hopper geometries at about 8 cm from the centre of the hopper outlet. The bulk density of the coloured granules inside the hopper has been measured fifteen times and averaged to ensure the initial packing density of the assemblies. The mean weight was calculated and the variations are within acceptable ranges ( $4.503 \pm$

$0.191$ ,  $10.471 \pm 0.247$  and  $13.386 \pm 0.209$  gm) for the  $30^\circ$ ,  $60^\circ$  and  $90^\circ$  hoppers respectively.

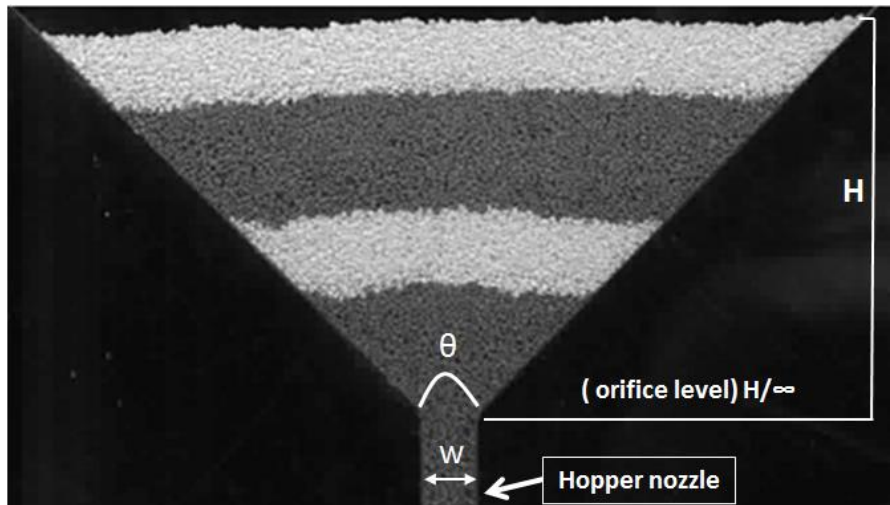


**Figure 6.1** Multiple pharmaceutical excipient granular materials layers inside the hopper ( $\theta = 90^\circ$ )

The 2D hopper experimental setup for DPIV flow process image capturing, consists mainly of multiple hopper geometries made of Perspex sheets for three cases of internal angle of hopper ( $\theta = 30^\circ$ ,  $60^\circ$  and  $90^\circ$ ) as shown in Figure 6.1. The dimensions of the hoppers used here are as follow; the height (H) is 8 cm ( $\approx 123d$ ), orifice width (w) is 7mm ( $\approx 11d$ ), nozzle length is 20mm ( $\approx 31d$ ) and the hopper thickness (perpendicular to the plane of hopper) is 4mm ( $\approx 6d$ ). Initially, the hopper internal surfaces and edges were finely polished to minimise particle wall friction. The selected hopper dimensions, which could be viewed as relatively small in some industries, are about the size of some of the hoppers used in the grain-processing sub-stations in the space industry. The selected dimensions have been verified such that ratios of the hopper dimensions to the average particle size (d) used here, are adequate to maintain continuous flow during the experiments.

The dynamic flow of the granular material was recorded, using a high speed digital camera (Photron fastcam viewer PFV, model SA5, the speed was 1000 frames per second, the resolution was 1024 x 1024 pixels and the maximum shutter speed is  $1\mu\text{s}$ ). At this high speed, the memory of the camera is able to record around 22 seconds (around 22 thousand frames). Due to this high capacity, recording events of the flow process starts immediately just before the outlet opens and continues until

the end of the flow. The recorded movies have been split into single image frames using Photron software. The software used in this study to analyse the captured digital images frame by frame is DynamicStudio software platform (DSSP). This software is an advanced imaging software platform created by Dantec Dynamics Ltd for images acquisition and processing for PIV data. An adaptive PIV application within this package has been used to import single frames, and calculates velocity vectors based on particle images. This method is an automatic and accurate adaptive method. The software imports these images for the data analysis as single frames. The non-interested areas outside the hopper geometry should be masked, to exclude any interference and noise as shown in Figure 6.2. This application iteratively adjusts the size and shape of the individual interrogation areas (IA) in order to adapt to local seeding densities and flow gradients, see Figure 6.2. The final calculated interrogation area in this study is 16x16 pixels

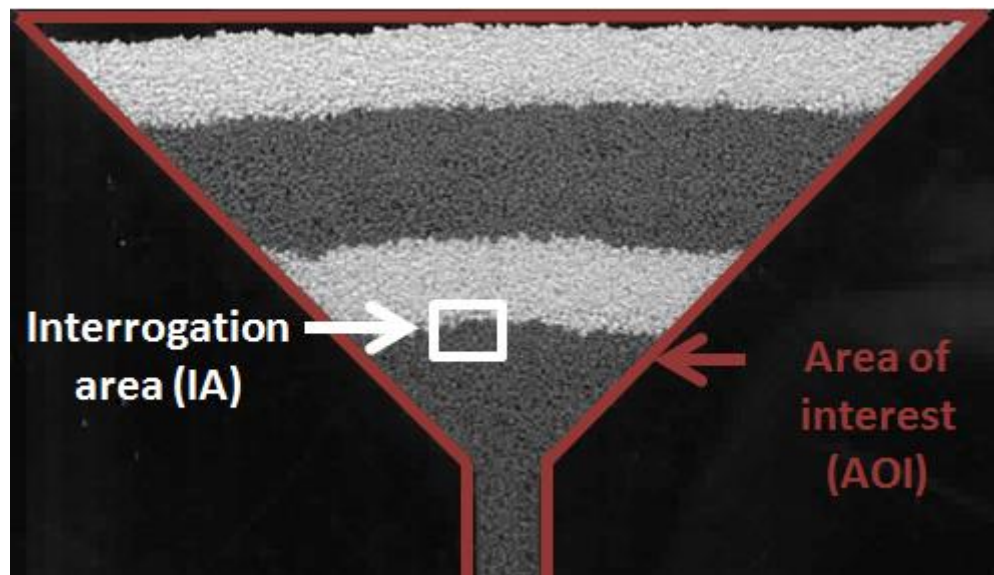


**Figure 6.2** Digital particle image velocimetry data analysis fundamentals; area of interest (AOI) and interrogation area (IA)

The illumination of the hopper geometries was optimised, using sufficient light sources to have the maximum image resolution for the captured images. A high speed camera shading procedure was calibrated to eliminate any image shadings. More details are available in Chapter 5 (Section 5.2.2). For each hopper angle, three experiments have been conducted and analysed to check the reproducibility and consistency of the DPIV results during the flow process. The variations within all hopper geometries across all height levels were in range of 0.217% to 0.871%.

## 6.3 Results and Discussion

Colouring the pharmaceutical excipient granules and filling in hoppers in multiple layers provides a good opportunity to visualise the flow trajectories and improve the image resolutions. The DPIV software applied in this experimental work, is able to measure spatial and temporal mean velocity vectors of particles in a cross-correlation style of the images. The mean velocity measurement in 2D experimental setup, is the mean of the vertical velocity component ( $v$ ) and horizontal velocity component ( $u$ ). In cases of three dimensional DPIV applications, the third velocity component is known as the perpendicular component ( $w$ ). The length of the velocity vectors is a primary indicator of the particle velocity at any location (Sielamowicz et al., 2005). Long vectors indicate high velocity value, while short ones correspond to much lower values. The colours scale of the velocity vectors map and velocity contours map are generated, according to the magnitude of the velocity at these particular areas (Ostendorf and Schwedes, 2005, Sielamowicz et al., 2005).

### 6.3.1 Hopper Geometry Having a 30° Internal Angle

The mean velocity vector map during the whole flow process is shown in Figure 6.3. In general, the direction of the mean resultant velocity vectors within the whole hopper is in a vertical or almost vertical direction. The axisymmetric axis of the hopper and its surrounding zones align dominantly along the vertical direction, while the hopper boundaries show almost vertical directions. The results show that the length and magnitude of the vertical velocity vectors are very high inside the hopper nozzle and at the orifice level of the hopper. These results are in a good level of agreement with the previous studies, obtained at the same hopper geometry using different grains (Bohrnsen et al., 2004, Ostendorf and Schwedes, 2005). The velocity vector gradient deceases in an upward direction. The highest hopper segment was the slowest layer to flow. The vertical to almost vertical direction of the mean velocity vectors during the whole flow process, is strong evidence that all granular material in all regions, are in continuous vertical motion within the entire geometry.

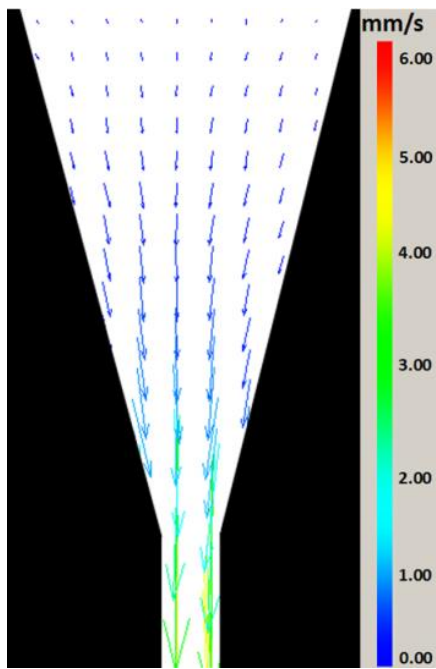


**Figure 6.3** Mean resultant velocity vectors map inside the 30° internal angle hopper geometry filled by coloured pharmaceutical excipient granules

Further analysis of the vertical velocity component within the hopper geometry during the whole dynamic flow process has been conducted across the hopper section at three different heights; ( $H/\infty$ ,  $H/4$  and  $H/2$ ). The aim of this analysis is to deeply investigate the spatial and temporal velocities of the particles inside the hopper geometry at multiple heights as well as to link that to the stress distribution profile reported earlier at the same heights (Section 4.3.1). The results of the vertical velocity component across the 30° internal angle hopper geometry at three height levels are illustrated in Figure 6.4. The results indicate that the highest vertical velocity component inside the hopper was obtained just above the hopper outlet ( $H/\infty$ ) where the maximum magnitude of the vertical component is 2.671(mm/s). The magnitudes of the vertical velocities decreased at higher levels to reach 1.748 (mm/s) and 1.056 (mm/s) at  $H/4$  and  $H/2$  respectively. The values of the vertical velocity are in negative value as the flow in the direction of the gravity and high value means high velocity magnitude. The plot is in polynomial regression 2<sup>nd</sup> order and the  $R^2$  ranges from 0.918 to 0.945. The data have been fitted to polynomial distribution, in order to smooth the shape of the plots.

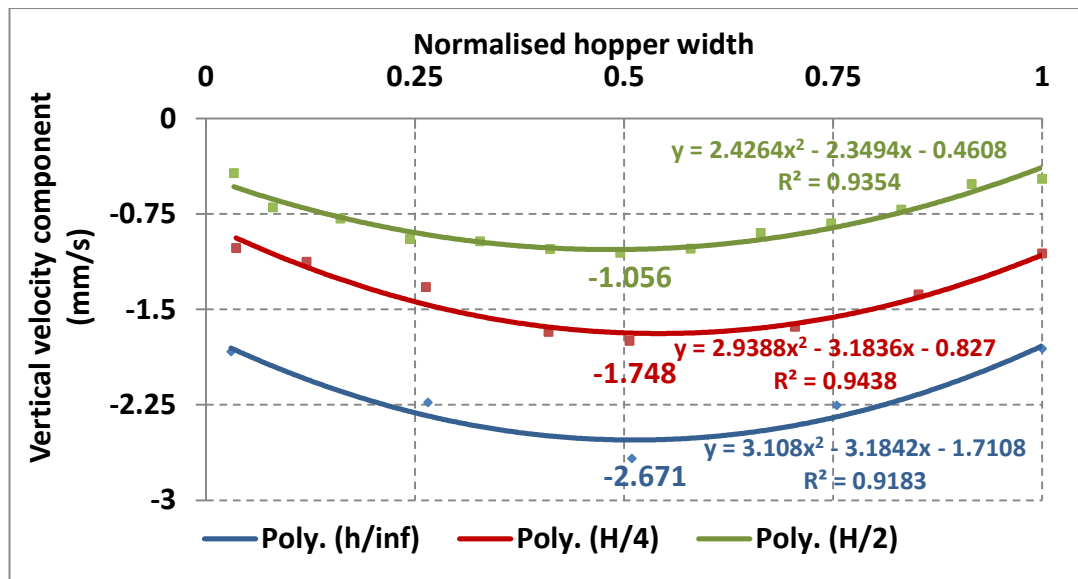


**Figure 6.4** Vertical velocity component plot inside 30° internal angle hopper geometry having a 7mm outlet size measured at three heights (H/∞, H/4 and H/2) in 2<sup>nd</sup> order polynomial plot

The percentage ratios of the maximum vertical velocity component at H/∞ to H/4 and H/2 are higher by 52.80% and 152.94% respectively. The ratios were recalculated using the mean velocity across the whole horizontal hopper section to give a more realistic comparison, and to avoid any bias in comparison, see Figure 6.5.

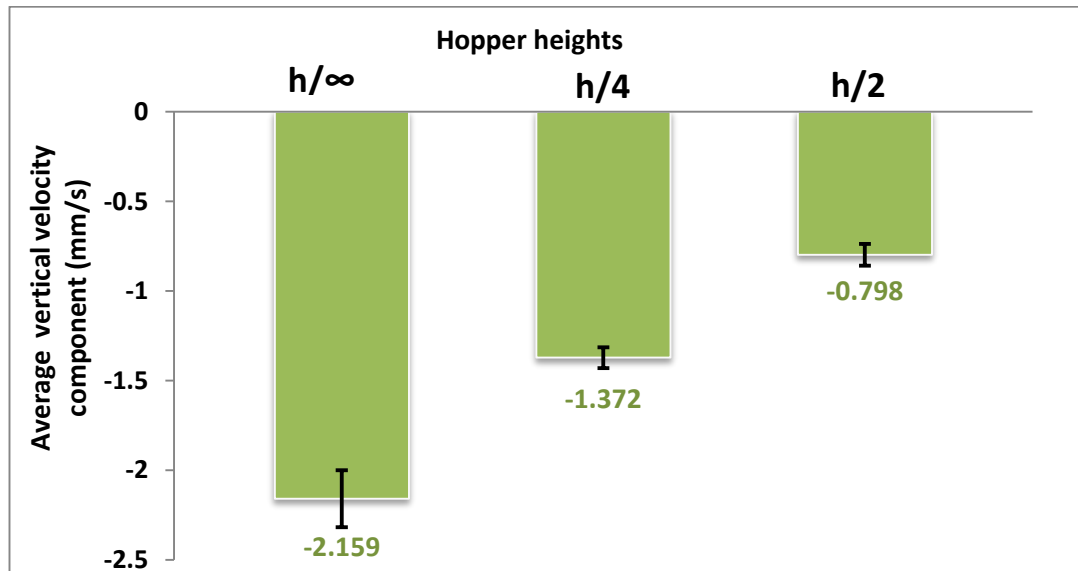


**Figure 6.5** Average vertical velocity component plot across the hopper width inside 30° internal angle hopper geometry having 7mm outlet size at three heights (H/∞, H/4 and H/2)

The average vertical velocity components across the hopper width at three heights  $H/\infty$ ,  $H/4$  and  $H/2$  are 2.159 (mm/s), 1.372 (mm/s) and 0.798 (mm/s) respectively as shown in Figure 6.5. The percentage ratios of the average vertical velocity component at  $H/\infty$  to  $H/4$  and  $H/2$  are higher by 57.36% and 170.55% respectively. At all three heights, the central axis of each height shows a higher velocity magnitude than the boundary at the same height. Similar results have been reported by Ostendorf and Schwedes (2005), using similar internal angle hopper geometry but with grains of high size. Both results illustrated in Figure 6.4 and Figure 6.5, either by using the maximum vertical velocity component or the average vertical velocity component, show that the velocity gradient is higher at the lower segment of the hopper and decreased at higher segments.

The maximum vertical velocity component values at hopper orifice ( $H/\infty$ ) through the whole flow process were tracked, and the results are illustrated in Figure 6.6.

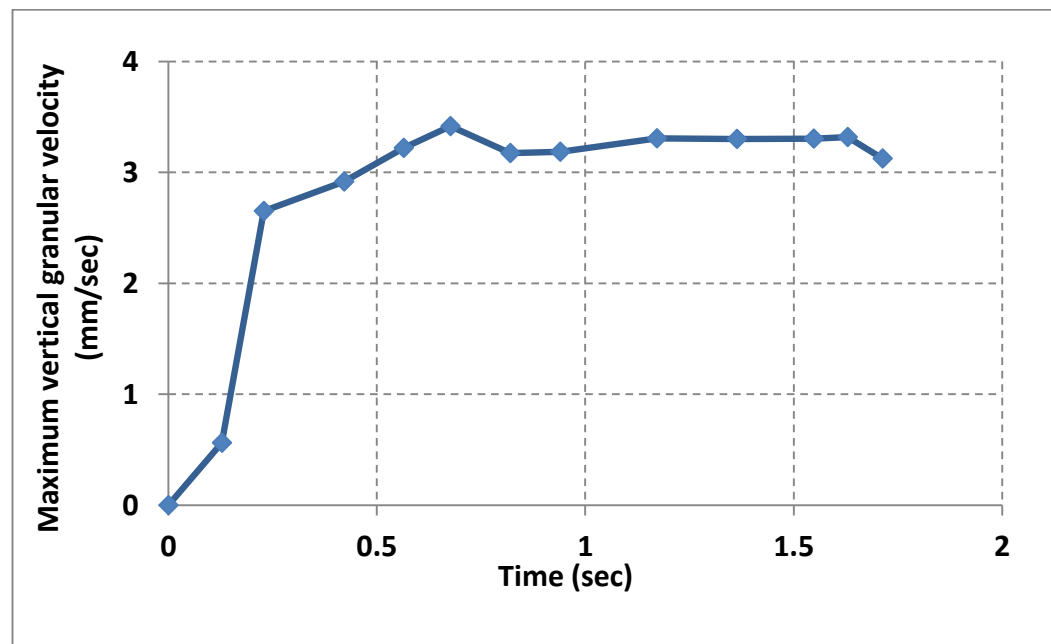


**Figure 6.6** The maximum recorded vertical velocity component values at selected time intervals during the flow process inside 30° internal angle hopper geometry

The obtained results show that the granules attain a maximum value in their vertical velocity quite rapidly, as flow begins at around 0.7 seconds and remains almost constant for the remaining duration until the flow is terminated. The onset of the vertical increases dramatically to reach (3mm/sec) within less than half a second. At

the second stage of the plot, the velocity gradient increases steadily to reach the maximum value, and then takes an almost flat trend until the flow process is terminated. Fast flow of the first granular portion close to the hopper outlet is the main reason for the granular bed dilation and high velocity gradient at early flow stage, more details are presented in Section 5.3.1.

Further analysis and cross matching of the results have been conducted using both mean velocity vectors map at multiple time intervals and its corresponding visual images, as shown in Figure 6.7. The aim of such analysis, is to identify the area of the granular bed nucleation (i.e., location of initial solid bulk dilation) and the subsequent progression of flow of the bulk solid.

The mean resultant velocity vector profiles inside 30° internal angle hopper geometry can be generally divided into two main stages; propagation phase and termination phase. The early images of the resultant velocity vectors map at 0.229 seconds and 0.317 seconds show vertical to almost vertical direction of the velocity vectors within the hopper geometry. The vectors propagate vertically in an upward direction at the centre of the hopper, as well as the boundaries. The corresponding images at these time intervals clearly show the bed dilation phenomenon at the zone, close to the hopper outlet. The magnitude of the velocity vectors at the lower hopper segment is the highest across all the segments. At 0.421 seconds, the mean velocity vectors map spread in all hopper segments and show vertical to almost vertical direction. The correspondent image at 0.421 seconds shows clearly that all grains inside hopper geometry are in continuous motion at all segments. During later stages of the flow process at 1.052 seconds, 1.205 seconds, and 1.584 seconds, images show the terminal discharge of the granular material from the hopper geometry. The general trend of the resultant velocity vectors in the termination phase is similar to that obtained in the propagation phase, but in a downward direction. The direction of the velocity vectors in the termination phase shows a vertical to almost vertical direction until the flow process totally terminated. According to the corresponding images at this stage, the bulk solid bed is denser than that reported at the earlier stage of flow characterised by bed dilation. The granules inside the hopper geometry are in continuous motion until the end of the flow process.

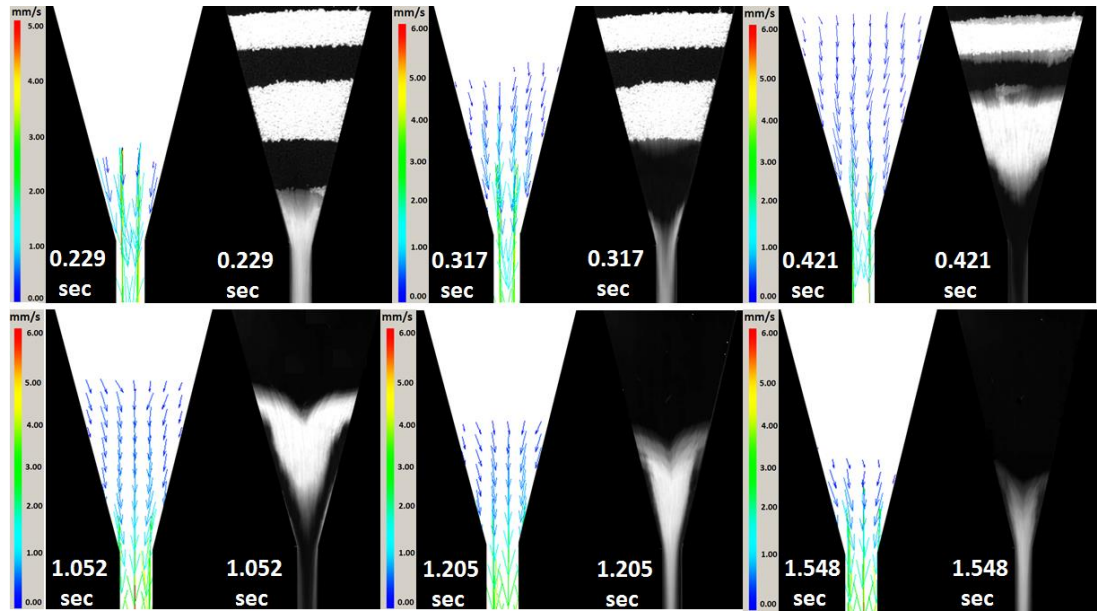


**Figure 6.7** Mean resultant velocity vectors profiles at 30° internal angle hopper during different time intervals and the corresponding visual images of the dynamic granular flow

In general, it is evident that 30° hopper geometry shows clearly velocity vectors acting dominantly along the vertical direction (direction of gravity) at all stages of the flow process. The corresponding visual images demonstrate clearly, that granular flow occurs in layers from the outlet region of the hopper – i.e., ‘first in-first out’ trend. The initial granular bed dilation at the lower hopper segment, discharges the dilated zone first and the material continued to exit in a relatively uniform manner, showing mass flow trend. This has been confirmed by adequate tracking of the reduction in the top level of the filling, where the outer layer drops as one layer. More details are available in section 5.3.1. This flow trend occurred uniformly across the width of the hopper for most time intervals of the flow process with minor exceptions just prior to the flow termination.

Dilation of the granular bed inside the hopper is common at the early stage of the flow process and crucially affects the granular bulk density and accordingly alters the wall stress (Bohrnsen et al., 2004). Applying DPIV in this research at very short time intervals and using the coloured granules, showed this dilation clearly as it is illustrated in Figure 6.7. More details are available in Chapter Five, Section 5.3.1. Referring to the PSAT results, the 30° internal angle hopper geometry showed relatively homogenous stress distribution across the three hopper heights and a

vertical to almost vertical direction for the major principal stress. These microscale findings enhance the chance of mass flow trend inside such hopper geometry. This expectation has been validated quantitatively using DPIV. The mean velocity vector maps and the corresponding images illustrated in Figure 6.7 show vertical direction for the vectors across the entire hopper geometries and continuous granular motion during the whole flow process. This means that the initial packing stress status and the internal hopper angle have great influence on the nature of the granular flow trend.

### 6.3.1.1 Evaluation of Variables Influencing Granular Flow Process Inside 30° Internal Angle Hopper Geometry

#### 6.3.1.1.1 Hopper Outlet Size

The hopper outlet size is increased from 7mm to 10 mm and the remaining experimental conditions are kept identical as the previous work. The influence of increasing hopper outlet size on the flow process and particle velocity magnitudes has been conducted and the results are illustrated in Figure 6.8.

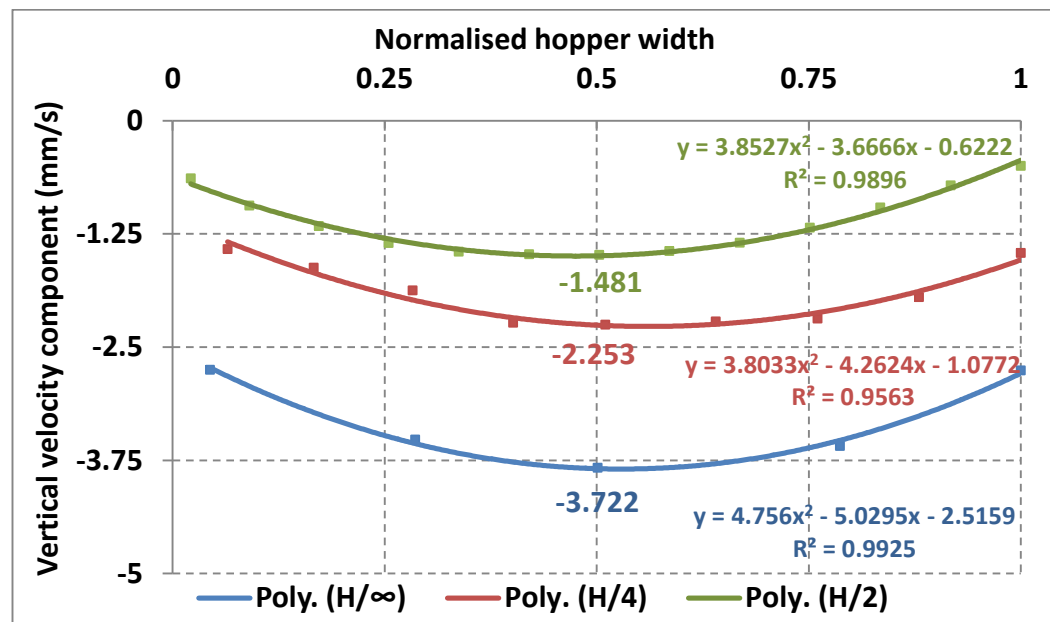


**Figure 6.8** Vertical velocity component plot inside 30° internal angle hopper geometry having 10 mm outlet size measured at three heights (H/∞, H/4 and H/2) in 2<sup>nd</sup> order polynomial plot

The maximum magnitudes of the vertical velocity components are 3.722 (mm/s), 2.253 (mm/s) and 1.481 (mm/s) at H/∞, H/4 and H/2 respectively. Similar to what

has been conducted in cases of (7mm) hopper outlet, the plot data are fitted into the 2nd polynomial plot and the  $R^2$  ranges from 0.956 to 0.993. The maximum magnitudes of the vertical velocities components in a hopper having 7mm outlet size were 2.671(mm/s), 1.748 (mm/s) and 1.056 (mm/s) at  $H/\infty$ ,  $H/4$  and  $H/2$  respectively. This indicates that increasing the outlet size from (7mm to 10 mm  $\approx 42.86\%$ ) increases the velocity magnitudes by 39.35%, 28.89% and 40.25% at  $H/\infty$ ,  $H/4$  and  $H/2$  respectively.

The previous findings have been recalculated using the average vertical velocity component across the whole section, at the three predetermined heights at both 7 and 10 mm hopper outlets and the results are illustrated in Figure 6.9.

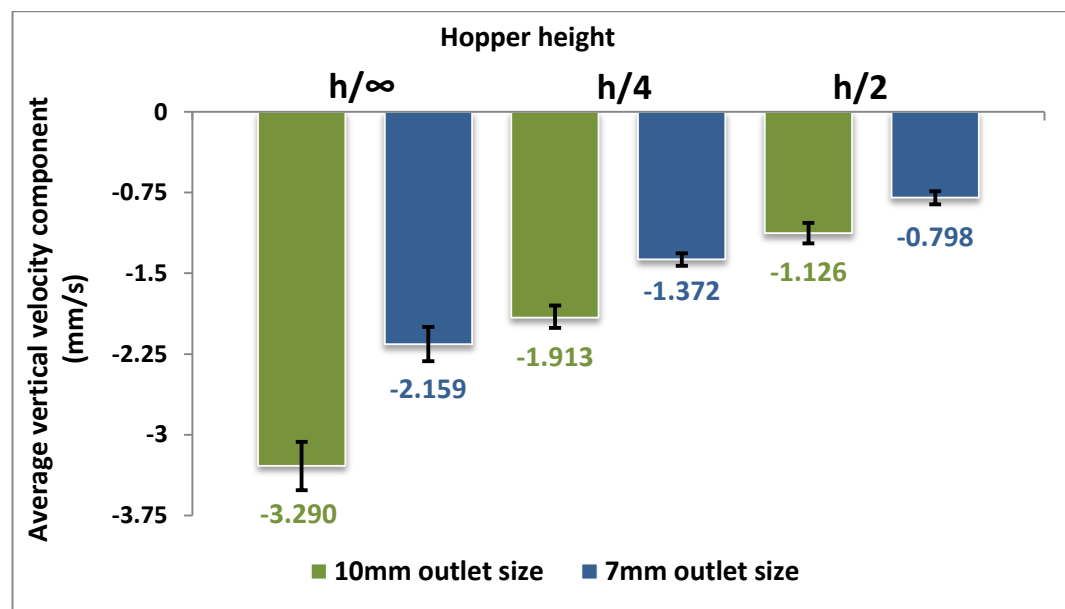


**Figure 6.9** Average vertical velocity component plot across the hopper width inside 30° internal angle hopper geometry at 7 mm and at 10mm outlet sizes at three heights ( $H/\infty$ ,  $H/4$  and  $H/2$ )

The results in Figure 6.9 show clearly that the average vertical velocity components in cases of 10 mm outlet size across the hopper width at all heights, were higher than those obtained in cases of 7mm size at the same heights. The percentage increments of the average vertical velocity component at  $H/\infty$ ,  $H/4$  and  $H/2$  in cases of 10 mm outlet size are 52.39%, 39.43% and 41.10% than those reported in case of 7mm size at the same heights respectively. Both calculations, either by using the maximum vertical velocity component or the average vertical velocity component are higher in cases of 10 mm size and across the whole width. The results also indicate that

increasing hopper outlet size, increases the granular velocities in different ratios and the maximum increment is obtained at the outlet region.

### 6.3.1.1.2 Granular Bed Lubrication

The granular bed lubrication has been conducted for 7mm hoppers outlets size using 2% magnesium stearate powder as a common lubricant in pharmaceutical industries and the results are shown in Figure 6.10.

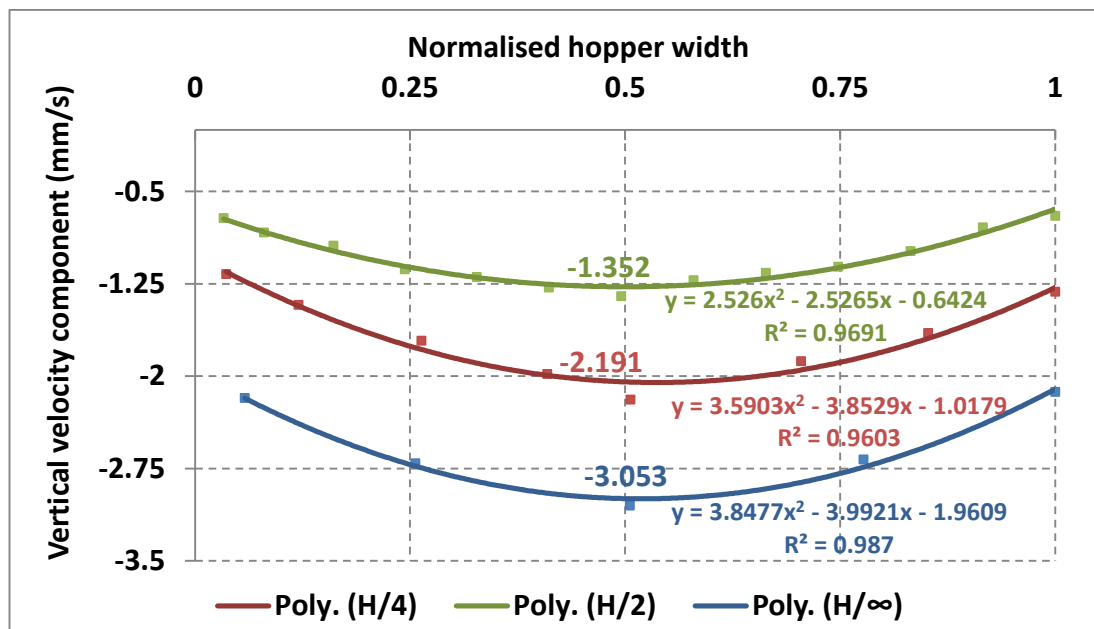


**Figure 6.10** Vertical velocity component plot inside lubricated 30° internal angle hopper geometry having 7mm outlet size measured at three heights (H/∞, H/4 and H/2) in 2<sup>nd</sup> order polynomial plot

The results show slight increases in the particle vertical velocity components among all height levels, compared to the non-lubricated 30° hopper geometry. The maximum values of the vertical velocity component are 3.053 (mm/s), 2.191 (mm/s) and 1.352 (mm/s) at H/∞, H/4 and H/2 respectively comparing to 2.671 (mm/s), 1.748 (mm/s) and 1.056 (mm/s) at the same levels. The percentage increments of the maximum reported vertical velocity component at H/∞, H/4 and H/2 in case of lubricated to non-lubricated system are 14.30%, 25.34% and 28.03% respectively. In addition to that, the R<sup>2</sup> values are improved in cases of lubricated geometry, compared to the non-lubricated ones. The R<sup>2</sup> values are 0.918, 0.944 and 0.945 at H/∞, H/4 and H/2 in cases of non-lubricated 30° hopper geometry, compared to 0.987, 0.960 and 0.969 in cases of lubricated geometry at the same heights

respectively. These results give an indication that the flow process inside the lubricated system is more uniform than that obtained inside a non-lubricated system. It is well known, that bed lubrication decreases the intergranular friction which could improve the flow behaviour.

The influence of the bed lubrication on particles velocity has been recalculated using average vertical velocity values across the hopper width at all heights and compared to the non-lubricated system as shown in Figure 6.11.

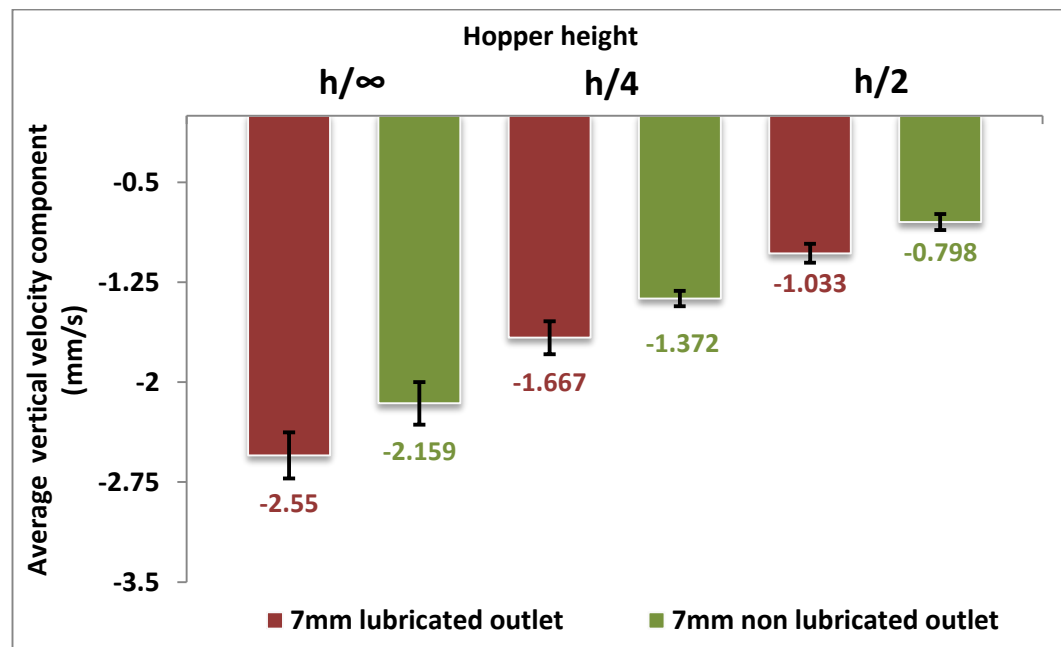


**Figure 6.11** Average vertical velocity component plot across the hopper width inside lubricated  $30^\circ$  internal angle hopper geometry for lubricated and non lubricated systems at three heights ( $H/\infty$ ,  $H/4$  and  $H/2$ )

The results clearly show that the mean velocity values at the lubricated system are higher than those obtained at non-lubricated system across the same heights. The percentage increments of the mean vertical velocity component across the hopper width at  $H/\infty$ ,  $H/4$  and  $H/2$  in case of lubricated system to non-lubricated system are 18.11%, 24.04% and 32.81% respectively.

Opposite to what have been reported in case of increasing the hopper outlet, the relative particle velocity increments due to bed lubrication have been achieved at the higher levels and not at the outlet region. This has been conformed using both calculations of maximum vertical velocity component and mean vertical velocity component across the bed as presented in Figure 6.10 and Figure 6.11.

The previous results and calculations, using mean vertical velocity components shown in Figure 6.9 and Figure 6.11 indicate that the influence of increasing the hopper outlet size on particle velocity magnitudes is more than the influence of lubrication of the granular bed. The obtained mean increments at  $H/\infty$ ,  $H/4$  and  $H/2$  in cases of using 10mm outlet size were 52.39%, 39.43% and 41.10%, compared to 18.11%, 24.04% and 32.81% for lubricated bed at 7mm outlet sizes respectively.

### 6.3.1.1.3 Hopper Walls Roughness

Further investigations have been conducted to report the influence of the hopper wall roughness on the general flow trend and particulates velocities using non-lubricated granules and 7mm hopper outlet size. The hopper wall surface roughness was induced by gluing sand paper on the inner hopper walls as shown in Figure 6.12.

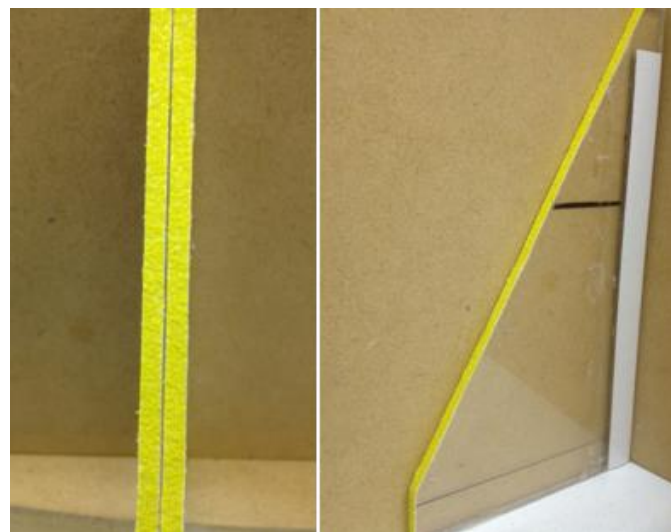


**Figure 6.12** Hopper walls roughness by gluing sandpapper on Perspex smooth walls

The wall roughness of both original smooth Perspex hoppers and the glued sandpaper on the walls was measured in a mechanical engineering laboratory using a surface roughness tester (Taylor-Hobson) as shown in Figure 6.13 and roughness average ( $R_a$ ) values were  $0.999 \mu m$  and  $79.82 \mu m$  respectively.

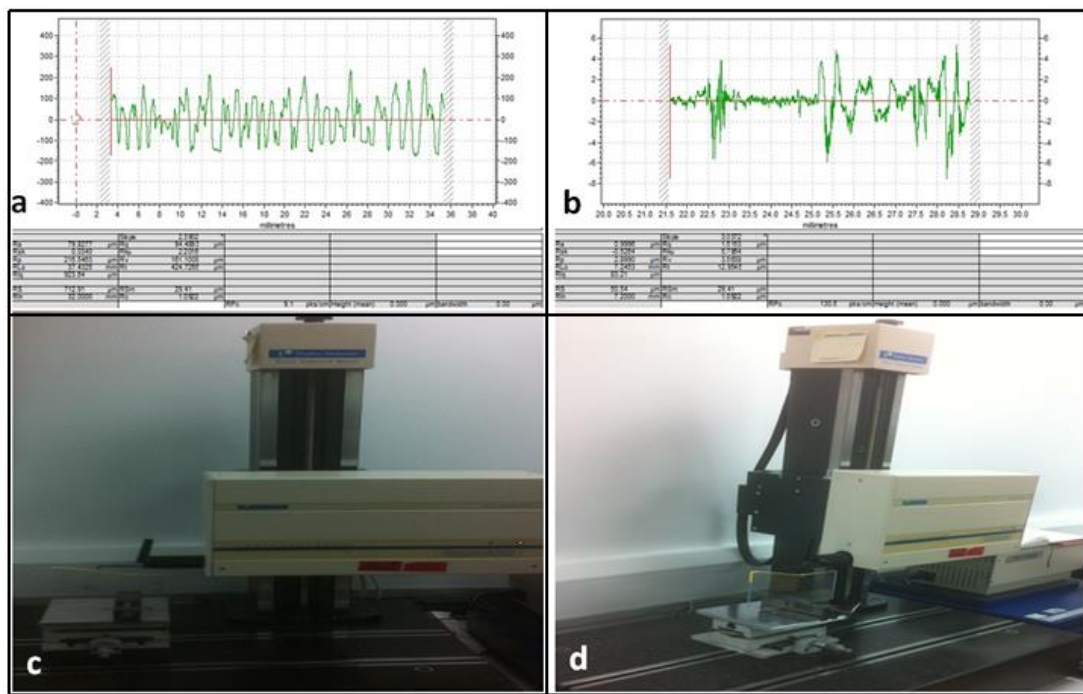


**Figure 6.13** Experimental measurements of the wall roughness in laboratory using Taylor-Hobson, (a) rough surface results, (b) smooth wall results and (c and d) the measurement procedure

The particulate velocity measurement results inside rough wall hopper geometry, show slight decreases in the values of the maximum vertical velocity components across all hopper heights as shown in Figure 6.14. The maximum vertical velocity components  $H/\infty$ ,  $H/4$  and  $H/2$  in cases of rough walls were 2.587 (mm/s), 1.576 (mm/s) and 0.898 (mm/s), compared to 2.671(mm/s), 1.748 (mm/s) and 1.056 (mm/s) in cases of smooth hopper walls at the same heights respectively.

The obtained results in Figure 6.14 show that the decrease of the maximum vertical velocity component due to wall roughness at  $H/\infty$ ,  $H/4$  and  $H/2$  are 3.14%, 9.84% and 14.96% respectively. On the other hand, the particles average vertical velocity, decreases at the hopper boundaries at  $H/\infty$ ,  $H/4$  and  $H/2$ , are 12.48%, 17.25% and 28.59% respectively. This indicates that the particles close to the boundaries are affected more by the wall roughness than those at the middle stream (Babout et al., 2013). Multiple factors, such as initial packing density, bin geometries and material characteristics greatly influence velocity variation due to wall roughness (Steingart and Evans, 2005, Babout et al., 2013, Lee and Yoon, 2015).

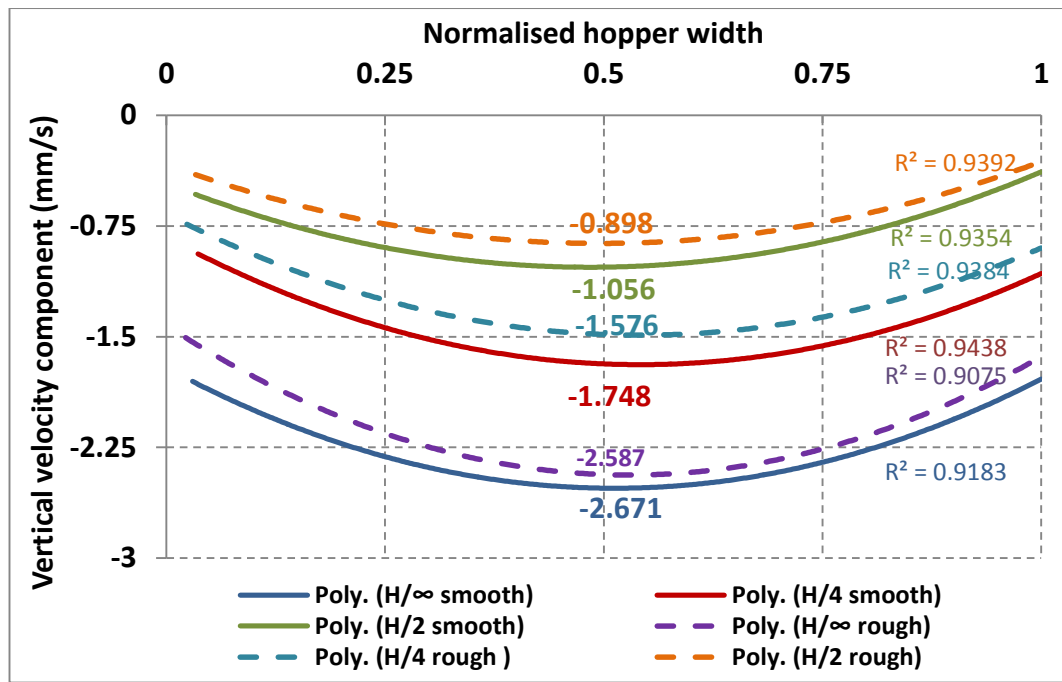


**Figure 6.14** Vertical velocity component plot inside smooth and rough wall 30° internal angle hopper geometry having 7mm outlet size, solid line are smooth walls and dashed lines are rough walls measured at three heights ( $H/\infty$ ,  $H/4$  and  $H/2$ ) in 2<sup>nd</sup> order polynomial plot

The results indicate that the reduction of the particle vertical velocity due to wall roughness depends on the location of the particles from the hopper boundaries. The results were recalculated using the average vertical velocity component across the hopper width and the results confirm the velocity declining trend at all hopper heights as shown in Figure 6.15. The average vertical velocities values across the bed at  $H/\infty$ ,  $H/4$  and  $H/2$  in cases of rough walls are 2.015 mm/s, 1.197 (mm/s) and 0.667 (mm/s), compared to 2.159 (mm/s), 1.372 (mm/s) and 0.79 (mm/s) for smooth wall at the same heights respectively. The declining ratios are 6.67%, 12.76% and 16.41% for the smooth walls at heights  $H/\infty$ ,  $H/4$  and  $H/2$  respectively. Both calculations using the maximum velocity values and the mean velocity values across the hopper width indicate that the higher velocity reduction, due to wall roughness, is obtained at high granular levels close to the boundaries. This could be attributed to the nature of the mass flow trend characterised by particulates wall sliding behaviour, increasing of wall roughness will increases the residence time of these particulates at high segments compared to those close to the outlet region.

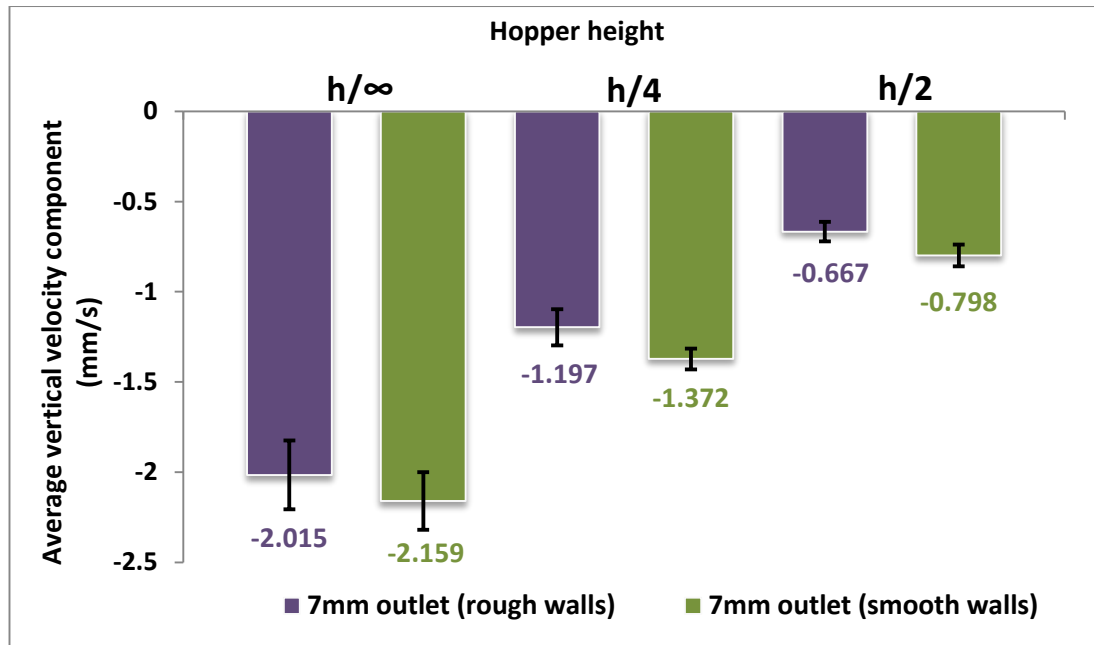


**Figure 6.15** Average vertical velocity component plot across the hopper width inside smooth and rough wall  $30^\circ$  internal angle hopper geometry for smooth and rough walls at three heights ( $H/\infty$ ,  $H/4$  and  $H/2$ )

### 6.3.2 Hopper Geometry Having a $60^\circ$ Internal Angle

The influence of the hopper internal angle on the spatial and temporal mean resultant velocity vectors is illustrated in Figure 6.16. The general flow trend in case of  $60^\circ$  internal angle hopper is totally different from that observed in  $30^\circ$  hopper geometry. This can be clearly observed through the directions of the mean resultant velocity vectors within the hopper geometry through the entire flow process. The mean velocity vectors map through the flow process, show clearly that there is a central region displaying a vertical or almost vertical direction of the velocity vectors, while the surrounding regions show inclined direction, parallel to the hopper walls. It is very important to mention that the lower hopper segment has a wide range of almost vertical velocity vectors, compared to the middle and top segments. This vertical direction indicates that there is relatively continuous motion of the granules at this region during the flow process. These results are in good agreement with the previous study conducted by Sielamowicza et al. (2006) and Choi et al. (2005) at the same hopper geometry, using high particle size amaranth grains and black glass beads respectively.

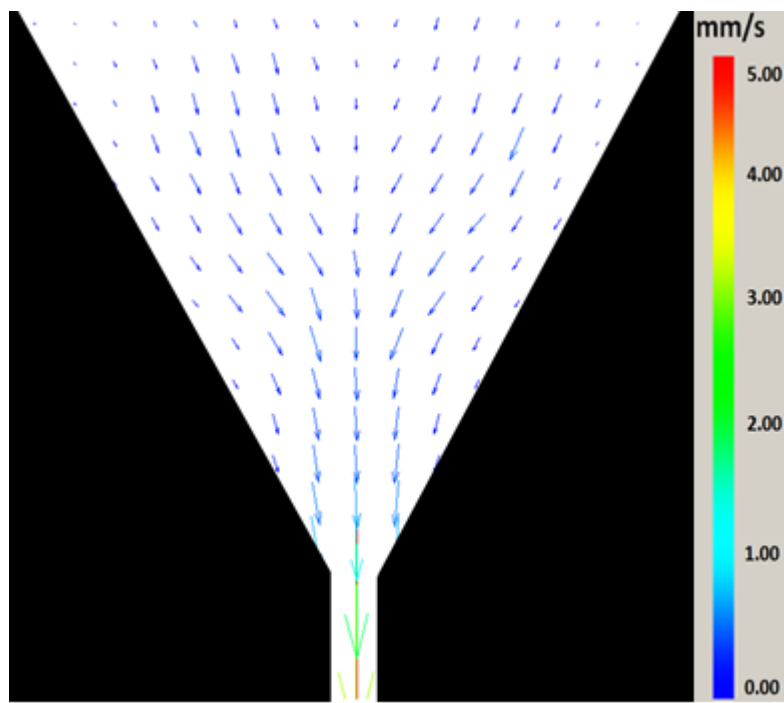


**Figure 6.16** Mean resultant velocity vectors map inside the 60° internal angle hopper geometry filled by coloured pharmaceutical excipient granules

The highest velocity values are obtained at the hopper orifice level as well as the hopper nozzle. The particle velocity magnitudes decreased in an upward direction. The higher hopper segment shows slower particle motion compared to that in the middle and lower segments. The hopper boundaries are the slowest region among all hopper geometry. This slow particle motion will enhance the extent of grain stagnation at the boundaries. The central flow trend takes place at the central region of the hopper, showing vertical direction of the velocity vectors, while the radial flow trend comes through the boundaries. The length of the velocity vectors at the lower hopper segment is longer than that reported at higher segments. It has been reported that some velocity vectors at high segments near the boundaries show long inclined velocity vectors. These could be attributed to the high radial flow trend from the boundaries toward the central zone in an avalanche trend during the dynamic flow process.

Further investigation has been conducted to measure the vertical velocity component within the hopper geometry during the whole dynamic flow process across the hopper section at three different heights;  $H/\infty$ ,  $H/4$  and  $H/2$  and the results are shown in Figure 6.17. Such investigations will report clearly the influence of the hopper

geometry on the spatial and temporal velocities of the particles during the flow process. This will provide an excellent opportunity to link the flow trend and velocity values to the stress profile distributions reported at the same heights (section 4.3.2) as well as cross match the results across all hopper geometries.

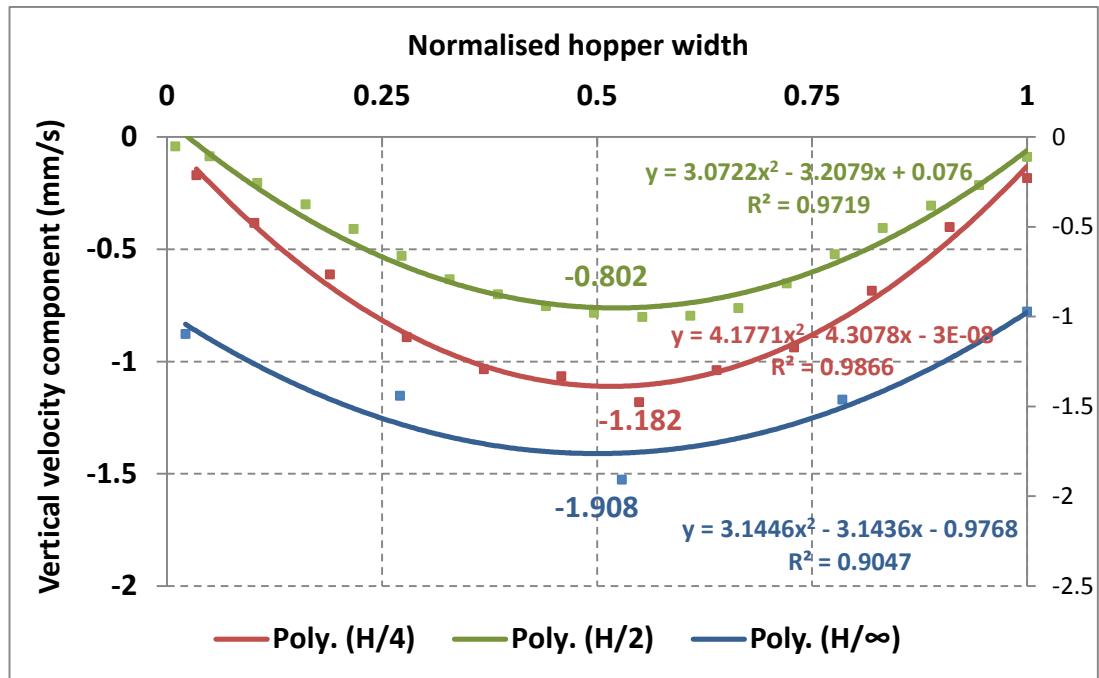


**Figure 6.17** Vertical velocity component plot inside  $60^\circ$  internal angle hopper geometry having 7mm outlet size measured at three heights ( $H/\infty$ ,  $H/4$  and  $H/2$ ) in 2<sup>nd</sup> order polynomial plot

The results in Figure 6.17 show that the maximum value of the vertical velocity component inside the hopper geometry during the whole dynamic flow process was obtained at the central axis of the lower hopper segment close to the outlet region ( $H/\infty$ ). The velocity values are 1.908 (mm/s), 1.182 (mm/s) and 0.802 (mm/s) at  $H/\infty$ ,  $H/4$  and  $H/2$  respectively. It is obvious that the velocity magnitudes declined at a higher level outside the outlet region. The data are plotted in polynomial regression 2<sup>nd</sup> order and  $R^2$  ranges from 0.905 to 0.987. The percentage ratios of the maximum vertical velocity component at  $H/\infty$  to  $H/4$  and  $H/2$  are higher by 61.42% and 137.90% respectively. The ratios were recalculated using the mean velocity across the whole horizontal hopper section to give a more descriptive comparison and to avoid any bias in the results. The average vertical velocity components across the hopper width at three heights  $H/\infty$ ,  $H/4$  and  $H/2$  are 1.377 (mm/s), 0.716 (mm/s) and 0.474(mm/s) respectively as shown in Figure 6.18. The percentage ratios of the

average vertical velocity component at  $H/\infty$  to  $H/4$  and  $H/2$  were higher by 92.32% and 190.50 % respectively.

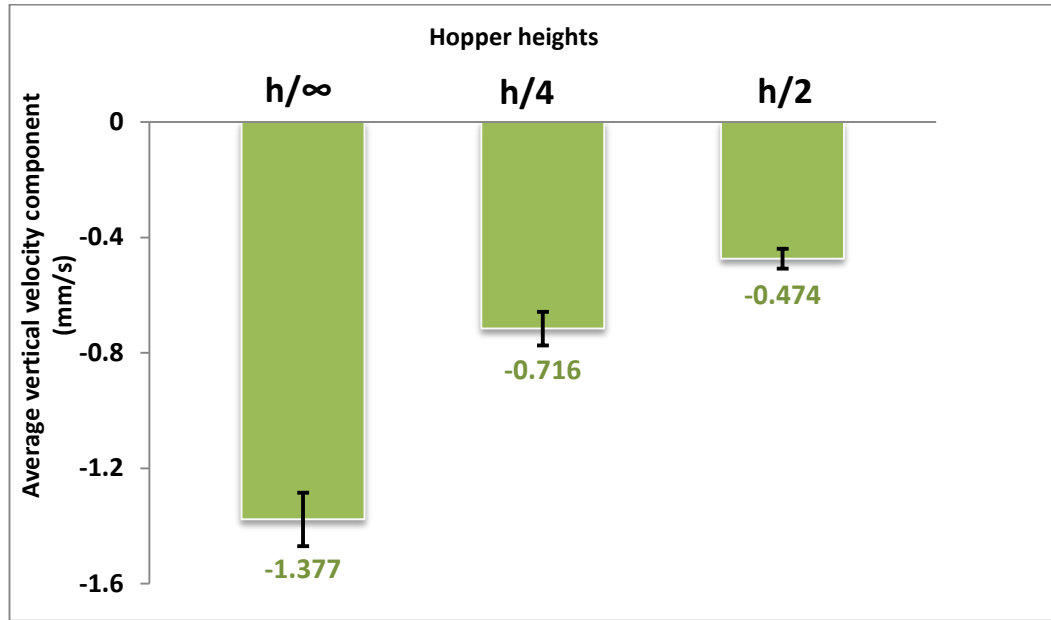
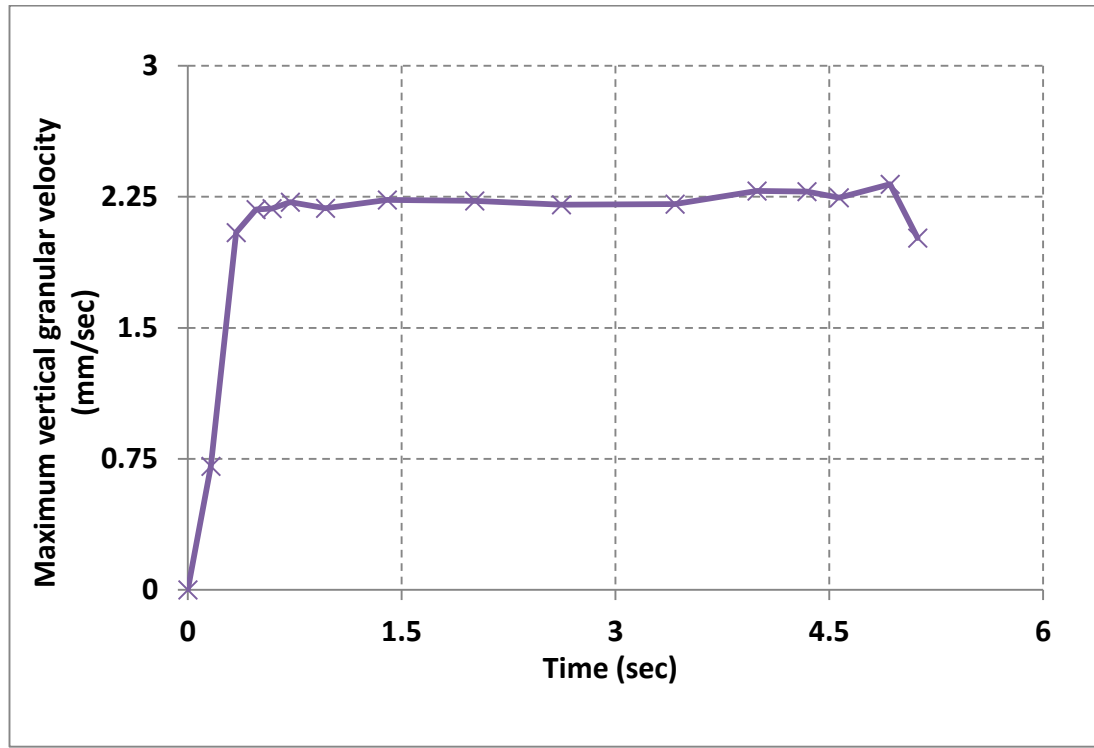


**Figure 6.18** Average vertical velocity component plot across the hopper width inside  $60^\circ$  internal angle hopper geometry having 7mm outlet size at three heights ( $H/\infty$ ,  $H/4$  and  $H/2$ )

The obtained results in Figure 6.17 using the maximum vertical velocity component and in Figure 6.18 using the average vertical velocity component indicate that the velocity magnitudes are very high at the regions close to the hopper outlet and gradually decreased at higher segments. Similar trend has been reported by Sielamowicza et al. (2006) using similar hopper geometry.

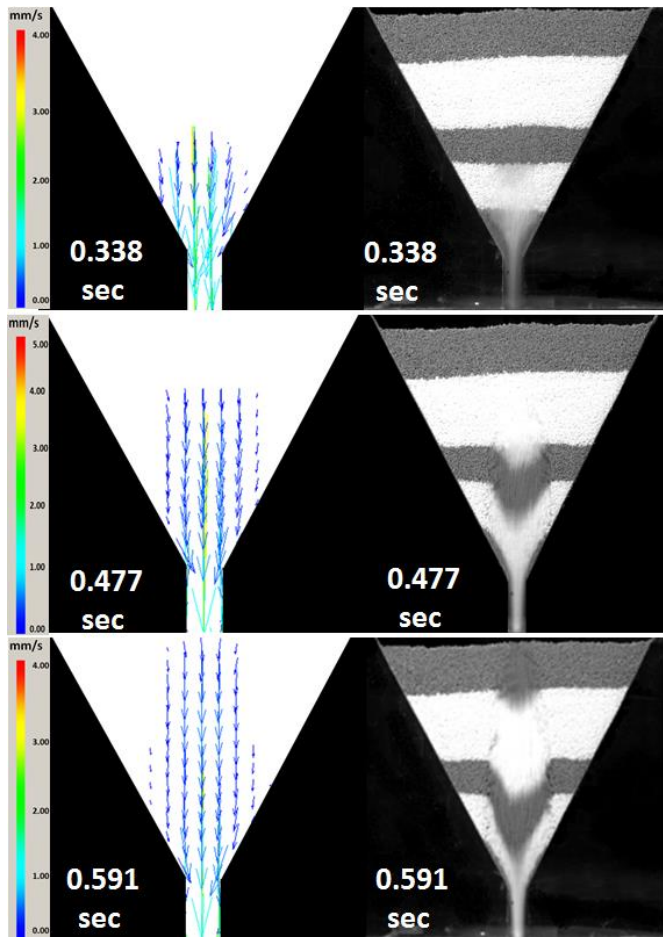
Further analysis of the maximum vertical velocity component magnitudes at the hopper orifice ( $H/\infty$ ) during different time intervals of the dynamic flow process has been conducted and the results are shown in Figure 6.19. The obtained results show that there are dramatic increases in the maximum vertical velocity at the early stage of the flow, reaching the maximum value at around 0.6 seconds and remains almost constant for the remaining duration until the flow is terminated. The flate shape of the velocity plot obtained in cases of  $60^\circ$  hopper geometry are more steady than those obtained in cases of  $30^\circ$  hopper geometry. Very minor flactuations have been observed at the flate segments of the plot. However, slight increases have been recorded at the end of the flow porcess and this is due to granules sliding at the last stage of the flow process. In general, the maximum vrtival velocity components

reported in cases of  $60^\circ$  hopper geometry is much less than those observed in cases of  $30^\circ$  hopper geometry. Further comparisons will be reported in the end of this chapter.



**Figure 6.19** The maximum recorded vertical velocity component values at selected time intervals during the flow process inside  $60^\circ$  internal angle hopper geometry

The mean velocity vectors map in Figure 6.16 displays the central region, showing the vertical to almost vertical direction of the velocity vectors. This indicates that there is high possibility of central plug flow generation at this location. DPIV technique is an excellent tool to track and visualise any granular bed changes over a short period of time. This advantage has been utilised properly here to report the formation and propagation of the central plug flow zone within the granular bed as well as the direction and magnitude of velocity vectors at this zone. The results of the mean velocity vector map and its corresponding visual images during the central plug flow propagation are illustrated in Figure 6.20. This deep investigation will help to report the granular bed dilation and stagnation tendency in order to link these results to the stress profiles distributions at static condition at corresponding sites.



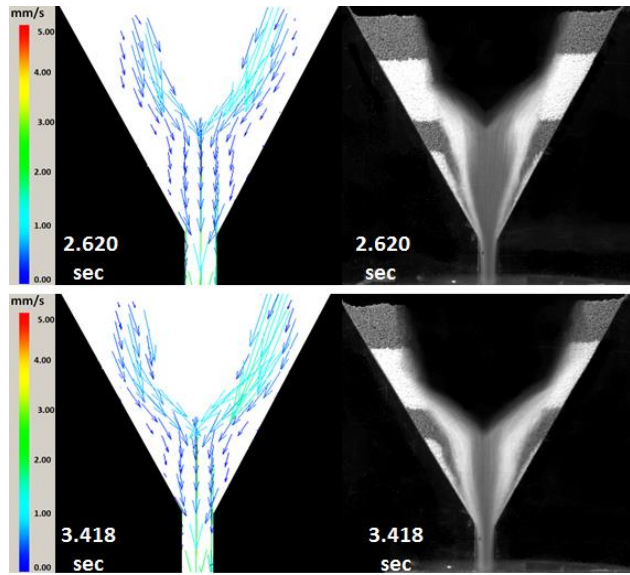
**Figure 6.20** Mean resultant velocity vector profiles at 60° internal angle hopper and its corresponding visual images during the central plug flow propagation (first flow zone)

Figure 6.20 shows in detail the generation and propagation of the central plug flow at the axisymmetric axis of the hopper geometry. The plug starts exactly above the hopper outlet and propagates in a vertical direction towards the outer layer of the granular bed. At 0.338 seconds, the resultant mean velocity map shows vertical to almost vertical direction of the vectors at the hopper lower segment. The vector regions include the region located directly above the outlet and the surrounding region. This indicates that all particles at this hopper segment are in continuous motion at this early stage of the flow process. The corresponding flow image shows that the granular bed shows marked dilation above the outlet region, and most of this layer is in continuous motion. The plug flow continues to propagate vertically at the axisymmetric axis at 0.477 seconds toward the outer granular layer. Concurrently, the corresponding image shows clearly that the granular bed continues to dilate in an

upward direction at the axisymmetric axis and the extent of stagnation increased at the boundaries, especially upper layers. Most of the lower granular layer in the dark colour close to the outlet has already been discharged. At 0.591 seconds, the plug reaches the outer granular layer at the same vertical trend and the direction of the resultant mean velocity vectors at this stage of the flow are taking a vertical direction aligned to the gravity direction. The lower hopper segment close to the outlet region shows few inclined vectors, due to the flow from the lower boundaries.

In general, this stage is characterised by continuous granular bed dilation, which starts exactly above the outlet and continue to the outer granular layer in a vertical direction. The granules rearranged themselves inside the hopper geometry after each discharged portion and shape the borders of the central plug flow. The lower hopper segment shows considerable particulate motion during the early stage of the flow. Referring to the PSAT results, the central zone of the 60° internal angle hopper geometry showed low value stress profiles and the direction of the major principal stress was in a vertical to almost vertical direction. The lower hopper segment showed low stress values and the stress direction was inclined parallel to the wall and towards the outlet direction. These microscale characteristics indicate that granules locates within this zone and close to the outlet, will flow first. This zone has been denoted as the first flow zone, more details are available in section 4.3.2 and Figure 4.12. This has been confirmed here through the analysis of the early flow stage mentioned in Figure 6.20. The results indicate that the initial stress packing profiles and directions have crucial influence on the general flow trend.

Further tracking and analysis have been conducted in the later stages of the flow process at this hoper geometry, as illustrated in Figure 6.21. This stage is characterised by the expansion of the plug flow horizontally towards the hopper boundaries. The flow behaviour during this phase is a mixture of both central and radial flow trends. At 2.620 seconds, the mean velocity vectors map shows radial velocity vectors at the flow stream having high velocity magnitudes and longer than those at the boundaries and those close to the outlet region. This indicates that the radial flow trend is more dominant at this stage of the flow, due to low angle of particles sliding toward the central flow zone.



**Figure 6.21** Mean resultant velocity vector profiles at 60° internal angle hopper and its corresponding visual images during 2<sup>nd</sup> stage of the flow process (second flow zone)

This trend is also reported at 3.418 seconds and the tendency is high. These results indicate that the flow process at this stage takes place mainly through the radial flow trend from the boundaries towards the central flow region at the axisymmetric axis of the hopper. The corresponding images at 2.620 and 3.418 seconds show clearly the high extent of the radial flow at this stage that flows towards the central zone through the outer zones of higher granular layers. The granules flow in avalanche trend at higher levels and slide at the lower levels. Both the mean velocity vectors map and the corresponding images show clearly that the granular material at the lower hopper segment is in continuous motion during the late flow stage. These results are in a good level of agreement with those obtained by Sielamowicza et al. (2006) using the same hopper geometry.

According to the PSAT results reported in section 4.3.2 and illustrated in Figure 4.12, this flow zone was expected to be the second flow zone, due to high stress magnitudes in comparison to the first zone, as well as the inclined direction of the major principal stress. The prediction according to stress profile distribution and direction is proved here, as illustrated in Figure 6.21 as the flow comes through the boundaries towards the central flow zone and the radial flow trend becomes dominant at this stage. The lower hopper segment boundaries close to the outlet

(H/ $\infty$ ) show continuous particulate motion and some stagnation is reported at H/4. The continuous motion of the particulates at this segment could be attributed to the low stress magnitudes and the inclined direction of the major principal stress towards the hopper outlet.

The tracking of the flow trajectories and trend at the third stage of the dynamic flow process is illustrated in Figure 6.22.

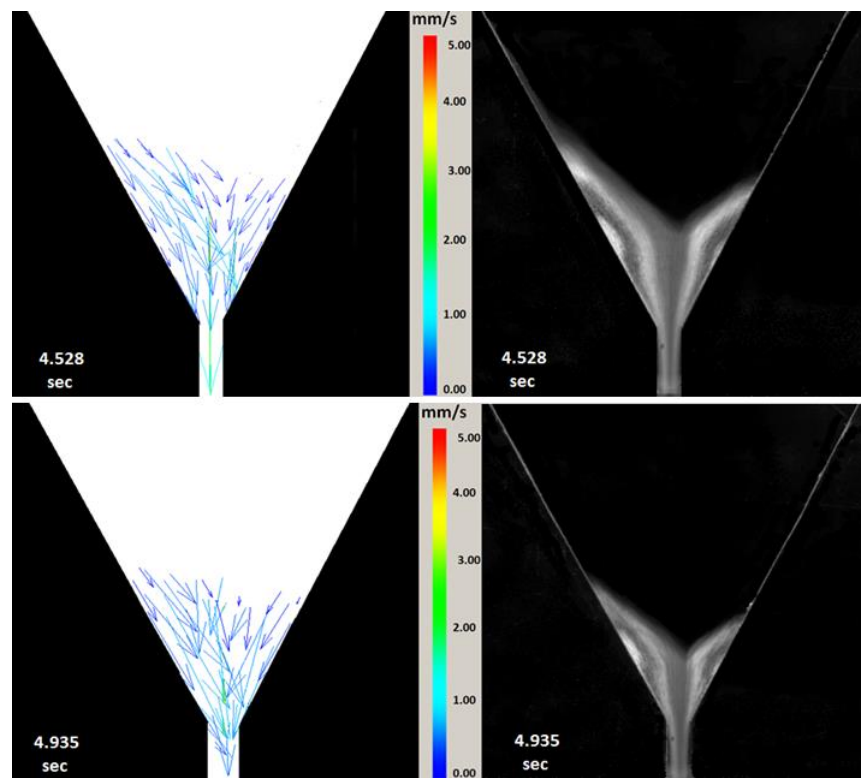


**Figure 6.22** Mean resultant velocity vector profiles at 60° internal angle hopper and their corresponding visual images during 3<sup>rd</sup> stage of the flow process (third flow zone)

The main route of the dynamic flow process at this stage is the radial flow from the boundaries to the central flow zone, as well as the sliding of the granules on the hopper walls. The stagnation of the granules is clearly shown in the images at the third stage and the flow trend takes the parabolic shape close to the walls. Free falling and sliding of the granules on the wall at 4.935 seconds during this stage increase the velocity at the outlet region, as seen from the length of the vectors at this region. The PSAT results in section 4.3.2 reported high values for the stress profiles close to the boundaries and total inclined direction for the major principal

stress parallel to the wall. The dynamic flow of the granules at the third stage of the flow occur exactly at this region where the high stress magnitudes delay the granular flow, showing parabolic shapes at the boundaries.

### 6.3.2.1 Evaluation of Variables Influencing Granular Flow Process Inside 60° Internal Angle Hopper Geometry

#### 6.3.2.1.1 Hopper Outlet Size

The hopper outlet size has been increased from 7mm ( $\approx 11d$ ) to 10mm ( $\approx 15.5 d$ ) to investigate the influence of the hopper outlet size on the flow process and particulate velocity magnitudes. The results of the particle vertical velocity components at  $H/\infty$ ,  $H/4$  and  $H/2$  are shown in Figure 6.23.

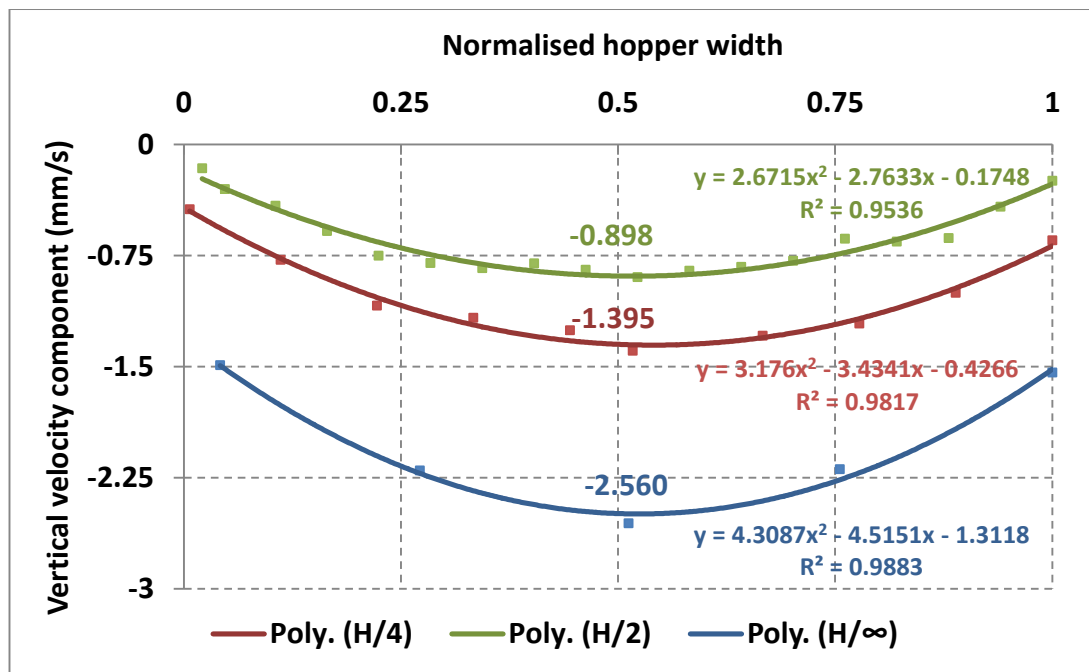


**Figure 6.23** Vertical velocity component plot inside 60° internal angle hopper geometry having 10 mm outlet size measured at three heights ( $H/\infty$ ,  $H/4$  and  $H/2$ ) in 2<sup>nd</sup> order polynomial plot

The maximum magnitudes of the vertical velocity components inside 60° internal angle hopper geometry are 2.560 (mm/s), 1.395 (mm/s) and 0.898 (mm/s) at  $H/\infty$ ,  $H/4$  and  $H/2$  respectively. The polt data are fitted in the 2<sup>nd</sup> polynomial plot and the  $R^2$  range is from 0.953 to 0.988. The recorded maximum magnitudes of the vertical velocities component inside this geometry having 7mm outlet size were 1.908

(mm/s), 1.182 (mm/s, and 0.802 (mm/s) at  $H/\infty$ ,  $H/4$  and  $H/2$  respectively. This indicates that increasing the outlet size by around 43% (7mm to 10 mm) increases the velocity magnitudes by 34.17%, 18.02 and 11.97 at  $H/\infty$ ,  $H/4$  and  $H/2$  respectively.

The previous outcomes have been recalculated using the average vertical velocity component across the whole section at  $H/\infty$ ,  $H/4$  and  $H/2$  inside both geometries having 7 and 10 mm hopper outlets and the results are illustrated in Figure 6.24.

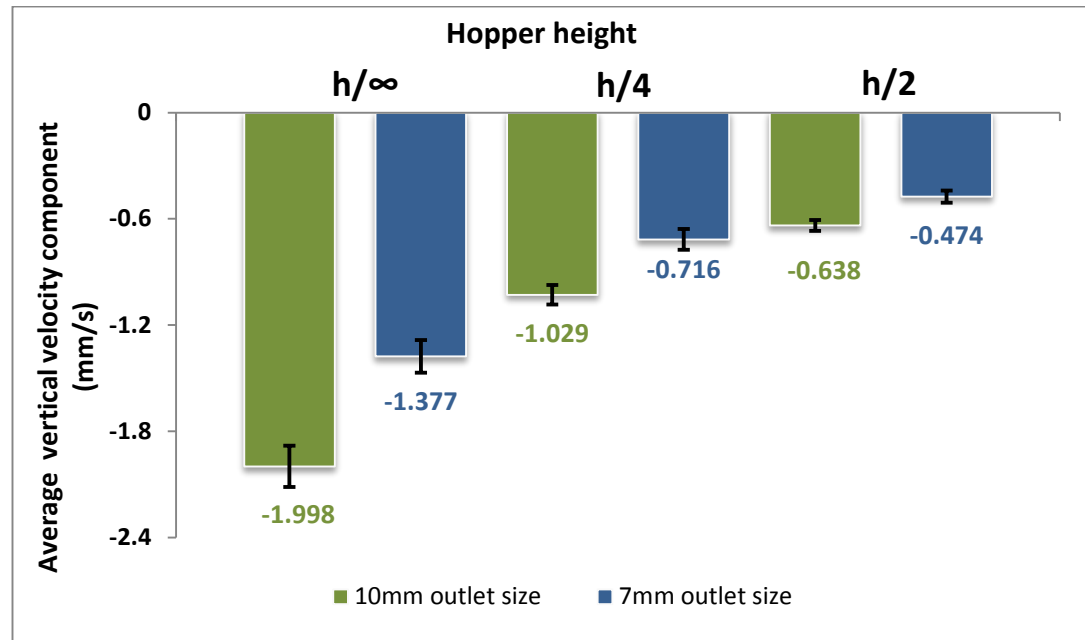


**Figure 6.24** Average vertical velocity components plot across the hopper width inside  $60^\circ$  internal angle hopper geometry at 7 mm and 10mm outlet sizes at three heights ( $H/\infty$ ,  $H/4$  and  $H/2$ )

The results in Figure 6.24 prove that the average vertical velocity components in the cases of 10 mm outlet size across the hopper width at all heights are higher than those obtained in the cases of 7mm size at the same hopper heights. The percentage increments of the average vertical velocity components at  $H/\infty$ ,  $H/4$  and  $H/2$  in cases of 10 mm outlet size are 45.10%, 43.72% and 34.60% than that reported in cases of 7mm size at the same heights respectively. In both calculations, using the maximum vertical velocity components and the average vertical velocity components, are higher in cases of 10 mm size. In general, the increment of both maximum vertical velocities and average vertical velocities are higher in cases of  $30^\circ$  internal angle hopper geometry than those obtained in cases of  $60^\circ$  hopper geometry. This could be

attributed to the dominant mass flow trend reported in cases of 30° hopper geometry and domination of the central flow route.

### 6.3.2.1.2 Granular Bed Lubrication

The influence of granular bed lubrication on particulate velocity gradients have been investigated in cases of 7mm hoppers outlets size using 2% magnesium stearate powder, and the results are illustrated in 6.25.

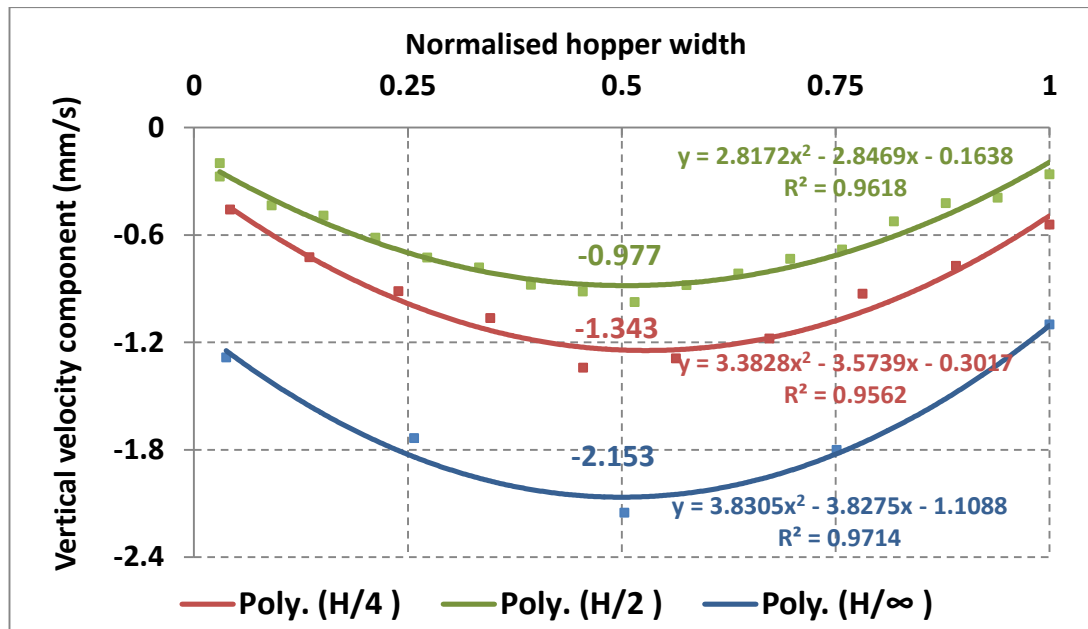


**Figure 6.25** Vertical velocity component plot inside lubricated 60° internal angle hopper geometry having 7mm outlet size measured at three heights ( $H/\infty$ ,  $H/4$  and  $H/2$ ) in 2<sup>nd</sup> order polynomial plot

The results indicate that bed lubrication increases particles vertical velocity components among all height levels at different percentages, depending on the particle location within the hopper geometry. The maximum vertical velocity components at  $H/\infty$ ,  $H/4$  and  $H/2$  inside the lubricated bed are 2.153 (mm/s), 1.343 (mm/s) and 0.977 (mm/s), compared to 1.908 (mm/s), 1.182 (mm/s) and 0.802 (mm/s) in case of non-lubricated bed at the same levels respectively. The percentage velocity increments due to lubrication are 12.842%, 13.621% and 21.820% at heights  $H/\infty$ ,  $H/4$  and  $H/2$  respectively.

Similar to what has been conducted in cases of 30° internal angle hopper geometry, the influence of bed lubrication inside lubricated and non-lubricated 60° internal

angle hopper geometry has been recalculated using average vertical velocities value across the hopper width at all predetermined heights. The results are shown in Figure 6.26 in comparison to the non-lubricated system for easy matching.

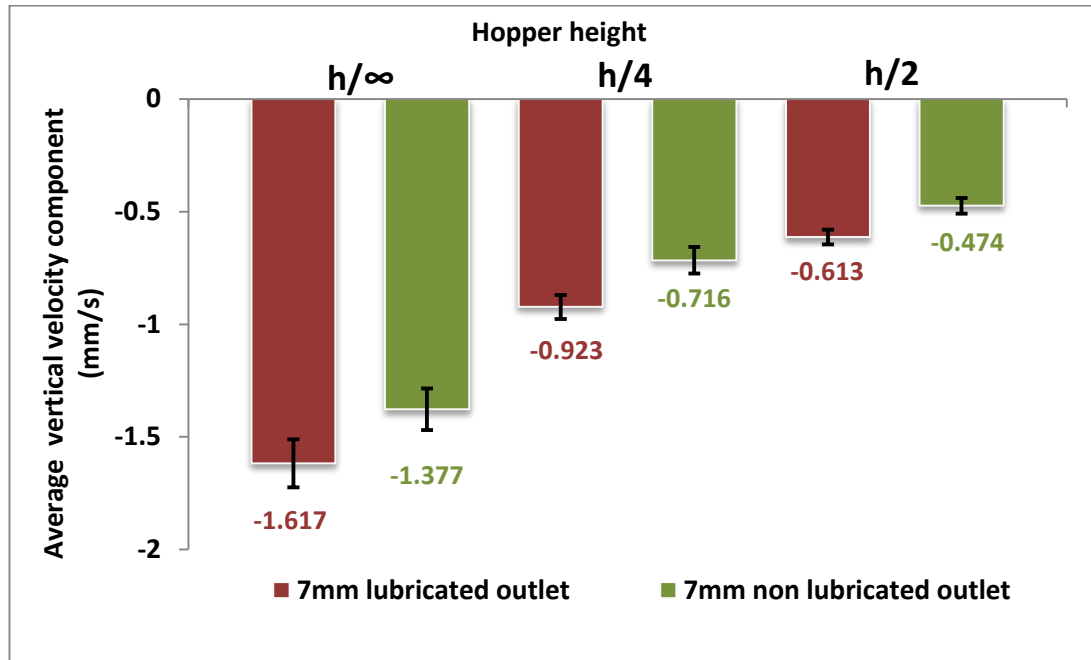


**Figure 6.26** Average vertical velocity component plot across the hopper width inside lubricated  $60^\circ$  internal angle hopper geometry for lubricated and non lubricated systems at three heights ( $H/\infty$ ,  $H/4$  and  $H/2$ )

In general, the average velocity values at the lubricated system are higher than those obtained in a non-lubricated system at the same pre-determined heights. The percentage increments of the average vertical velocity component at  $H/\infty$ ,  $H/4$  and  $H/2$  in cases of lubricated system to non-lubricated system were 17.43%, 28.91% and 29.32% respectively.

The obtained results in Figure 6.24 and Figure 6.26 indicate that the impact of increasing the hopper outlet on particle velocity gradients is higher than bed lubrication. The obtained increments at  $H/\infty$ ,  $H/4$  and  $H/2$  in cases of using a 10mm outlet size were 45.10%, 43.72% and 34.60%, compared to 17.43%, 28.91% and 29.32% for the lubricated bed at 7mm outlet size respectively. Moreover, the impact of the granular bed lubrication on vertical particle velocities is less than that obtained in cases of  $30^\circ$  hopper geometry.

### 6.3.2.1.3 Hopper Walls Roughness

The influence of hopper wall roughness on vertical particle velocities magnitudes has been conducted and the results are shown in Figure 6.27.

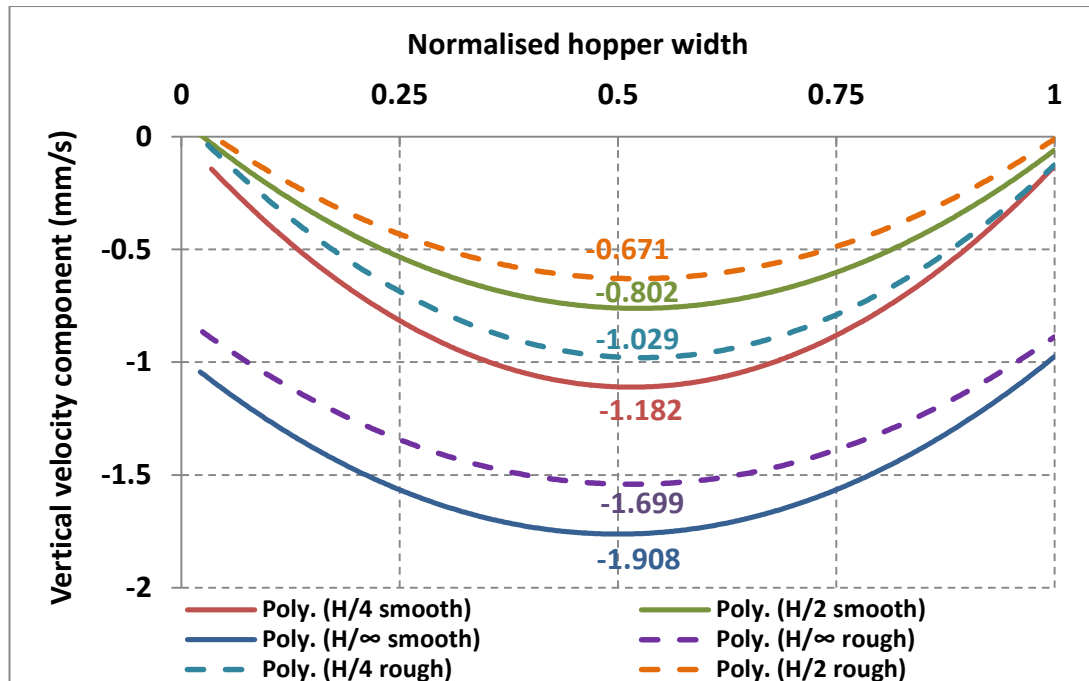


**Figure 6.27** Vertical velocity component plot inside smooth and rough wall 60° internal angle hopper geometry having 7mm outlet size, solid line are smooth walls and dashed lines are rough walls measured at three heights ( $H/\infty$ ,  $H/4$  and  $H/2$ ) in 2nd order polynomial plot

The maximum vertical velocity components  $H/\infty$ ,  $H/4$  and  $H/2$  in cases of rough hopper walls are 1.699 (mm/s), 1.029 (mm/s) and 0.671 (mm/s), compared to 1.908 (mm/s), 1.182 (mm/s) and 0.802 (mm/s) in cases of smooth hopper walls at the same heights respectively.

The percentage reduction in the maximum vertical velocity component due to wall roughness at  $H/\infty$ ,  $H/4$  and  $H/2$ , are 10.95%, 12.94% and 16.33% respectively. Further investigation has been conducted on average particle velocity at the hopper boundaries which will obviously reflect the influence of the wall surface on flow trend as the central region affected by particle-particle friction mainly. The particle velocity decreases at the hopper boundaries at  $H/\infty$ ,  $H/4$  and  $H/2$  are 14.44%, 25.31% and 33.57% respectively. These results indicate that the flow of the particles close to the boundaries, is more influenced by the wall surface state more than that

at the axisymmetric axis (Babout et al., 2013). Another confirmation of the previous results for the influences of the hopper wall roughness on the vertical particle velocity has been obtained by the average values of the vertical velocities plot as shown in Figure 6.28. The results show that the average vertical velocity component across the hopper width at  $H/\infty$ ,  $H/4$  and  $H/2$  in cases of rough walls are 1.213 (mm/s), 0.601(mm/s) and 0.383 (mm/s), compared to 1.377 (mm/s), 0.716 (mm/s) and 0.474 (mm/s) for smooth walls at the same heights respectively. The declining ratios, due to surface roughness are 11.91%, 16.06% and 19.20% at heights  $H/\infty$ ,  $H/4$  and  $H/2$  respectively. These results indicate that the influence of wall roughness on particulates residence time in case of 60° hopper geometry is more than that reported in 30° hopper geometry as shown in Figure 6.14 and 6.27. Moreover, the wall roughness of 60° hopper geometry reduces the particulates velocity at the boundaries more than that at the central zone.

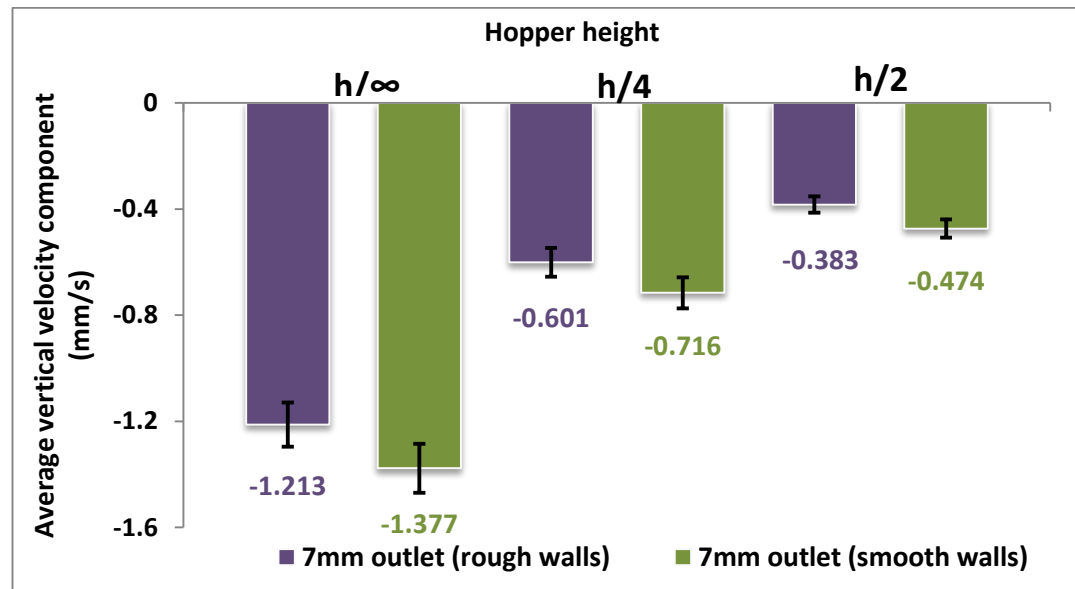


**Figure 6.28** Average vertical velocity component plot across the hopper width inside smooth and rough wall 60° internal angle hopper geometry at three heights ( $H/\infty$ ,  $H/4$  and  $H/2$ )

Generally, the flow trend of the 60° internal angle hopper geometry is a funnel flow trend showing radial and central flow trend. The flow performed mainly through the central flow zone and particulates radial sliding toward the central region in an avalanche trend. Stagnation zones at the hopper boundaries are clearly reported here. At the late stage, the granule sliding mechanism dominates and granules slide

towards the outlet on the hopper boundaries. Increasing wall roughness will enhance the stagnancy and decrease granules sliding on the walls and concurrently decreases particulates velocity close to the walls. Similar to 30° hopper geometry, increasing hopper outlet has more influence on particulate velocities than bed lubrication and wall roughness influences on particulate velocities is more than that reported in case of 30° hopper geometry.

### 6.3.3 Hopper Geometry Having a 90° Internal Angle

The general dynamic flow trend and the influence of 90° internal angle hopper geometry on the granular material flow velocities and trajectories are illustrated in Figure 6.29. The mean resultant velocity vectors shown in Figure 6.29 are able to show detailed spatial and temporal particulate characteristics during the flow process. In general, the flow behaviour inside this hopper geometry is to some extent similar to that reported in cases of 60° hopper geometry with some exceptions.

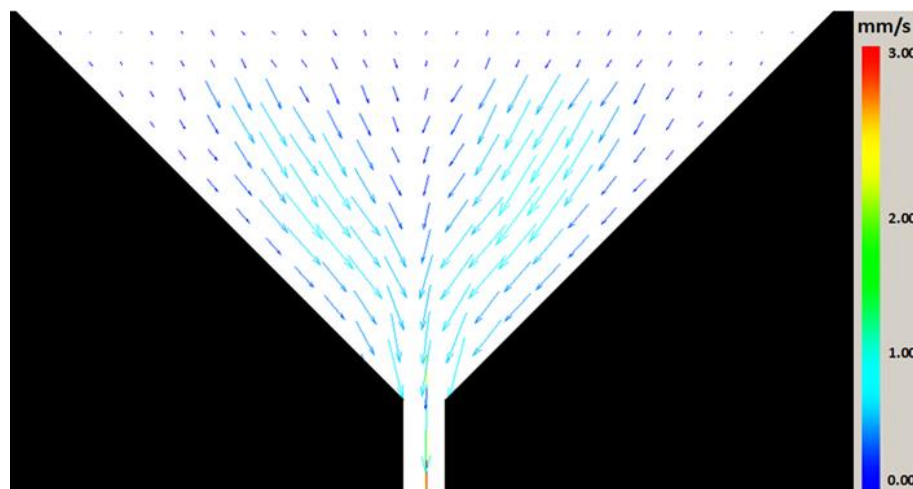


**Figure 6.29** Mean resultant velocity vectors map inside the 90° internal angle hopper geometry filled by coloured pharmaceutical excipient granules

The similarity of the flow process inside 60° and 90° internal angles hopper geometries comes from more than one perspective. Firstly, both geometries show clearly that there is a central flow region which displays a vertical to almost vertical direction of the velocity vectors. Second the surrounding regions show inclined velocity vectors to the hopper boundaries. On the other hand, the main difference between the two angles is the domination of the radial flow trend in cases of 90° hopper angle than those reported in cases of 60°. This is clearly detected from the

lengths and magnitudes of the inclined velocity vectors outside the central flow region. Figure 6.29 shows that there is a very narrow central flow region showing a vertical to almost vertical direction of the mean velocity vectors. The dimension of this central region is less than that reported in cases of 60° hopper geometry, see Figure 6.16. The lower hopper segment shows an inclined direction of the mean resultant velocity vectors, compared to the almost vertical directions reported in cases of 60° geometry at the same segment. This indicates that not all particulates at this segment show continuous particulates motions during the dynamic flow process.

The highest mean velocities values are reported through the colour scale and the length of the vectors at the hopper orifice, avalanche flow trend region from the boundaries toward the central zone and at hopper nozzle. Similarly to what has been reported in cases of 30° and 60° geometries and apart from the previous mentioned regions, particle velocity magnitudes decrease at higher segments and close to the boundaries. As in other cases of 30° and 60° hopper geometries, the vertical velocity components during the whole dynamic flow process across the hopper section at three different heights; H/∞, H/4 and H/2 were measured and the results are shown in Figure 6.30.

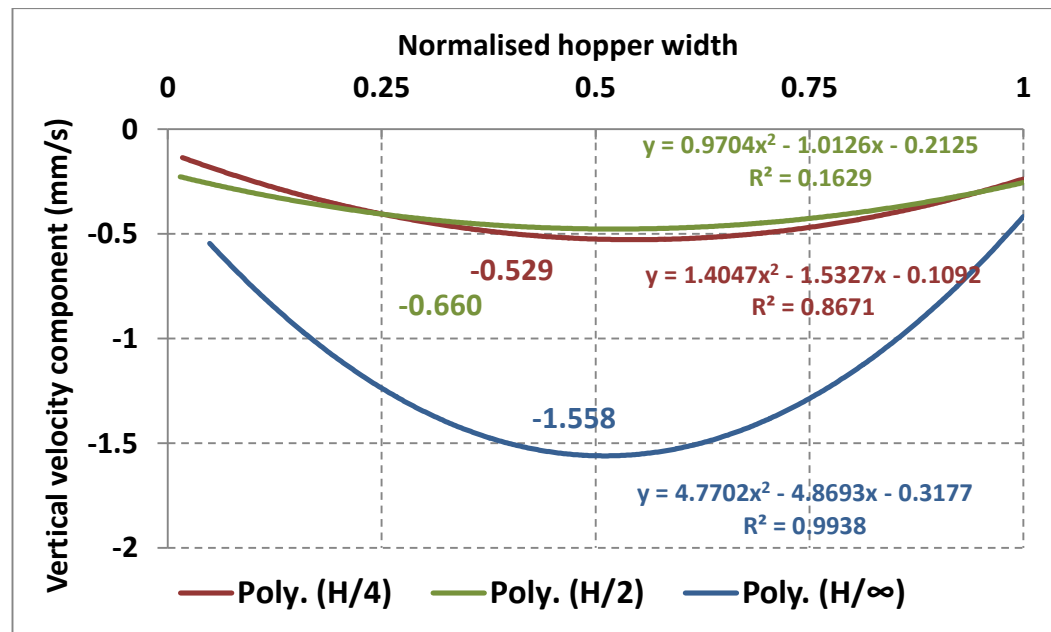


**Figure 6.30** Vertical velocity component plot inside 90° internal angle hopper geometry having 7mm outlet size measured at three heights (H/∞, H/4 and H/2) in 2<sup>nd</sup> order polynomial plot

The plot shows clearly the high magnitude of the radial flow trend from the boundaries at H/4 and H/2 towards the central flow zone as mentioned previously in Figure 6.29. The results show that the maximum value of the vertical velocity component inside the hopper geometry during the whole dynamic flow process was obtained at the hopper outlet region ( $H/\infty$ ). The velocity values are 1.558 (mm/s), 0.550 (mm/s) and 0.682 (mm/s) at  $H/\infty$ , H/4 and H/2 respectively.

The data are plotted in polynomial regression 2<sup>nd</sup> order and the coefficient values ( $R^2$ ) are 0.994, 0.867 and 0.163 at  $H/\infty$ , H/4 and H/2 respectively. Differently from what has been reported in cases of 30° and 60° hopper geometries, the coefficient values  $R^2$  are very low at H/4 and H/2 and the maximum velocity at the middle of the hopper H/2 is higher than that reported at lower segment H/4. In addition to this, the polynomials plot at H/2 cross H/2 plot at the boundaries. It is obvious that the mean velocity magnitudes at higher levels are affected dramatically by the dominant radial flow trend and this prediction is confirmed by the  $R^2$  value at H/2.

Further analysis of the influence of hopper geometry on the vertical velocity component across the hopper width has been conducted using the statistical t-test at  $P = 5\%$  assuming no statistical difference at  $H/\infty$ . The P-values at H/4 and H/2 were  $7.24 \times 10^{-13}$  and  $1.86 \times 10^{-20}$ . The t-values and critical t-values at the same two heights of H/4 and H/2 were 12.37, 14.65 and 2.05, 2.01 respectively. The P-values at both heights H/4 and H/2 are extremely smaller than 0.05 and t-values are greater than the critical t-values indicate significant difference between the data at  $H/\infty$  and that at H/4 and H/2. This indicates that polynomial best fit function is not valid for the vertical velocity component results at H/4 and H/2 levels.

In order to give more explanation for the velocity variations at higher levels, the plot was re-plotted as a normal plot and the results are illustrated in Figure 6.31. The results show clearly the distribution of the actual recorded velocities across each granular bed height. The maximum vertical velocity component inside 90° hopper geometry has been recorded in the central axis at the outlet region. High velocity magnitudes are reported at levels H/4 and H/2 outside the hopper central zone. These regions have a high velocity magnitude as clearly reported in Figure 6.29. The length of the inclined velocity vectors at these sites are longer than those recorded in the hopper centre or close to the walls at the same height centre.

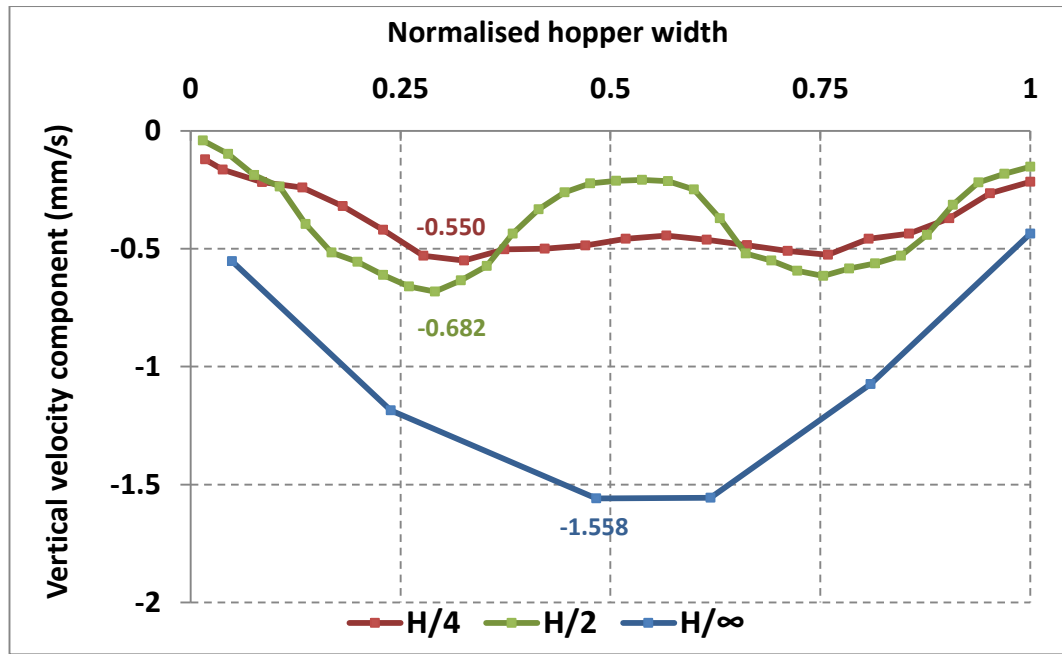


**Figure 6.31** Vertical velocity component plot inside 90° internal angle hopper geometry having 7mm outlet size measured at three heights ( $H/\infty$ ,  $H/4$  and  $H/2$ ) in normal plot distribution

The flow at this area is characterised by the dominant of radial flow trend in an avalanche trend from the boundaries toward the central flow region. On the other hand, the velocity values at the hopper boundaries at  $H/4$  are higher than those reported in case of  $H/2$ .

The low  $R^2$  at  $H/2$  reported in Figure 6.30 is attributed to the low central region velocity magnitudes, compared to their boundaries. The percentage ratios of the maximum vertical velocity components at  $H/\infty$  to  $H/4$  and  $H/2$  are higher by 183.27 % and 128.45% respectively. The ratios were recalculated using the average velocity across the whole horizontal hopper section to provide a more realistic comparison and to avoid any results bias as shown in Figure 6.32.

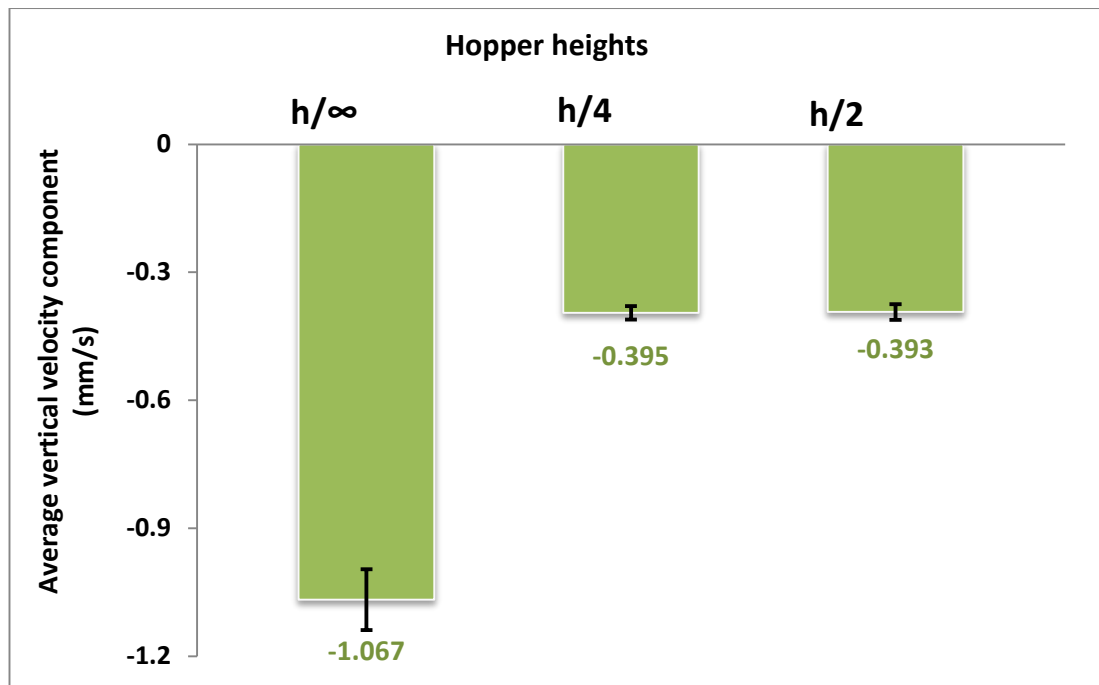


**Figure 6.32** Average vertical velocity component plot across the hopper width inside 90° internal angle hopper geometry at three heights ( $H/\infty$ ,  $H/4$  and  $H/2$ )

The average vertical velocity components across the hopper width at three heights  $H/\infty$ ,  $H/4$  and  $H/2$  are 1.067 (mm/s), 0.395 (mm/s) and 0.393(mm/s) respectively as shown in Figure 6.32. The vertical velocity component plots at  $H/4$  and  $H/2$  in Figure 6.31 show marked overlapping at these levels and their average level across the bed values are almost equal as shown in Figure 6.32. The percentage ratios of the average vertical velocity components at  $H/\infty$  to  $H/4$  and  $H/2$  were higher by 170.13% and 171.50 respectively.

Similar to what has been conducted in cases of the previous two hopper geometries, the maximum vertical velocity component magnitudes at hopper orifice ( $H/\infty$ ) during different time intervals have been measured and the results are shown in Figure 6.33. The results show that there is substantial increment in the values of maximum vertical velocity at the initial stage of the flow, reaching the maximum value at around 0.85 seconds and remains almost constant with minor fluctuations for the rest of the flow process. Slight increases have been reported at the end of the flow stage and this is attributed to high avalanche and particle wall sliding tendencies at this stage .

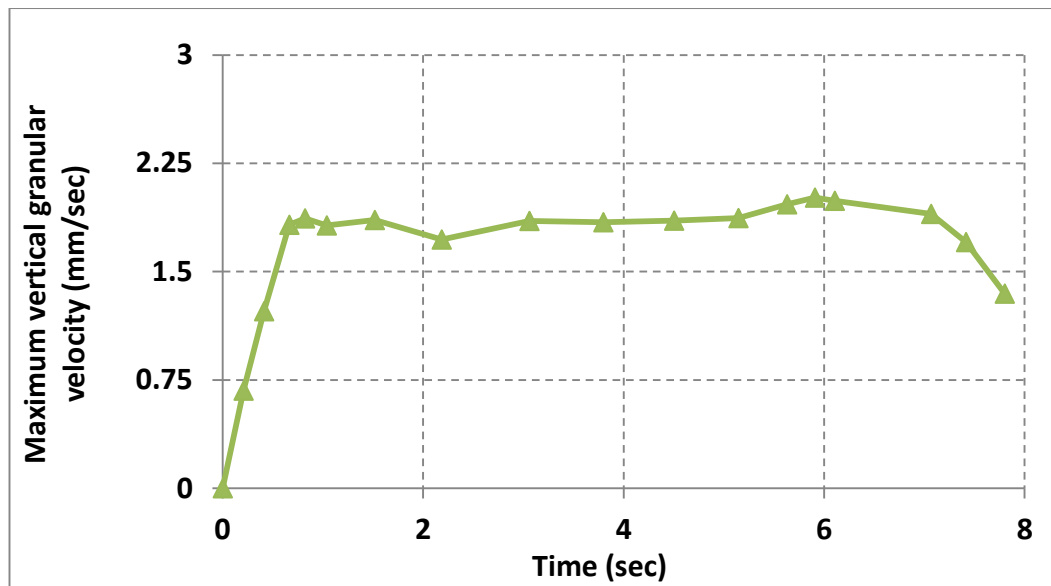


**Figure 6.33** The maximum recorded vertical velocity component values at selected time intervals during the flow process inside 90° internal angle hopper geometry

The initial velocity increases are associated with the initial granular bed dilation forming the central plug flow. In late stage the velocity plot become steadier with minor fluctuations. The time required to discharge all the granules from the hopper is longer than that reported in cases of 30° and 60° hopper geometries. The maximum vertical velocity components recorded here are the least among all hopper geometries.

The overall flow trend and mean resultant velocity vector profiles inside 90° internal angle hopper geometry are illustrated in Figure 6.29 indicates that the flow behaviour inside such geometry is a combination of radial and central flow trends. Further, deep investigation of the flow nature and stages have been conducted and showed that dynamic flow inside such geometry subdivided to three flow stages. The first stage of the flow is the propagation of the central plug flow at the axisymmetric axis of the hopper at the early stage of the flow process as illustrated in Figure 6.34. For easy comparison, Figure 6.34 illustrates both mean velocity vector maps and their corresponding visual images at multiple time intervals, showing clearly the central plug flow initiation and its vertical propagation toward the outer granular layer.

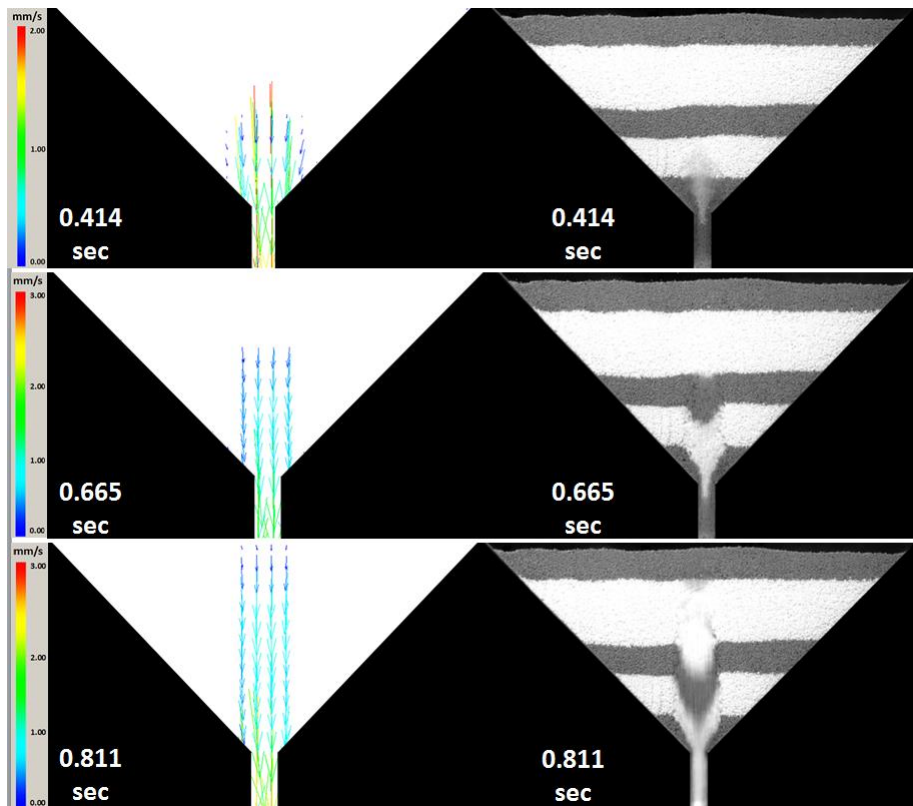


**Figure 6.34** Mean resultant velocity vector profiles at 90° internal angle hopper and its corresponding visual images during the central plug flow propagation (first flow zone)

The central plug flow is located at the axisymmetric axis of the hopper, starting directly above the hopper outlet and propagating vertically toward the outer layer of the granular bed. At 0.414 seconds, the direction of the resultant mean velocity vectors are in a vertical to almost vertical direction at the region close to the hopper outlet. The corresponding visual image at this time, shows clearly the initial bed dilation occurring in the region above the hopper outlet. The motion at this region is mainly reported at the centre of the granular layer located above the hopper outlet with no boundaries involved. The propagation of the plug continues vertically, and at 0.665 seconds it reaches the middle of the hopper, showing the same central trend of spreading. At this stage, the direction of the velocity vectors are vertical and the central plug shows the granular stagnation at both plug sides. The stagnation tendency starts at the level of the first granular layer and expands upward. The granular bed dilation and central plug flow propagation continue and optimize at 0.811 seconds when the plug reaches the outer slice. The plug shows the vertical direction of the mean velocity vectors started at the outlet region and ended at the

outer layer. At 0.811 seconds, the stagnant granular zones are clear at both sides of the central flow zone. Opposite to what has been reported in cases of 60° hopper geometry, the lower hopper segment shows a clear stagnant zone at both sides and the central plug flow expansions and dimensions are much less. These characteristics give an idea that the stagnation tendency in cases of 90° hopper geometry is higher than that reported in cases of 60° geometry.

Quick linking of the first dynamic flow stage outcomes to the stress profiles distributions and direction reported at static condition using PSAT shows strong level correlation and influences. The central plug flow generated at the first flow stage, locates exactly at the expected central zone according to PSAT analysis that shows low stress magnitudes and vertical direction of the major principal stress, more details are available in section 4.3.3 and Figure 4.16. The low stress values and alignment of the stress direction to the gravity will enhance the flow of this zone at the central axis, while the deviation of the stress direction to the hopper wall out of this region increases the extent of stagnation at the boundaries. The spatial and temporal particulate dynamic flow changes at the second stage of the flow process inside 90° internal angle hopper geometries are summarised in Figure 6.35.

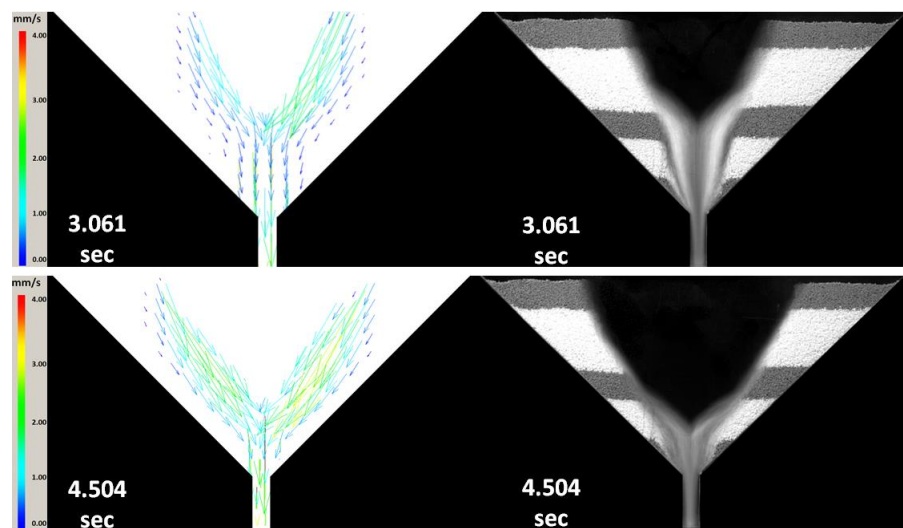


**Figure 6.35** Mean resultant velocity vector profiles at 90° internal angle hopper and its corresponding visual images during the 2<sup>nd</sup> stage of flow process

During this phase, the central plug flow expanded toward the hopper boundaries and the general flow behaviour shows the combination of both the dominant radial flow trend in avalanche style that comes from the boundaries toward the central region

and the uniform central flow trend at hopper's central axis. The particulate velocity vectors colour scale and the length of the velocity vectors prove that the avalanche flow stream shows higher velocity magnitudes than that at the centre of the hopper at some stages. At 3.061 and 4.504 seconds, the velocity vector's map shows that the inner granular layers have particles velocities less than that obtained at the superficial layer while the regions close to the hopper boundaries show no motion. This indicates that the radial velocity trend is dominant at this stage of the flow and the stagnation tendency is persisted.

During the experimental work, the recorded visual tracking of the granular flow process, reports that the tendency of avalanche formation and duration is relatively higher in cases of 90° hopper, than those reported in case of 60° hopper geometry. Hence for a typical case of 90° hopper, Figure 6.36 presents the vertical velocity contour distribution map and its corresponding visual image taken at an identical time interval.

It has been confirmed that the flow trend of the granular material inside 90° hopper geometry is primarily performed through the Y-shaped avalanche trend along their inner surfaces. The visual image shows significant amounts of the stagnant granular material close to the hopper boundaries outside the Y-shape contours.

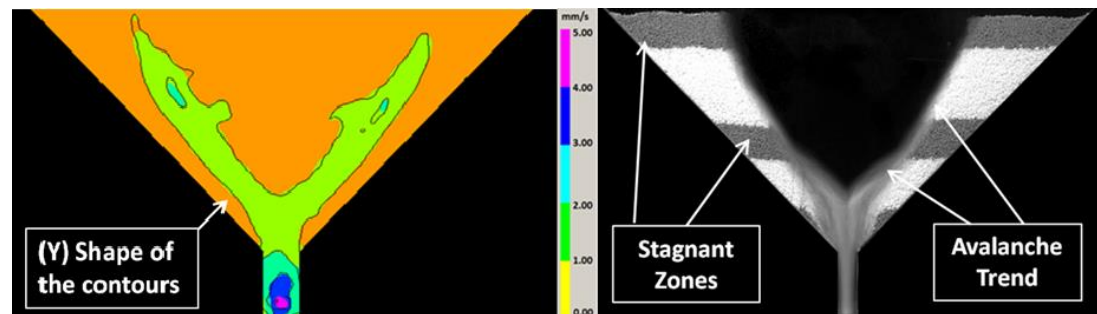


**Figure 6.36** Mean vertical velocity contour map Y-shaped flow region (a) and its corresponding visual image (b) inside 90° hopper geometry at 4.504 sec

The stagnant zones are very clear at this stage of the flow and take mainly the parallelogram shape in most layers. More investigations have been reported in (Section 5.3.2).

Thorough investigation of the flow behaviours using the visual images at this stage, the solid, liquid and gaseous behaviour of the granular material during their flow process has been reported clearly as showing in Figure 6.36 (Forterre and Pouliquen,

2008). The stagnant layers at the hopper boundaries show no motion to represent the solid state, while the flow stream at the axisymmetric axis of the hopper and the flow boundaries represent the liquid status characterised by continuous motion. The gaseous state represented by the messy bounced particulates at the outer layer of the granular flow stream.

The corresponding PSAT results reported at second stage of the flow, show that this region has relatively higher stressed profiles than that at the central zone and less than that at the boundaries, more details are available in section 4.3.3 and Figure 4.16. The direction of the major principal stress at this zone is perpendicular to the walls which increase the stagnation tendency.

The last stage of the granular flow inside 90° internal angle hopper geometry is denoted as the third flow zone and illustrated in Figure 6.37.

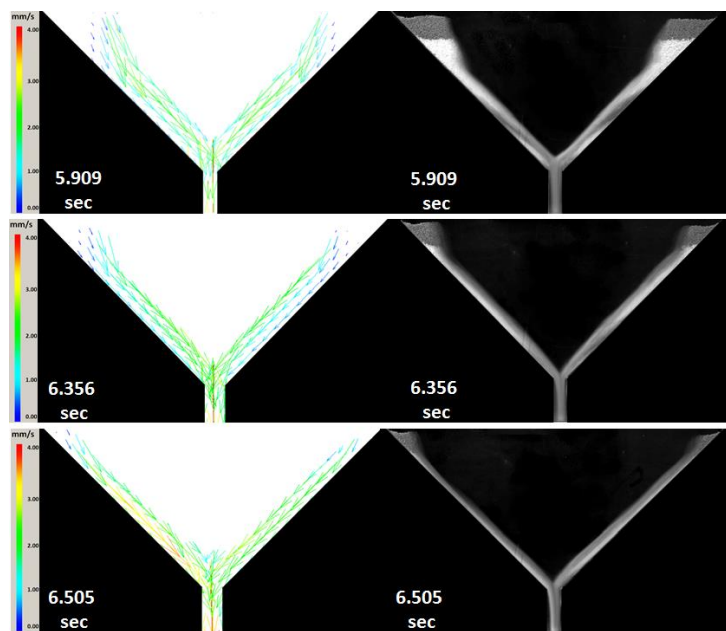


**Figure 6.37** Mean resultant velocity vectors profiles at 90° internal angle hopper and its corresponding visual images during the 3<sup>rd</sup> stage of flow process

During this phase of the flow process, the dynamic flow process mainly occurs through the radial flow trend. In general, the granules flow in avalanche trend toward the outlet direction or slid on the hopper walls at late stage. The mean velocity vector maps show high magnitudes at the flow stream region. The last stage of the flow at 6.505 second is characterised by granules sliding on the hopper walls where all granules are in continuous motion. Stagnant zones at this stage are existed

at early flow time and diminished at late stages when granules slide in continuous radial motion towards the hopper outlet.

The obtained results are in a good level of agreement with the PSAT results obtained in Section 5.3.3 and Figure 4.16 as this region showed high stress profile values compared to the previous two zones, and the direction of the major principal stress is perpendicular to the hopper wall. These microscale properties will delay the flow of granules at this region and increase the stagnation tendency close to the boundaries.

### 6.3.3.1 Evaluation of Variables Influencing Granular Flow Process Inside 60° Internal Angle Hopper Geometry.

#### 6.3.3.1.1 Hopper Outlet Size

Similar to what has been conducted in the previous two hopper geometries, the hopper outlet has been increased to 10mm instead of 7mm to investigate the influence of this increment on the particle spatial and temporal vertical velocities, as well as the general flow trend. Increasing the outlet size changes the outlet mean particle size ratio to around ( $\approx 15.5$  d) instead of ( $\approx 11$  d) in cases of 7mm outlet size. The results of the particle vertical velocity components at  $H/\infty$ ,  $H/4$  and  $H/2$  are shown in Figure 6.38.

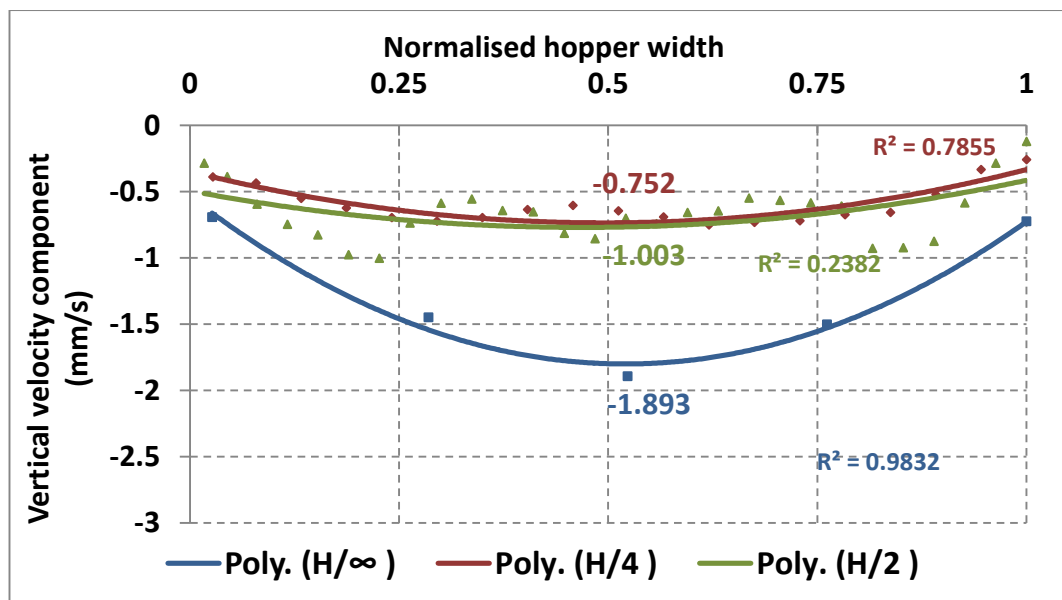


**Figure 6.38** Vertical velocity component plot inside 90° internal angle hopper geometry, having a 10 mm outlet size measured at three heights ( $H/\infty$ ,  $H/4$  and  $H/2$ ) in 2<sup>nd</sup> order polynomial plot

The obtained maximum vertical velocity components of the particles inside 90° internal angle hopper geometry, having 10mm outlet size, are 1.893 (mm/s), 0.752 (mm/s) and 1.003 (mm/s), compared to 1.558 (mm/s), 0.550 (mm/s) and 0.682 (mm/s) for 7mm outlet size at  $H/\infty$ ,  $H/4$  and  $H/2$  respectively. The results indicate that increasing the outlet size from ( $\approx 11d$ ) to ( $\approx 15.5 d$ ) raised the velocity magnitudes by 21.50%, 36.73% and 47.07 at  $H/\infty$ ,  $H/4$  and  $H/2$  respectively.

Similar to what has been reported in cases of 7mm outlet size 90° hopper geometry, the values of correlation coefficient ( $R^2$ ) at  $H/4$  and  $H/2$  are very small and this could be attributed to a high scattering of the points at these levels. In addition to that, the polynomial plots at  $H/4$  and  $H/2$  be overlap at multiple points and level  $H/2$  shows higher maximum vertical velocity than  $H/4$  level. In order to clarify low ( $R^2$ ) values and plot overlapping, the actual velocity values have been plotted in normal distribution as seen in Figure 6.39.

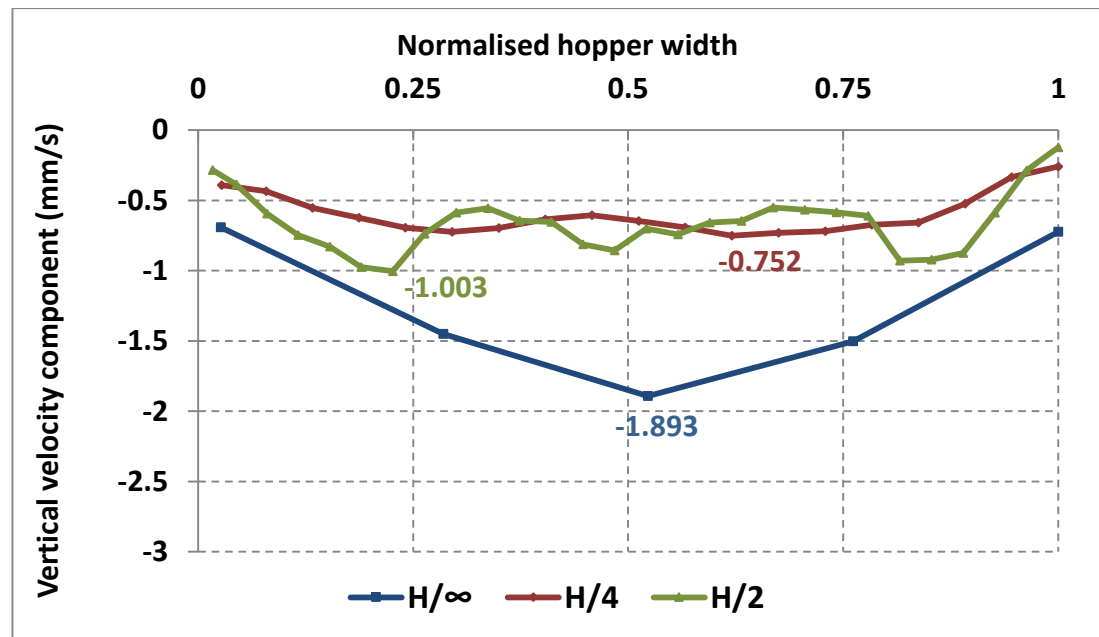


**Figure 6.39** Vertical velocity component plot inside 90° internal angle hopper geometry having 7mm outlet size measured at three heights ( $H/\infty$ ,  $H/4$  and  $H/2$ ) in normal plot distribution

The results display clearly the distribution of the actual recorded velocities across each granular bed height. The magnitudes of the velocities at the boundary regions at  $H/4$  and  $H/2$  are much higher than those recorded at their centres, due to high radial velocity inside such geometries. The velocities close to the hopper walls are

higher in the case of H/4 than at H/2. The results also show clearly that at level H/4 and H/2, velocity value point scattering is less than that obtained in cases of 7mm as illustrated in Figure 6.31 especially at level H/2.

Further analysis has been conducted using mean values of the average vertical velocity component across the bed height to avoid any bias of the analysis, and the results are shown in Figure 6.40, results of 7mm outlet size have been superimposed in the same plot for ease of comparison.

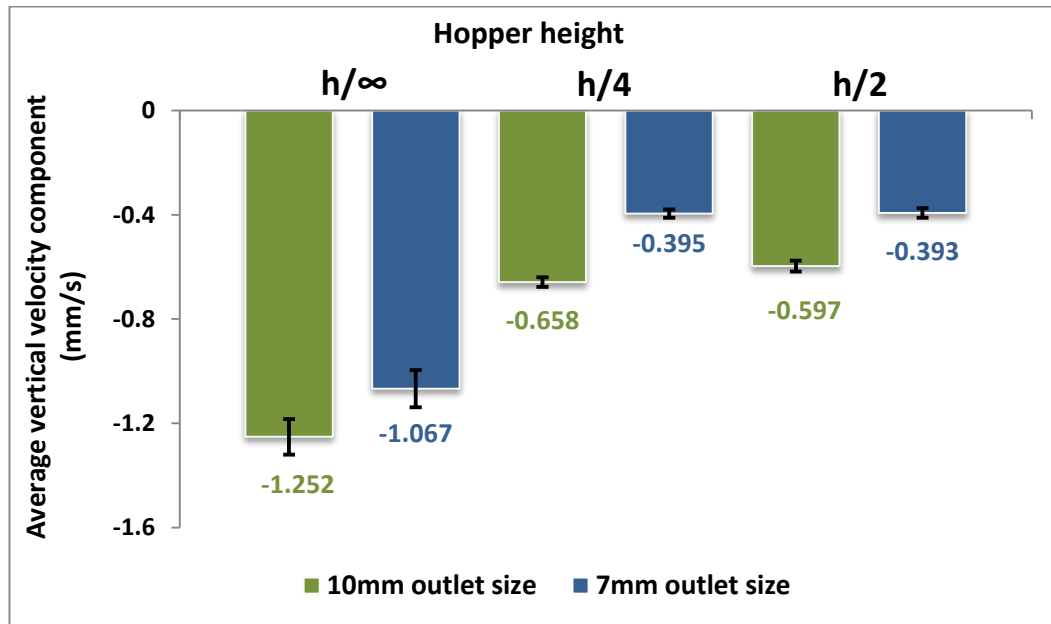


**Figure 6.40** average vertical velocity component plot across the hopper width inside 90° internal angle hopper geometry at 7 mm and 10mm outlet sizes at three heights ( $H/\infty$ ,  $H/4$  and  $H/2$ )

In general, increasing the outlet size markedly increases the velocity gradients at all height levels and alters the general flow trend. The percentage increments in the average velocity at 10mm outlet size, compared to 7mm size, are 17.34%, 46.58% and 67.30% at  $H/\infty$ ,  $H/4$  and  $H/2$  respectively.

### 6.3.3.1.2 Granular Bed Lubrication

Granular bed lubrication influence on particulate velocity gradients has been investigated in cases of 7mm hoppers outlets size using 2% magnesium stearate powder and the results are illustrated in 6.41.

It is clear from Figure 6.41 that bed lubrication increases vertical particle velocity components across all height levels. The maximum vertical velocity components at  $H/\infty$ ,  $H/4$  and  $H/2$  inside the lubricated bed are 1.686 (mm/s), 1.105 (mm/s) and 0.824 (mm/s), compared to 1.558 (mm/s), 0.529 (mm/s) and 0.660 (mm/s) in cases of non-lubricated bed at the same levels respectively. Opposite to what has been reported in cases of the non-lubricated system at Figure 6.30, the particulate velocities at  $H/2$  are less than those recorded at  $H/4$ . This indicates that lubrication of the granular bed increases the central flow via decreasing particle-particle friction. Furthermore, ( $R^2$ ) values of the polynomial plot show a marked improvement in cases of lubricated geometry compared to the non-lubricated one especially at higher levels  $H/4$  and  $H/2$ . These results indicate that lubrication of the granular makes the flow process more uniform than the non-lubricated system as the particle-particle friction tends to reduce in such conditions.

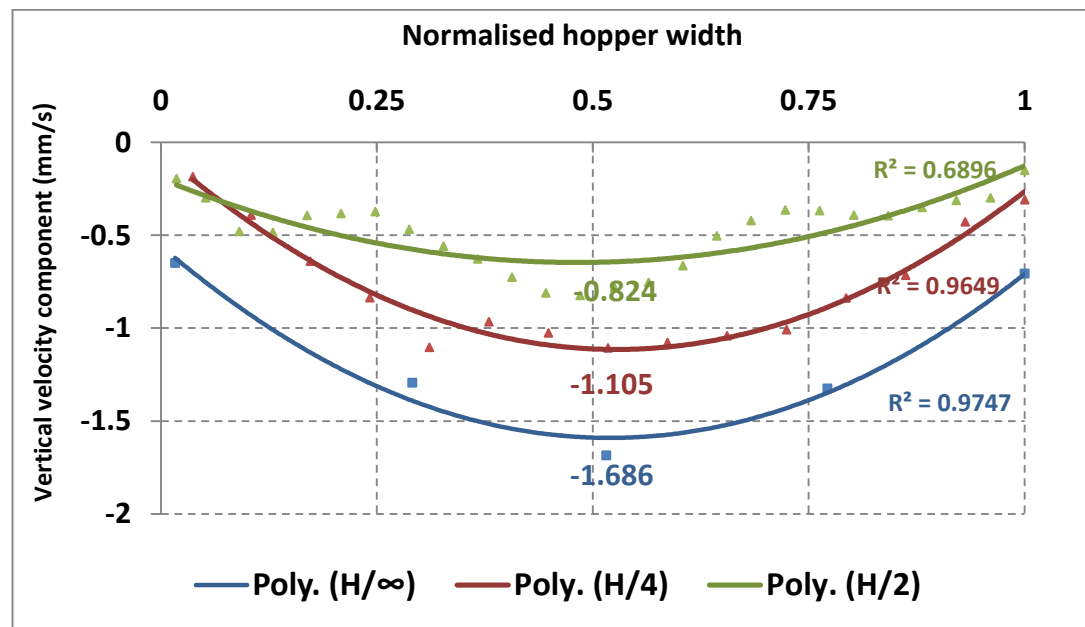


**Figure 6.41** Vertical velocity component plot inside lubricated  $90^\circ$  internal angle hopper geometry having 7mm outlet size measured at three heights ( $H/\infty$ ,  $H/4$  and  $H/2$ ) in 2<sup>nd</sup> order polynomial plot

These results have been confirmed using the average vertical velocity components across the whole granular bed as shown in Figure 6.42.

The obtained results prove that the average velocity is higher at  $H/\infty$  followed by  $H/4$  and  $H/2$  respectively. The percentage increases are 6.09%, 96.96% and 20.77%

respectively. Both results in Figure 6.41 and 6.42 prove the uniformity of the flow inside the lubricated bed comparing to the non-lubricated bed.

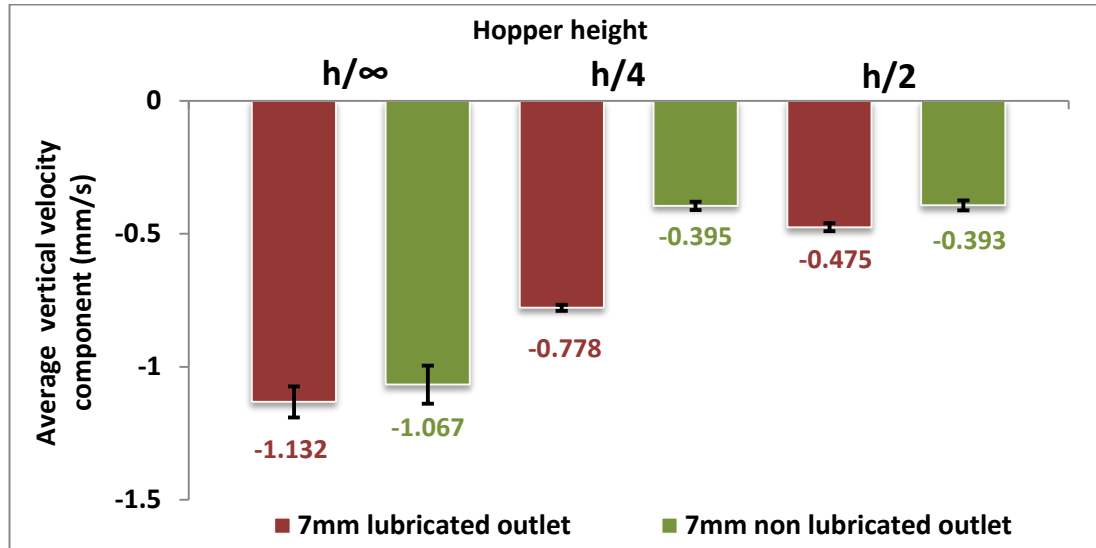


**Figure 6.42** Average vertical velocity component plot across the hopper width inside lubricated  $60^\circ$  internal angle hopper geometry for lubricated and non lubricated sysytems at three heights ( $H/\infty$ ,  $H/4$  and  $H/2$ )

The obtained results from granular bed lubrication and outlet size increment show clearly the complexity of the flow process inside  $90^\circ$  hopper geometry, and how changing some variables, crucially alters the flow behaviour.

### 6.3.3.1.3 Hopper Walls Roughness

The results of the influence of hopper wall roughness on particle vertical velocity magnitudes are shown in Figure 6.43, where clear overlapping is reported at  $H/4$  and  $H/2$  levels. The maximum vertical velocity components at  $H/\infty$ ,  $H/4$  and  $H/2$  in cases of rough hopper walls are 1.369 (mm/s), 0.497 (mm/s) and 0.574 (mm/s) comparing to 1.559 (mm/s), 0.550 (mm/s) and 0.682 (mm/s) in case of smooth hopper walls at the same heights respectively.

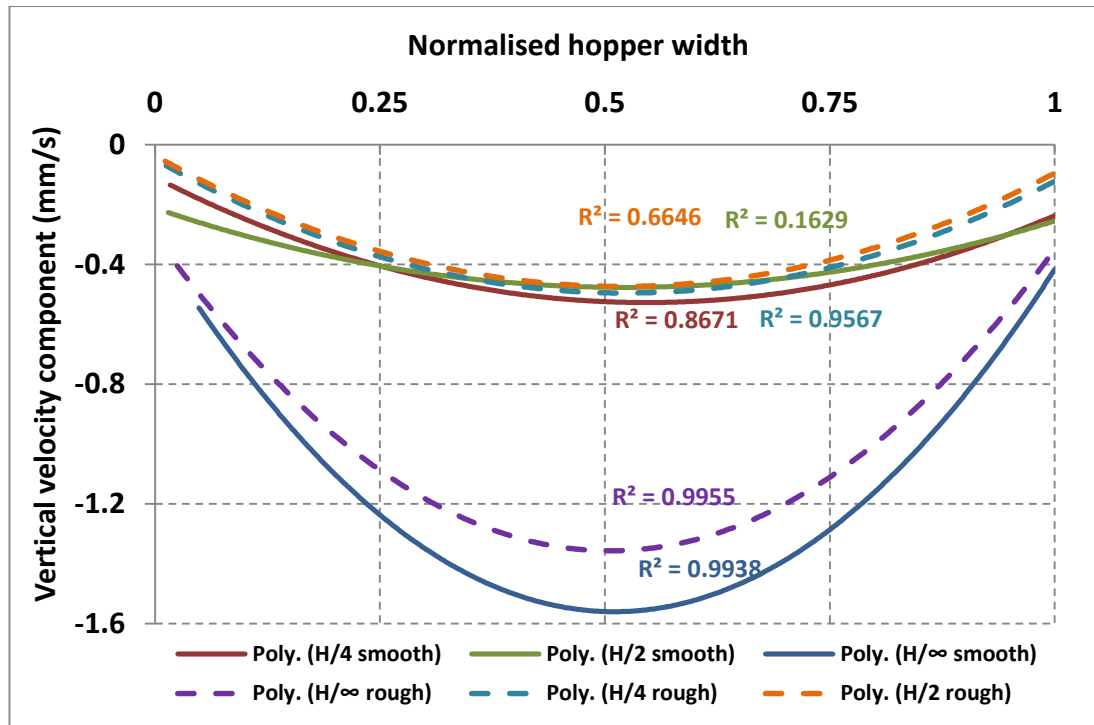


**Figure 6.43** Vertical velocity component plot inside smooth and rough wall 90° internal angle hopper geometry having 7mm outlet size, solid line are smooth walls and dashed lines are rough walls measured at three heights ( $H/\infty$ ,  $H/4$  and  $H/2$ ) in 2nd order polynomial plot

The percentage reduction in the maximum vertical velocity components due to wall roughness at  $H/\infty$ ,  $H/4$  and  $H/2$  are 12.19%, 9.64% and 15.84% respectively. The reductions of the particle velocity at the hopper boundaries have been measured, and the results were 22.42%, 31.09% and 55.42% at  $H/\infty$ ,  $H/4$  and  $H/2$  respectively. A high reduction of particles velocities at the boundaries show clearly the significant influences of hopper wall roughness on the particle velocity gradients at the boundaries (Babout et al., 2013). The reduction of particulates velocity at the hopper boundaries inside 90° hopper geometry is higher than that obtained in case of 30° and 60° hopper geometries.

Further clarification of the overlapped polynomial plots in Figure 6.43 at  $H/4$  and  $H/2$  levels for both cases has been conducted using normal data plot as illustrated in Figure 6.44. The results show relatively high velocity magnitudes outside the central hopper zone in cases of both rough and smooth walls. Increasing walls roughness increases the particles velocities at the hopper central region. This could be

attributed to low radial flow in cases of rough surface as the particles sliding on the hopper walls were affected crucially by the surface smoothness.

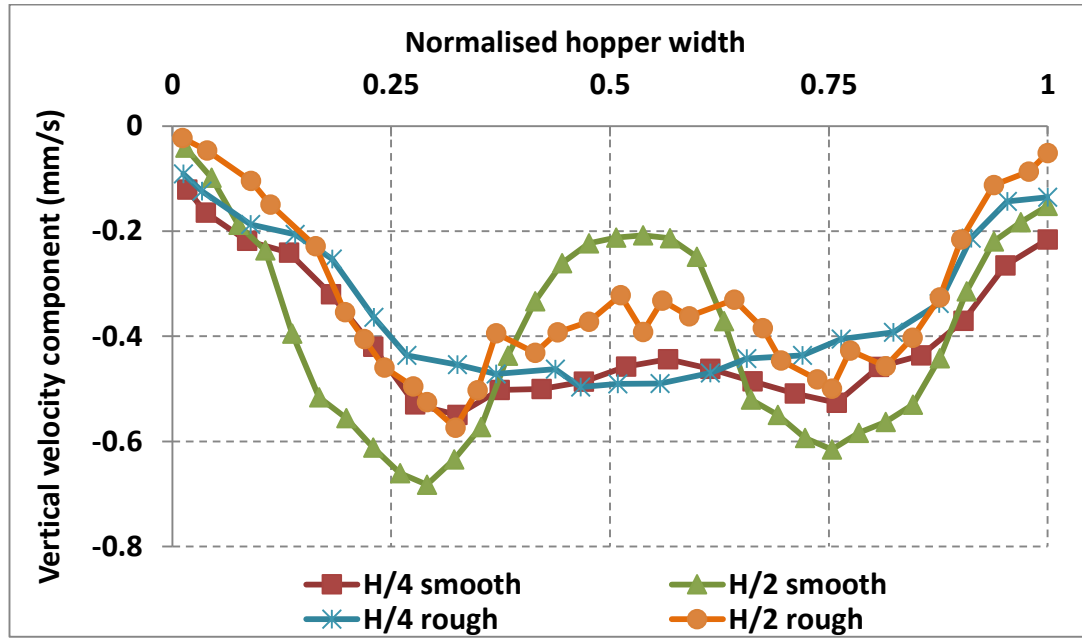


**Figure 6.44** Vertical velocity component plot inside 90° internal angle hopper geometry having 7mm outlet size and rough walls measured at three heights (H/4 and H/2)

Furthermore analysis of the influences of the wall roughness on the particles vertical velocity have been conducted, using the average values of the vertical velocities across the horizontal sections as shown in Figure 6.45.

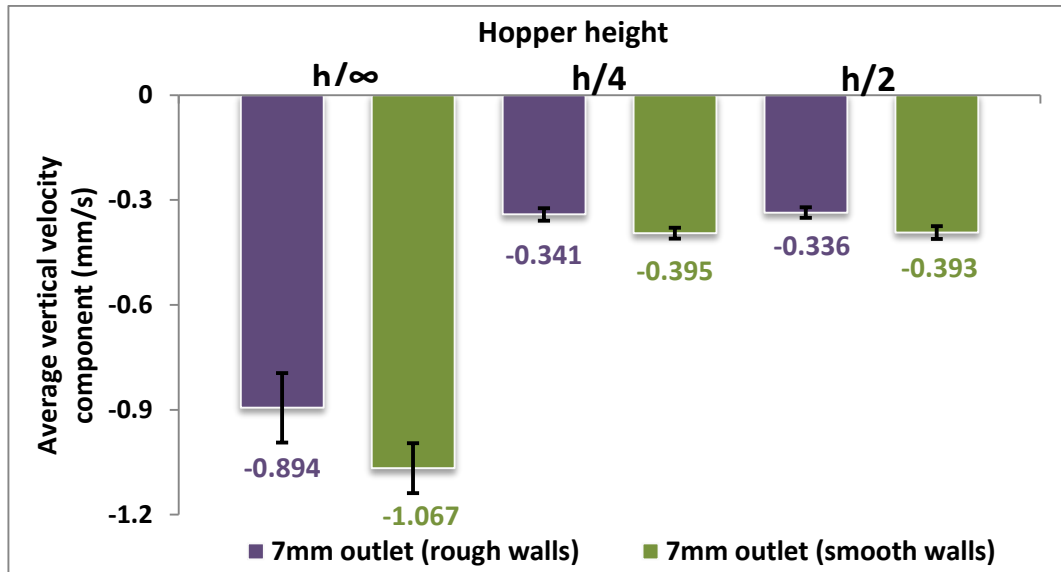


**Figure 6.45** Average vertical velocity component plot across the hopper width inside smooth and rough walls at 90° internal angle hopper geometry for smooth and rough walls at three heights (H/∞, H/4 and H/2)

The results show that the average vertical velocity component across the hopper width at H/ $\infty$ , H/4 and H/2 in case of rough walls are 0.894 (mm/s), 0.341 (mm/s) and 0.336 (mm/s), compared to 1.067 (mm/s), 0.395 (mm/s) and 0.393 (mm/s) for smooth walls at the same heights respectively. The declining ratios in the average velocity values are 16.21%, 13.74% and 14.50% at heights H/ $\infty$ , H/4 and H/2 respectively. In general, increasing wall roughness, decreases the particulate resultant velocities and the maximum decrease are reported at boundaries as a result of decreasing granular radial flow.

### 6.3.4 General Remarks

#### 6.3.4.1 Theoretical and Experimental Discharging Rates

The average granular material discharge rates from all hopper geometries were performed experimentally using an equal amount of the granules, and the results are presented in Figure 6.46. The results are the mean values of eight readings for each hopper angle, and recorded in assistance with the high speed camera digital recordings. The obtained results have been compared with the theoretical results by applying the Rose and Tanaka equation (Eq.6.1) (Rose and Tanaka, 1959) as shown in Figure 6.46.

$$W = 0.16 D^{2.5} \rho \sqrt{g} \left( \frac{D}{d} - 3 \right)^{0.3} f(\alpha) (Z - 5)^{-0.5} \quad \text{Eq. 6.1}$$

$$f(\alpha) = [\tan \frac{\theta}{2}]^{-0.35} \quad \text{if } \frac{\theta}{2} < 90 - \phi \quad \text{Eq. 6.2}$$

$$f(\alpha) = [\tan(90 - \phi)]^{-0.35} \quad \text{if } \frac{\theta}{2} \geq 90 - \phi \quad \text{Eq. 6.3}$$

Where D is the hopper outlet diameter,  $\rho$  is the solid bulk density, g is the gravity, d is the (average) particle diameter, Z is particle shape factor, equal to 6 for the grains used here (Heywood, 1933) and  $\alpha$  is the bulk solid static angle of repose. Both theoretical and experimental results show that the discharge rate is the highest for the lowest internal angle and decreases dramatically with an increase in the internal angle.

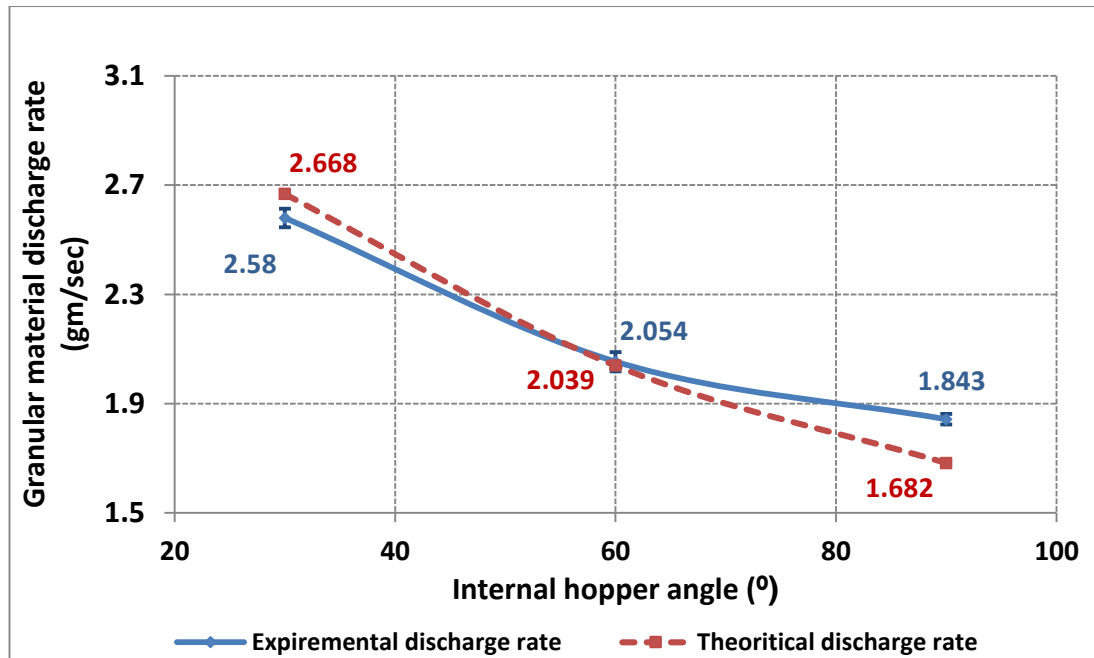


**Figure 6.46** Comparison of the theoretical and the experimental granular discharging rates at different internal hopper angle

The results in Figure 6.46 show a fairly good level of agreement between the experimental and the theoretical discharge rates for all the cases of hopper angles. The deviations among the experimental and theoretical results are 3.4%, 0.73% and 8.71% respectively. However, the relatively high value of deviation in the case of the 90° hopper is noted with the consideration that the theoretical prediction did not rigorously account for the complex modes of granular flow observed in the experimental trials and discussed in detail in section 6.3.3 (Albaraki and Antony, 2014).

#### 6.3.4.2 Granular Flow Wave at Central Plug Flow

Very interesting phenomenon has been reported in cases of lubricated granular bed flow inside silos having high internal angle geometries; 60° and 90° filled in industrial filling method and having large outlet size (10mm). This phenomenon has been denoted as central flow zone wave propagation cycle and illustrated in Figure 6.47. Although, analysis of granular flow trend or stress profile distribution inside silos is not part of this research project, multiple trials have been conducted for future work using DPIV, and this phenomenon has been reported during these experiments and reported here for documentation. The incidence of this

phenomenon in cases of hopper industrial filling is very minimal, compared to the silo geometry.

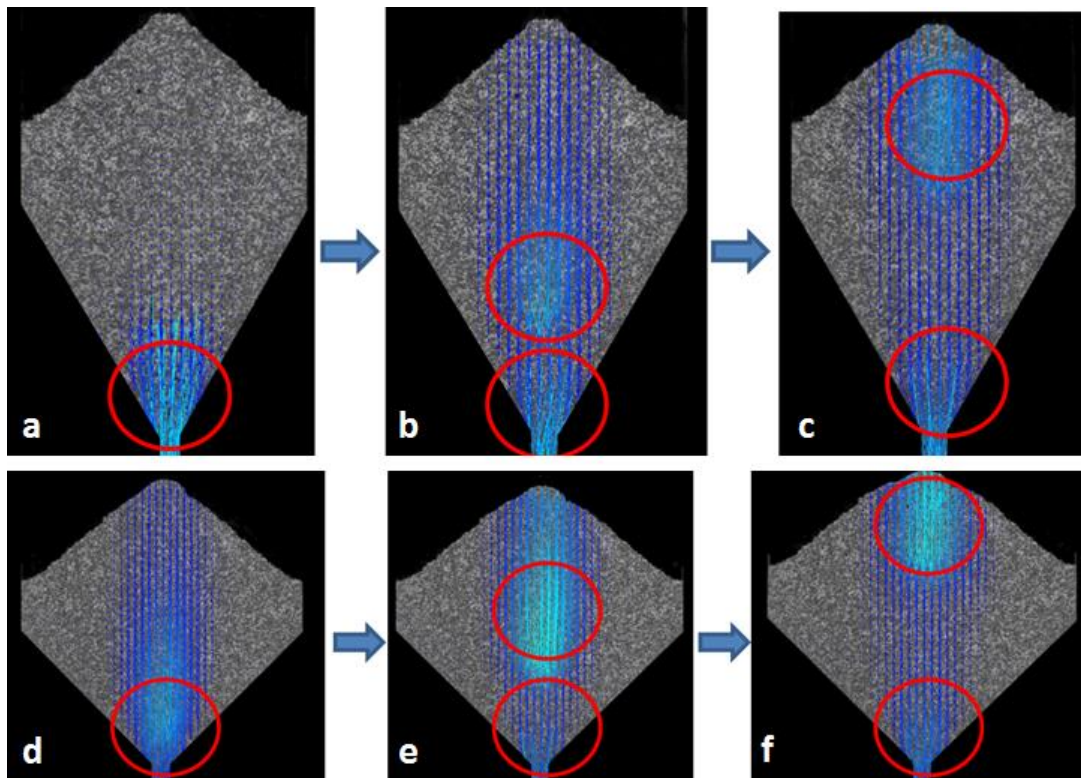


**Figure 6.47** Central flow zone wave propagation cycle inside high internal angle silo geometries; (a,b and c) inside  $60^\circ$  silo geometry and (d,e and f) inside  $90^\circ$  silo geometry

The superimposed real time velocity vectors on actual images of the dynamic granular flow in Figure 6.47 show clearly the stages of this cycle, inside both silo geometries at the axisymmetric axis. The time required for the cycle initiation and propagation is very short and occurs during the development of the central plug flow. The wave starts exactly above the outlet region, directly after the outlet opening, as seen in Figure 6.47 (a and d). It propagates upward in a vertical direction at the axisymmetric axis of the silo till it reaches the outer granular layer, see Figure 6.47 (b, c, e and f). As the first wave diminished at the top section of the silo, another wave starts to generate at the outlet region, as clearly shown in Figure 6.47 (c and f). This cycle generates, propagates and diminishes in a very short period of time and is greatly influenced by the lubrication of the granular bed and outlet sizes.

## 6.4 Conclusions

Dynamic flow behaviours of the granular materials inside multiple hopper geometries have been assessed using the DPIV method. The results show that though the granular materials characterised here are classified conventionally as free flowing, the hopper geometries still have great influence on their flow trend and the impact increases with increasing the internal angle. Hopper having small internal angle, shows in general, uniform mass flow behaviour where granules are discharged via central flow trend at high velocity. Increasing hopper internal angle shows a clear non-uniform flow trend and granular stagnation at hopper boundaries. The general flow trend inside higher angles is funnel flow trend, and flow occurs through the central and radial flow routes. The central flow route occurs during the generation and propagation of the central plug flow, while the central flow route comes later from the boundaries toward the central axis. The higher the internal angle is, the higher the extent of stagnation, non-uniform flow behaviour and the domination of radial flow is observed. Increasing the outlet size has greatly influences particulate velocity, rather than lubrication of the granular bed. In general, increasing hopper wall roughness decreases the overall particulates velocity and more reductions have been reported at the boundaries compared to the central region. The influence of wall rough at the boundaries was higher at the higher internal hopper angle. Hopper geometry having (90°) internal angle shows very complex flow behaviour and changing any flow variable such as bed lubrication affect the flow trend dramatically.

The general dynamic flow results here are in good level of agreement with the PSAT results and assumptions reported in chapter 4 for the general flow behaviours. The predictions of the flow trend and the flow zones inside multiple hopper geometries, based on the stress profile distributions and the direction of the major principal stress are validated here quantitatively using DPIV. From earlier PSAT results, the smaller internal angle hopper geometry (30°) displayed uniform stress distribution and a vertical direction of the major principal stress favoured mass flow trend, and also characterised by a vertical to almost vertical direction of the velocity vectors inside all hopper segments using DPIV. This means that all particles were in continuous motion inside the hopper geometry during the flow process. This is

directly related to the uniform stress status inside the hopper as well as the alignment of the major principal stress to the direction of the gravity. On the other hand, higher internal hopper angles ( $60^\circ$  and  $90^\circ$ ) showed clear funnel flow trend and divided into three consequent flow zones. The early central plug flow with vertical velocity vectors at the central hopper axis (first zone) which locates exactly at the low stressed central zone, having vertical direction of the major principal stress. The second flow zone comes next, where the flow is a combination of both radial and central flow routes, with an inclined direction of the velocity vectors toward the central zone and outlet region. This zone locates at the second stressed zone, where the major principal stress is inclined in a parallel and perpendicular direction to the hopper wall inside  $60^\circ$  and  $90^\circ$  hopper geometries respectively. The third flow zone contains the last flowable particulates, and the direction of the velocity vectors are inclined toward the central zone and outlet region, due to avalanche flow trends. According to PSAT analysis, this zone showed the highest stress magnitudes within the higher hopper angle geometries and the direction of the major principal stress is totally parallel or perpendicular towards the wall for both  $60^\circ$  and  $90^\circ$  geometries respectively.

Overall, this chapter has strongly quantified the flow velocities using advanced DPIV and supports the generic hypotheses of PSAT results, i.e., the initial state of shear stress distribution in particulate fillings to their subsequent dynamic flow characteristics are quite strong. When a dynamic stress measurement in micron size particulates becomes feasible in future such fundamental links could be further enriched.

## **Chapter 7 Visual Mapping of Stress Distribution Profiles within Pharmaceutical Granular Bed Subjected to Relatively Low Uniaxial Confined Compression Using PSAT**

This chapter aims to report, experimentally, the maximum shear stress profile propagation and distribution inside pharmaceutical excipient granules subjected to relatively low uniaxial confined compression, using PSAT. Whereas compression characteristics of granular materials are studied extensively in the previous literature under high levels of external compression loading, information is lacking on their response under low levels of compression loading and this aspect is the focus of the current work. In this chapter, stress analysis of micron size grains under low compression loading is presented, whereas Chapter 8 will present investigations for the displacement profiles of grains using DPIV under identical loading conditions. The investigations focused mainly on the influence of interparticle frictions and wall friction on stress propagation inside the compressed bed. In this study, the maximum compression force applied is 34 Newton. The pharmaceutical excipient granules are the same fabricated sensor particles used in Chapter 4 and characterised in Section 3.2.2, having particle size distribution (300-1000 $\mu$ m).

### **7.1 Introduction**

The granules and powders compression process in the pharmaceutical industry for solid dosage form manufacturing consists of four to five consequent stages, occurring within a very short space of time (Carstensen and Toure, 1980, Denny, 2002, Mallick et al., 2011). The available information in the literature about the nature of stress changes at the early stage of the compression process during particles rearrangement, is still ambiguous to researchers and deeper investigation of this stage is needed and recommended (Denny, 2002, Davies, 2009). The early compression stage in Heckel's plot, characterised by nonlinear behaviour of the plot, is attributed to the changes which occur during the particles rearrangement stage (Mallick et al., 2011, Mallick, 2014). The rearrangement phase is characterised by relatively free particle motion and sliding without any significant deformation (Mallick et al., 2011). Mallick (2014) provided some new characteristics for the

early nonlinear approach of the Heckel equation which represents the changes occurring during the rearrangement compression stage in order to estimate the granule compressibility. He subdivided the early curved approach into two linear lines; primary and secondary rearrangement stage, and the Heckel equation becomes a triexponential equation. Although such a new model is limited to the bed density changes, it might be advantageous and provide greater insight and understanding of the compaction process. Literature mainly investigates the influence of high compression force on powders density profile changes and occurrence of capping or lamination phenomena (Sorensen et al., 2005, Sorensen et al., 2006, Lou et al., 2015, Yohannes et al., 2015, Sarkar et al., 2015). Capping is simply defined as removal of the top crown or bottom part of the compressed bed. Akseli et al. (2014) studied the influence of manufacturing variables, such as compression force, manufacturing devices shape and compression speed on tablet capping tendency. They have reported that the use of capping tendency ratio (EG), which is based on an extraction of Young's modulus ( $E$ ) in axial and radial directions, is an efficient non-destructive indicator of tablet capping tendency. The dimensionless capping tendency ratio  $EG = E_{axial}/E_{radial}$  is able to show the tablet's weakest plane and provide valuable information for both the formulators and manufacturers. Sarkar et al. (2015) studied the influence of compression force on the tablet capping tendency using a specially designed roll compression device with fitted air compensator, in order to increase the dwelling time of the compressed granules. The results indicated that increasing in-die dwelling time of the compressed granules decreases the capping tendency at low compression forces. At high compression force and above the required force for particles deformation, the influence of applied force rate is more significant.

In pharmaceutical industries and due to the nature of the raw materials, rearrangement stage of the compression cycle occurs under relatively low external loading conditions and greatly influences the bed densification and internal stress propagation (Nordstrom et al., 2008, Nordstrom et al., 2009). On the other hand, the rearrangement phase for titanium powder during the compaction process occurs within 200 MPa (Lou et al., 2015). Discrete fine particles significantly alter the particulates initial packing and the rearrangement phase, but have no influence on the compaction and tensile strength of the compressed bed. The literature agrees that this phase is a critical phase during the compression cycle and the changes during

this phase are still ambiguous (Mallick, 2014). Clear understanding of the influence of interparticle friction as well as the particle wall friction on the stress propagation and distribution, has not been investigated deeply yet and is addressed in the present work.

## 7.2 Material and Methodology

### 7.2.1 Material

Materials used in this chapter are the fabricated stress responsive granules, characterised in Section 3.2.2 having a particle size range of 300 to 1000  $\mu\text{m}$ . A special rig able to apply uniaxial compression has been designed and fabricated in our laboratory at the University of Leeds to fulfil the requirements of both the PSAT and DPIV setup and requirements as shown in Figure 7.1.

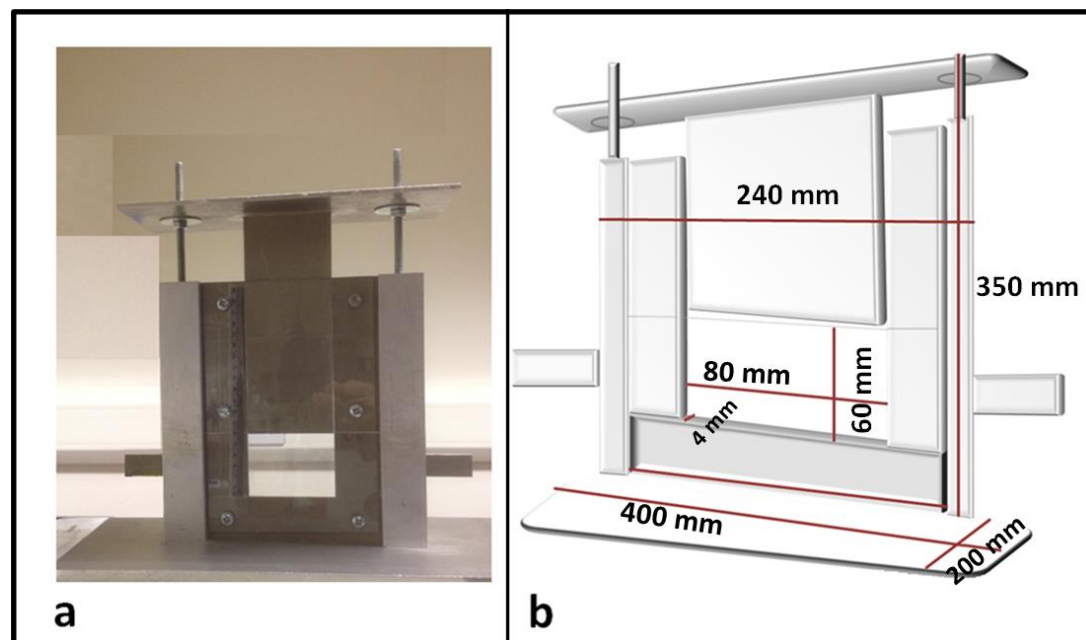


**Figure 7.1** Fabricated compression chamber (a) actual image of the rig and (b) schematic diagram of the rig and its dimensions

The dimensions of the compression rig base is 400mm X 350mm, the compression chamber dimensions are 60mm height, 80mm width and 4mm thickness (perpendicular to the plane of the rig). The rig's front and rear sides have been fabricated using transparent Perspex sheets that allow sufficient light illumination of the granular bed. Compression load was applied at the centre of the top punch. The

preliminary studies prove that the rig is able to tolerate a relatively low compression force up to 150N, showing no damage or deformation to the test rig (rigid and smooth walls) and no granular leakage was observed.

### 7.2.2 Methodology

The major components of the PSAT experimental set up for granules compression are the circular polarised light projector, digital PSAT camera and software, manual compression rig with digital force gauge, fabricated compression rig, as illustrated in Figure 7.2. The applied compression force was adjusted at the centre of the top part of the rig, also illustrated in Figure 7.2(a).

The sensor particles were loaded into the compression chamber very carefully to minimise segregation of granules. A proper funnel with a flexible nozzle has been used to feed granules into the die cavity where the nozzle was aligned along the central axis of the die which was filled with the granules in layers and built up to the boundary. The maximum height of the granular bed inside the chamber was 6cm. The die filling procedure was repeated 15 times to assess the initial packing density of the granules within the die cavity and the results showed steady results with reasonable variation range,  $8.13 \pm 0.295\text{gm}$ .

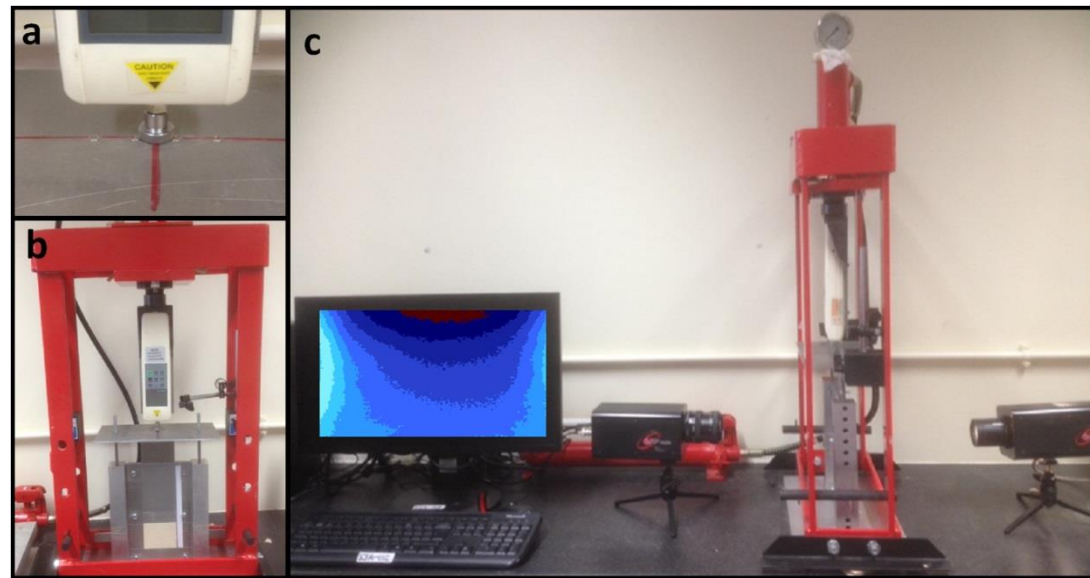


**Figure 7.2** Experimental setup for granular material compression at relatively low uniaxial compression using the PSAT technique: (a) central guide lines at the top part of the rig (b) manual compression rig and (c) PSAT system arrangement

Once the optimum PSAT setup conditions were completed, the emitted circular polarised light illuminated the birefringent sensor particles inside the compression rig and the PSAT camera captured multiple images at different static loading conditions. The force gauge in the manual loading rig directly measures the amount of applied loads. The captured images were analysed for the stress distribution characterised inside the compressed granules using PSAT quantitative software.

#### **7.2.2.1 Limitations of PSAT for Granular Compression**

In the case of compression, the optimum distance between the birefringent sample and the light source ranges from 33 to 35cm, the optimum sample depth is 4mm and the maximum applied load allowing around 180 bed light intensity is not more than 38N. The maximum force applied in this study was restricted to 34N due to high light retardation within the granular bed under compression load. On the other hand, these limitations were used properly to investigate thoroughly the stress status of the compressed granular bed at low external loading conditions.

### **7.3 Results and Discussion**

The profiles of maximum shear stress propagation and distribution within the sensor particles inside the die chamber under different levels of compression are shown in Figure 7.3. The image colour scale was adjusted and calibrated, in order to simplify the comparison of the image fringes and simply represent the spatial and temporal stress magnitudes. The images show clearly that the propagation of the maximum shear stress profiles start directly below the upper punch and diffuse through the granular bed vertically and laterally to the die chamber base, and to boundaries respectively. Diffusion and distribution of the maximum shear stress within the die chamber are strongly in a non-homogenous manner. The top section of the granular bed directly below the punch shows higher stress magnitudes than those observed at the middle and bottom sections, as well as die boundaries at all loading conditions. It is clear that the stress profiles propagate in a downward direction reaching the base of the compression die and then deviate toward the wall boundaries.

Elevation of the compression load increases the density of granular bed as the inter-particles voids are minimised and the granules are rearrange within the die.

Increasing both compression load and granular bed density, though to increases the contact between granules as well as the interparticle friction, resulting in high shear stress propagation and increasing contacting force network between the particulates.

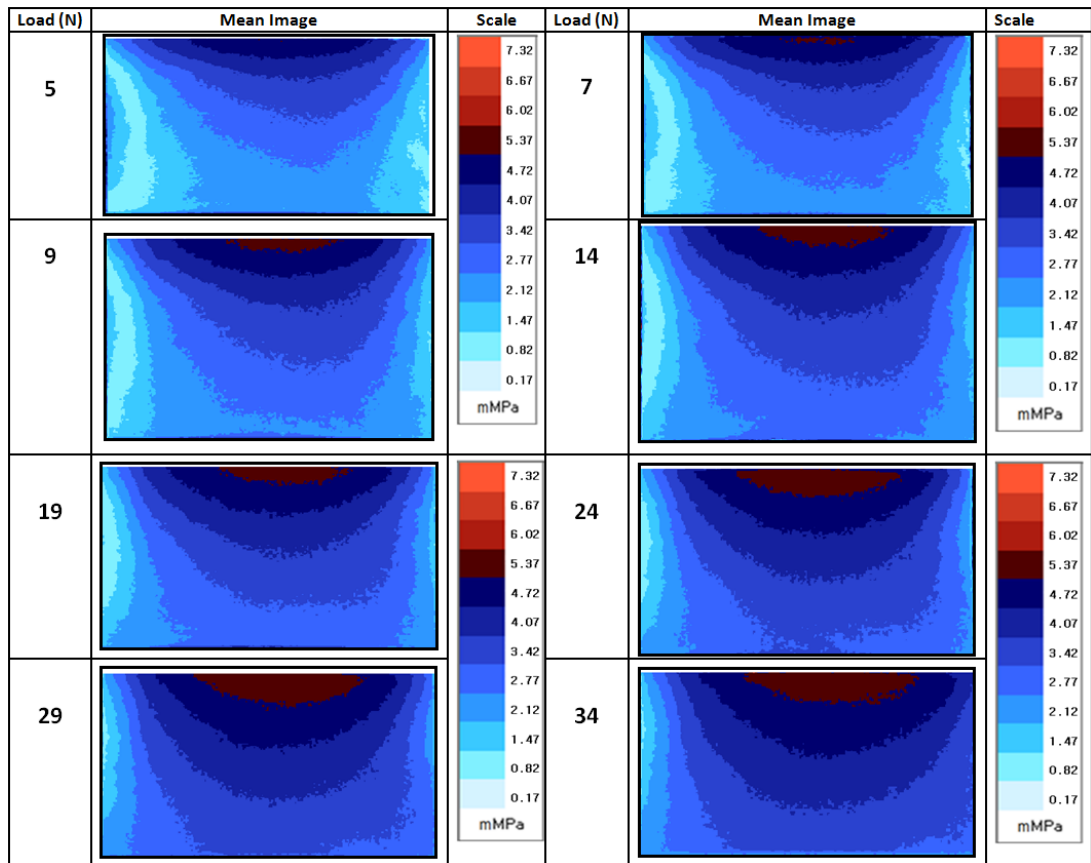


**Figure 7.3** Maximum shear stress profiles propagation within the sensor particles under different external loads and their corresponding heights

The relatively low stressed zone at the bottom die segment and at the die boundaries compared to that along the central zone of the granular bed could be attributed to low particles motion at these locations. This assumption will be investigated in detail in the next chapter during application of the DPIV technique on granular bed compression and deformation at similar conditions.

Increasing the external compression loads from low magnitudes (5N) to higher loads (34N) leads to marked increases of the stress magnitudes within all the die segments. Higher increment has been reported at the zone located directly below the punch and the central zone. A high level of stress at these regions is attributed to the ability of such particulates to transmit the stress via relatively strong contacts within the

particulates of micron size, referred to here as micronised granular system. It has been reported that the micronised granular system transmitted stress in stronger contacts more than macro-granules, suggesting that such micronised particulates act like continuum materials and shear dominates (Antony et al., 2014b). This characteristic is observed here in this part of the research project as the maximum shear stress profiles diffused through the granular bed, forming multiple continuous stress contours in a downward direction. As the stress contour reaches the compression die base, it starts to spread towards the die walls. The micronised compressed granular system shows gradual stress status saturation inside the die geometry under loading conditions.

Furthermore, tracking of the stress propagation toward the die boundaries has been conducted and the results are illustrated in Figure 7.4. It is obvious that increasing the stress magnitudes from 5 to 34N leads to marked increases in overall stress status within the whole die, including the boundaries; the scale is the same as in Figure 7.3.

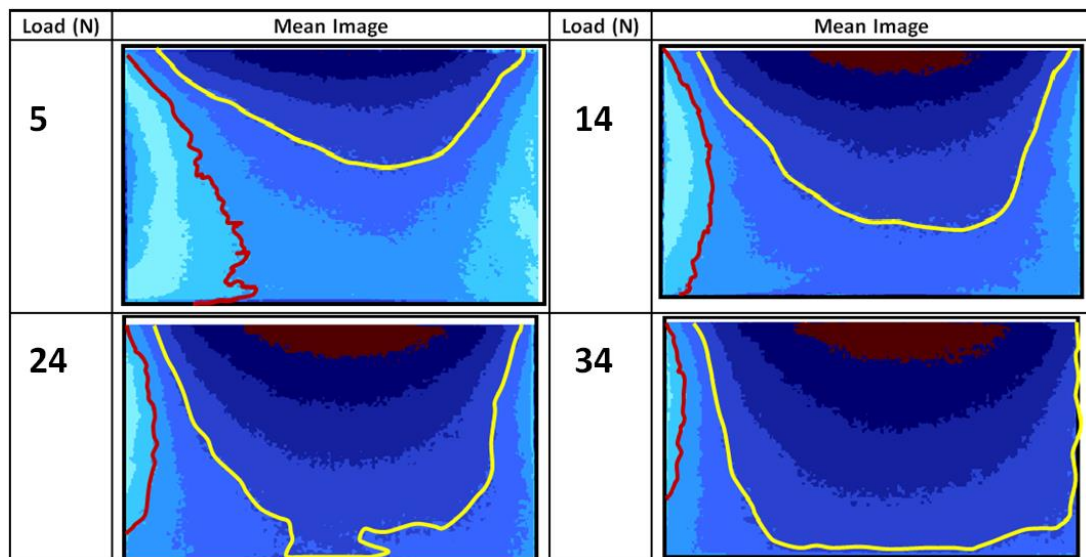


**Figure 7.4** Tracking of increasing wall pressure at left side of the die boundaries (marked by red line) and stress diffusion from the die top to the base (yellow lines)

The results in Figure 7.4 show that at 5N uniaxial loads, there are four stressed colours (bands) inside the red line at the left side of the die. Increased loading condition to 14N leads to marked changes in the zone dimensions and only two

contours exist. At 24N and 34N, the stress profiles sizes continue to decrease and are almost very close to disappearing. This marked decrease of the relatively low stressed zones at the boundaries is concurrently occurring with gradual stress saturation of the compressed system within all the die segments. The stress diffuses from the upper layers towards the base and then to the boundaries, as shown within the yellow colour marked stress profiles and behaves like continuum materials. Similar results indicate low stress magnitude at die base and boundaries as well as general trend of shear stress diffusion and transmission has been reported earlier using FEM modelling (Michrafy et al., 2002) under higher loads. However, the present experimental findings visualises the stress distribution more realistically under lower external loading conditions.

Several researchers have successfully used FEM to predict the shear stress zones and shear band generation of the compressed pharmaceutical powders using relatively high compression forces (Michrafy et al., 2002, Han et al., 2008). The results showed how simulation and modelling of the compaction process is very complex with the difficulty to predict micro-scale properties of the material and their actual relevance on the macro behaviour. This mainly occurs because the powder compression simulation model, deals with the powders as continuum materials, and some microscale characteristics of the powder such as particle shape and size were not taken into consideration (Michrafy et al., 2002). However, modelling is still considered as a powerful technique, offering unique insights into the influence and linkage of material micro characteristics and manufacturing process variables (Sinka, 2007).

In general, although FEM used high external loading, the obtained PSAT results showed qualitative agreement with that obtained using FEM (Michrafy et al., 2002, Wu, 2008, Wu et al., 2005). Both methods report that the bottom section of the compression die showed less shear stress, compared to the upper zone. Moreover, the shear stress magnitude within the bed is increasing from the upper section of the die to the bottom section, and strongly distributed in non-homogenous trend through the compressed bed. The deviation of FEM results from those obtained by the PSAT method is that FEM showed high stress magnitude at the upper die section close to the die wall, while the highest stressed zone, using PSAT, is obtained at the central

zone below the upper punch. The dislocation of high shear stress zones in PSAT results from the die top boundaries to the upper central section of the compression die, could be attributed to the low influences of wall friction at a relatively low compression force (Michrafy et al., 2003, Ismail, 2008). Recent studies predict that the main two mechanisms controlling pharmaceutical powder compaction and the powder density profile distribution under external loads are interparticle friction and die wall friction (Michrafy et al., 2003, Michrafy et al., 2004, Ismail, 2008). These two factors also have a great influence on the non-homogenous distribution of stress within the compressed powder bed, as well as the propagation of density gradient (Michrafy et al., 2003). During the particles rearrangement stage of the compression cycle, particles tend to be rearranged within the die chamber, and the bed density is increased as the air voids decrease. The particles at the upper die segment boundaries close to the punch dilate and are driven downward to the central axis of the compressed bed (Macleod and Marshall, 1977). At this stage of the compression cycle, interparticle friction seem to becomes the dominant mechanism for stress propagation (Michrafy et al., 2003, Ismail, 2008) and the die wall influence is almost negligible. As the external load increases, the contact between the particles increases and the particles show limited rotation and slip motions, and the die wall friction becomes the dominant mechanism and greatly influences the stress status and density distribution (Michrafy et al., 2003, Michrafy et al., 2004).

The previously reported findings indicate that the propagation of a highly stressed zone directly below the punch at the central zone of the die thought to be attributed to the high influence of interparticle friction due to particles motion. Dilation and downward drive of the particles to the central axis of the die increase interparticle friction and subsequently, stress propagation. At this early stage of compression, the die wall influence on the stress profiles generation almost negligible. According to the previous results, it is expected that the particles motion in the central axis of the compressed granular bed will be higher than at the boundaries, due to more available space for particles motion compared to the boundaries. These findings and predictions will be investigated in Chapter 8 of this research project by analysing the particles' spatial and temporal velocities inside the compression chamber under uniaxial loading conditions, using the DPIV method.

In order to investigate the nature and magnitude of shear stress distribution within the compressed granular bed, further analysis of the distribution of the maximum shear stress profiles across the width of the compression die has been conducted at three heights; top, middle and bottom sections, see Figure 7.5. Two compression loads have been selected for the evaluation of stress distribution; 5N and 34N. These compression loads represent low and high loads, within this compression cycle.

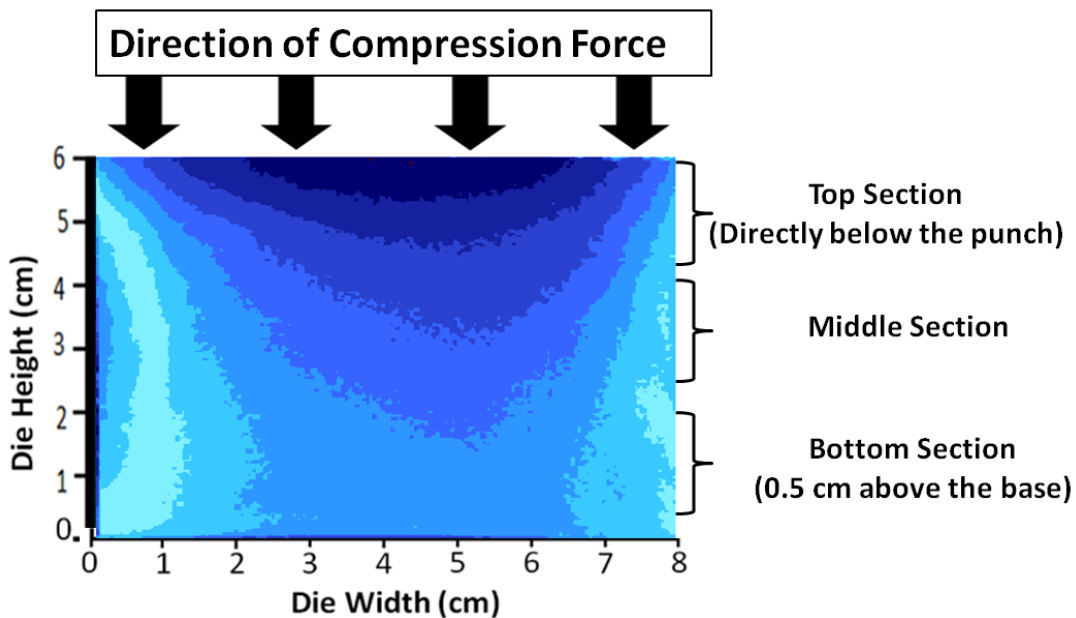


**Figure 7.5** Three levels of maximum shear stress distribution profiles evaluation inside compression die

The locations of stress measurement at the top and middle sections under each loading force are selected according to the granular bed height under the given load level. The obtained results of the maximum shear stress distribution across the compression die show a strong non-homogeneous distribution trend at all three sections, under all compression loads. The analysis has been conducted at all three sections under selected loading conditions and the results show higher stress magnitudes at the top section, compared to the middle and bottom sections at both central zone and wall boundaries. The normalised maximum shear stress distributions across the die width at three selected heights, at 5N and 34N loads, are illustrated in Figure 7.6. All obtained data were normalised (maximum shear stress at each section is normalised with respect to the maximum shear stress obtained at top section under 34N load) and plotted on one graph for accurate analysis of the

result and for ease of comparison. This also will show clearly the influence of increasing loading conditions on the magnitudes and nature of stress distribution within die geometry.

PSAT post-processing software is able to track and measure the magnitude of maximum shear stress exerted on each particle within the cross sectional plot. For example, the plot in Figure 7.6 represents more than 250 stressed points within the horizontal die section at each height. The zigzag shape of the stress plots indicate that each particulate has a different stress magnitude, compared to the adjacent or neighbouring particles. This indicates that the stress magnitude and the interparticle force network strength vary from point to point, depending on the location of the granular material within the die chamber.

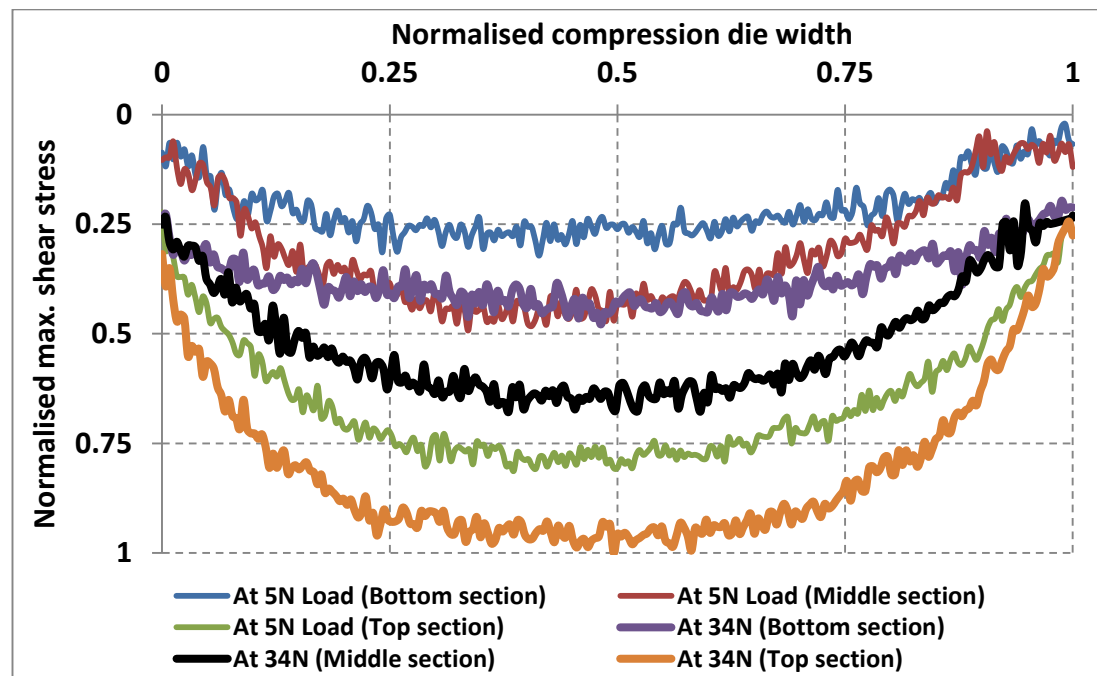


**Figure 7.6** Normalised maximum shear stress magnitudes across the compression die at three selected heights at 5N and 34N compression forces

In general, the results show that increasing external compression load increases the shear stress magnitudes at both central zone and die boundaries. The overall normalised shear stress magnitudes reported at the die central zone and its corresponding boundaries at 34N is higher than that obtained at 5N corresponding heights. The central zone of the compressed granular bed across three horizontal

widths at the top, middle and bottom sections shows higher stress values than that reported at their corresponding boundaries under both loads.

The normalised maximum shear stress values reported at central zone of the top, middle and bottom sections at 5N load are 0.813, 0.493 and 0.322 respectively. Moreover, the normalised minimum stress values at the boundaries of the top, middle and bottom sections are 0.223, 0.104 and 0.067 respectively, as shown in Table 7.1. The ratios of the normalised maximum shear stress at the boundaries to the central zone at top, middle and bottom sections are less by 72.57%, 78.90% and 79.19% respectively.

To avoid any bias in the previous calculation because of the zigzag shape of the plot and non-homogeneous distribution of the stress, the calculation has been repeated according to the average of 5 points at both compression die boundaries and at the die centre and the results are presented in Figure 7.7 and Table 7.1.

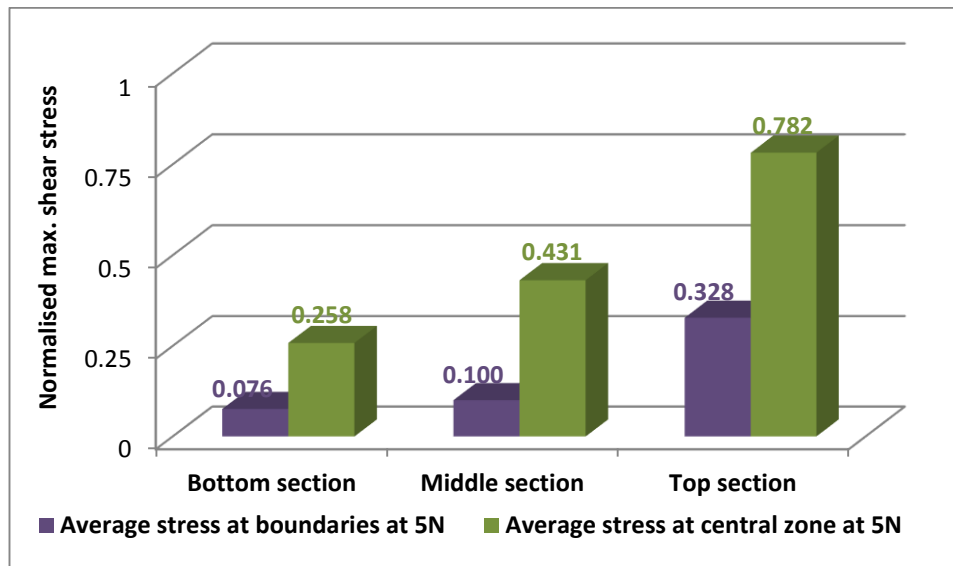


**Figure 7.7** Normalised average shear stress at the die central zone and boundaries at 5N load

The results show that the average normalised stress values at the centre of the top, middle and bottom sections are 0.782, 0.431 and 0.258 while the values at the boundaries are 0.328, 0.100 and 0.076 respectively. The ratio of the average normalised stress values of the boundaries to the central zone at the top, middle and bottom sections are less by 58.06%, 76.80% and 70.54% respectively. The results presented in Table 7.1 show clearly that the stress magnitudes and ratios at the

centre and boundary of the top section of the dies are higher than that reported at the middle and bottom sections at 5N loads.

**Table 7.1** Shear stress comparisons inside the compressed granular bed at 5N load

	Top	Middle	Bottom
Maximum normalised ( $\tau_{max}$ ) at (DC)	0.813	0.493	0.322
Normalised ( $\tau_{max}$ ) at (DB)	0.223	0.104	0.067
Stress ratio (DB) < (DC)	72.57%	78.90%	79.19%
Stress ratio at the (DC), Top > Middle and Top > Bottom		64.91%	152.49%
Stress ratio at the (DB), Top > Middle and Top > Bottom		114.42%	232.84%
Average normalised ( $\tau_{max}$ ) at (DC)	0.782	0.431	0.258
Average normalised ( $\tau_{max}$ ) at (DB)	0.328	0.100	0.076
Average stress ratio (DB)<(DC)	58.06%	76.80%	70.54%
Av. stress ratio at the (DC), Top > Middle and Top > Bottom		81.44%	203.10%
Av. stress ratio at the (DB), Top > Middle and Top > Bottom		228%	331.59%
* (DC) is Die central zone			
* (DB) is Die boundary			

On the other hand, the normalised maximum shear stress values reported at the top, middle and bottom sections of the central zone at 34N load are 1, 0.678 and 0.479 respectively. Moreover, the normalised minimum stress values at the boundaries of the top, middle and bottom sections are 0.276, 0.230 and 0.215 respectively, see Figure 7.6 and Table 7.2. The ratios of the normalised maximum shear stress at the boundaries to the central zone at top, middle and bottom sections are less by 72.40%, 66.07% and 55.11%.

The stress ratios calculations have been repeated according to the average stress values at the compression die boundaries and the die centre and the results are presented in Figure 7.8 and Table 7.2. The average normalised stress values at the centre of the top, middle and bottom sections are 0.965, 0.642 and 0.435, while the values at the boundaries are 0.384, 0.270 and 0.253 respectively. The ratio of the average normalised stress values of the boundaries to the central zone at the top, middle and bottom sections are less by 60.22%, 57.94% and 41.84% respectively. The results in Tables 7.1 and 7.2 show that, though shear stress magnitude increased at the central die region and boundaries due to increasing the external loading condition from 5N to 34N, the stress ratio between the die centre and the boundaries

decreases. This is attributed to the dramatic increases in the magnitude of shear stress at the die boundaries, 0.067 to 0.215 at 5N and 34N respectively.

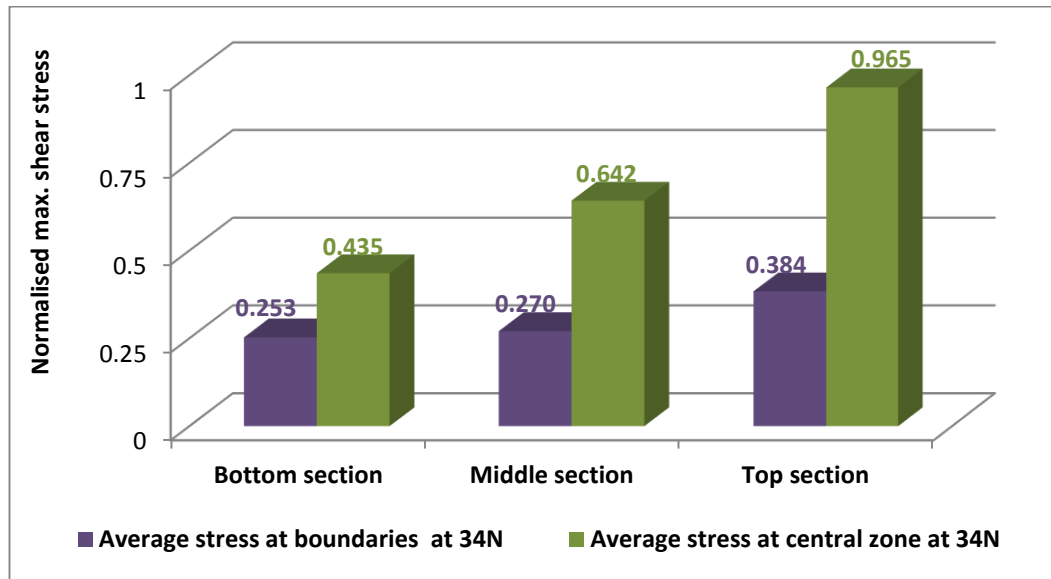


**Figure 7.8** Normalised average shear stress at the die central zone and boundaries at 34N load

The previous stress measurements and comparisons indicate that the compressed system undergoes stress saturation status as stress diffuses from the top layers to the bottom layer.

**Table 7.2** Shear stress comparisons inside the compressed granular bed at 34N load

	Top	Middle	Bottom
Maximum normalised ( $\tau_{max}$ ) at (DC)	1	0.678	0.479
Normalised ( $\tau_{max}$ ) at (DB)	0.276	0.230	0.215
Stress ratio (DB) < (DC)	72.40%	66.07%	55.11%
Stress ratio at the (DC), Top > Middle and Top > Bottom		47.49%	108.77%
Stress ratio at the (DB), Top > Middle and Top > Bottom		20%	28.37%
Average normalised ( $\tau_{max}$ ) at (DC)	0.965	0.642	0.435
Average normalised ( $\tau_{max}$ ) at (DB)	0.384	0.270	0.253
Average stress ratio (DB)<(DC)	60.22%	57.94%	41.84%
Av. stress ratio at the (DC), Top > Middle and Top > Bottom		50.31%	121.84%
Av. stress ratio at the (DB), Top > Middle and Top > Bottom		42.22%	51.78%
* (DC) is Die central zone			
* (DB) is Die boundary			

Further assessment of the average normalised shear stress magnitudes has been conducted across the entire horizontal die section at all three heights, at 5N and 34N loads, and the results are illustrated in Figure 7.9.

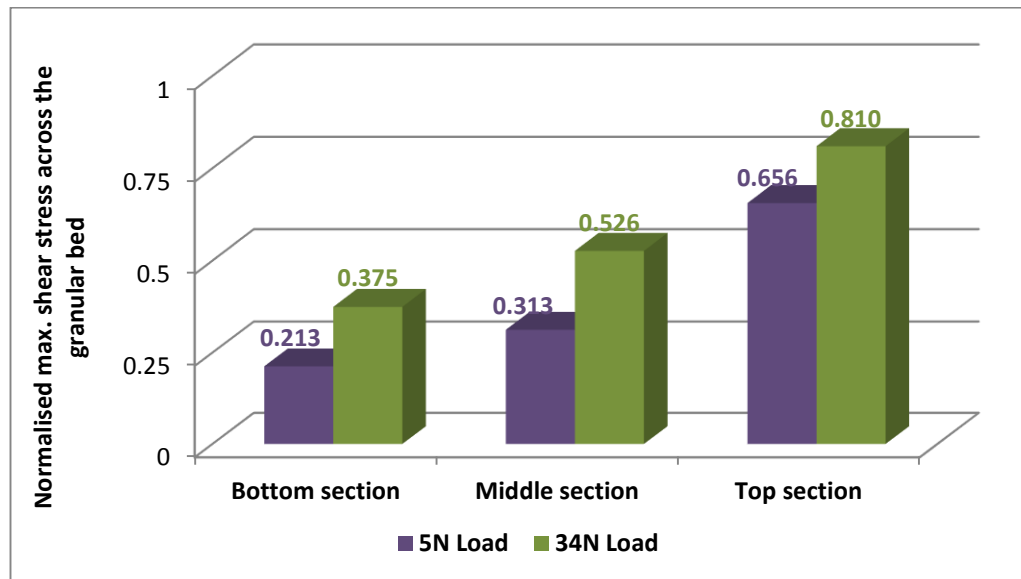


**Figure 7.9** Normalised average shear stress at the selected die heights at 5N and 34N loads

The average normalised stress values at top, middle and bottom sections are 0.656, 0.313 and 0.213 at 5N and 0.810, 0.526 and 0.375 at 34N loads. The percentage stress increments at top, middle and bottom sections due to increasing compression load are 23.45%, 68.05% and 76.05% respectively. Overall, this result indicates that the stress increment ratio at the die bottom section due to increasing loading conditions is higher than that reported at the other heights and confirms the stress saturation status of the compressed granular material at low die segment.

For ease of comparison, the reported results in Figure 7.10 summarise the normalised maximum shear stress distribution across the compression die at top and bottom sections, under 4N and 34N compression loads. The plots have been fitted in a 2<sup>nd</sup> order polynomial plot to smooth the plot and to assess the stress distribution homogeneity via the R<sup>2</sup> values at each height.

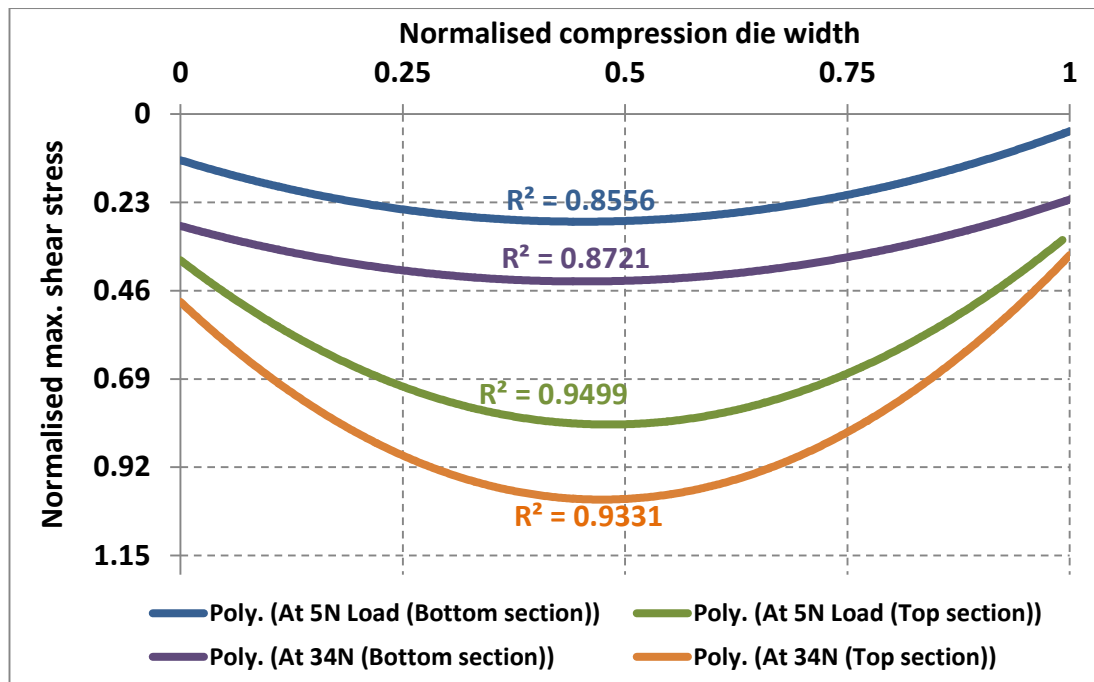


**Figure 7.10** Normalised maximum shear stress values across the compression die at the top and bottom sections under 5N and 34N compression loads

In general, the plot indicates that increasing the uniaxial compression forces increases the stress values within the die chamber at both sections and the stress saturation at the bottom section boundaries is more than that at top section. The stress distribution across the top section of the die width is more homogenous than the bottom section, as reported through the ( $R^2$ ).

#### 7.4 Conclusions

The stress status inside the confined compression die during the rearrangement compression stage displays a strong non-homogenous trend. The top die section, located directly below the compression punch, shows high stress profiles at the centre and the boundaries during the whole compression process. Among all die segments during the whole compression process, the central zone shows higher stress values than the boundaries. This could be attributed to the early driven particles at the upper die segment toward the central die zone and the high influences of intergranular friction. Overall, the obtained experimental results show a good level of generic agreement with the published computational simulation results obtained using FEM on the general characteristics of stress distribution

behaviour similar to continuum materials. The stress profiles are diffused from the top section of the die to the die base and deviated to the boundaries. The results indicate that the compressed granular system displayed gradual stress saturation status, starting from the top and moving down to the base of the die and then diffusing to the side wall boundaries. The stress saturation ratio at the die bottom section is higher than that at the top section.

## **Chapter 8 Velocity Profiles Distribution inside Pharmaceutical Granules Subjected to Relatively Low Uniaxial Confined Compression Using DPIV**

The aim of this chapter is to investigate, experimentally, the influence of the relatively low uniaxial confined compression on granular bed deformation and particle velocity profiles inside the die chamber using DPIV. The maximum uniaxial applied external load was 34N, using the Instron compression machine at a constant speed. The particulate velocity profiles were evaluated at the top and middle sections of the die. The investigations are essential to understand the spatial and temporal particulate motion during the rearrangement compression stage at a more fundamental level. In particular, this helps to understand the influence of interparticle friction and wall particle friction resulting from particulates' motion and their subsequent links to the shear stress distribution profiles propagation, as presented in Chapter 7 under similar compression loading conditions. The pharmaceutical excipient granules used in this part of the research are the fabricated stress responsive granules characterised in Section 3.2.2.

### **8.1 Introduction**

The granular material compression process is crucial and greatly influences the integrity and quality of the final product in the pharmaceutical industry, as well as in other multiple engineering industries (Carstensen and Toure, 1980, Denny, 2002, Michrafy et al., 2002). Applying a visual technique, such as DPIV at relatively low confined compression forces, will help investigate in detail the dynamics of particulates motion inside a die chamber. This will help to shed light on the influences of particle-particle friction and particle wall friction at the early stage of compression and link this to the stress distribution profiles obtained under higher compression loads (Michrafy et al., 2003, Michrafy et al., 2004, Ismail, 2008). Such visual information will provide better insight and understanding of the stress development and propagation style at the early compression stage and the influence of the variables that may help with final product quality improvements.

## 8.2 Material and Methodology

### 8.2.1 Material

Materials used in this chapter for compression are the fabricated stress responsive granules, as characterised in (Section 3.2.2), and having a particle size range of 300 to 1000  $\mu\text{m}$ . The fabricated uniaxial compression rig used in Chapter 7 for the shear stress profiles investigation has been used in this part of the research using the DPIV method. The die wall roughness was measured in a mechanical engineering laboratory using a surface roughness tester (Taylor-Hobson) and roughness average ( $\text{Ra}$ ) value was  $2.284 \mu\text{m}$ .

### 8.2.2 Methodology

The major components of the DPIV experimental set up for granules compression are the light source, Instron compression machine (Model 5566 Test Bench), fabricated compression rig and high resolution digital camera, as illustrated in Figure 8.1(b). The applied compression force was adjusted at the centre of the top part of the rig, as illustrated in Figure 8.1(a).

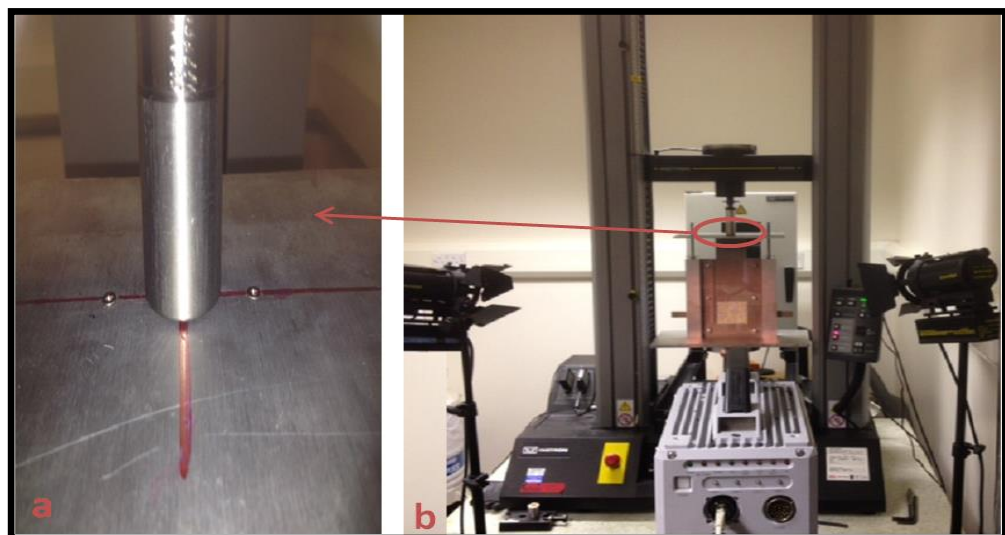


**Figure 8.1** Compression of pharmaceutical granules using the Instron machine: (a) central guide lines at the top part of the rig, and (b) DPIV experimental setup

The filling procedure of the stress responsive granules into the compression rig was identical to that reported in Chapter 7. The granules were loaded into the compression chamber systematically to minimise segregation of the granules. To

achieve this, a funnel, having a flexible nozzle was used to feed granules into the die cavity where the nozzle was aligned along the central axis of the die, and the granules were fed in and built up to the required level at the boundaries. The maximum height of the granular bed inside the chamber was 6cm. For the purpose of the initial packing density assessment, the compression die filling procedure was repeated 15 times and the results showed steady results, with a reasonable variation range,  $8.21 \pm 0.309$  gm.

The granular material was compressed inside the die chamber using the Instron apparatus as illustrated in Figure 8.1(b). The transparent front side of the die chamber was illuminated, using two lamps, located at both sides of the rig. The position of the lamps, image resolution, image shading and light contrast were optimised to obtain clear frames, suitable for the further analysis. The Instron machine was operated at 34N load and the uniaxial compression performed at a constant speed, 0.25mm/s. Due to the high capacity of the digital camera, compression process recording was started just immediately before releasing the loading condition programme. The lower part of the compression punch was adjusted directly above the granular bed and compressed the bed at a constant speed and accelerated load. The granular bed deformation was recorded, using a high speed digital camera (Photron fastcam viewer PFV, model SA5; the speed was 250 frames/ second, the resolution was 1024 x 1024 pixels and the maximum shutter speed was 1 $\mu$ s). All the collected data were analysed frame by frame, using the DynamicStudio software platform (DSSP) built in the adaptive PIV correlation application. Further information is available in Chapter 6 and in Albaraki and Antony (2014). The application analyses the mean velocity vectors of the granules during bed deformation, under the selected compression forces.

The area of interest was defined to the adaptive technique by masking the area outside the die chamber in order to eliminate any interference, see Figure 8.2. The adaptive PIV application iteratively adjusts the size of the individual interrogation areas (IA) for analysis, in order to adapt to local seeding densities and the particle flow gradients. Similar to what was used in the previous work in Chapter 6, the final interrogation areas were in 16x16 pixel dimensions.

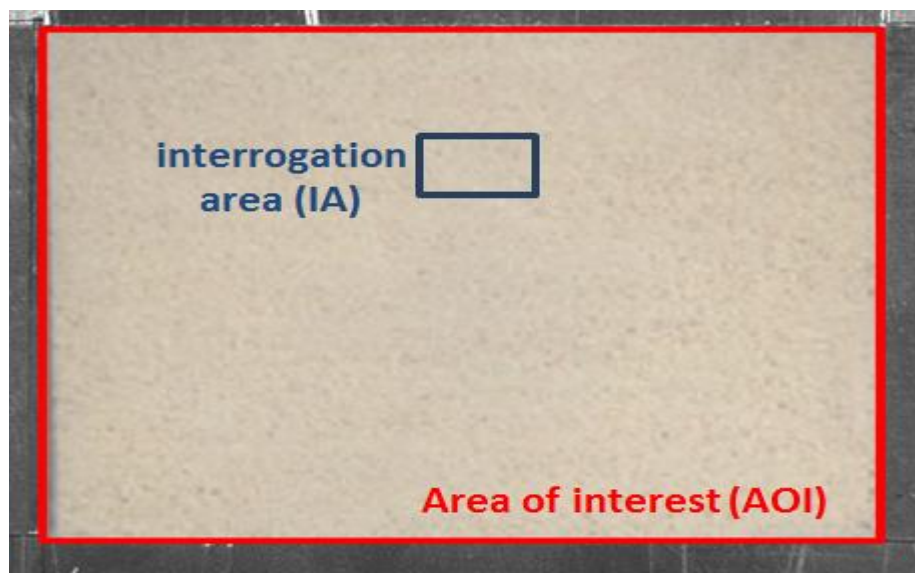
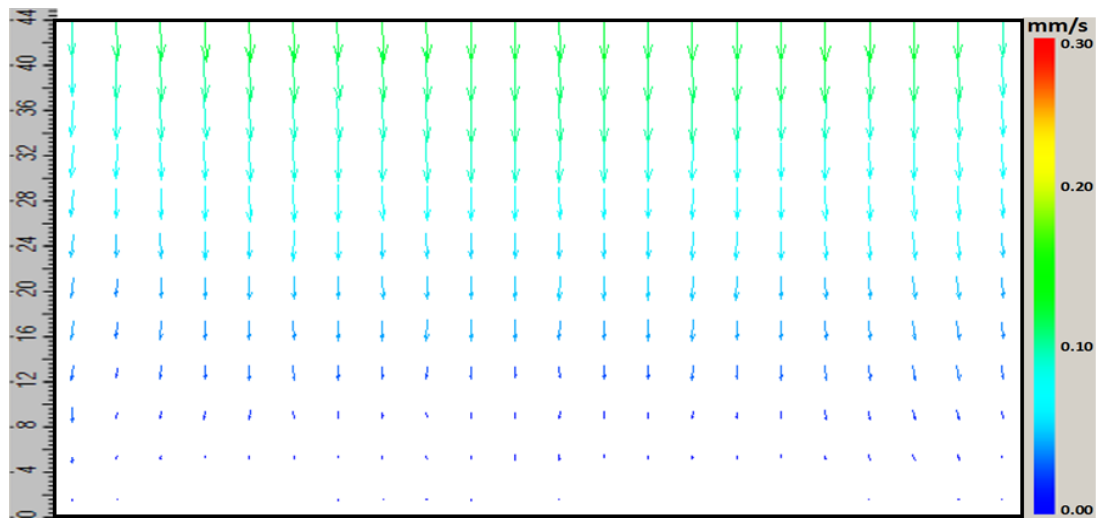


**Figure 8.2** Area of interest (AOI) within the compression die (red colour) and interrogation area (IA) in (blue colour)

### 8.3 Results and Discussions

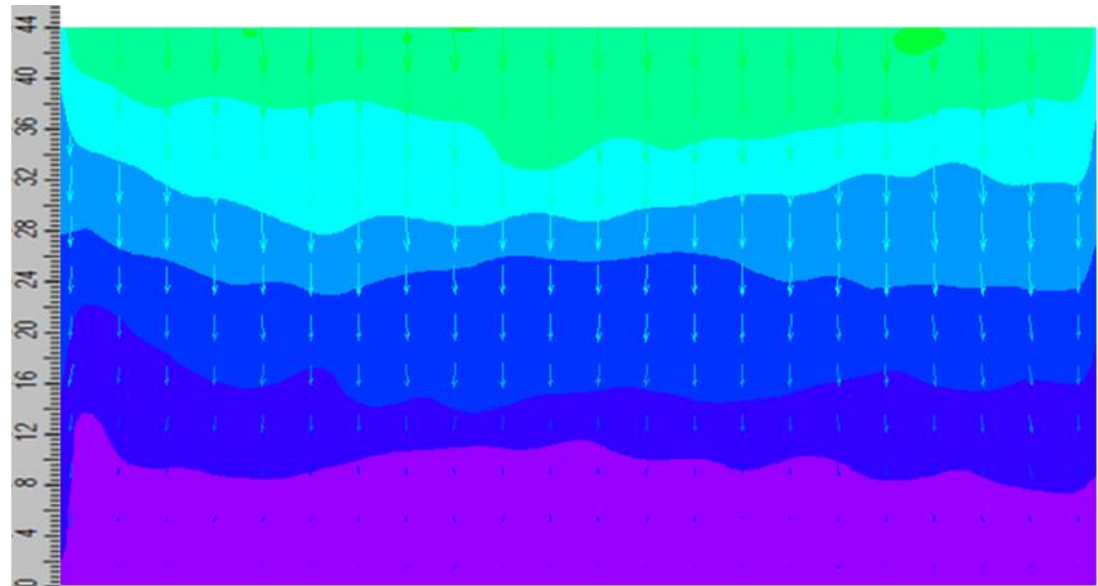
Clear and visual quantitative understanding of the nature of granular material deformation within confined die geometry at the early stage of the compression cycle is crucially needed, and has not yet been widely investigated in the pharmaceutical industry. The DPIV method applied in this part of the study is non-invasive, and real time technique is able to measure the mean velocity vectors of the compressed particles inside the chamber at a constant compression speed. The post processing software is able to show the distribution of the velocity vectors within the area of interest of the compressed particles and scale it according to the colour coding scale. The length of velocity vectors illustrated in mean velocity profiles indicates the spatial and temporal distribution of the velocity components (Ostendorf and Schwedes, 2005, Sielamowicz et al., 2005).

Figure 8.3 shows the distribution map of the mean values of velocity vectors within the interrogation areas of the whole compression die inside the die chamber at the end of the compression cycle.



**Figure 8.3** Mean velocity vectors map of pharmaceutical stress responsive granules inside the compression die at the end of the compression cycle at 34N

Vectors have higher velocity magnitudes across the horizontal die section located directly below the compression punch and decreased toward the base of the die. The velocity magnitudes at the base of the die are almost close to zero and granules show very limited or no motion. This is clearly observed through the length of the vectors at each die segment and the velocity scale. The results in Figure 8.4 show clearly the velocity contour according to the length of the vectors at the end of the compression process at 34N.



**Figure 8.4** Superimposed mean velocity vectors on the resultant velocity contours according to the vectors length within the die geometry at 34N

The contours are in a non-uniform shape inside the die geometry. The upper contour under the compression punch includes the longest vectors, while the contour at the base contains the shortest vectors. It is worth remembering that the length of the velocity vectors is a primary indicator of the particle velocity at any location (Sielamowicz et al., 2005). The velocity vectors map has been superimposed onto a contours map for an easy comparison. The contours are split into multiple colour coded layers, according to the length of the mean velocity vectors, which are calculated using the following equation;

$$\text{Vector length} = \text{Sqr } (U^2 + V^2) \quad \text{Eq. 8.1}$$

Where

$U$  is the horizontal velocity component.

$V$  is the vertical velocity component.

Very low velocity gradients indicate the high ability of the DPIV to detect the spatial and temporal particulate velocities. The non-homogeneous distribution of velocity contours is related to both, velocity vector length and magnitude as well as the granular layer density at each die segment. Variable cross sectional plots, almost across any section, pass through at least two contour layers, if not more, and this is further evidence of the non-homogeneity of the distribution across both vertical and horizontal sections.

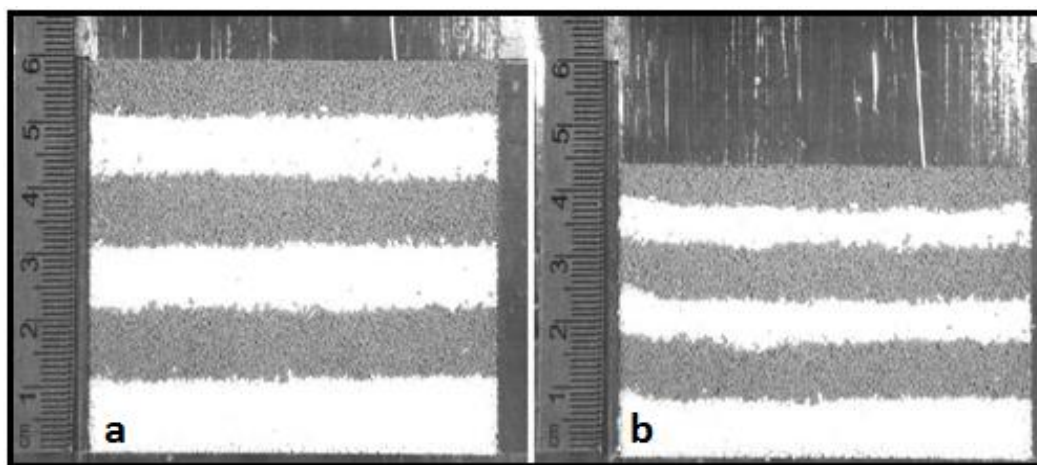


**Figure 8.5** Qualitative analysis of the granular materials density profiles distributions using multiple colour coded granular layers: (a) initial uniform packing, and (b) non-uniform packing at the end of the compression process at 34N

Another qualitative analysis has been conducted to evaluate the initial packing of the granular material and the density profiles distribution under loading conditions, as illustrated in Figure 8.5. This simple experimental method is able to show visual images more easily for density changes due to external loading (Train, 1956, Sinha et al., 2010). The coloured pharmaceutical excipient granules were filled in the compression die in multiple layers. Each layer has a different colour and the particle size distribution range is from 300 $\mu$ m to 1000 $\mu$ m. The granular material initial packing and density profiles distribution are uniform, as clearly shown in Figure 8.5 (a), all layers having almost the same height. At the end of the compression process the density distribution profile was totally non-homogenous across the granular bed. The height of the upper two layers close to the compression punch is decreased markedly, compared to the lower layers. Minor changes can be observed at the last layer in the base of the compression die.

The results in Figures 8.4 and 8.5 illustrate clearly that the layer at the base of the die, shows minor deformation and contains the shortest velocity vectors having negligible magnitudes. This indicates that the particulates motion at this segment is very limited, compared to the upper layers. This could be attributed to the limited spaces available for particulates' motion at the base, compared to the higher layers, as the base is constrained more by three rigid walls.

Further analysis has been conducted to evaluate the vertical velocity component across the die chamber at three levels: the top section which is located directly below the punch and the middle section, however, the bottom die section located at the level of the die base showed almost no motion with negligible values and was not included in the analysis. The results in Figure 8.6 illustrate the vertical velocity component of the particulates during the compression process at the top section of the die (directly below the punch) and the middle section of the die. The blue line is the normal plot of the vertical velocity component, the green line is the average vertical velocity across the bed and the red line is the polynomial plot of the vertical velocity component in 2<sup>nd</sup> order.

Overall, at both die sections, the reported results using polynomial and normal plot indicate that the particle vertical velocities at the central zone of the die are higher than those observed at the die boundaries. Moreover, the results show steadier

normal plot of particulate velocities at the middle section compared to the top section and this was confirmed by the ( $R^2$ ) of the polynomial plot at both sections, the values were 0.6831 and 0.4906 respectively. The zigzag shape of the normal plot of the vertical velocity component, as in Figure 8.6, indicates variable velocity magnitudes of the compressed particulates depend on their locations within the granular material bed. The relatively high velocities magnitudes at the centre of the compressed granular bed are thought to be attributed to the particles motion through the inter particles air voids. Particles close to the boundaries show relatively limited motion, compared to those at the bed centre due to rigid boundaries.

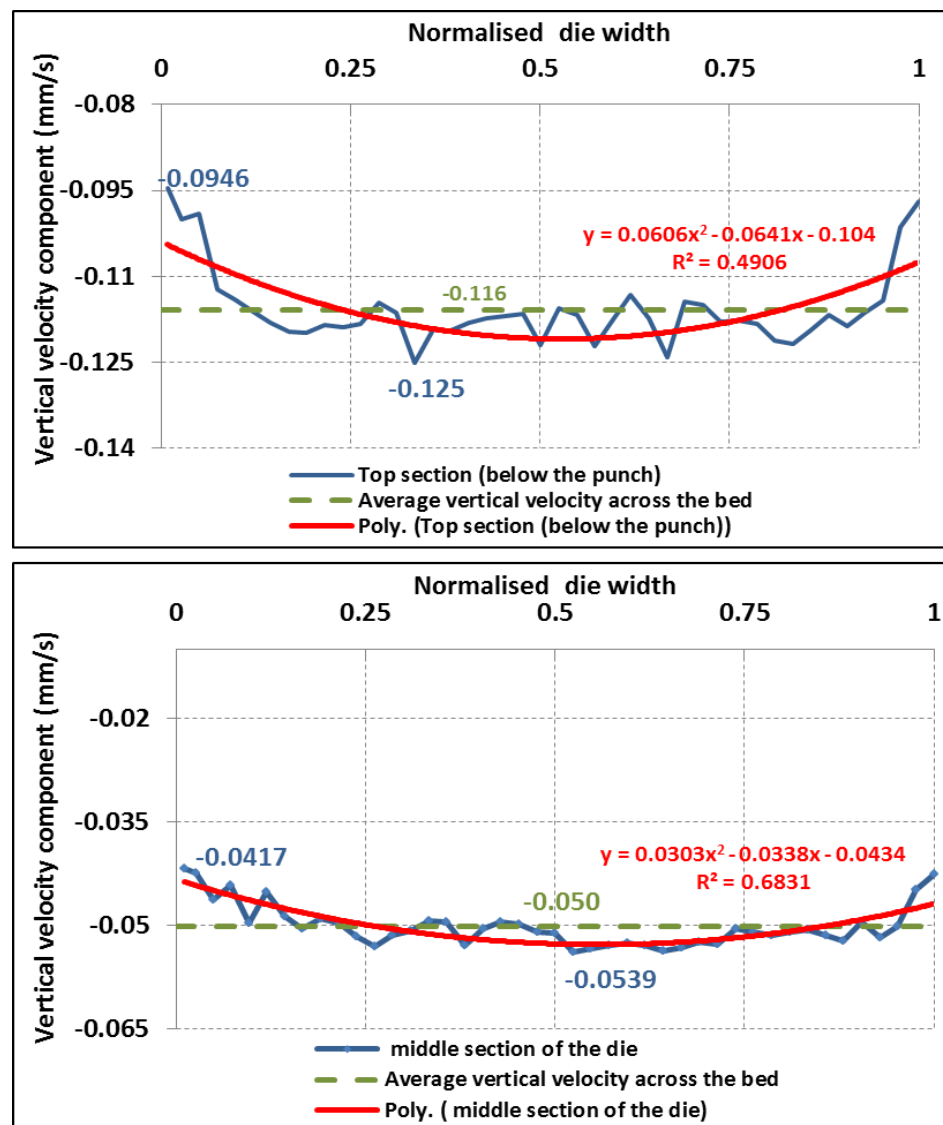


**Figure 8.6** Vertical velocity components and average vertical velocity across the compressed granular bed at the top and middle sections of the die at 34N

overall, the top die section showed higher average velocity across the compressed bed than that reported at the middle section, 0.116 (mm/s) and 0.05 (mm/s) respectively. The relative average velocity across the compressed bed at the top section is 132% higher than that at the middle section.

The maximum and average vertical velocity component reported at the top and middle die sections' central zone and boundaries are reported in Figure 8.7. The average vertical velocity component was calculated using 5 points at the boundaries and the central zone of the hopper.

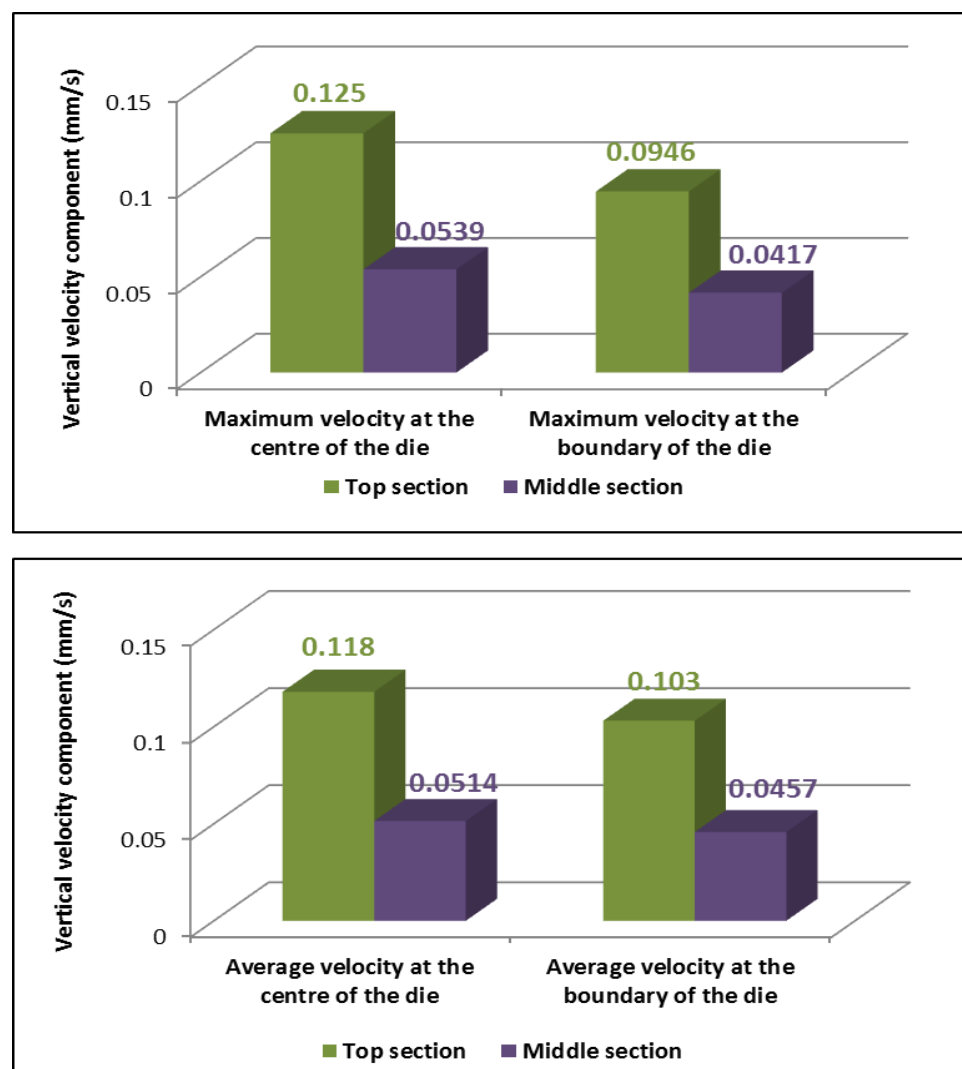


**Figure 8.7** Maximum and average vertical velocity component at the top and middle section reported at the centre and boundaries of the die at 34N load

In general, both calculations indicate that the velocity at the central zone of the die is more than that at the boundaries. The relative maximum and average vertical

velocity of particles at the top section of the die at the central axis are higher than that at the boundary by 32.14% and 14.56% respectively. Moreover, the relative maximum and average vertical velocity of particles at the middle section of the die at the central axis are higher than that at the boundary by 29.26% and 12.47% respectively.

Generally, relatively high particles motion in the top and middle sections of the die in general and at the central zone of the die in particular, is expected to increase the interparticle contact and friction, and subsequently high stressed zones are expected to be developed at these particular zones.

Linking the obtained findings of relatively high particulate motions at the top section of the die and along the central die zone at top and middle sections and the reported PSAT results in Chapter 7, supports the close behavioural links between shear stress and velocity distributions. High stress profile values reported directly below the compression punch, comparing to the die boundary, thought to be attributed to the high particulates motion at the central zone of the top section resulting in more particulates friction. The particulates motion at the middle section is less than that at the top section, resulting in less motion and subsequently less friction and stress development. This could indicate high influences of interparticle friction on the magnitude of the generated stress profile more than the effect of the particle wall friction at this level of compression forces. It is worth remembering that the negligible particulates motion at the bottom section of the die would lead to less stress generation. The PSAT results in Chapter 7, Figures 7.3 and 7.4, showed very low stress magnitudes at this section of the die, especially at the boundaries. The shear stress profiles diffused from the top die segment toward the lower segment via interparticle force network lead to gradual stress status saturation of both middle and bottom segments.

Moreover, the superimposed mean velocity vectors on the resultant velocity contours, according to the vectors length within the die geometry at early and late compressions, are illustrated in Figures 8.8 and 8.9. The velocity vector contours map in Figure 8.8 shows multiple contours, according to the spatial and temporal length of the correspondent particulates velocity. At the early stage of the compression phase, the top section of the die chamber shows the longest velocity

vectors among the whole die chamber, and the length of the vectors decreased towards the base of the die.

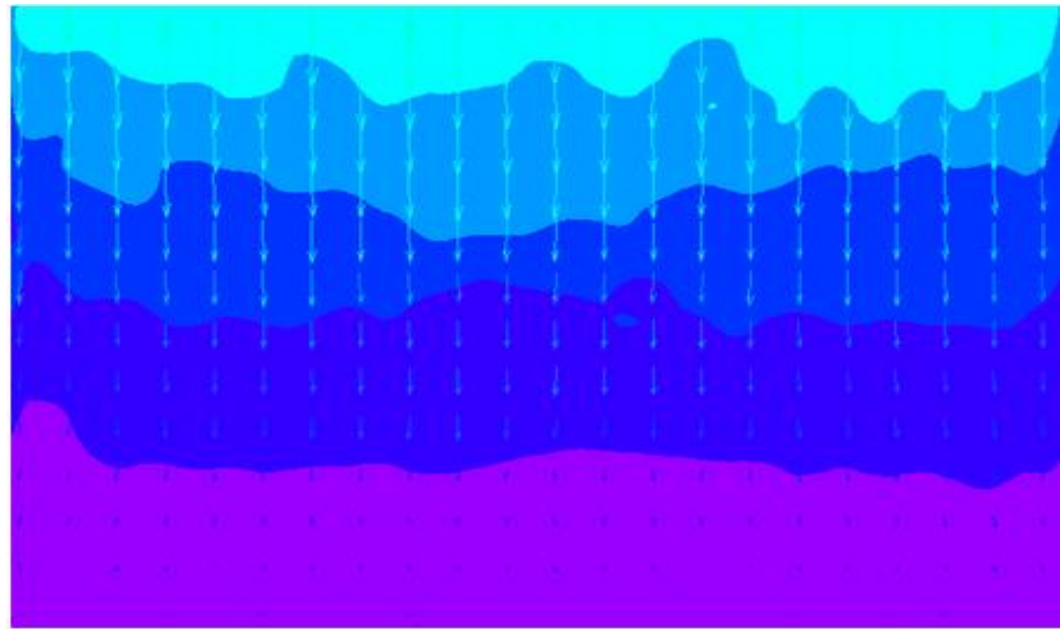


**Figure 8.8** Superimposed mean velocity vectors on the resultant velocity contours, according to vector length within the die geometry at early stage of compression force at 5N load

The middle section of the die has multiple contours showing variable vector lengths, while the die base shows the shortest vector lengths impeded in one contour. The direction of the velocity vectors is aligned with the direction of the gravity, and slight deviations to the boundaries have been reported at the lower segments. The multiple contours map indicates various velocity gradients related to the granular bed density.

The last package of the compression load close to 34N load in Figure 8.9 show marked decreases in the number of contours, only two contours are available. These marked decreases in the contour numbers is directly related to the length and magnitudes of the vectors. The area of the pink contour involves the shortest vectors and almost double or triple that reported at the early stage at 5N load. This indicates a very limited motion of the particles within the die chamber at a higher loading condition.

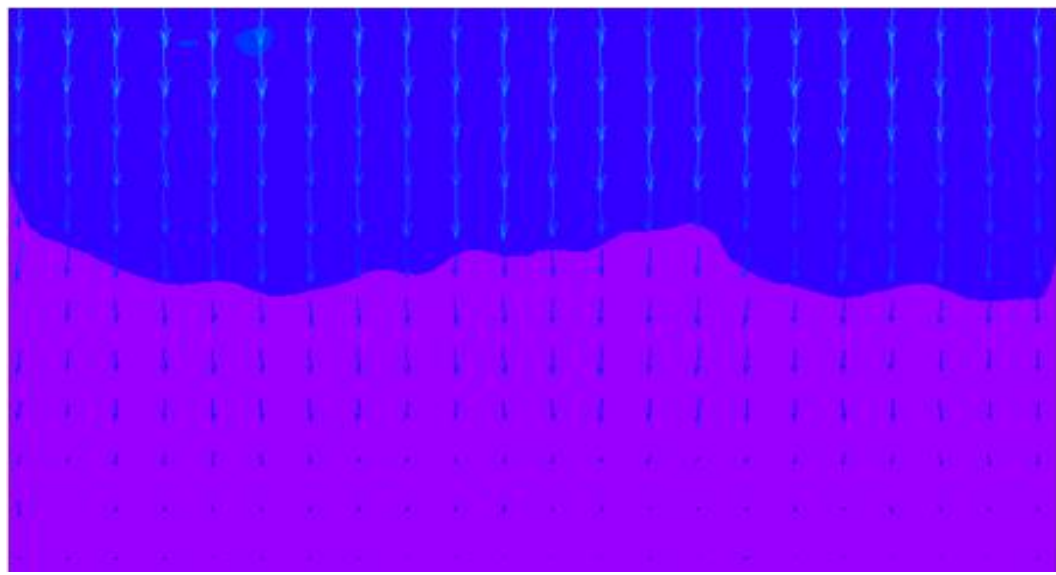


**Figure 8.9** Superimposed mean velocity vectors on the resultant velocity contours according to the vectors length within the die geometry at last stage of compression cycle at 34N load

For ease of comparison, the particulates vertical and average vertical velocities across the compressed granular bed at the top, middle and bottom sections of the die, are illustrated in Figure 8.10.

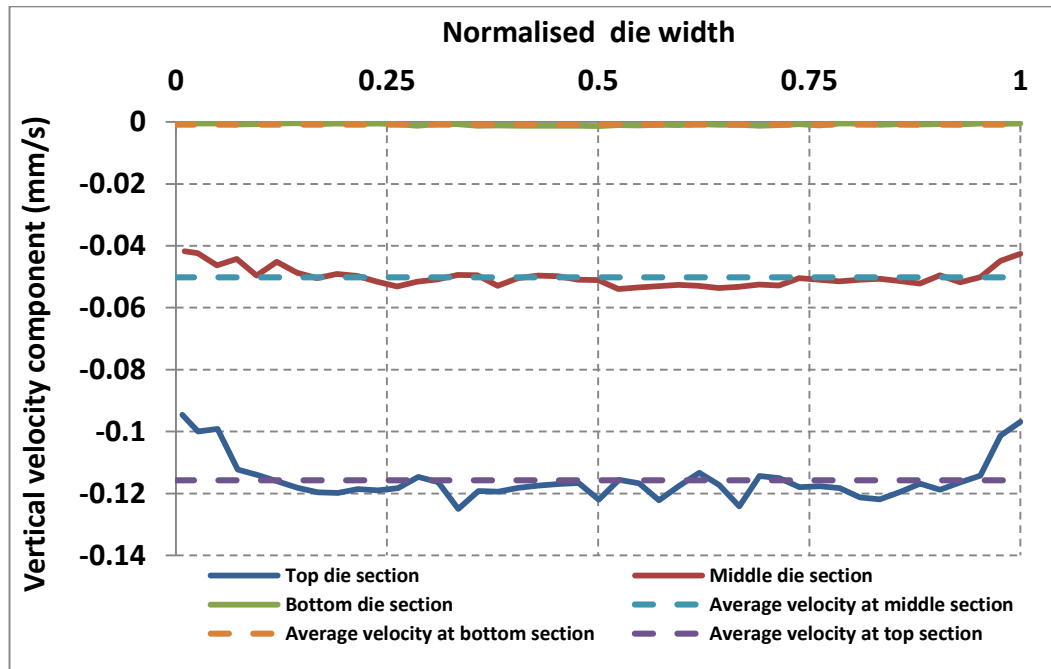


**Figure 8.10** Vertical velocity components and average vertical velocity across the compressed granular bed at the top, middle and bottom sections of the die at 34N compression force

The particulates motion in the bottom of the die is very limited or almost zero. It is very obvious that the top section of the die geometry shows the highest velocity magnitudes among all die segments at the central zone and the boundaries. The central region at each height level shows higher velocity gradient than that at the boundaries. High particulate motion at the central zone of the die across all heights seems to increase the extent of interparticle friction at these locations more than the boundary and subsequently increase the stress gradient at these zones. These findings are able to show clearly the mechanism of stress propagation within the compressed granular bed under relatively low loading conditions and the domination of interparticle friction influences over wall friction.

The above reported observations confirm and in a good level of agreement with the previous stress profiles distribution results reported in Chapter 7 and are illustrated below in Figure 8.11.

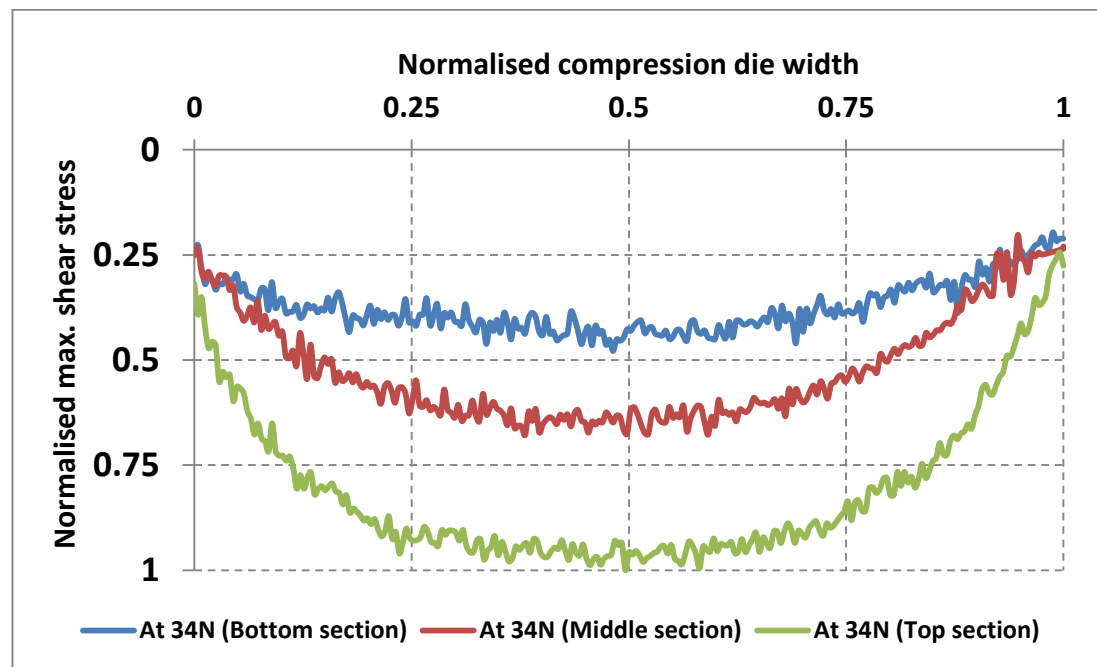


**Figure 8.11** Maximum shear stress magnitudes across the compression die at the top, middle and bottom sections of the die at 34N compression force, Section 7.2

In general, the stress profiles distribution show high stress magnitudes at the top section, compared to the middle and bottom sections across the whole die width. Moreover, the central zone of each profile has higher stress magnitudes than its corresponding boundaries. The high stress magnitudes at the top section of the die

chamber, compared to the other two sections are thought to be attributed to the high particulates motion across the whole of this section, and at the central zone in particular. The bottom die section shows a relatively low stress profile, due to limited motion of the particles, and most of the stress gradient at this particular section diffuses from higher layers through the interparticle force network.

The previous results are able to provide quantitative understanding of the nature and mechanism of shear stress propagation inside compressed granular assembly at relatively low compression force. The continuous particulate motion under low compression force, interparticle friction and wall-particle friction influences have been presented quantitatively in this part of the research and very interesting findings have been presented.

#### **8.4 Conclusions**

DPIV has been successfully used to predict the particulate velocity profiles inside the compression die chamber under relatively low uniaxial compression loading conditions. The results indicate that the top die section, located directly below the punch, exhibits higher velocity magnitudes than the velocities reported at the middle and bottom sections. In addition, the central region at each level has higher velocity values than those measured at their corresponding boundaries. The results also indicate that the motion of the particles at the bottom section of the die is very restricted due to limited available space for motion. High particulate motion at any die segment thought to increase the tendency of particle-particle friction, leading to highly mobilising stress regions. These prospects are in a good level of agreement with the reported PSAT results in Chapter 7. The top section of the die chamber, exhibiting high velocity values, is the highest stressed zone within the compression chamber, and the central axis of each level is more stressed than its corresponding boundaries. Overall, the good level of agreement of the experimental results reported in Chapters 7 and 8 of this research project are at an equal level of agreement with the stress distribution nature reported in literatures using FEM under higher loading conditions.

## **Chapter 9 Conclusions and Recommended Future Work**

### **9.1 Conclusions**

The overall aim of this thesis was to investigate experimentally the influence of pharmaceutical granules microscale characteristics on its macroscale behaviour during their initial packing, dynamic flow process and relatively low confined compression. To achieve this aim, three imaging methodologies, photo stress analysis tomography (PSAT), digital particle image velocimetry (DPIV) and colour coding technique (CCT) were adapted to address this, using freely flow granules in range 300-1000 $\mu\text{m}$ .

In the early stages of the research project, PSAT has been adapted to probe and visualise the initial packing of maximum shear stress profiles within actual micron sizes granular assemblies, stored inside different hopper geometries; 30°, 60° and 90° internal angles. Applying such advanced tomographic methods helps to show the influences of hopper geometries on stress profiles distribution and direction at static condition, and subsequently predict a hypothesis of the dynamic flow behaviour of the stored granular materials. To achieve this, pharmaceutical birefringent stress-responsive particulates with a particle size range of 300 $\mu\text{m}$  to 1000 $\mu\text{m}$ , have been fabricated in our laboratory, using native starch powder and iodine solution, by applying a manual wet granulation technique at cold conditions.

The obtained results show that the internal hopper angle has great influence on the initial maximum shear stress distribution profiles and direction. In general, smaller internal hopper angle (30°), shows relative homogenous stress distribution across the hopper geometry and the direction of the major principal stress, acting in the vertical direction (gravity direction). However, higher internal angle hoppers (60° and 90°), and apart from the central axisymmetric axis of the hopper, the direction of major principal stress, deviated from a vertical direction to incline towards the hopper boundaries. The degree of inclination and stress distribution non-homogeneity are greater at higher internal angle hopper (90°). In addition to this, the stress profile magnitudes were much less than those reported at the smaller internal angle hopper, and the stress distribution across the hoppers geometries is strongly non-homogenous. The experimental and DEM results of stress non-homogeneity and

distributions across hopper width showed a good level of agreement within all hopper geometries. According to the previous stress status findings, the anticipated hypothesis of the dynamic flow process of such free-flowing granules indicated that the smaller hopper angle might show mass flow trend, while higher hopper angles could show funnel flow trend, with high stagnation tendency at the boundaries especially in case of higher angle ( $90^\circ$ ).

To prove the previous hypothesis, the dynamic granular flow trend was assessed qualitatively and quantitatively using CCT and DPIV methods respectively. The reported results using both methods proved that the smaller hopper angle shows clear mass flow trend, where all particulates inside the hopper geometry are in continuous motion during the flow process and no stagnant zones are reported. The direction of mean resultant velocity vectors was vertical, within all hopper segments. The spatial and temporal length of the velocity vectors within the map, varied depending on the location inside the hopper geometry. The granular material at the orifice level, located directly above the hopper outlet, showed higher velocity magnitudes, compared to that at the middle and top hopper segments for all hopper geometries. The mass flow trend in such hopper geometry is thought to be clearly attributed to the vertical direction of the major principal stress, as well as the homogenous stress distribution inside this hopper geometry.

On the other hand, the higher hopper angle ( $60^\circ$  and  $90^\circ$ ) showed clear funnel flow trend occurs through three main flow zones with high stagnation tendency. The flow zones were subdivided according to the shear stress distribution and direction in each zone. The first flow zone was generated initially at the relatively low stressed central hopper axis, forming central plug flow with vertical direction of the velocity vectors. This plug is located exactly at the hopper axisymmetric zone, exhibited vertical direction of the major principal stress and lower stress magnitude, compared to the surrounding boundaries. The second flow zone occurs next to the central plug flow propagation and the general flow inside this zone is a mixture of both the central and radial flow mechanism. The velocity vectors direction during this stage of the flow is vertical at the centre and inclined at the boundaries towards the central flow zone. The inclined velocity vectors represent the radial flow in an avalanche trend from the boundaries toward the hopper centre. In cases of  $60^\circ$  hopper

geometry, the lower hopper segment showed some extent of particulate motion during the flow process which is attributed to the relative low stress values at this zone and the inclined direction of the major principal stress toward the outlet region. According to the PSAT results, the stress magnitudes inside the second flow zone is less than those close to the boundaries, and the direction of the major principal stress is inclined to wall direction towards the hopper outlet. The third flow zone represents the last discharged particulates from both hopper geometries, where the main flow trend is occurring via the radial flow route from the boundaries toward the outlet in an avalanche trend. The direction of the mean velocity vectors is inclined toward the hopper outlet and the length of the vector is high, especially in cases of 90° geometry. The PSAT results for both higher hopper angle (60° and 90°) indicated that this zone is the most stressed zone and the direction of the major principal stress is totally parallel or perpendicular to the wall respectively. Stagnant zones at the hopper boundaries are clearly reported at these hoppers geometries, and the extent of stagnation is higher in cases of 90° hopper geometry. In general, the particle velocity at the lower segment, close to the outlet, inside all hopper geometries, is faster than that reported at upper segments. In addition, the smaller internal angle hopper has the faster particle flow among all hopper geometries at all heights.

Multiple variables influencing granular materials flow behaviours including hopper outlet size, granular bed lubrication and hopper wall roughness have been evaluated in this project using the DPIV method. The results indicated that increasing the hopper outlet has greater influences than bed lubrication on particulates velocity. Moreover, wall roughness decreases particles velocity at hopper boundaries, more than the central hopper zone and the influence of wall roughness is more noticeable at higher hopper internal angles.

At a later stage of the research, the shear stress profiles propagation, particulate velocity and bed deformation under relatively low uniaxial compression forces have been evaluated using PSAT and DPIV methods. The aim of this part of the research was to evaluate the influences of particulates motion, location, inter particle friction and particle wall friction on the evolution and distribution of shear stress profiles inside compressed assembly. The PSAT results showed a highly stressed zone

directly below the compression punch, and the overall stress status increases by raising the compression force. The stress diffuses from the higher granular layers downward to the bottom section of the compression chamber and then deviates to the boundaries. The most stressed zone was the top die section, followed by the middle and bottom sections respectively. At any die level, the central zone across the die, showed higher stress values than its corresponding boundaries and stress magnitudes at the boundaries greatly influenced by increasing the compression load. In general, the compressed granular system showed gradual stress saturation directly proportional to the applied loads. The discrete micro-particles granular assembly behaves like continuum materials in the way of stress transferring and in good level of generic agreement with that reported in literatures using FEM.

The DPIV results clearly reported that the particulates located directly below the compression punch showed higher velocity magnitudes than those located at the middle and bottom die sections. Particles close to the die base showed almost no motion which is attributed to the rigid surrounded boundaries. The central zone of the top die section reported high velocity magnitudes and thought to be attributed to available air voids at this segment and due to the driven particulates from the upper die segment to the central axis (Macleod and Marshall, 1977). Linking PSAT results to the DPIV results showed obviously that the particles motion at the top section of the die though to increases the interparticle friction under low compression force leading to more stress generation at the central zone of the die. This suggests that interparticle friction becomes more dominant during shear stress profile propagation inside the compressed granular assembly than particle wall friction. On the other hand, very limited particulates motion at the bottom of the die, minimised the chance of interparticle friction and consequently decreased the stress magnitudes and propagation. Stress evolution at the bottom section depends on the amounts of stress quantities transmitted from the top sections toward the die base through interparticle force network.

## 9.2 Relevance of Experiments to the Framework of Forces and Mobilised Shear Stress Propagation under Relatively Low Uniaxial Compression

The experimental findings reported in Chapter 7 for stress profiles development using PSAT and Chapter 8 for mean resultant velocity vectors using DPIV during early stage of compression under low load level are summarised in Figure 9.1.

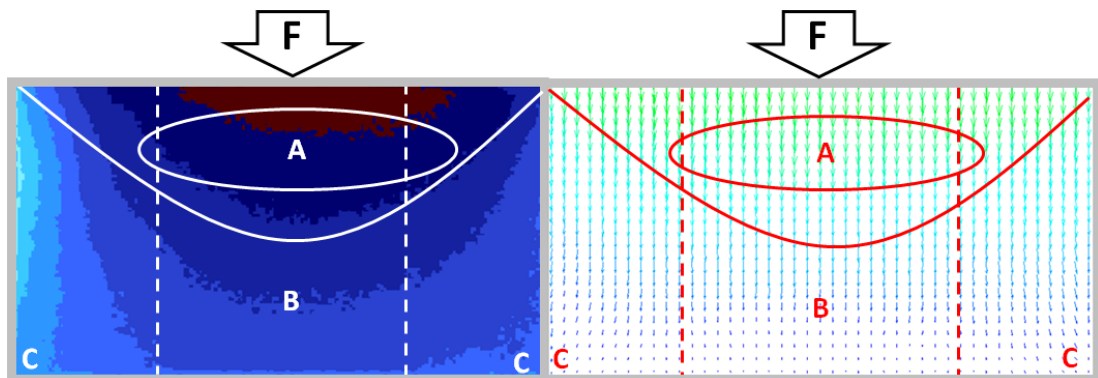


**Figure 9.1** Maximum shear stress profiles development (a), and the mean resultant velocity vectors of granules under relatively low uniaxial compression

In general, the obtained experimental results suggested that under relatively low uniaxial compression conditions, the influence of particle wall friction seems to be negligible and the interparticle friction thought to becomes dominant during in-die shear stress propagation. The stress image in Figure (9.1a) shows totally non-homogenous stress distribution inside the whole die geometry. Overall, highly stressed central regions (A) are located directly below the punch at the axisymmetric die axis while the lowest stressed zones are reported at the die base adjacently to the boundaries, region (C). At any cross sectional line, the maximum shear stress magnitudes are obtained at the central region (B). The obtained resultant mean velocity vectors map in Figure (9.1b) shows obviously that region (A) has high velocity magnitudes in downward trend; the maximum velocity value at each cross sectional line is obtained at the central region (B). As a result, region (A) will be highly stressed zone and the maximum shear stress values were reported within region (B) due to continuous particulates motion and high extent of interparticle friction. In general, the particulates close to the base, show very low velocity

magnitudes especially at regions (C) located adjacent to the base boundaries due to rigid surroundings.

The suggested framework for acting forces and mobilised shear stress is based on eight main assumptions based on the compression fundamentals and the experimental findings in this research project;

- The applied axial compression load is transmitted vertically to the compression die as a shearing force (Train, 1957).
- The force is transmitted radially to the die base and walls through the interparticle forces network, continuum material like behaviour (Train, 1957).
- The compression forces direction at the top die section will be toward the central region of the compressed bed (Macleod and Marshall, 1977).
- The influence of the wall particle friction is negligible at relatively low compression forces, therefore, no arch effect.
- The influence of interparticle friction is more dominant under relatively low compression forces.
- The particulates inside the die are in continuous motion at different velocity gradients and almost zero at the base of the die.
- The particulates motion close to the die boundaries is less than that at the central axis.
- The compressed discrete granular materials behave like continuum materials and shear stress transmitted downward via the interparticle force network leading to gradual stress saturation status of the compressed regions.

According to the experimental results in this research project using PSAT and DPIV methods, and based on the previous studies conducted by Train (1957), Macleod and Marshall (1977), Michrafy et al. (2002), Denny (2002) and Diarra et al. (2012), the forces act on the compressed granular assembly under relatively low uniaxial compression force are the axial applied force ( $F_u$ ), transmitted force ( $F_L$ ), Frictional force ( $F_W$ ) and radial force ( $F_D$ ), see Figure 9.2.

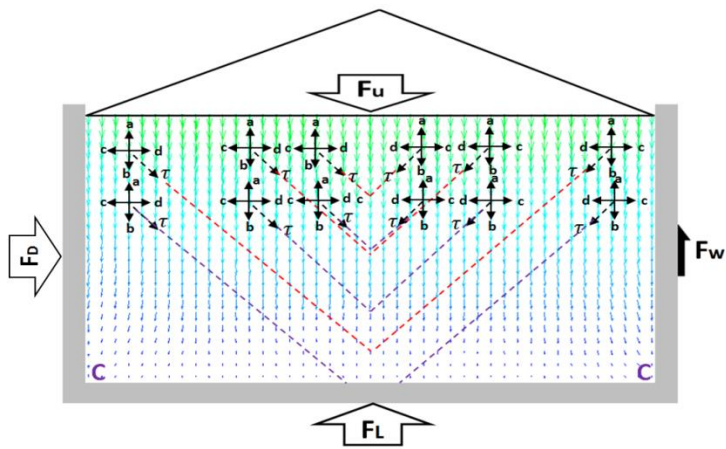


**Figure 9.2** Forces act on compressed granular assembly and mobilised shear stress development under relatively low uniaxial compression at early stage of the compression cycle

At balance, the acting forces on the compressed bed are equated as

$$F_u = F_L + F_w \quad \text{Eq. 9.1}$$

The Frictional force ( $F_w$ ) is directly related to both die particle wall friction ( $f_w$ ) and interparticle friction ( $f_i$ ) and equated as

$$F_w = (f_w) + (f_i) \quad \text{Eq. 9.2}$$

The friction force in equation 9.2 can be equated in relation to the developed radial force ( $F_D$ ) and the friction coefficients as follow;

$$F_w = (F_D * \mu_w) + (F_D * \mu_i) \quad \text{Eq. 9.3}$$

Where

$\mu_w$  is the particle wall friction coefficient.

$\mu_i$  is the interparticle friction coefficient

At early stage of the compression process, the influence of  $\mu_w$  is negligible and  $\mu_i$  is more dominant. Therefore, equation 9.3 can be written as follow;

$$F_w = (F_D * \mu_i) \quad \text{Eq. 9.4}$$

The radial force ( $F_D$ ) at early compression stage is directly related to the axial compression force and inversely with the compressed bed porosity ( $\varepsilon$ ) due to particles rearrangement and equated as

$$F_D \propto \frac{1}{\varepsilon} \quad \text{Eq. 9.5}$$

$$F_D \propto F_u \quad \text{Eq. 9.6}$$

From equations 9.5 and 9.6, the radial force at rearrangement compression stage can be equated as

$$F_D = \left(1 - \frac{\varepsilon_a}{\varepsilon_i}\right) F_u \quad \text{Eq. 9.7}$$

Where

$F_u$  is the axial compression force

$\varepsilon_a$  is the compressed bed porosity within rearrangement compression phase

$\varepsilon_i$  is the initial granular bed porosity under zero load

From equations 9.1, 9.4, 9.5, 9.6 and 9.7, the forces acting on compressed granular assembly during rearrangement compression stage at equilibrium are equated as follow;

$$F_u = F_L + \left( \left(1 - \frac{\varepsilon_a}{\varepsilon_i}\right) * F_u * \mu_i \right) \quad \text{Eq. 9.8}$$

or

$$F_L = F_u - \left( \left(1 - \frac{\varepsilon_a}{\varepsilon_i}\right) * F_u * \mu_i \right) \quad \text{Eq. 9.9}$$

As a result of particulates continuous motion, and according to Train (1957) and Macleod and Marshall (1977), the compressed bed develops multiple internal mobilised shearing forces as illustrated in Figure 9.2. In general, the maximum mobilise shearing force will be obtained at the central region of the die at all heights, due to higher velocity magnitudes at this region comparing to the boundaries. The particulates at the lower die segment in general and at the boundaries in particular at

region C, show limited particulate motion and this region will show the minimum shearing forces. The mobilised shear stress ( $\tau_\alpha$ ) directions will be toward the central die region due to particulates motion and the central region will show the maximum shear stress values. According to Mohr stress circle, the mobilised shear stress for all possible angles  $\alpha$  will be equated as follows:

$$\tau_\alpha = \frac{\sigma_1 - \sigma_3}{2} \sin (2\alpha) \quad \text{Eq. 9.10}$$

And the maximum shear stress at any point can be calculated as follow;

$$\tau_{max} = \frac{\sigma_1 - \sigma_3}{2} \quad \text{Eq. 9.11}$$

Where

$\tau_\alpha$  shear stress acting on a plane inclined by an arbitrary angle  $\alpha$

$\tau_{max}$  Maximum shear stress

$\sigma_1$  and  $\sigma_3$  are the major and minor principal stresses respectively.

The suggested framework in this project needs further future experimental and numerical work for validation.

### 9.3 Recommended Future Work

- (i) The birefringent response of the granules could be improved by fine-tuning their crystallinity using different types of ingredients in their fabrications, for example using sucrose and bovine gelatine.
- (ii) To achieve the above, molecular dynamics simulations for the optical responses of granular materials could be considered in future
- (iii) Due to the limitations on the availability of technology, dynamic tracking of stress distribution in granular systems is not available at this stage, but can be developed in future.
- (iv) The current experimental study considered spherical granules and future studies could be extended for non-spherical granules to understand their stress distribution and dynamic flow properties

- (v) The current research is primarily focused on applying experimental tomographic methodologies for granular systems. More detailed and extensive level of simulations using DEM, FEM and analytical methods could be used in future for further understanding the micromechanical properties of granular systems at different spatial and temporal dimensions.
- (vi) Further modifications of the fabricated compression chamber used in this thesis could help for future work to test the validity of the framework suggested in this project by embedding a multiple force gauges on the chamber walls and measure the acting forces. This can be conducted concurrently with simulation method such as DEM or FEM.

## References:

- Aben, H. 2007. On the role of T. J. Seebeck in the discovery of the photoelastic effect in glass. *Proc. Estonian Acad. Sci. Eng*, 13, 283–294.
- Aben, H., Ainola, L. & Anton, J. 2000. Integrated photoelasticity for nondestructive residual stress measurement in glass. *Optics and lasers in engineering*, 33, 49-64.
- Adrian, R. J. 1991. Particle-imaging techniques for experimental fluid mechanics. *Annual Review of Fluid Mechanics*, 23, 261-304.
- Adrian, R. J. 2005. Twenty years of particle image velocimetry. *Experiments in Fluids*, 39, 159-169.
- Agrawal, R. & Naveen, Y. 2011. Pharmaceutical processing—A review on wet granulation technology. *International J Pharmaceutical Frontier Research*, 1, 65-83.
- Ajovalasit, A., Petrucci, G. & Scafidi, M. 2012. RGB photoelasticity applied to the analysis of membrane residual stress in glass. *Measurement science and technology*, 23, 1-8.
- Akhmetzyanov, M. & Albaut, G. 2004. Study of large plastic strains and fracture in metal elements by photoelastic coating method. *International journal of fracture*, 128, 223-231.
- Akseli, I., Stecula, A., He, X. R. & Ladyzhynsky, N. 2014. Quantitative correlation of the effect of process conditions on the capping tendencies of tablet formulations. *Journal of Pharmaceutical Sciences*, 103, 1652-1663.
- Al-Suwayeh, S. A., El-Shaboury, M. H., Al-Baraki, S. M., Elgorashy, A. S. & Taha, E. I. 2009. In vitro and in vivo evaluation of sustained release hydralazine hydrochloride tablets prepared by thermal granulation technique. *Aust J Basic Appl Sci*, 3, 2866-2875.
- Alanazi, F., El-Bagory, I. M., Alsarra, I. A., Bayomi, M. A. & Abdel-Kawy, M. A. 2008 Saudi corn starch as a tablet excipient compared with imported starch. *Saudi Pharmaceutical Journal.*, 16 (2), 112 – 121.
- Albaraki, S. & Antony, S. J. 2013. Investigation on the effects of initial stress state of powder packing on macroscopic powder flow properties *The International Porous and Powder Materials Symposium and Exhibition Izmir, Turkey.* Available online at [http://www.researchgate.net/publication/271503638\\_Investigation\\_on\\_the\\_effects\\_of\\_initial\\_stress\\_state\\_of\\_powder\\_packing\\_on\\_macroscopic\\_powder\\_flow\\_properties](http://www.researchgate.net/publication/271503638_Investigation_on_the_effects_of_initial_stress_state_of_powder_packing_on_macroscopic_powder_flow_properties) [ Accessed at 9 March 2015]

- Albaraki, S. & Antony, S. J. 2014. How does internal angle of hoppers affect granular flow? Experimental studies using Digital Particle Image Velocimetry. *Powder Technology*, 268, 253-260.
- Albaraki, S., Antony, S. J. & Arowosola, C. B. 2013. Visualising shear stress distribution inside flow geometries containing pharmaceutical powder excipients using photo stress analysis tomography and DEM simulations. *AIP Conference Proceedings*, 2013. 706-709.
- Alexandrov, I., Zhu, Y., Lowe, T. & Valiev, R. 1998. Severe plastic deformation: new technique for powder consolidation and grain size refinement. *Powder metallurgy*, 41, 11-13.
- Alonso-Marroquín, F., Mühlhaus, H. B. & Herrmann, H. J. 2008. Micromechanical investigation of granular ratcheting using a discrete model of polygonal particles. *Particuology*, 6, 390-403.
- Amorós, J., Mallol, G., Sánchez, E. & Garcia, J. 2000. Design of bins and hoppers for the storage of particulate materials; problems associated with the discharge operation. *Tile and Brick International* 16, 168-179.
- Andreyev, V. 1975. The application of birefringent coatings to metal surfaces which are to undergo large plastic strains. *Experimental Mechanics*, 15, 394-395.
- Andrushchak, A., Bobitski, Y. V., Kaidan, M., Tybinka, B., Kityk, A. & Schranz, W. 2004. Spatial anisotropy of photoelastic and acoustooptic properties in  $\beta$ -BaB<sub>2</sub>O<sub>4</sub> crystals. *Optical Materials*, 27, 619-624.
- Antony, S. 2007. Link between single-particle properties and macroscopic properties in particulate assemblies: role of structures within structures. *Philosophical Transactions of the Royal Society A: Mathematical, Physical and Engineering Sciences*, 365, 2879-2891.
- Antony, S. & Sarangi, F. 2006. Computational study investigating the influence of long-range repulsive forces on the collective behaviour of particulate media. *Journal of Computational and Theoretical Nanoscience*, 3, 487-496.
- Antony, S. J. 2001. Evolution of force distribution in three-dimensional granular media. *Physical Review E*, 63, 011302.
- Antony, S. J. 2015. Imaging shear stress distribution and evaluating the stress concentration factor of the human eye. *Scientific reports*, 5.
- Antony, S. J., Albaraki, S., Arowosola, B. C. & Agarwal, N. 2012. Novel visual Probing of shear stress distribution inside pharmaceutical powder packing within constrained geometries using photo stress analysis tomography *PharmSci*. Nottingham, UK, available online at [http://www.researchgate.net/publication/271503647\\_Novel\\_visual\\_probing\\_of\\_shear\\_stress\\_distribution\\_inside\\_pharmaceutical\\_powder\\_packing\\_within\\_constrained\\_geometries\\_using\\_photo\\_stress\\_analysis\\_tomography](http://www.researchgate.net/publication/271503647_Novel_visual_probing_of_shear_stress_distribution_inside_pharmaceutical_powder_packing_within_constrained_geometries_using_photo_stress_analysis_tomography) [Accessed at 3 March 2015]

- Antony, S. J., Albaraki, S., Mandare, A. & Arowosola, B. C. 2014a. Current developments on the flow behaviour of particulate materials using advanced simulations and tomography experiments  
*Particulate Systems Analysis 2014, Manchester, UK*. Available online at <http://www.researchgate.net/publication/271503497>
- Antony, S. J., Barakat, T., Hammond, R. B., Sheeba, K. N., Amanbayev, T., Okeke1, G., Albaraki, S., Arowosola, C. B. & Olugbenga, A. 2013. Multiscale particulate mechanics in multi-disciplinary engineering applications *UK-China International Particle Technology Forum China*, available online at [http://www.researchgate.net/publication/271503721\\_Multiscale\\_particulate\\_mechanics\\_in\\_multidisciplinary\\_engineering\\_applications](http://www.researchgate.net/publication/271503721_Multiscale_particulate_mechanics_in_multidisciplinary_engineering_applications) [ Accessed at 3 March 2015].
- Antony, S. J. & Chapman, D. 2010. Probing shear stress distribution within single particle scale inside particulate packing. *Kona Powder and Particle Journal*, 28, 180-188.
- Antony, S. J., Imafidon, O. & Barakat, T. 2014b. Micromechanical analysis of inclusions in particulate media using digital photo stress analysis tomography. *Optical Engineering*, 1-18.
- Antony, S. J. & Kuhn, M. R. 2004. Influence of particle shape on granular contact signatures and shear strength: new insights from simulations. *International Journal of Solids and Structures*, 41, 5863-5870.
- Antony, S. J., Kuhn, M. R., Barton, D. C. & Bland, R. 2005. Strength and signature of force networks in axially compacted sphere and non-sphere granular media: micromechanical investigations. *Journal of Physics D-Applied Physics*, 38, 3944-3952.
- Aole, D., Jain, M. K. & Bruhis, M. 2012. New characterization methods for powder die fill process for producing powder metallurgical components. *Powder Technology*, 232, 7-17.
- Atewologun, A. & Riskowski, G. 1991. Experimental determination of Janssen's stress ratio by four methods for soybeans under static conditions. *Transactions of the ASAE*, 34, 2193.
- Atkins, A. & Mai, Y.-W. 1986. Deformation transitions. *Journal of materials science*, 21, 1093-1110.
- Babout, L., Grudzien, K., Maire, E. & Withers, P. J. 2013. Influence of wall roughness and packing density on stagnant zone formation during funnel flow discharge from a silo: An X-ray imaging study. *Chemical Engineering Science*, 97, 210-224.
- Bagster, D. 1971. A note on the pressure ratio in the Janssen equation. *Powder Technology*, 4, 235-237.

- Baker, F. & Whelan, W. 1950. Birefringence of amylose and amylopectin in whole structural starches. *166*, 34-34.
- Baxter, G., Behringer, R., Fagert, T. & Johnson, G. 1990. Pattern formation and time-dependence in flowing sand. *Two phase flows and waves*. Springer Verlag, New York, 1-29.
- Baxter, J., Abou-Chakra, H., Tuzun, U. & Lamptey, B. M. 2000. A DEM simulation and experimental strategy for solving fine powder flow problems. *Chemical Engineering Research & Design*, *78*, 1019-1025.
- Beckett, C. & Augarde, C. 2011. A Novel image-capturing technique for the experimental study of soil deformations during compaction. *Geotechnical Testing Journal*, *34*, 571-578.
- Behringer, R., Bi, D., Chakraborty, B., Clark, A., Dijksman, J., Ren, J. & Zhang, J. 2014. Statistical properties of granular materials near jamming. *Journal of Statistical Mechanics: Theory and Experiment*, 2014, P06004.
- Berne, B. J. & Pecora, R. 2000. *Dynamic light scattering: with applications to chemistry, biology, and physics*, NY, USA, Courier Dover Publications NY, USA.
- Bohrnsen, J. U., Antes, H., Ostendorf, M. & Schwedes, J. 2004. Silo discharge: Measurement and simulation of dynamic behavior in bulk solids. *Chemical Engineering & Technology*, *27*, 71-76.
- Bratberg, I., Maloy, K. J. & Hansen, A. 2005. Validity of the Janssen law in narrow granular columns. *European Physical Journal E*, *18*, 245-252.
- Bridgwater, J., Forrest, S. & Parker, D. 2004. PEPT for agglomeration? *Powder technology*, *140*, 187-193.
- Calvert, G., Lesniak, J. & Honlet, M. 2002. Applications of modern automated photoelasticity to industrial problems. *Insight*, *44*, 224-227.
- Cambou, B., Dubujet, P. & Nouguier-Lehon, C. 2004. Anisotropy in granular materials at different scales. *Mechanics of materials*, *36*, 1185-1194.
- Campbell, C. S. 1990. Rapid granular flows. *Annual Review of Fluid Mechanics*, *22*, 57-92.
- Carson, L. J. 2001. Silo failures: Case histories and lessons learned. In: LEVY, A. & KALMAN, H. (eds.) *Handbook of Conveying and Handling of Particulate Solids*. The Netherlands: Elsevier Science, 153-166.
- Carstensen, J. T. & Toure, P. 1980. Compression cycles in tabletting. *Powder Technology*, *26*, 199-204.

- Castellanos, A., Valverde, J. M., Pérez, A. T., Ramos, A. & Watson, P. K. 1999. Flow regimes in fine cohesive powders. *Physical Review Letters*, 82, 1156-1159.
- Celik, M. 1992. Overview of compaction data-analysis techniques. *Drug Development and Industrial Pharmacy*, 18, 767-810.
- Chang, C.-W., Chen, P. H. & Lien, H. S. 2009. Evaluation of residual stress in pre-stressed concrete material by digital image processing photoelastic coating and hole drilling method. *Measurement*, 42, 552-558.
- Chen, J., Rotter, J. & Ooi, J. 1998. Statistical inference of unsymmetrical silo pressures from comprehensive wall strain measurements. *Thin-walled structures*, 31, 117-136.
- Chen, P., Yu, L., Chen, L. & Li, X. 2006. Morphology and microstructure of maize starches with different amylose/amyopectin content. *Starch-Stärke*, 58, 611-615.
- Cheng, Y., White, D., Bowman, E., Bolton, M. & Soga, K. 2001. The observation of soil microstructure under load. *Powders & Grains*. Balkema, 69-72.
- Choi, J., Kudrolli, A. & Bazant, M. Z. 2005. Velocity profile of granular flows inside silos and hoppers. *Journal of Physics-Condensed Matter*, 17, S2533-S2548.
- Chou, C. S. & Chen, R. Y. 2003. The static and dynamic wall stresses in a circulatory two-dimensional wedge hopper. *Advanced Powder Technology*, 14, 195-213.
- Cleary, P. W. & Sawley, M. L. 2002. DEM modelling of industrial granular flows: 3D case studies and the effect of particle shape on hopper discharge. *Applied Mathematical Modelling*, 26, 89-111.
- Comoglu, T. 2007. An overview of compaction equations. *Journal of Faculty of Pharmacy*, 36, 123-133.
- Coral, D., Pineda-Gómez, P., Rosales-Rivera, A. & Rodriguez-Garcia, M. Determination of the gelatinization temperature of starch presented in maize flours. *Journal of Physics: Conference Series*, 2009. IOP Publishing, 1-5.
- Coube, O., Cocks, A. C. F. & Wu, C. Y. 2005. Experimental and numerical study of die filling, powder transfer and die compaction. *Powder Metallurgy*, 48, 68-76.
- Cundall, P. & Strack, O. 1980. A discrete numerical model for granular assemblies. *Geotechnique*, 29, 331-336.
- Cundall, P. A. & Strack, O. D. L. 1979. A discrete numerical model for granular assemblies. *Geotechnique*, 29, 47-65.

- Davies, P. 2009. *Oral Solid Dosage Forms*. In: Gibson, M. ed. *Pharmaceutical Preformulation and Formulation: A Practical Guide from Candidate Drug Selection to Commercial Dosage Form*: Informa Healthcare, USA, pp. 367-430.
- De Gennes, P.-G. 2008. From rice to snow. *Nishina Memorial Lectures*. Springer.
- Denny, P. J. 2002. Compaction equations: a comparison of the Heckel and Kawakita equations. *Powder Technology*, 127, 162-172.
- Desrues, J. & Viggiani, G. 2004. Strain localization in sand: an overview of the experimental results obtained in Grenoble using stereophotogrammetry. *International Journal for Numerical and Analytical Methods in Geomechanics*, 28, 279-321.
- Dhumal, R. S., Kelly, A. L., York, P., Coates, P. D. & Paradkar, A. 2010. Cocrystallization and simultaneous agglomeration using hot melt extrusion. *Pharmaceutical research*, 27, 2725-2733.
- Diarra, H., Mazel, V., Boillon, A., Rehault, L., Busignies, V., Bureau, S. & Tchoreloff, P. 2012. Finite Element Method (FEM) modeling of the powder compaction of cosmetic products: Comparison between simulated and experimental results. *Powder Technology*, 224, 233-240.
- Ding, S. & Enstad, G. 2003. Stress distribution in the material and development of loads on the wall during hopper filling. *Task Quarterly*, 7, 513-524.
- Ding, S., Rotter, J., Ooi, J. & Enstad, G. 2011. Development of normal pressure and frictional traction along the walls of a steep conical hopper during filling. *Thin-Walled Structures*, 49, 1246-1250.
- Dora, P. T. & Ramesh, K. Measurement of residual birefringence in thin glass plates using digital photoelasticity. International Conference on Experimental Mechanics 2013 and the Twelfth Asian Conference on Experimental Mechanics, 2014. International Society for Optics and Photonics, 1-6.
- Duberg, M. & Nyström, C. 1986. Studies on direct compression of tablets XVII. Porosity—pressure curves for the characterization of volume reduction mechanisms in powder compression. *Powder technology*, 46, 67-75.
- Duran, J. 2000. *Sands, Powders and Grains. An Introduction to the Physics of Granular Materials.*, Springer, New York.
- Emery, E., Oliver, J., Pugsley, T., Sharma, J. & Zhou, J. 2009. Flowability of moist pharmaceutical powders. *Powder Technology*, 189, 409-415.
- Evans, A., Mcnish, N. & Thompson, D. B. 2003. Polarization Colors of Lightly Iodine-stained Maize Starches for Amylose-Extender and Related Genotypes in the W64A Inbred Line. *Starch-Stärke*, 55, 250-257.
- Ezz El-Arab, I. 2014. Seismic analysis of RC silos dynamic discharge

Phenomena. *International Journal of Engineering and Advanced Technology*, 4, 91-99.

Fannon, J. E., Shull, J. M. & Bemiller, J. N. 1993. Interior channels of starch granules. *Cereal chemistry* 70, 611-613.

Fedorchenko, I., Kovynev, R., Makovetskii, V. & Sitnikov, L. 1968. A photoelastic technique for examining contact stresses in powder compaction. *Soviet Powder Metallurgy and Metal Ceramics*, 7, 850-854.

Forterre, Y. & Pouliquen, O. 2008. Flows of dense granular media. *Annual Review of Fluid Mechanics*, 40, 1-24.

Fortuna, T., Januszewska, R., Juszczak, L., Kielski, A. & Pałasiński, M. 2000. The influence of starch pore characteristics on pasting behaviour. *International journal of food science & technology*, 35, 285-291.

Freeman, R. & Fu, X. 2008. Characterisation of powder bulk, dynamic flow and shear properties in relation to die filling. *Powder Metallurgy*, 51, 196-201.

Frenning, G. 2010. Compression mechanics of granule beds: A combined finite/discrete element study. *Chemical Engineering Science*, 65, 2464-2471.

Frost, K., Kaminski, D., Kirwan, G., Lascaris, E. & Shanks, R. 2009. Crystallinity and structure of starch using wide angle X-ray scattering. *Carbohydrate Polymers*, 78, 543-548.

Fu, X., Elliott, J. A., Bentham, A. C., Hancock, B. C. & Cameron, R. E. 2006. Application of X-ray Microtomography and Image Processing to the Investigation of a Compacted Granular System. *Particle & particle systems characterization*, 23, 229-236.

Futterknecht, O., Macqueen, M. O., Karman, S., Diah, S. Z. M. & Gebeshuber, I. C. 2013. Biomimetic MEMS sensor array for navigation and water detection. SPIE Microtechnologies, 2013. International Society for Optics and Photonics, 1-9.

Ganesan, V., Rosentrater, K. A. & Muthukumarappan, K. 2008. Flowability and handling characteristics of bulk solids and powders—a review with implications for DDGS. *biosystems engineering*, 101, 425-435.

Gardner, G. 1966. The region of flow when discharging granular materials from bin-hopper systems. *Chemical Engineering Science*, 21, 261-273.

Geng, J. F., Longhi, E., Behringer, R. P. & Howell, D. W. 2001. Memory in two-dimensional heap experiments. *Physical Review E*, 64, 6, 060301.

Gilber, S. & Neil, R. 1987. Tablets. In: Lachman,L., Liebermann, H., and Kanig,L. 3rd Ed *The theory and practice of Industrial pharmacy.*: Lea and Febiger. pp. 293-345.

- Goda, T. J. & Ebert, F. 2005. Three-dimensional discrete element simulations in hoppers and silos. *Powder technology*, 158, 58-68.
- Goering, K., Fritts, D. & Allen, K. 1974. Comparison of loss of birefringence with the percent gelatinization and viscosity on potato, wheat, rice, corn, cow cockle, and several barley starches. *Cereal chemistry*, 51, 764 - 771.
- Goldstein, D. H. 2011. *Polarized Light, revised and expanded, Second Edition*, CRC Press.
- Grantham, S. G. & Forsberg, F. 2004. Measurement of granular flow in a silo using Digital Speckle Radiography. *Powder Technology*, 146, 56-65.
- Grudzieñ, K., Maire, E., Adrien, J. & Sankowski, D. 2010. Analysis of funnel flow in rectangular silo based on ECT data. *Nature*, 5, 681-694.
- Guo, Y., Wu, C.-Y., Kafui, K. & Thornton, C. 2011. 3D DEM/CFD analysis of size-induced segregation during die filling. *Powder Technology*, 206, 177-188.
- Guyon, E., Roux, S., Hansen, A., Bideau, D., Troadec, J.-P. & Crapo, H. 1990. Non-local and non-linear problems in the mechanics of disordered systems: application to granular media and rigidity problems. *Reports on Progress in Physics*, 53, 373-419.
- Hall, S., Bornert, M., Desrues, J., Pannier, Y., Lenoir, N., Viggiani, G. & Bésuelle, P. 2010. Discrete and continuum analysis of localised deformation in sand using X-ray µCT and volumetric digital image correlation. *Géotechnique*, 60, 315-322.
- Han, L., Elliott, J., Bentham, A., Mills, A., Amidon, G. & Hancock, B. 2008. A modified Drucker-Prager Cap model for die compaction simulation of pharmaceutical powders. *International Journal of Solids and Structures*, 45, 3088-3106.
- Hancock, B. C. & Mullarney, M. P. 2005. X-ray microtomography of solid dosage forms. *Pharm. Technol.*, 29, 92–100.
- Hapgood, K. P., Litster, J. D., Biggs, S. R. & Howes, T. 2002. Drop penetration into porous powder beds. *Journal of Colloid and Interface Science*, 253, 353-366.
- Haque, E. 2013. Estimating bulk density of compacted grains in storage bins and modifications of Janssen's load equations as affected by bulk density. *Food Science & Nutrition*, 1, 150-156.
- Hassanpour, A., Antony, S. J. & Ghadiri, M. 2007. Effect of size ratio on the behaviour of agglomerates embedded in a bed of particles subjected to shearing: DEM analysis. *Chemical Engineering Science*, 62, 935-942.
- Hassanpour, A., Ding, Y. & Ghadiri, M. 2004. Shear deformation of binary mixtures of dry particulate solids. *Advanced Powder Technology*, 15, 687-697.

- Hassanpour, A. & Ghadiri, M. 2004. Distinct element analysis and experimental evaluation of the Heckel analysis of bulk powder compression. *Powder Technology*, 141, 251-261.
- Hassanpour, A., Kwan, C., Ng, B., Rahamanian, N., Ding, Y., Antony, S., Jia, X. & Ghadiri, M. 2009. Effect of granulation scale-up on the strength of granules. *Powder Technology*, 189, 304-312.
- Hassanpour, A., Pasha, M., Susana, L., Rahamanian, N., Santomaso, A. C. & Ghadiri, M. 2013. Analysis of seeded granulation in high shear granulators by discrete element method. *Powder Technology*, 238, 50-55.
- Heckel, R. 1961a. An analysis of powder compaction phenomena. *Transactions of the Metallurgical Society of AIME*, 221, 1001-1008.
- Heckel, R. 1961b. Density-pressure relationships in powder compaction. *Trans Metall Soc AIME*, 221, 671-675.
- Hemmingsson, J., Herrmann, H. J. & Roux, S. 1997. Vectorial cellular automaton for the stress in granular media. *Journal De Physique I*, 7, 291-302.
- Hersey, J. 1974. Powder consolidation during pharmaceutical tabletting. *Drug Development and Industrial Pharmacy*, 1, 223-229.
- Hesselink, L. 1988. Digital image processing in flow visualization. *Annual Review of Fluid Mechanics*, 20, 421-486.
- Hewitt, R., Wallace, W. & Demalherbe, M. 1974. Plastic deformation in metal powder compaction. *Powder Met.*, 17, 1-12.
- Heybey, O. W. & Lee, D. M. 1967. Optical Birefringence and Crystal Growth of Hexagonal-Close-Packed He4 from Superfluid Helium. *Physical Review Letters*, 19, 106-108.
- Heywood, H. 1933. Calculation of the Specific Surface of a Powder. *Proceedings of the Institution of Mechanical Engineers*, 125, 383-459.
- Hitzenberger, C., Gotzinger, E. & Pircher, M. 2006. Birefringence properties of the human cornea measured with polarization sensitive optical coherence tomography. *Bull. Soc. belge Ophtalmol.*, 302, 153-168.
- Holdich, R. G. 2002. *Fundamentals of particle technology*, UK, Midland information technology and publishing, Available online at [http://www.particles.org.uk/particle\\_technology\\_book/particle\\_book.htm](http://www.particles.org.uk/particle_technology_book/particle_book.htm). [Accessed June 17 2015].
- Hua, L., Qin, X., Mao, H. & Zhao, Y. 2006. Plastic deformation and yield criterion for compressible sintered powder materials. *Journal of Materials Processing Technology*, 180, 174-178.

- Huan, C., Yang, X., Candela, D., Mair, R. & Walsworth, R. 2004. NMR experiments on a three-dimensional vibrofluidized granular medium. *Physical Review E*, 69, 041302.
- Huang, Q., Li, L. & Fu, X. 2007. Ultrasound effects on the structure and chemical reactivity of cornstarch granules. *Starch-Starke*, 59, 371-378.
- Huber, K. & Bemiller, J. 2000. Channels of maize and sorghum starch granules. *Carbohydrate Polymers*, 41, 269-276.
- Huber, K. C. & Bemiller, J. N. 1997. Visualization of channels and cavities of corn and sorghum starch granules 1. *Cereal Chemistry*, 74, 537-541.
- Imberty, A., Buléon, A., Tran, V. & Pérez, S. 1991. Recent advances in knowledge of starch structure. *Starch-Starke*, 43, 375-384.
- Ismail, A. E. 2008. Sound generated during the compaction of alumina reinforced aluminum powders. 4th International Colloquium on Signal Processing and its Applications,, 2008 Malaysia., 577-580.
- Iveson, S. M., Litster, J. D., Hapgood, K. & Ennis, B. J. 2001. Nucleation, growth and breakage phenomena in agitated wet granulation processes: a review. *Powder Technology*, 117, 3-39.
- Jaeger, H. M., Nagel, S. R. & Behringer, R. P. 1996. Granular solids, liquids, and gases. *Reviews of Modern Physics*, 68, 1259-1273.
- Jane, J.-L. 2006. Current understanding on starch granule structures. *Journal of Applied Glycoscience*, 53, 205-213.
- Jankowski, L. J., Jasieńko, J. & Nowak, T. P. 2010. Experimental assessment of CFRP reinforced wooden beams by 4-point bending tests and photoelastic coating technique. *Materials and Structures*, 43, 141-150.
- Jenike, A., Johanson, J. & Carson, J. 1973. Bin Loads—Part 3: Mass-Flow Bins. *Journal of Engineering for Industry*, 95, 6-12.
- Jenike, A. W. 1964. Storage and flow of solids, bulletin no. 123. *Bulletin of the University of Utah*, 53.
- Jenike, A. W. & Johanson, J. 1969. On the theory of bin loads. *Journal of Engineering for Industry*, 91, 339-344.
- Jenkins, P. & Donald, A. 1995. The influence of amylose on starch granule structure. *International Journal of Biological Macromolecules*, 17, 315-321.
- Kadiri, M., Michrafy, A. & Dodds, J. 2005. Pharmaceutical powders compaction: experimental and numerical analysis of the density distribution. *Powder technology*, 157, 176-182.

- Karathanos, V. & Saravacos, G. 1993. Porosity and pore size distribution of starch materials. *Journal of food engineering*, 18, 259-280.
- Kawakita, K. 1956. Compression of powder. *Kagaku*, 26, 149-150.
- Kawakita, K. & Lüdde, K.-H. 1971. Some considerations on powder compression equations. *Powder technology*, 4, 61-68.
- Ketterhagen, W. R., Curtis, J. S., Wassgren, C. R. & Hancock, B. C. 2009a. Predicting the flow mode from hoppers using the discrete element method. *Powder Technology*, 195, 1-10.
- Ketterhagen, W. R., Ende, M. T. A. & Hancock, B. C. 2009b. Process modeling in the pharmaceutical industry using the discrete element method. *Journal of Pharmaceutical Sciences*, 98, 442-470.
- Kheiripour Langroudi, M., Sun, J., Sundaresan, S. & Tardos, G. 2010. Transmission of stresses in static and sheared granular beds: The influence of particle size, shearing rate, layer thickness and sensor size. *Powder Technology*, 203, 23-32.
- Kim, H.-S. & Huber, K. C. 2008. Channels within soft wheat starch A-and B-type granules. *Journal of Cereal Science*, 48, 159-172.
- Kondic, L. 2014. Simulations of two dimensional hopper flow. *Granular Matter*, 16, 235-242.
- Kondic, L., Goulet, A., O'hern, C. S., Kramar, M., Mischaikow, K. & Behringer, R. P. 2012. Topology of force networks in compressed granular media. *Europhysics Letters*, 97, 1-7.
- Kottke, M., Chueh, H.-R. & Rhodes, C. 1992. Comparison of disintegrant and binder activity of three corn starch products. *Drug development and industrial pharmacy*, 18, 2207-2223.
- Kozicki, J. & Tejchman, J. 2011. Numerical simulations of sand behaviour using DEM with two different descriptions of grain roughness. In: E. O'naté, D.R.J. Owen (eds.) II International Conference on Particle-based Methods—Fundamentals and Applications. Particles, 2011.
- Kremer, D. M. & Hancock, B. C. 2006. Process simulation in the pharmaceutical industry: A review of some basic physical models. *Journal of Pharmaceutical Sciences*, 95, 517-529.
- Kristensen, H. G. & Schaefer, T. 1987. Granulation: A review on pharmaceutical wet-granulation. *Drug development and industrial pharmacy*, 13, 803-872.
- Krok, A., Peciar, M. & Fekete, R. 2014. Using the DPIV optical technique to measure the velocity of powder material in the space between the rollers in a roll compactor. *Powder Technology*, 262, 131-141.

- Kruyt, N. 1993. Results of Jenike's (1987) radial stress field theory for the flow of granular materials in conical hoppers: flow regimes and flow factors. *Powder Technology*, 76, 109-112.
- Kruyt, N. P. & Antony, S. J. 2007. Force, relative-displacement, and work networks in granular materials subjected to quasistatic deformation. *Physical Review E*, 75, (5), 051308.
- Kuentz, M. & Schirg, P. 2013. Powder flow in an automated uniaxial tester and an annular shear cell: a study of pharmaceutical excipients and analytical data comparison. *Drug development and industrial pharmacy*, 39, 1476-1483.
- Landry, J. W., Grest, G. S. & Plimpton, S. J. 2004. Discrete element simulations of stress distributions in silos: crossover from two to three dimensions. *Powder Technology*, 139, 233-239.
- Langston, P. A., Tuzun, U. & Heyes, D. M. 1995. Discrete element simulation of granular flow in 2d and 3d hoppers - dependence of discharge rate and wall stress on particle interactions. *Chemical Engineering Science*, 50, 967-987.
- Lee, Y. J. & Yoon, W. B. 2015. Flow behavior and hopper design for black soybean powders by particle size. *Journal of Food Engineering*, 144, 10-19.
- Lee, Y. S., Poynter, R., Podczeck, F. & Newton, J. M. 2000. Development of a dual approach to assess powder flow from avalanching behavior. *AAPS PharmSciTech* 1: Article 21), [Online], Available at [http://www.ncbi.nlm.nih.gov/pmc/articles/PMC2750349/pdf/12249\\_2008\\_Article\\_1344.pdf](http://www.ncbi.nlm.nih.gov/pmc/articles/PMC2750349/pdf/12249_2008_Article_1344.pdf), [Accessed February 13 2015].
- Leuenberger, H., Puchkov, M., Krausbauer, E. & Betz, G. 2009. Manufacturing pharmaceutical granules: Is the granulation end-point a myth? *Powder technology*, 189, 141-148.
- Litster, J., Ennis, B. & Lian, L. 2004. *The science and engineering of granulation processes*, Kluwer Academic Publishers, The Netherlands.
- Lou, J., Gabbitas, B., Zhang, D. & Yang, F. 2015. Effects of Initial Powder Compact Thickness, Lubrication, and Particle Morphology on the Cold Compaction Behavior of Ti Powder. *Metallurgical and Materials Transactions A*, 1-10.
- Lueptow, R., Akonur, A. & Shinbrot, T. 2000. PIV for granular flows. *Experiments in Fluids*, 28, 183-186.
- Lumay, G., Boschini, F., Traina, K., Bontempi, S., Remy, J.-C., Cloots, R. & Vandewalle, N. 2012. Measuring the flowing properties of powders and grains. *Powder Technology*, 224, 19-27.
- Lund, D. & Lorenz, K. J. 1984. Influence of time, temperature, moisture, ingredients, and processing conditions on starch gelatinization. *Critical Reviews in Food Science & Nutrition*, 20, 249-273.

- Macleod, H. & Marshall, U. 1977. The determination of density distribution in ceramic compacts using autoradiography. *Powder Technology*, 16, 107-122.
- Madou, M. J. 2011. *Solid-State Physics, Fluidics, and Analytical Techniques in Micro-and Nanotechnology*, CRC Press.
- Majmudar, T. S. & Behringer, R. P. 2005. Contact force measurements and stress-induced anisotropy in granular materials. *Nature*, 435, 1079-1082.
- Majmudar, T. S., Sperl, M., Luding, S. & Behringer, R. P. 2007. Jamming transition in granular systems. *Physical Review Letters*, 98, 5, 058001.
- Mallick, S. 2014. Rearrangement of particle and compactibility, tabletability and compressibility of pharmaceutical powder: A rational approach. *Journal of Scientific & Industrial Research*, 73, 51-56.
- Mallick, S., Pradhan, S. K., Chandran, M., Acharya, M., Digdarsini, T. & Mohapatra, R. 2011. Study of particle rearrangement, compression behavior and dissolution properties after melt dispersion of ibuprofen, Avicel and Aerosil. *Results in pharma sciences*, 1, 1-10.
- Mankoc, C., Janda, A., Arevalo, R., Pastor, J. M., Zuriguel, I., Garcimartin, A. & Maza, D. 2007. The flow rate of granular materials through an orifice. *Granular Matter*, 9, 407-417.
- Marconi, U., Petri, A. & Vulpiani, A. 2000. Janssen's law and stress fluctuations in confined dry granular materials. *Physica A: Statistical Mechanics and its Applications*, 280, 279-288.
- Marshall, K. 1987. Compression and consolidation of powdered solids.In: Lachman,L., Liebermann, H., and Kanig,L. 3rd Ed *The Theory and Practice of Industrial Pharmacy*. Lea and Febiger. pp. 66-99.
- Martinez, M. A., Alfaro, I. & Doblaré, M. 2002. Simulation of axisymmetric discharging in metallic silos. Analysis of the induced pressure distribution and comparison with different standards. *Engineering Structures*, 24, 1561-1574.
- Matuttis, H., Luding, S. & Herrmann, H. 2000. Discrete element simulations of dense packings and heaps made of spherical and non-spherical particles. *Powder technology*, 109, 278-292.
- Mckenzie, H. & Hand, R. 1999. *Basic optical stress measurement in glass*. *Sheffield*: Society of Glass Technology
- Mcmahon, K. A. 2004. Practical botany—the Maltese cross. 25th workshop/conference of the association for biology laboratory education, 2004 Poland. 352-357.
- Medina, A., Cordova, J., Luna, E. & Trevino, C. 1998. Velocity field measurements in granular gravity flow in a near 2D silo. *Physics Letters A*, 250, 111-116.

- Michrafy, A., Dodds, J. & Kadiri, M. 2004. Wall friction in the compaction of pharmaceutical powders: measurement and effect on the density distribution. *Powder technology*, 148, 53-55.
- Michrafy, A., Kadiri, M. & Dodds, J. 2003. Wall friction and its effects on the density distribution in the compaction of pharmaceutical excipients. *Chemical Engineering Research and Design*, 81, 946-952.
- Michrafy, A., Ringenbacher, D. & Tchoreloff, P. 2002. Modelling the compaction behaviour of powders: application to pharmaceutical powders. *Powder Technology*, 127, 257-266.
- Misseroni, D., Dal Corso, F., Shahzad, S. & Bigoni, D. 2014. Stress concentration near stiff inclusions: validation of rigid inclusion model and boundary layers by means of photoelasticity. *Engineering Fracture Mechanics*, 121, 87-97.
- Muite, B. K., Quinn, S. F., Sundaresan, S. & Rao, K. K. 2004. Silo music and silo quake: granular flow-induced vibration. *Powder Technology*, 145(3), 190-202.
- Murthy, T. G., Gnanamanickam, E. & Chandrasekar, S. 2012. Deformation field in indentation of a granular ensemble. *Physical Review E*, 85.
- Muzzio, F. J., Goodridge, C. L., Alexander, A., Arratia, P., Yang, H., Sudah, O. & Mergen, G. 2003. Sampling and characterization of pharmaceutical powders and granular blends. *International Journal of Pharmaceutics*, 250, 51-64.
- Muzzio, F. J., Shinbrot, T. & Glasser, B. J. 2002. Powder technology in the pharmaceutical industry: the need to catch up fast. *Powder technology*, 124, 1-7.
- Nedderman, R. 1992. *Statics and kinematics of granular media*. Cambridge: Cambridge University Press, Cambridge, England.
- Nedderman, R. 1995. The use of the kinematic model to predict the development of the stagnant zone boundary in the batch discharge of a bunker. *Chemical Engineering Science*, 50, 959-965.
- Nedderman, R., Tüzün, U., Savage, S. & Houlsby, G. 1982. The flow of granular materials—I: Discharge rates from hoppers. *Chemical Engineering Science*, 37, 1597-1609.
- Nitka, M., Bilbie, B., Combe, G., Dascalu, C. & Desrues, J. A micro-macro (DEM-FEM) model of the behavior of granular solids. In: 1st International symposium on computational geomechanics (ComGeo I), Juan-les-Pins, France, 2009. 38-48.
- Nordstrom, J., Klevan, I. & Alderborn, G. 2009. A Particle Rearrangement Index Based on the Kawakita Powder Compression Equation. *Journal of Pharmaceutical Sciences*, 98, 1053-1063.

- Nordstrom, J., Welch, K., Frenning, G. & Alderborn, G. 2008. On the physical interpretation of the Kawakita and Adams parameters derived from confined compression of granular solids. *Powder Technology*, 182, 424-435.
- Oda, M. & Iwashita, K. 1999. *Mechanics of granular materials: an introduction*, Balkema, Rotterdam, The Netherlands. .
- Odeku, O. A. 2007. The Compaction of Pharmaceutical Powders. *Pharm Inf.-Latests Reviews* 5 (2). Available online at <http://www.pharmainfo.net/reviews/compaction-pharmaceutical-powders>, [Accessed May 05 2015].
- Ooi, J., Chen, J., Lohnes, R. & Rotter, J. 1996. Prediction of static wall pressures in coal silos. *Construction and Building Materials*, 10, 109-116.
- Ooi, J. Y. & She, K. M. 1997. Finite element analysis of wall pressure in imperfect silos. *International Journal of Solids and Structures*, 34, 2061-2072.
- Osei-Yeboah, F., Feng, Y. & Sun, C. C. 2014. Evolution of Structure and Properties of Granules Containing Microcrystalline Cellulose and Polyvinylpyrrolidone During High-Shear Wet Granulation. *Journal of pharmaceutical sciences*, 103, 207-215.
- Ostendorf, M. & Schwedes, J. 2005. Application of Particle Image Velocimetry for velocity measurements during silo discharge. *Powder Technology*, 158, 69-75.
- Ovryn, B. 2000. Three-dimensional forward scattering particle image velocimetry applied to a microscopic field-of-view. *Experiments in Fluids*, 29, S175-S184.
- Pakowski, Z. & Mujumdar, A. S. 2006. Drying of pharmaceutical products. In: MUJUMDAR, A. E. (ed.) *Handbook of Industrial Drying*. Singapor: Taylor & Francis Group, LLC. pp.689-712.
- Parikh, D. M. 2009. *Handbook of pharmaceutical granulation technology*, NY, Taylor & Francis Group, LLC.
- Paronen, P. 1986. Heckel plots as indicators of elastic properties of pharmaceuticals. *Drug Development and Industrial Pharmacy*, 12, 1903-1912.
- Parry, R. H. 2004. *Mohr circles, stress paths and geotechnics*, NY, Taylor & Francis Group, LLC.
- Pérez, S., Baldwin, P. & Gallant, D. 2009. Structural features of starch granules I. In: BEMILLER, J. & WHISTLER, R., 3RD. (eds.) *Starch: chemistry and technology* Academic Press, USA. pp.149-192.
- Perge, C., Aguirre, M. A., Gago, P. A., Pugnaloni, L. A., Le Tourneau, D. & Géminard, J.-C. 2012. Evolution of pressure profiles during the discharge of a silo. *Physical Review E*, 85, 2, 021303.

- Peters, J. F., Muthuswamy, M., Wibowo, J. & Tordesillas, A. 2005. Characterization of force chains in granular material. *Physical Review E*, 72,4, 041307.
- Pietrzak, M. & Leśniewska, D. 2012. Failure evolution in granular material retained by rigid wall in active mode. *Studia Geotechnica et Mechanica*, 34, 1-9.
- Post, D. 1989. *Photoelasticity*. In: Doyle JF, Phillips JW, editors. *Manual on experimental stress analysis*. 5th ed. Bethal: Society for Experimental Mechanics; 1989. p. 80-105.
- Powrie, W. 2004. *Soil mechanics: concepts and applications*, NY, Taylors & Francis Group, LLC.
- Prescott, J. K. & Barnum, R. A. 2000. On powder flowability. *Pharmaceutical technology*, 24, 60-85.
- Puglisi, A. 2001. *A numerical approach to the kinetics of driven and cooling granular gases* PhD, Sapienza University of Rome, Available online at <http://denali.phys.uniroma1.it/~puglisi/thesis/thesis.html>, [Accessed February 25 2015].
- Radjai, F., Jean, M., Moreau, J. J. & Roux, S. 1996. Force distributions in dense two-dimensional granular systems. *Physical Review Letters*, 77, 274-277.
- Radjai, F., Wolf, D. E., Jean, M. & Moreau, J. J. 1998. Bimodal character of stress transmission in granular packings. *Physical Review Letters*, 80, 61-64.
- Rahmanian, N. & Ghadiri, M. 2013. Strength and structure of granules produced in continuous granulators. *Powder Technology*, 233, 227-233.
- Rahmanian, N., Ghadiri, M. & Jia, X. 2011. Seeded granulation. *Powder Technology*, 206, 53-62.
- Rehula, M., Adamek, R. & Spacek, V. 2012. Stress relaxation study of fillers for directly compressed tablets. *Powder technology*, 217, 510-515.
- Ridgway, K. 1966. The use of photoelastic techniques in the measurement of die-wall stress in tabletting. *Journal of Pharmacy and Pharmacology*, 18, 176S-181S.
- Ridgway, K. & Rosser, P. 1971. The application of photoelastic techniques to a rotary tabletting machine. *Journal of Pharmacy and Pharmacology*, 23, 202S-209S.
- Riera, M. D., Istúriz, Á. & Prado, J. M. 2005. Experimental study of mass flow and apparent density in powder metallurgy die filling. European Powder Metallurgy, 2005 Praque. 175-181.
- Rosato, A. D. & Blackmore, D. L. 2000. IUTAM symposium on segregation in granular flows. In: GLADWELL, G. L. E. (ed.) *Solid Mechanics*. NJ: Springer.

- Rose, H. & Tanaka, T. 1959. Rate of discharge of granular materials from bins and hoppers. *The Engineer*, 208, 465-469.
- Rotter, J. M., Holst, J. M. F. G., Ooi, J. Y. & Sanad, A. M. 1998. Silo pressure predictions using discrete-element and finite-element analyses. *Philosophical Transactions of the Royal Society a-Mathematical Physical and Engineering Sciences*, 356, 2685-2712.
- Saad, R. E., Bonen, A., Smith, K. C. & Benhabib, B. 1996. Distributed-force recovery for a planar photoelastic tactile sensor. *Instrumentation and Measurement, IEEE Transactions on*, 45, 541-546.
- Saada, O. S. 2005. *Finite Element Analysis for Incipient Flow of Bulk Solid in a Diamondback Hopper*. PhD, University of Florida.
- Saikh, M. a. A. 2013. A technical note on granulation technology: a way to optimise granules. *Int J Pharm Sci Res*, 4, 55-67.
- Sajilata, M., Singhal, R. S. & Kulkarni, P. R. 2006. Resistant starch—a review. *Comprehensive reviews in food science and food safety*, 5, 1-17.
- Sakr, W. F., Ibrahim, M. A., Alanazi, F. K. & Sakr, A. A. 2012. Upgrading wet granulation monitoring from hand squeeze test to mixing torque rheometry. *Saudi Pharmaceutical Journal*, 20, 9-19.
- Santiago, J., Wereley, S., Meinhart, C., Beebe, D. & Adrian, R. 1998. A particle image velocimetry system for microfluidics. *Experiments in Fluids*, 25, 316-319.
- Sarkar, S., Ooi, S. M., Liew, C. V. & Heng, P. W. S. 2015. Influence of rate of force application during compression on tablet capping. *Journal of Pharmaceutical Sciences*, 104, 1319-1327.
- Sarraguca, M. C., Cruz, A. V., Soares, S. O., Amaral, H. R., Costa, P. C. & Lopes, J. A. 2010. Determination of flow properties of pharmaceutical powders by near infrared spectroscopy. *Journal of Pharmaceutical and Biomedical Analysis*, 52, 484-492.
- Schulze, D. 2008. *Powders and bulk solids: behavior, characterization, storage and flow*, Springer Berlin Heidelberg
- Senatore, C., Wulfmeier, M., MacLennan, J., Jayakumar, P. & Iagnemma, K. 2012. Investigation of stress and failure in granular soils for lightweight robotic vehicle applications. In: Proceedings of NDIA ground vehicle systems engineering and technology symposium modeling & simulation, testing and validation (MSTV) mini-symposium, 2012 Cambridge, MA. DTIC Document, 1-12.
- Shabana, H. 2006. The role of iodine treatment in enhancing the optical and structural properties of stretched nylon 6 fibres. *Journal of Physics D: Applied Physics*, 39, 2843-2850.

- Shah, R. B., Tawakkul, M. A. & Khan, M. A. 2008. Comparative evaluation of flow for pharmaceutical powders and granules. *Aaps Pharmscitech*, 9, 250-258.
- Shamai, K., Bianco-Peled, H. & Shimoni, E. 2003. Polymorphism of resistant starch type III. *Carbohydrate Polymers*, 54, 363-369.
- Shannon, J., Garwood, D. & Boyer, C. 2009. Genetics and physiology of starch development. In: BeMiller, J. & Whistler, R., 3rd (Ed). *Starch: chemistry and technology*. Academic Press, USA. pp.23-82.
- Shapiro, I. 1997. Compaction of powders XII. Evaluation of published compaction equations for modeling purposes. *Adv. Powder Metall. Part. Mat.*, 1, 22.
- Shapiro, I. & Kolthoff, I. 1947. Studies on the Aging of Precipitates and Coprecipitation. XXXVIII. The Compressibility of Silver Bromide Powders. *The Journal of Physical Chemistry*, 51, 483-493.
- Shi, L., Feng, Y. & Sun, C. C. 2011. Massing in high shear wet granulation can simultaneously improve powder flow and deteriorate powder compaction: A double-edged sword. *European Journal of Pharmaceutical Sciences*, 43, 50-56.
- Sielamowicz, I., Blonski, S. & Kowalewski, T. A. 2005. Optical technique DPIV in measurements of granular material flows, Part 1 of 3 - plane hoppers. *Chemical Engineering Science*, 60, 589-598.
- Sielamowicz, I., Czech, M. & Kowalewski, T. A. 2011. Empirical analysis of eccentric flow registered by the DPIV technique inside a silo model. *Powder Technology*, 212, 38-56.
- Sielamowicza, I., Blonski, S. & Kowalewski, T. A. 2006. Digital particle image velocimetry (DPIV) technique in measurements of granular material flows, Part 2 of 3-converging hoppers. *Chemical Engineering Science*, 61, 5307-5317.
- Siiriä, S. M., Antikainen, O., Heinämäki, J. & Yliruusi, J. 2011. 3D simulation of internal tablet strength during tableting. *Aaps Pharmscitech*, 12, 593-603.
- Singh, A. V. 2011. Biopolymers in drug deliver: A review. *Pharmacologyonline* 1. 62, 666-674.
- Singh, R., George, D. K., Benedict, J. B., Korter, T. M. & Markelz, A. G. 2012. Improved mode assignment for molecular crystals through anisotropic terahertz spectroscopy. *The Journal of Physical Chemistry A*, 116, 10359-10364.
- Sinha, T., Bharadwaj, R., Curtis, J. S., Hancock, B. C. & Wassgren, C. 2010. Finite element analysis of pharmaceutical tablet compaction using a density dependent material plasticity model. *Powder Technology*, 202, 46-54.

- Sinka, C. 2007. Modelling powder compaction. *KONA Powder and Particle Journal*, 25, 4-22.
- Sinka, I., Cunningham, J. & Zavaliangos, A. 2004. Analysis of tablet compaction. II. Finite element analysis of density distributions in convex tablets. *Journal of pharmaceutical sciences*, 93, 2040-2053.
- Slominski, C., Niedostatkiewicz, M. & Tejchman, J. 2007. Application of particle image velocimetry (PIV) for deformation measurement during granular silo flow. *Powder Technology*, 173, 1-18.
- Smith, A. M., Denyer, K. & Martin, C. R. 1995. What controls the amount and structure of starch in storage organs? *Plant physiology*, 107, 673-677.
- Smith, G. N. 1990 *Elements of soil mechanics* London, BSP Professional Books. .
- Smith Neto, P., Palma, E. & Figueiredo Bicalho, V. 2006. Stress Analysis in Automobile Components Using Reflexive Photoelasticity Technique. *Applied Mechanics and Materials*, 5, 117-124.
- Solanki, H. K., Basuri, T., Thakkar, J. H. & Patel, C. A. 2010. Recent advances in granulation technology. *Int J of Pharm Sci Rev Res*, 5, 48-54.
- Sonam, D., Pa, K., Jitendra, B. & Manoj, T. 2013. A Review: Roller Compaction for Tablet Dosage Form Development. *Research & reviews: Journal of pharmacy and pharmaceutical sciences*, 2, 68-73.
- Sonnergaard, J. M. 1999. A critical evaluation of the Heckel equation. *International Journal of Pharmaceutics*, 193, 63-71.
- Sorensen, A. H., Sonnergaard, J. M. & Hovgaard, L. 2005. Bulk characterization of pharmaceutical powders by low-pressure compression. *Pharmaceutical Development and Technology*, 10, 197-209.
- Sorensen, A. H., Sonnergaard, J. M. & Hovgaard, L. 2006. Bulk characterization of pharmaceutical powders by low-pressure compression II: Effect of method settings and particle size. *Pharmaceutical Development and Technology*, 11, 235-241.
- Srivastava, S. & Mishra, G. 2010. Fluid bed technology: overview and parameters for process selection. *International Journal of Pharmaceutical Sciences and Drug Research*, 2, 236-246.
- Staniforth, J. & Aulton, M. 2002. Powder flow. *Pharmaceutics: the science of dosage form design*, 197-210.
- Starches 2015. Micromagus.net: Starches. [online] Available at: <http://www.micromagus.net/pharma/starch.html> [Accessed 02 Jan. 2015].

- Steingart, D. A. & Evans, J. W. 2005. Measurements of granular flows in two-dimensional hoppers by particle image velocimetry. Part I: experimental method and results. *Chemical Engineering Science*, 60, 1043-1051.
- Sujka, M. & Jamroz, J. 2007. Starch granule porosity and its changes by means of amylolysis. *International agrophysics*, 21, 107-113.
- Sujka, M. & Jamroz, J. 2010. Characteristics of pores in native and hydrolyzed starch granules. *Starch-Stärke*, 62, 229-235.
- Sun, C. & Grant, D. J. 2001. Influence of elastic deformation of particles on Heckel analysis. *Pharmaceutical development and technology*, 6, 193-200.
- Tan, S. & Fwa, T. 1991. Influence of voids on density measurements of granular materials using gamma radiation techniques. *Geotechnical Testing Journal*, 14, 257-265.
- Tardos, G. I., Mcnamara, S. & Talu, I. 2003. Slow and intermediate flow of a frictional bulk powder in the Couette geometry. *Powder Technology*, 131, 23-39.
- Tekade Bharat, W., Chaudhari Yogita, A. & Patil Vijay, R. 2011. Evaluation of acacia catechu gum as a binder in tablet formulations. *Int.J.Res.Pharm.Sci*, 2(4), 616-620.
- Teng, J., Zhao, Y. & Lam, L. 2001. Techniques for buckling experiments on steel silo transition junctions. *Thin-walled structures*, 39, 685-707.
- Thornton, C. & Antony, S. J. 1998. Quasi-static deformation of particulate media. *Philosophical Transactions of the Royal Society a-Mathematical Physical and Engineering Sciences*, 356, 2763-2782.
- Tordesillas, A., Walker, D. M. & Lin, Q. 2010. Force cycles and force chains. *Physical Review E*, 81, 011302.
- Tousey, M. D. 2002. The granulation process 101, basic technologies for tablet making. *Pharm. Technol. (Tableting and Granulation)*, 1, 8-13.
- Train, D. 1956. An investigation into the compaction powders. *Journal of Pharmacy and Pharmacology*, 8, 745-761.
- Train, D. 1957. Agglomeration of solids by compaction. *Trans. Inst. Chem. Eng*, 35, 258-262.
- Tüzün, U. & Nedderman, R. 1982. An investigation of the flow boundary during steady-state discharge from a funnel-flow bunker. *Powder Technology*, 31, 27-43.
- Ulissi, F., Ippolito, I. & Calvo, A. 2009. PIV Technique applied to granular flows in hoppers. X Meeting on recent advances in the physics of fluids and their

applications, Conference Series 166 2009 Argentina. Journal of Physics, 012004.

- Vidyapati, V. & Subramaniam, S. 2013. Granular flow in silo discharge: discrete element method simulations and model assessment. *Industrial & Engineering Chemistry Research*, 52, 13171-13182.
- Walker, D. M. 1966. An Approximate Theory for Pressures and Arching in Hoppers. *Chemical Engineering Science*, 21(11), 975-997.
- Walker, D. M. & Blanchard, M. 1967. Pressures in Experimental Coal Hoppers. *Chemical Engineering Science*, 22(12), 1713-1745.
- Walker, E. 1923. The properties of powders. Part VI. The compressibility of powders. *Trans. Faraday Soc.*, 19, 73-82.
- Walters, J. 1973a. A theoretical analysis of stresses in axially-symmetric hoppers and bunkers. *Chemical Engineering Science*, 28, 779-789.
- Walters, J. 1973b. A theoretical analysis of stresses in silos with vertical walls. *Chemical Engineering Science*, 28, 13-21.
- Wambaugh, J. F., Hartley, R. R. & Behringer, R. P. 2010. Force networks and elasticity in granular silos. *European Physical Journal E*, 32, 135-145.
- Wang, W., Gu, W. & Liu, K. 2015. Force chain evolution and force characteristics of shearing granular media in taylor-couette geometry by DEM. *Tribology Transactions*, 58, 197-206.
- Wang, Y., Lu, Y. & Ooi, J. Y. 2013. Numerical modelling of dynamic pressure and flow in hopper discharge using the Arbitrary Lagrangian-Eulerian formulation. *Engineering Structures*, 56, 1308-1320.
- Wang, Y. & Ooi, J. Y. 2015. A Study of granular flow in a conical hopper discharge using discrete and continuum approach. *Procedia Engineering*, 102, 765-772.
- Waters, A. & Drescher, A. 2000. Modeling plug flow in bins/hoppers. *Powder Technology*, 113, 168-175.
- Watson, G. R. & Rotter, J. M. 1996. A finite element kinematic analysis of planar granular solids flow. *Chemical Engineering Science*, 51, 3967-3978.
- Wehner, R. 2001. Polarization vision—a uniform sensory capacity? *Journal of Experimental Biology*, 204, 2589-2596.
- Westerweel, J. 2000. Theoretical analysis of the measurement precision in particle image velocimetry. *Experiments in Fluids*, 29, S003-S012.
- Whistler, R. L. & Bemiller, J. N. 1997. Carbohydrate chemistry for food scientists. MN, U.S.A: Eagan Press.

- Willert, C. & Gharib, M. 1991. Digital particle image velocimetry. *Experiments in Fluids*, 10, 181-193.
- Wu, C.-Y. & Cocks, A. C. 2006. Numerical and experimental investigations of the flow of powder into a confined space. *Mechanics of Materials*, 38, 304-324.
- Wu, C.-Y., Ruddy, O., Bentham, A., Hancock, B., Best, S. & Elliott, J. 2005. Modelling the mechanical behaviour of pharmaceutical powders during compaction. *Powder Technology*, 152, 107-117.
- Wu, C. Y. 2008. DEM simulations of die filling during pharmaceutical tabletting. *Particuology*, 6, 412-418.
- Wu, C. Y., Dihoru, L. & Cocks, A. C. F. 2003. The flow of powder into simple and stepped dies. *Powder Technology*, 134, 24-39.
- Xu, J.-M., Cheng, C.-H. & Lu, H.-P. 2011. Strain field investigation of limestone specimen under uniaxial compression loads using particle image velocimetry. *Journal of Central South University of Technology*, 18, 1619-1625.
- Xu, P., Duan, X., Qian, G. & Zhou, X.-G. 2015. Dependence of wall stress ratio on wall friction coefficient during the discharging of a 3D rectangular hopper. *Powder Technology*, 284, 326-335.
- Yohannes, B., Gonzalez, M., Abebe, A., Sprockel, O., Nikfar, F., Kang, S. & Cuitino, A. M. 2015. The role of fine particles on compaction and tensile strength of pharmaceutical powders. *Powder Technology*, 274, 372-378.
- Zhang, J., Majmudar, T. & Behringer, R. 2008. Force chains in a two-dimensional granular pure shear experiment. *Chaos*, 18, 41107.
- Zhang, N. H. & Rosato, A. D. 2004. Analysis of instantaneous dynamic states of vibrated granular materials. *Mechanics Research Communications*, 31, 525-544.
- Zhao, Y. & Teng, J. 2004. Buckling experiments on steel silo transition junctions: I: Experimental results. *Journal of Constructional Steel Research*, 60, 1783-1801.
- Zheng, Q. J. & Yu, A. B. 2015. Finite element investigation of the flow and stress patterns in conical hopper during discharge. *Chemical Engineering Science*, 129, 49-57.
- Zobel, H. 1988. Starch crystal transformations and their industrial importance. *Starch-Stärke*, 40, 1-7.